STUDY OF RUTHENIUM-BASED BARRIER LAYER FOR COPPER METALLIZATION

MARTINA DAMAYANTI

School of Materials Science and Engineering

A thesis submitted to the Nanyang Technological University
in fulfillment of the requirement for the degree of
Doctor of Philosophy

2009

ACKNOWLEDGEMENT

First and foremost, I would like to express my gratitude and thanks to God; without His will, I would not have made it this far.

I am very grateful to my supervisor, Assoc. Prof. Thirumany Sritharan for his guidance, support and constant encouragement throughout the course of the research work. I would like to thank Assoc. Prof. Subodh G. Mhaisalkar for all the necessary supports. Furthermore, his enthusiasm and words of advice on non-technical side have been a constant motivation for me.

I am indebted to Dr Li Yibin and Dr Gan Zhenghao from Materials Science and Engineering for helping me especially on x-ray photoelectron spectroscopy analyses. I really appreciate their constructive remarks throughout all the discussions. I would like to acknowledge Dr Hans-Juergen Engelmann and Dr Ehrenfried Zschech from Materials Analysis Department, Advanced Micro Devices in Dresden, Germany for the enriching collaboration. Their constant support during the three months fruitful attachment has been very valuable.

I would like to extend my thanks to Dr Lap Chan and Dr Ng Chee Mang, my advisors from Chartered Semiconductor Manufacturing Ltd., Singapore for their teaching, guidance and advice.

I thank all the technical staff in Microelectronics laboratory, Heryani, Mastura and Sandy Leong for their support on lab expendables, furnace, magnetron sputtering system, and electrical measurement set up. I also want to mention people in the laboratory of Electron Microscopy & X-ray Diffraction, Guo Jun, Irene Heng and Wang Lee Chin for their assistance and support.

I thank all my friends for the cherished friendship and precious time spent together. Finally, I would like to present deep appreciations to my husband, my little girl and my big family for the endless love, encouragements, understanding and supports during the years.

TABLE OF CONTENTS

LIST OF TABLES

LIST OF FIGURES

ABSTRACT

Bilayer of Ta/TaN is the common diffusion barrier for Cu metallization in microelectronics. However, this bilayer is not conducive for electrochemical plating of Cu as it has a poor seeding ability. Consequently, an additional seed layer becomes inevitable. As the feature size of interconnects has become smaller, the composite barrier cum seed layer has become disproportionately thick in comparison to via/trench dimensions and hence the search for a thinner composite layer is taking technological importance. One obvious avenue to explore is a single layer that could provide adequate barrier function while serving as an effective seed for Cu nucleation. Some recent work indicates that Ru is a probable candidate for this purpose. Hence, this project was launched to conduct a systematic investigation into the barrier properties of Ru.

The performance of pure Ru was examined in the first phase with and without Ta, in a Cu/low-κ system. Pure Ru was found to promote the nucleation of the beneficial Cu(111) texture in the Cu overlayer when compared to seeding on pure Ta. Adhesion tests indicated sufficient adhesion strength of ~6 J/m^2 in Ru/low-κ interface which is comparable to that in Ta/low-κ interface (~6.5 J/m^2). The barrier performance was assessed in Cu/Si, Ru/Si, and Cu/Ru/Si systems. Barrier failure could be detected at relatively low temperatures in the resistivity of the films, which ultimately led to detectable silicide formation at higher temperatures.

Attempts were made to improve the barrier performance in the second phase of this project. It was envisaged to obstruct the easy grain boundary diffusion path by dissolving N atoms in Ru, in order to "stuff" the grain boundaries. This however led to amorphization of the Ru thin film and increased its sheet resistance almost 10 fold. Annealing at temperatures higher than 250°C caused out diffusion of dissolved N, accompanied by crystallization and a sharp decrease in sheet resistance. The rejected N was found to form voids at the Cu/Ru interface. The amorphous Ru-N film gave a better barrier performance than pure Ru until it was annealed at temperatures above 250°C.

Silicide formation was not detected until 900°C in Ru-N/Si system while it reduced to 700°C when the Cu overlayer was present (in Cu/Ru-N/Si).

To improve the thermal stability of Ru-N film and to suppress the out diffusion of N, addition of a nitride forming element (W or Ta) was investigated in the third phase of the project. Ru films containing W and N (Ru-W-N) and, Ta and N (Ru-Ta-N) were investigated in this context. It was found N was actually in the form of nitrides in these films although x-ray diffraction could not detect any nitride phases. Ru crystallization and N out diffusion were delayed to about 500 - 600°C. Further, a N enriched layer was found at the film/substrate interface in Ru-W-N film when annealed at 400°C. This implies the formation of a self assembled bilayer of Ru-rich top layer (which can be a good seed layer) and a N/W-rich under layer (which is equivalent to a nitride barrier layer) in the Ru-W-N film. Such a self assembled bilayer was not evident in Ru-Ta-N film.

This project has provided a fundamental understanding of the behaviour of pure Ru as a barrier cum seed layer. A method of improving the barrier performance of pure Ru by alloying with N and, W or Ta, is proposed. An interesting formation of a self assembled bilayer whose chemistry is well suited for the intended barrier cum seed function is disclosed.

CHAPTER 1

INTRODUCTION

1.1 Background

As integrated circuits are scaled down to achieve miniaturization and greater integration, the quality of thin film interconnections is becoming a critical factor that determines their performance and reliability. The *RC* interconnection delay is one of the most important factors influencing circuit performance, where *R* is resistance of the interconnection and *C* is its associated total capacitance. Reducing *RC* delay to lower than or to equal to device delay has become both a material as well as an interconnection design/architecture challenge.

During past decades, aluminum has been the most widely used material for metallization in very large-scale (VLSI) and ultra large-scale (ULSI) integrated circuits. However, as critical dimensions of devices have approached submicron levels, requirement for an increased reliability demands materials with improved properties compared to pure aluminum. Aluminum alloys with different additives (Si, Cu, Ti, Pd, Cr, Mg and Mn) have been examined to improve reliability but the improvement in electromigration (EM) resistance remains limited and is offset by a corresponding increase in interconnection resistivity [1]. In consequence, a radical change in the metallization material is required. Cu is a good candidate material in this regard.

Hence, importance has been placed on switching from Al/W based to Cu based interconnections to reduce the interconnect resistance. Research on low-κ

dielectric material development has been underway concurrently to decrease parasitic capacitance. Unfortunately, interaction between Cu and Si is rapid and detrimental to the electrical performance of Si even at temperatures below 200°C [2-4]. Cu also has high mobility in SiO_2 and low-κ dielectric materials and also can easily corrode upon exposure to moisture or oxygen [5]. Therefore, it is necessary to include a diffusion barrier and an encapsulation layer into Cu metallization scheme. In addition, utilization of Cu in IC metallization requires a continuous seed layer to enable Cu electrodeposition process. Kim *et al.* [6] reported that electrodeposition is the most preferred method out of the several deposition techniques available to Cu metallization, owing to its excellent superconformal filling capability.

1.2 Motivation for Studying Ru-based Barrier Layers

(1) Current Challenges with PVD Ta/TaN Barrier

The barriers currently used in 130 nm technology node are PVD Ta/TaN bilayers. The applicability of this Ta/TaN bilayer barriers has been extended down to 90 nm node and is likely to go down up to 65 nm node [7]. However, if lines shrink further, PVD-deposited barriers cannot be made thin enough and the option would be to move towards CVD or ALD deposition techniques. Some reports are available on the use of ALD for Ta [8] and TaN [9, 10] deposition.

While PVD TaN is really N-doped tantalum with an approximate stoichiometry of $TaN_{0.5}$ which has a resistivity < 200 μΩ.cm, ALD TaN tends to be the stochiometric TaN with much higher resistivity of the order of mΩ.cm.

The high nitrogen content and the amorphous structure obtained in ALD TaN are responsible for the good barrier properties of this film. Generally, organometallic precursors are used for ALD TaN and depending on the choice of the precursor, residual carbon could become an issue. Carbon concentrations from 2 at% up to 10 at% have been reported in these films. At ~10 at% carbon, the film has an approximate chemical composition of $TaN_{0.09}C_{0.1}$ which has a very high resistivity of 1 mΩ.cm [11].

While the nitrides of Ta can be fabricated using organometallic precursors, metallic Ta requires the use of halogen precursors (such as $TaCl_5$) [12]. Halogen precursors are a well known corrosion risk for the Cu metallization.

(2) Current Challenges with PVD Cu Seed Layer

There are some challanges for PVD-deposited Cu seed layer:

a. It must be deposited in the correct thickness
   - It needs to be thin enough to avoid overhang at the top of high-aspect-ratio features which can cause pinch off and create voids.
   - It also must not be too thin. If the Cu seed layer is too thin, the whole thickness will get oxidized readily in atmosphere. During electroplating process, the oxide will be easily dissolved in plating solution. This could result in a discontinuous seed layer and give a low quality plated Cu with voids. A discontinuous seed layer will also lead to poor adhesion strength which eventually can cause peeling of a Cu layer during the chemical mechanical planarization

(CMP) process [13, 14]. Another problem with a thin Cu seed layer is that there will be a very large voltage drop between wafer edge and center, resulting in non-uniform plating [11].

b. Additionally as feature size shrinks, it is difficult to deposit a continuous and thin PVD Cu seed layer into a high-aspect-ratio feature by sputter technique due to its intrinsically poor step coverage [15]. Several studies [16, 17] have reported the use of an advanced Cu seed layer deposition methods, such as the metalorganic chemical vapor deposition (MOCVD) because of their higher conformal characteristics. However, it was reported that Cu seed film deposited by MOCVD has a very rough surface and a poor adhesion strength [18].

(3) Ru for Rescue

With the requirement of an additional Cu seed layer deposited on Ta/TaN, Cu-seed/Ta/TaN trilayer configuration will encounter scaling difficulties at 45 nm node where an ultrathin ($\leq$ 5 nm) diffusion barrier is needed to scale IC technology while maintaining a low effective interconnect resistivity [19]. A single-layer, Cu-plateable diffusion barrier is desirable to optimize overall integration by eliminating the need for PVD Cu seed layer in the advanced 65 and 45 nm nodes [20, 21]. However, refractory metals such as W, Ta, and Ti, which are used as barriers for Al cannot be used for direct Cu plating due to the formation of a native surface oxide which limits adhesion to Cu. In order to avoid this adhesion problem, metals that form oxides which are less stable than those of Cu should be considered. Thus the motivation for this project is to identify and characterize a new material that can serve both as a diffusion barrier as well as a seed layer for Cu metallization scheme.

Lane *et al.* [22] recommends a group of materials, namely Pt, Pd, Ru, Rh, Ir, Ag, Te, and Tc as probable candidates for barrier cum seed layer application in Cu metallization based on the relative oxide stability in the acidic Cu plating condition. It is required that the metal must be able to form less stable oxide compared to Cu-oxide during electroplating ($|\Delta G_f^0$ (M-O)$|$ < $|\Delta G_f^0$ (Cu-O)$|$). The probable candidates with their enthalpy of formation (kcal/mol) of metal oxide per oxygen atom are listed in Table 1.1.

Table 1.1 Enthalpy of formation (kcal/mol) of metal oxide per oxygen atom [22]

Metal	Cu	Pt	Pd	Ru	Rh	Ir	Ag
$\|\Delta H_f^0$ (M-O)$\|$	39	10	20	18	27	33	5

Recent research and development works appear to indicate that Ru is a leading candidate among these potential materials. Below are some characteristics of Ru which promote it as a strong candidate for this application:

- Ru is an air-stable transition metal and has a high melting point (2310°C).
- Ru has lower resistivity than the currently used barriers (Ta, TaN, and Ta/TaN bilayer) as shown in resistivity data listed in Table 1.2.
- As shown in the binary Ru-Cu phase diagram [23], Ru and Cu show negligible solid solubility in each other even at 900°C (Figure 1.1).
- Ru and Cu do not appear to form any intermediate phases even when annealed at 800°C, as reported by Chyan *et al.* [24].
- Electroplatability of Cu on polycrystalline and single crystal Ru has been reported by several workers in the literatures [24-28].

- Ru could reportedly promote the beneficial Cu(111) texture [24, 29]. Enhanced Cu(111) texture has been shown to reduce defects at Cu/diffusion barrier interface, which further improves electromigration reliability of the Cu interconnects [30].
- The adhesion reported between Cu and Ru in Cu/(20 nm) Ru/Si stacks measured using scribe and tape-peel test has been good [29].
- Annealing of Cu/Ru sample up to 600°C does not cause any de-wetting (buckling or delamination) of Cu from Ru [24].
- Ru can function as a directly plateable Cu diffusion barrier [24, 29, 31, 32].
- Successful seedless superfill with Ru barrier has been reported [31, 32].

Table 1.2 Resistivity data of some diffusion barrier and seed materials at room temperature [33]

Metals	ρ (μΩ.cm)
Ti	42
Ta	13.5
TaN	300 - 1800 [34]
Ru	7.1
W	5
Al	2.65
Cu	1.7
Ag	1.6

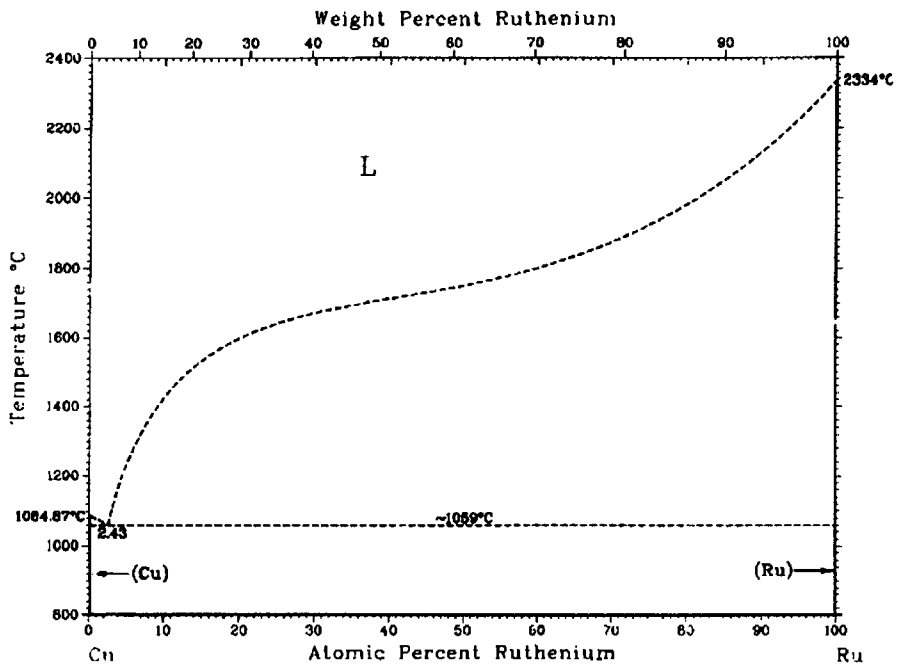

Figure 1.1 Cu-Ru phase diagram [23]

1.3 Objectives

In view of the information available in the literature and the pressing need for a single material barrier cum seed layer for Cu metallization, the objectives of this project are formulated as follows:

- To investigate the suitability of Ru and some of its alloys for barrier cum seed application for Cu metallization.
- To understand properties of different Ru-based barrier layers and their effects on Cu diffusion and reaction under thermal annealing.
- To study reliability, stability, and interdiffusion characteristics of these layers when subjected to high temperature annealing (reaction mechanism, phase formation sequence, etc.).
- To obtain a better understanding on Ru-based barriers failure mechanisms resulting from their microstructures and thermal stabilities.

It must be noted that the emphasis remain in its barrier performances than the seeding ability because this aspect has not been adequately investigated by anybody previously. Limited investigation will be carried out on Ru seeding ability to confirm literature reports.

CHAPTER 2

LITERATURE REVIEW

2.1 Interaction of Cu with Si

In order to study a diffusion barrier layer for Cu, an understanding of the physics of Cu in Si is necessary. Copper belongs to 3d transition metals group in periodic table. Electronic structure of 3d transition metals in vacuum is $1s^1 2s^2 2p^6 3s^2 3p^6 3d^x 4s^2$, where x varies from 1 for ^{21}Sc to 10 for ^{30}Zn. However, ^{29}Cu is the only 3d element whose electronic structure violates this rule. Instead of the $3p^6 3d^9 4s^2$ configuration, one of 4s electrons is moved to 3d shell to complete it, leaving Cu in an irregular electron configuration: $3p^6 3d^{10} 4s^1$ [35]. The simplest model for electron configuration of interstitial Cu in Si is identical to that in vacuum i.e. $3d^{10} 4s^1$ for neutral charge state (Cu_i^0) and $3d^{10}$ for positively charged state (Cu_i^+). Since interstitial Cu is a shallow, single donor in Si [36], it is always in the ionized state (Cu_i^+) [35].

Another feature of Cu in Si which distinguishes it from the other 3d metals, is that it forms a Cu-rich silicide, Cu_3Si, with a much larger unit cell volume than that of Si [35]. It has been reported by Liu *et al.* [36] that when Cu is directly deposited on Si crystals, Cu_3Si forms readily at moderate temperatures (e.g. 200°C). Figure 2.1 shows that the first phase to form in Cu-Si system is orthorhombic η'' Cu_3Si phase.

The extremely high diffusivity of Cu in Si, which is a consequence of its small ionic radius and its relatively weak interaction with Si lattice, makes it highly mobile at room temperature [35]. Therefore, the diffusion barriers for Cu

can not be successfully characterized using the same techniques developed for Al diffusion barriers [35].

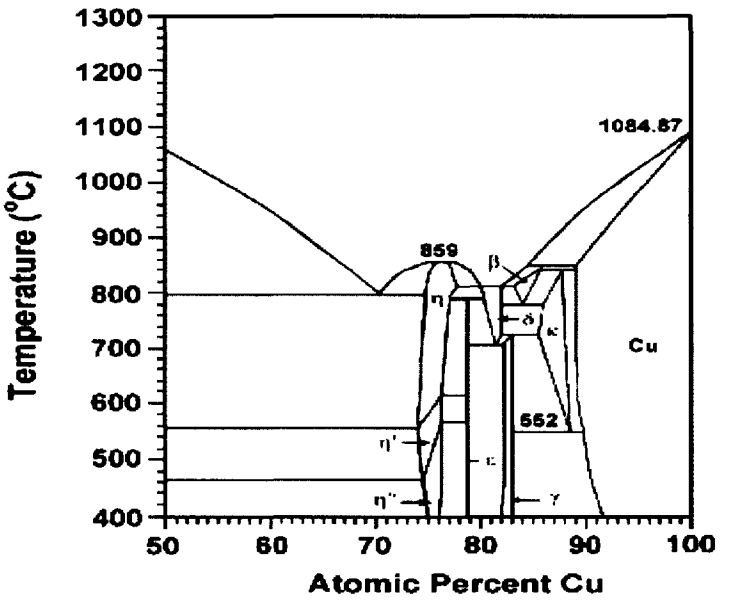

Figure 2.1 Cu-Si phase diagram [23]

According to Hull [37], diffusivity of Al in Si is less than 10^{-20} cm^2/s at 500°C which is very small in comparison to Cu in Si (~2 x 10^{-5} cm^2/s at 500°C). Therefore, if Al penetrates through the barriers it will only agglomerate at a spot where it has penetrated without diffusing any further into the wafer. The detrimental effect of Al arises primarily from its reaction with barrier material and accumulation of Al at Si/diffusion barrier interface.

In contrast to Al, Cu is an extremely fast diffuser in Si. Diffusion coefficient of Cu at 500°C is 15 orders of magnitude higher than that of Al. This means that when a local penetration of Cu through the barrier occurs at a spot, it can result in contamination of about 45 mm^2 of the die in 30 min at 500°C whereby Cu concentration in the contaminated area may reach its solubility limit of 10^{14} cm^{-3} at 500°C [35]. Moreover, since Cu remains mobile even after

the wafer has been removed from the furnace; it can diffuse by significant distances in the substrate from a local barrier breakdown spot until it finds stable sinks [35].

2.2 The Concept of Diffusion Barrier

Harmful interactions betweens Si and Cu impose the use of diffusion barriers in order to reliably fabricate Cu-metalized integrated circuits. The most important barrier properties are considered in this section. First, a concept of a diffusion barrier is introduced and then several materials systems that are viable candidates for diffusion barrier applications in Cu-based metallization are classified. Finally, several diffusion barrier solutions found from the literature are summarized.

2.2.1 Barrier Requirements

The concept of barrier layers in metallization systems is to separate two materials that have unfavorable chemical interaction by an intermediate layer. If a barrier layer X separates two materials A and B, such a barrier should posses several features, which include [38, 39]:

1) It should be thermodynamically stable in contact with both A and B.
2) X should prevent interdiffusion between A and B. Thus, diffusivity of both materials A and B in barrier layer should be very low.
3) The barrier layer should form low resistance contacts with both materials A and B and be, at least, a reasonable thermal conductor. Resistivity of the barrier layer itself is usually not too significant up to a

certain value (< 2500 μΩ.cm) [40] because of its small thickness compared to that of materials A and B.

4) X should adhere well to materials A and B in the metallization scheme. This implies that some reactivity is required in order to establish good adhesion between the barrier and the materials A and B.
5) The material X should not have an electrochemical potential very different from that of A and B in order to avoid formation of galvanic corrosion cells with the metallization layers.
6) Stresses of the order of GPa exert significant effects upon thin-film diffusion processes [41]. Therefore, stresses in the barrier layer should not be too high.

As can be seen from the list of requirements, compromises are often needed and some contradictions cannot be avoided. In addition to above physicochemical demands, there are also process conditions related to step coverage, capability of selective patterning, reasonable rate and ease of deposition etc. that must be fulfilled by a satisfactory diffusion barrier.

Furthermore, the continued shrink in device dimensions requires a continuous reduction in barrier thickness to maximize space availability for the actual Cu conductor to maintain an effective resistivity of 2.2 μΩ.cm as defined by the International Technology Roadmap for Semiconductor (ITRS) [19]. The maximum allowable barrier thickness for minimum-pitch Cu global wiring is predicted to decrease from 12 nm (for 130 nm device node) to 6 nm (for the 70 nm device node) according to the ITRS prediction tabulated in Table 2.1. Such severe reduction in barrier thickness places significantly more stringent

requirements on barrier integrity, continuity, conformality, and stability for successful integration into Cu-based metallization schemes.

Table 2.1 ITRS prediction for barrier layer thickness [19]

	Near Term								
Year	2003	2004	2005	2006	2007	2008	2009		
Device node (nm)	130		100			70			
Barrier thickness (nm)	12	10	9	8	7	6	6		
	Long term								
Year	2010	2011	2012	2013	2014	2015	2016	2017	2018
Device node (nm)		50			35				
Barrier thickness (nm)	4.9	4.5	4	3.6	3.3	2.9	2.5	2.2	2

2.2.2 Barrier Classification

Practical diffusion barriers are generally divided into three categories [39] as schematically presented in Figure 2.2:

(i) Sacrificial barriers

The concept of a sacrificial barrier is that the barrier layer X reacts with either or both of the materials A and B in a laterally uniform manner with characterized reaction rates. Effectiveness of this type of barrier is determined by the reaction rate. As long as the barrier layer is not completely consumed in the reactions, separation between the materials A and B will be effective. Therefore, reaction rate between X and A or/and B should not be too high in

order to have a useful barrier life. The existence of a definite lifetime is a major limitation of sacrificial barriers.

For a more permanent protection, the barrier layer X should be thermodynamically stable with A and B. This means that there should be no driving forces for reactions at the interfaces, A/X and X/B. This is a necessary but not a sufficient condition for a stable diffusion barrier. It is also necessary to prevent diffusion of A and B across X via short-circuits paths, since there could still be a driving force for diffusion. The diffusion rate could be limited by eliminating the short-circuit paths or by filling the easy paths with appropriate atoms/molecules to increase obstacles for diffusion [39].

(ii) Stuffed barriers

The latter approach suggested above leads to the concept of "stuffed" barriers. When atoms of A and B cannot use the short-circuit paths (as they are now occupied by the deliberately introduced foreign atoms or molecules) diffusion rate is slowed down considerably by several orders of magnitude.

(iii) Amorphous diffusion barriers

The elimination of short-circuit paths can also be achieved by removing the grain boundaries by making the barrier amorphous. It is emphasized that amorphous layers are metastable and will crystallize on exposure to high temperature. When crystallization takes place, grain boundaries are formed. Thus, crystallization temperature of amorphous layer will be of critical importance in choosing amorphous barriers.

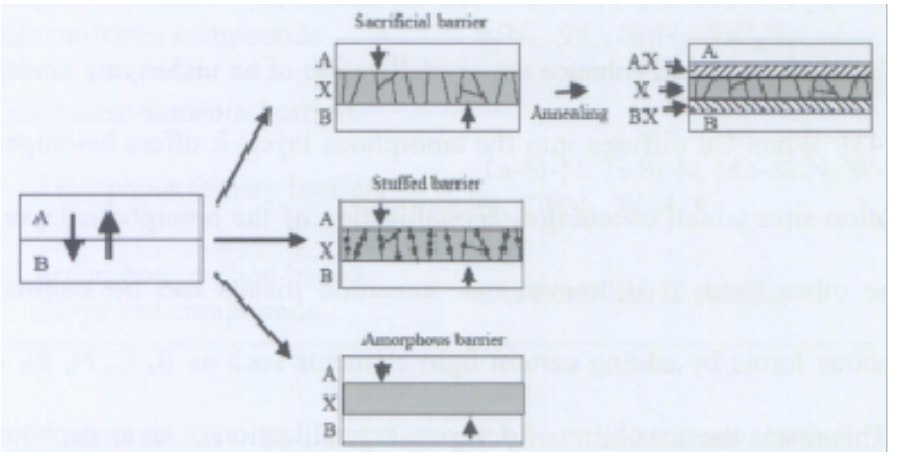

Figure 2.2 Schematic illustrations of the three classes of diffusion barriers [42]

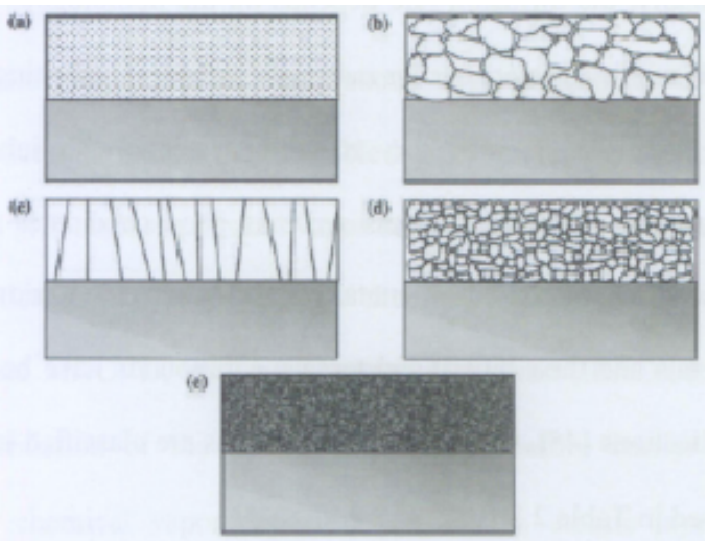

Figure 2.3 Classification of barrier material based on the microstructure (a) single crystal (b) polycrystalline (c) polycrystalline columnar (d) nanocrystalline and (e) amorphous [42]

Diffusion barriers can also be classified by their microstructures as shown in Figure 2.3. The most preferred barrier microstructure is single crystalline, but achieving this in practice means epitaxial layer growth of complex materials which is beyond the capabilities of current technologies. A practical second choice is an amorphous structure; however, this contradicts the requirement of the structural stability due to the metastable nature of amorphous materials. Amorphous materials generally have a considerably large driving

force for crystallization [39]. It has been experimentally found that the presence of a Cu overlayer could enhance the crystallization of an underlying amorphous film [43]. When Cu diffuses into the amorphous layer, it offers heterogeneous nucleation sites which encourages crystallization of the amorphous layer [43]. On the other hand, it is known that transition metals can be stabilized in amorphous forms by adding certain light elements such as B, C, N, Si, and P [44]. This opens the possibility of delaying crystallization of an amorphous film in contact with crystalline Cu overlayer by choosing appropriate additives.

Additionally, the diffusion rate depends on the homologous temperature. Hence, it is desirable to select barrier materials with a high melting point as the host lattice. Accordingly, refractory metallic systems with inherently high melting points and chemical inertness serve as good candidates for diffusion barrier applications in Cu-based metallization schemes. Various refractory transition metals and their binary and ternary compounds have been suggested for such applications [45]. These materials systems are classified into six major groups as listed in Table 2.2.

Table 2.2 Classification of barrier materials

	Barrier type	Example
1.	Refractory metal	Cr, Ti, Ta, W, Mo, Co, Pd, Nb
2.	Refractory metal alloy	TiW, FeW, NiNb, NiMo, IrTa, IrZr
3.	Refractory metal-silicide	$TiSi_2$, $CoSi_2$, WSi, $TaSi_2$, Mo_xSi_{1-x}, $Ta_{74}Si_{26}$, and $CrSi_2$
4.	Refractory metal	
	Nitrides	TiN, TaN, Ta_2N
	Oxides	RuO_2, MoO
	Carbides	TiC, TaC
	Borides	TiB_2

5.	Silicon-based compounds	SiN_x, SiC, Si_3N_4, SiC_xN_y
6.	Other miscellaneous barriers	
	Amorphous ternary barriers	Ta-Si-N, Ti-Si-N, Mo-Si-N, W-Si-N, $TiPN_2$, W-B-X
	Amorphous carbon-based alloys and compounds	Diamond-like C coating

Of all these, W-, Ta-, and Ti-based binary and ternary compounds are the most widely used and studied materials owing to their desirable physical, chemical, and electrical properties.

In addition to materials, continuous developments have occurred on deposition process to realize the desirable barrier microstructure, conformality, and thickness [42] such as physical vapor deposition (PVD), inorganic chemical vapor deposition (CVD), metal-organic chemical vapor deposition (MOCVD), plasma-assisted MOCVD, ion beam-assisted deposition (IBAD), hybrid barrier (selective nitridation of the interlayer dielectric before barrier deposition), atomic layer chemical vapor deposition (ALCVD), atomic layer deposition (ALD), etc.

2.2.3 Diffusion Barriers in the Literature

For Al-based metallization, Ti and TiN are the most commonly used materials as a diffusion barrier/adhesion promoter to improve the wettability and texture of the Al interconnects and enhance its mechanical stability. In the case of Cu, the need for a diffusion barrier is even more critical in view of the high diffusivity of Cu into Si and SiO_2. Since Ti/TiN are widely employed in Al- and W-based interconnect systems, the possibility of extending their

applicability to Cu-based interconnects represents a highly attractive option, both technically and economically. Unfortunately, Ti and TiN have not been able to provide adequate Cu barrier performance for thickness at or below 20 nm [46]. A Ti barrier failed primarily through a metallurgical reaction with Cu, which occurred readily at 350°C, while TiN typically failed through grain boundary diffusion [42].

The most frequently proposed diffusion barriers for Cu metallization are based on refractory metals as well as their binary and ternary nitrides and carbides. The binary compounds rely on their excellent stability. The ternary films can also be classified in the same category, but their unique property is the amorphous structure, which is produced in order to slow down the diffusion processes in these barriers. Several material combinations have been deposited by a variety of techniques for use as barrier layers. Table 2.3 summarizes them along with reported maximum working temperature above which their barrier performance fails.

Table 2.3 Different barrier materials for Cu reported recently (not earlier than year 2001)

	Barrier material	Thickness (nm)	Process	Max working temp. (°)*	Ref.
Ru-based	Ru	5	sputter	300 (10 mins)	[47]
	Ru	20	sputter	450 (10 mins)	[48]
	Ru/TaN_x	5/5	sputter	750 (1 min)	[49]
Ta-based	Ta	10	sputter	600 (30 mins)	[50]
	TaN	10	sputter	625 (30 mins)	
	Ta/TaN	10/10	sputter	750 (30 mins)	
	Ta/TaN/Ta	10/10/10	sputter	650 (60 mins)	[51]

	TaB_x	40	sputter	750 (60 mins)	[52]
	TaWN	50	sputter	700 (30 mins)	[53]
	TaC	70	sputter	600 (30 mins)	[54]
Ti-based	TiAlNO	100	sputter	800 (60 mins)	[55]
	TiSiN	20	sputter Ti + high rapid thermal annealing (RTA) + N implantation	650 (30 mins)	[56]
	TiN_x	100	sputter	750 (30 mins)	[57]
	TiN/Al/TiN	5/2/5	sputter	650 (30 mins)	[58]
	Ti/TiN_x	7/3	CVD	500 (60 mins)	[59]
W-based	WN_xC_y	12	ALD	700 (30 mins)	[60]
	WN_x	1.5	ALD	600 (30 mins)	[61]
Other	AlMoNbSiTaTiVZr (high entropy alloy)	100	sputter	700 (30 mins)	[62]
	ZrSiN	100	sputter	800 (30 mins)	[63]
	HfN	50	sputter	575 (30 mins)	[64]
	Mo	50	sputter	600 (30 mins)	[65]
	MoN	50		700 (30 mins)	
	Mo/MoN	20/30		700 (30 mins)	
	a-SiC:H	84	Hot wire CVD	400 (60 mins)	[66]

* The maximum working temperature is taken as the temperature 50°C lower than the silicide formation temperature normally detected by x-ray diffraction (XRD).

In modern semiconductor manufacturing, the temperatures after the contact metal deposition do not rise above 700°C. Thus, this could be set as an upper limit for the working temperature of the barrier layer. The whole metallization scheme (Cu/barrier/dielectric) should be stable for 30 - 60 minutes at this temperature [67].

2.2.4 Key Issues on Barrier Layer

The issue of barrier layer deposition technology should be discussed with respect to the overall Cu interconnect process. The "dual damascene" approach is the method of choice for submicron ULSI technology. In this approach the inter-level dielectric (ILD) is deposited first and the Cu is then deposited into features/vais-trenchs that are etched into the ILD. Therefore, barrier deposition technologies should be compatible with this approach.

Barrier layers can be prepared by various methods. The main features of those methods in regard to barrier properties are summarized in Table 2.4. Physical-vapor-deposition (PVD) methods are widely used. The dominant PVD methods for barrier applications are collimated sputtering, ionized metal plasma (IMP), and hollow cathode magnetron (HCM) method.

Table 2.4 The Pros and Cons of the Thin-Film Deposition Methods for Barrier Application (assuming that the Cu Interconnects are deposited by electroplating)

Deposition method	Advantages	Disadvantages
Physical Vapor Deposition (PVD)	Available platforms	Resputtering problem Limited step coverage in high aspect ratio feature Difficult to integrate with Cu electroplating process
Chemical Vapor Deposition (CVD)	Available tools Excellent step coverage in high aspect ratio feature	Complex chemistry Elevated temperature process (ILD compatibity issue) High resistivity Difficult to integrate with electroplating process
Plasma Enhanced CVD (PECVD)	Available tools Fast deposition rate	May cause damage to ILD

Atomic Layer CVD (ALCVD)	Excellent step coverage	Immature technology

PVD methods yield excellent barrier properties over flat surfaces but encounter increasing step coverage problems as the features aspect ratio continues to increase. PVD methods yield acceptable solutions for 0.18 μm technology with aspect ratios of up to 3:1 but may face severe difficulties in the future 0.1 μm technologies with aspect ratio > 5:1 [68]. Chemical vapor deposition (CVD) methods offer excellent step coverage for high aspect ratios. One major difficulty in developing CVD processes is in the intensive research and development in developing new precursors and their application methods. It is difficult to forecast the relation between the precursors' properties and the resultant barrier quality. Therefore, it is a long process to develop a barrier layer using CVD. Being chemical processes by nature, CVD methods are limited to the products of the deposition chemical reactions. The thin film properties and the process parameters are determined by both the thermodynamics and the kinetics of the reactions. The system dimensions and the flow patterns in the reactors are also important. CVD layers also tend to be with higher resistivity than similar sputtered layers. This increased resistivity may be due to the incorporation of carbon and oxygen into the layer. The advantage of sputtering can be also due to the fact that it is easier to deposit metal rich layers that tend to have higher conductivity than stoichiometrically deposited layers, which are typical for CVD.

The main problems of barrier deposition are step coverage and the control of the material properties. Typical step-coverage problems and failures of the barrier are shown in Figure 2.4. The step coverage is affected by the

sputtering system geometry and the shapes of the feature on the wafer. It depends also on the sidewall wetting and surface diffusion of the barrier material. The maximum wafer temperature is limited by reliability considerations that are derived from the properties of the ILD and metal systems.

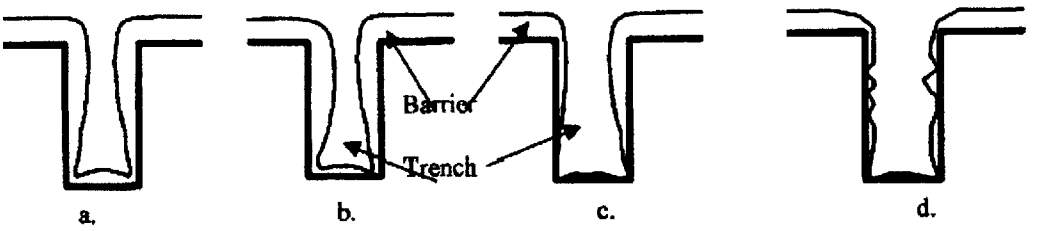

Figure 2.4 Typical step coverage issues: (a) uneven coating with less coverage at the bottom corners and necking at the top (b) asymmetrical coating (c) insufficient coating and (d) agglomeration on the sidewalls [68]

The general way to overcome step-coverage problems is to use conformal deposition methods such as CVD, ALCVD, and electroless plating. Those methods are characterized with very high step coverage even for very narrow structures with high aspect ratio. For example, electroless plating of features with aspect ratio larger than 4:1 showed good step coverage. Similar results were demonstrated for ALCVD where features with aspect ratio of 85:1 were coated with bottom side uniformity of ~76%.

Barrier layers are also affected by almost every process step, such as pre-deposition cleaning. The pre-clean step is required to ensure the removal of any contamination from the via-contact or the trench. The presence of contamination reduces the barrier efficiency since it affects its overall thickness and may cause delaminating or other physical damage to the barrier.

Barrier layers are known to affect the texture and electrical properties as well as reliability of the Cu interconnect material. It is a critical issue since the texture has an important role on determining the interconnect reliability. It was reported that the electromigration properties of Cu interconnects are improved when there is good wetting of the electroplated copper and the film is mostly (111) oriented [30].

One of the advantages of currently used Ta/TaN barrier material, besides being good barriers, is that they offer better wetting and highly (111) deposited copper when compared to other barriers such as CVD TiN [69]. It was noted that sometimes the best texture is achieved with the poorest barrier characteristics. Therefore, the development of a good barrier with the best copper interconnect scheme requires a multi-variable experimental design in order to optimize the system.

2.2.5 Cu Diffusion Barrier Reliability

For Cu interconnects, Cu/cap interface and Cu/liner (diffusion barrier) interface are critical for Cu reliability. For commonly used liners, such as Ta/TaN, the Cu/liner interface is relatively easy to control compared to the Cu/cap interface. For dual-damascene Cu lines, a Cu via is used to connect the lower level to the upper level. Unlike the robust W stud used in Al interconnects, the Cu via has been identified as a weak link in dual-damascene Cu connections; the majority of early reliability failures can be attributed to the Cu vias. The most critical process factors and elements affecting Cu interconnect reliability are Cu vias and interfaces and the liner coverage. Using a low-κ dielectric with a Cu interconnect introduces several new challenges to

reliability, including dielectric breakdown, temperature cycle, and stability within packages.

For Cu interconnects embedded in oxide insulators, electromigration and stress migration are the two predominant reliability concerns. Much more attention has been devoted to these two failure mechanisms compared to other reliability concerns such as interior intra-level dielectric breakdown. In scaling to 90-nm node technology, time-dependent inter- and intra-level dielectric breakdown (TDDB) does not seem to cause oxide dielectric reliability concerns within a product lifetime. In addition to a high breakdown field, the oxide dielectric robustness is partially due to good oxide confinement to the metals and good adhesion between the cap and Cu, making it difficult for Cu to diffuse out from the line.

To further reduce RC delay in the new technologies, various low-κ materials are being integrated with Cu interconnects. Low-κ dielectric materials are more porous and have a much lower mechanical hardness and elastic modulus. While these mechanical characteristics complicate the integration process and may cause serious reliability consequences, it is still too early to understand the full reliability impact of low-κ dielectrics on Cu interconnects. The low elastic modulus of the low-κ dielectric materials surrounding the Cu provides less confinement, or less back-flow resulting in shorter electromigration failure times. Due to poor thermal conductivity, low-κ dielectric materials can aggravate joule heating problem to cause Cu electromigration degradation, further limiting the current carrying capability of Cu.

The minor oxide dielectric reliability concerns, TDDB, could become major reliability concerns with low-κ dielectric insulators. Low-κ dielectric materials generally have less breakdown strength than oxide, and poor barrier confinement can result in higher electronic leakage from Cu diffusion and premature TDDB. Due to these emerging reliability concerns, low-κ dielectric TDDB proved to be a popular topic at the International Interconnect Technology Conference (IITC). Jow *et al.* [70] reported on TDDB and voltage ramp failures at the cap/low-κ dielectric interface and at the corner of the liner, cap, and low-κ dielectric (a triple point). This triple point is extremely sensitive to process-induced damage, such as liner CMP control, and is essential to electromigration performance (Cu extrusion). The porous nature of low-κ materials confounds the understanding of TDDB properties. Ogawa *et al.* [71] reported on TDDB performance degradation with a degree of porosity in the dielectric layers. Further understanding is needed to clarify the impact of pores and pore size distribution on TDDB degradation. The root causes of TDDB degradation in low-κ dielectrics, Cu diffusion out from the line, transport in low-κ, and so forth, are yet to be clearly identified. Furthermore, the implication of TDDB degradation on product lifetime at application conditions needs to be better established.

2.3 The Concept of Seed Layer

Cu interconnections could be fabricated by conventional methods, such as PVD and CVD. However, electrochemical plating has been found to be the most cost-effective method to deposit a Cu metallization layer. Electrochemical plating has several advantages compared to PVD and CVD such as low cost,

low processing temperature, and good ability to fill high-aspect-ratio vias and trenches [18, 72].

Electrochemical plating of Cu requires a seed layer to be deposited first to provide a conductive path for electric current required for subsequent electroplating. As such, an underlying conductive seed layer is generally applied to the wafer before it is subjected to an electrochemical deposition process. Surface condition and microstructure of the seed layer will affect texture and grain size of the overlying Cu film that will eventually determine the interconnect reliability. This dependency will become more complicated due to complex grain structure and texture of Cu films in narrow trenches and vias in damascene integration [73]. A strongly textured seed layer will promote the growth of a similar texture in the electroplated film. Moreover, large Cu grains are easier to grow on a smooth seed layer. With proper seed layer, the grains of electroplated Cu films in trenches will be quite large and a near-bamboo structure, which is desirable, can be obtained [69].

2.3.1. Seed Layer Requirements

Materials to be considered as good candidates for seed layers in Cu electroplating should posses the following criteria:

- Have a suitable texture to drive nucleation and growth of the subsequent Cu layers with desirable morphology.
- Have the ability to form less stable oxide compared to Cu-oxide to enable Cu electrodeposition process ($\left|\Delta G_f^0 \text{(M-O)}\right| < \left|\Delta G_f^0 \text{(Cu-O)}\right|$, where ΔG_f^0 (M-O) and ΔG_f^0 (Cu-O) are the Gibbs free energy of

formation per non-metal atom of the metal oxide and copper oxide, respectively) [22].

- Have a low resistivity to enable the electroplating process.
- Have a similar crystal structure (FCC) and a low lattice mismatch with Cu to ensure good wettability and hence, good adhesion with Cu.
- Have negligible reaction with Cu to prevent any increase in effective resistivity.
- Must be easy to obtain a thin and conformal layer, especially in high aspect ratio features.
- Precursors for ALD and CVD must be available.

2.3.2. Seed Layers in the Literature

Predeposited Cu is the most widely used seed layer for Cu electroplating in the industry. However, other materials such as Cu-alloys, Al, Mg, Zr, Ir, Os, Pd, etc. have also been studied for barrier/seed layer application. Table 2.5 summarizes data on several barrier/seed layers that are reported in literature. The main findings of these reports are also summarized in this table.

Table 2.5 Summary of material studied for barrier/seed layer

Sample configuration (thickness in nm)	Remarks	Ref.
Cu/Al (15)/SiO_2	Rutherford backscattered electron spectroscopy (RBS) study has shown no Cu diffusion up to 700°C annealing.	[74, 75]
Al as the barrier cum seed layer	No Cu^+ transport in Cu/Al/SiO_2 system at bias temperature stress (BTS) 1.5MV/cm, 250°C for 60 mins.	[76]
	Good adhesion of Cu/Al bilayer to SiO_2 has been confirmed using scotch tape test.	

	As the Al seed layer thickness increase, Cu(111) XRD peak becomes sharper and stronger. Formation of Al_2Cu precipitate in grain boundaries (GB) of Cu retard GB diffusion thus enhances EM resistance.	[77]
CuZr/Zr/ZrN/SiO_2 Zr as the seed layer, ZrN as the barrier layer	Zr has tendency to react with Si to form stable $ZrSi_2$ compound and interdiffusion of Cu and Si is reported to occur at 570°C. Cu(111) single-oriented state could be realized with increasing annealing temperature to 500°C. EM lifetime is enhanced 10-100 times due to precipitation of Zr at Cu grain boundary as well as at SiO_2 interface.	[78]
CuMg/SiO_2 Mg will form self align MgO barrier layer at Mg/SiO_2 interface	Formation of MgO layers at both Cu surface and interface prevent Cu diffusion and oxidation (stable up to 800°C). Improves film stability (both morphology and diffusion) on SiO_2. Improves adhesion to SiO_2 and improve mechanical strength of the film.	[79]
Cu/Rh (5)/W (45)/Si Rh as the seed layer, W as the barrier layer	Auger electron spectroscopy (AES) depth profiles show no interfacial contaminates at the direct plated Cu/Rh interface.	[22]
Cu/Pd (5)/W (45)/Si Pd as the seed layer, W as the barrier layer	Resulting Cu grain size was ~0.1 μm in the as-deposited state. Room temperature Cu recrystallization was found to occur but at a rate much slower than in samples plated on a Cu seed layer. RBS data indicates Pd diffusion to Cu surface after 400°C of annealing.	[22]
Cu/Ir (10-15)/SiO_2 (in patterned wafer) Ir as the barrier cum seed layer	Cu electrodeposition was demonstrated on submicron trenches with high conformal Ir barrier layers deposited by ALD. Good wetting and superfiling have been reported.	[80]
Cu/Os (30-40)/SiO_2 (in patterned wafer) Os as the barrier cum seed layer	It has been demonstrated that PVD Os barriers permit Cu wetting and superfill of damascene trenches by direct electrodeposition.	[81]

CHAPTER 3

Experiments

3.1 Sample Splits and Deposition Conditions

The study was initiated by assessing general barrier properties of Ru in comparison to Ta to get an immediate impression of the Ru performance. For this purpose, low-κ covered Si substrate was chosen since currently low-κ has already been implemented in real manufacturing to replace the SiO_2 dielectric. It would be interesting to see directly the interaction of Cu and Ru with the low-κ material. The initial studies include:

- Examination of the effect of Ru on Cu texture and surface roughness.
- Study on adhesion between Ru and low-κ.
- Diffusion study of Cu and Ru into the low-κ dielectric.

Table 3.1 shows the sample splits and the deposition conditions used in this study. Note that the deposition of Ru was done in a PVD Endura system whereas that of Cu was done on Cryo Vac sputtering system. PVD Endura system was expected to give a better base pressure (up to 10^{-7} Torr) compared to the Cryo Vac sputtering system (~10^{-6} - 10^{-5} Torr) and hence, result in a better film purity. However, due to inasssessibility of the machine for further study, Cryo vac sputtering system was used for all subsequent depositions.

Cu and Ru diffusion into low-κ substrate was found to be fast even at temperatures as low as 300°C which is a challenge in understanding the barrier failure mechanism. Hence, Si substrate was chosen for the subsequent studies to

characterize the barrier failure more conclusively, indicated by formation of silicides. The next studies focus on Ru-based barrier failure mechanism. Table 3.2 shows the sample details and process conditions used for this study. Note that in Table 3.2:

- Ru and Ru-N films were also deposited on SiO_2/Si substrate. These samples were used to compare the diffusion of Cu and Ru in Cu/Ru/SiO_2 system with that in Cu/Ru-N/SiO_2 system.
- The Ru-W-N and Ru-Ta-N films were purposely deposited in a thickness range of ~100 nm to result in a clearer x-ray diffraction signal which may arise from W- or Ta-nitride during analyses. Thicker film is also easier for transmission electron microscopy sample preparation.
- The thicknesses of Ru-W-N and Ru-Ta-N films listed in the Table 3.2 are the results of the same deposition time of 180 s.
- The working pressure used for pure Ru and Ru-N film deposition was 5 mTorr. The lower working pressure used was to produce a purer film since ion bombardment in the chamber will be less. The same working pressure could not be employed for the Ru-W-N and Ru-Ta-N film deposition as the plasma would not be generated in the chamber for pressures lower than 30 mTorr.

Table 3.1 Sample split for initial study

Purpose	Samples		Deposition	
			Ru deposition	Cu deposition
Study on the effect of Ru on Cu texture and surface roughness	as-deposited	10 nm Ru/low-κ 25 nm Ru/low-κ 50 nm Ru/low-κ	PVD Endura system Ar 10 sccm 5 mTorr working pressure 450 W power at room temp.	-
Study of Ru adhesion to low-κ		10 nm Ru/10 nm Ta/low-κ 25 nm Ru/10 nm Ta/low-κ 50 nm Ru/10 nm ta/low-κ 50 nm Ta/low-κ		
Study of diffusion of Cu and Ru into low-κ	as-deposited, annealed at 300°C and 500°C	Cu/10 m Ru/low-κ	PVD Endura system Ar 10 sccm 5 mTorr working pressure 450 W power at room temp.	Cryo Vac sputtering system Ar 10 sccm 20 mTorr working pressure -0.8 A target current at room temp.

Table 3.2 Sample split for study of Ru-based barrier in Cu metallization

	Samples		Ru thickness (nm)	Deposition conditions			
	w/o Cu overlayer	with Cu overlayer		Gas and flow rate (sccm)		Working pressure (mTorr)	Target current (-A)
				Ru dep.	Cu dep.		
control sample	-	50 nm Cu/Si	-	-	Ar (10)	5	0.8
pure Ru	Ru/Si	Cu/Ru/Si Cu/Ru/SiO_2/Si	10 20 30	Ar (10)			
Ru-N	Ru-N/Si	Cu/Ru-N/Si Cu/Ru-N/SiO_2/Si	20	N_2 (10)			
Ru-W-N	*Ru-W-N (N=0)/Si	-	109	Ar (20)	Ar (20)	30	
	Ru-W-N (N=5)/Si	-	126	Ar (20) + N_2 (5)			
	Ru-W-N (N=10)/Si	Cu/Ru-W-N (N=10)/Si	133	Ar (20) + N_2 (10)			
Ru-Ta-N	Ru-Ta-N (N=0)/Si	-	154	Ar (20)			
	Ru-Ta-N (N=5)/Si	-	125	Ar (20) + N_2 (5)			
	Ru-Ta-N (N=10)/Si	Cu/Ru-Ta-N (N=10)/Si	115	Ar (20) + N_2 (10)			

*N=0 means N_2 flow rate = 0 sccm

3.2 Thin Film Deposition and Annealing

Blanket samples used for the study were prepared using direct current (DC) sputtering method onto pre-cleaned wafers in a sputtering machine at room temperature. Process parameters include working pressure, gas flow rate, target current and deposition time. Control parameters are deposition rate and film structure. Figure 3.1 shows a schematic of the system setup and sputtering mechanism. When Ar gas is introduced into the chamber, it will be ionized positively. Ar^+ ions are then accelerated towards the target and sputter neutral target atoms. The sputtered target atoms travel to the substrate. They will arrive at the substrate and implant, bounce, or diffuse around a bit, or simply deposit, depending on their kinetic energies.

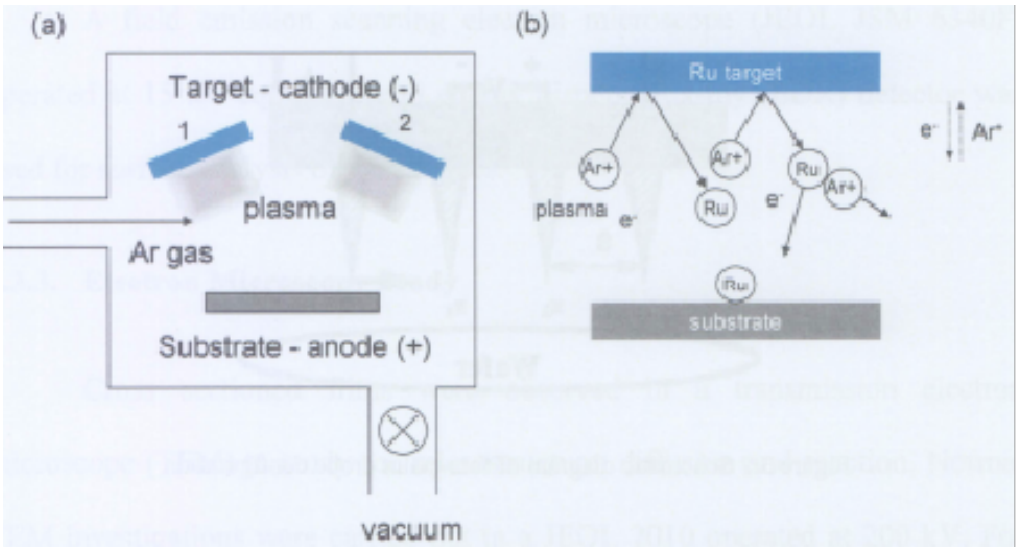

Figure 3.1 Schematic of (a) simplified DC sputtering system (b) sputter deposition mechanism

Annealing was done in a vacuum furnace with a good vacuum ambient of 10^{-5} Torr to minimize any oxidation. As mentioned in the literature review in Chapter 2, a good barrier layer should be workable up to 700°C for 30 - 60

minutes. Based on these values, annealing temperature for this study was varied from 200°C to 800°C for 1 hour. The low annealing temperatures were to monitor microstructural changes of the Ru-based films whereas the higher temperatures were to examine the silicide formation and subsequent barrier failure.

3.3 Materials Characterization

3.3.1. Sheet Resistance Measurement

A common way to measure a film resistivity is in terms of sheet resistance (R_s) value. Consider a film with length *l*, width *w*, and thickness *d*. Film resistance according to Ohm's law is $R = \rho.l/w.d$. In a special case of a square film when $l = w$, then $R = R_s = \rho/d$. The unit of sheet resistance is Ω/□.

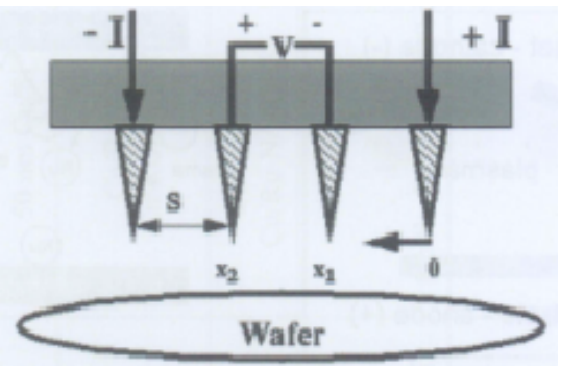

Figure 3.2 Schematic diagram of four-point probe configuration

CDE Resmap sheet resistance analyzer with four-point probe configuration was utilized to measure the resistance as shown in Figure 3.2. This method serves as a convenient way of monitoring interfacial changes. The film sheet resistance (R_s) was measured by contacting the four-point metal-tip probes onto the film surface. The outer probes are connected to the current (*I*)

source whereas the inner probes detect the voltage (V) drop. Electrostatic analysis of the electric potential and field distributions within the film yields R_s = k.V/I where k is a constant dependent on the configuration and spacing of the contacts. In our measurements, the R_s value is automatically calculated using a software provided by the manufacturer.

3.3.2. Surface Roughness and Morphological Observation

The root mean square (RMS) surface roughness of the Cu layer was measured using Digital Instrument Dimension 3100 atomic force microscope (AFM), employing a tapping mode, in a scan area of 1 x 1 μm^2 and raster resolution of 256 lines per area. The RMS value was obtained from the AFM software after data acquisition.

A field emission scanning electron microscope (JEOL JSM 6340F) operated at 15 kV equipped with energy dispersive x-ray (EDX) detector was used for surface analysis of the samples.

3.3.3. Electron Microscopy Study

Cross sectioned films were observed in a transmission electron microscope (TEM) to study the microstructure, diffusion and reaction. Normal TEM investigations were carried out in a JEOL 2010 operated at 200 kV. For elemental analysis using electron energy loss spectroscopy (EELS) and energy dispersed x-ray spectroscopy (EDX), FEI Tecnai F30 (300 kV) was used. The TEM samples were prepared conventionally using mechanical grinder and polisher, dimpling, and ion milling as schematically illustrated in Figure 3.3.

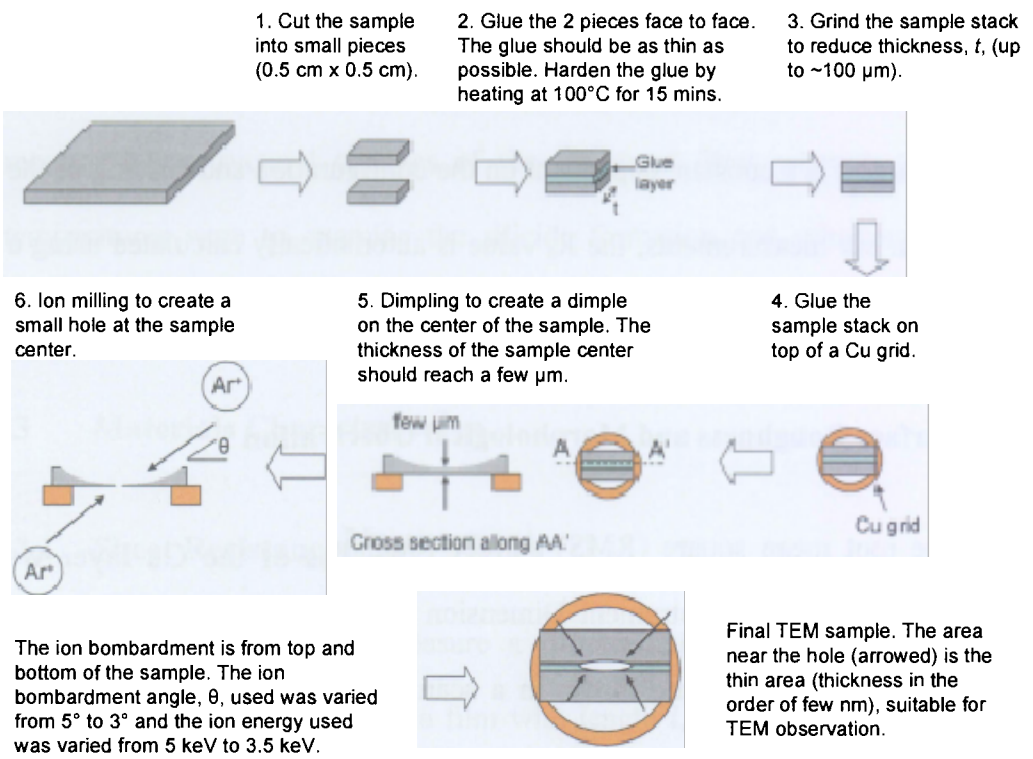

Figure 3.3 Schematic of TEM sample preparation steps

3.3.4. Crystal Structure and Phases Analysis

X-ray diffractometer (XRD) Rigaku Dmax 2200 was employed to examine the crystal structure and phases of the samples using 2θ technique. The 1.54 Å Cu K_α x-ray source was set at 40 kV and 45 mA. The x-ray source angle was kept at 2° while the 2θ can range from 20° to 80°. The diffraction analysis was mainly done qualitatively by identifying the phase present and examining if texturing appears in the film. Some strain measurement based on XRD data was done on some samples related to adhesion study to understand the effect of film residual strain on its adhesion properties. The calculation was done by the Williamson-Hall method [82], which uses the following equations:

$$\delta(2\theta) = B(1 - (b^2/B^2)) \qquad ...(3.1)$$

$$\delta(2\theta).\cos\theta_0 = 0.9\lambda/L + 4e.\sin\theta_0 \qquad ...(3.2)$$

B and b are the width (in radian) of the same Bragg peak from the XRD scans of the experimental and reference samples respectively. The reference sample was a 75 nm pure Ru film deposited on Si and annealed at high temperature of 600°C for 1 hour to minimize the peak broadening due to residual strain. Both B and b are determined by Origin software from the full-width half maximum (FWHM). θ_0 is the position of the analyzed peak maximum, λ is the x-ray wave length of 0.154056 nm, L is crystal size, and e is the strain value. By plotting $sin\ \theta_0$ against $\delta(2\theta).cos\ \theta_0$ in equation 3.2, film residual strain, e, can be obtained from the slope of the graph.

3.3.5. Chemical Analyses

(1) X-ray Photoelectron Spectroscopy (XPS)

To study the chemical states of elements, x-ray photoelectrons spectroscopy (XPS) shallow surface measurement was performed in a Kratos AXIS Ultra spectrometer with a monochromatized Al K_α x-ray source (1486.71 eV) operated at a reduced power of 150 W (15 kV and 10 mA). The base pressure in the analysis chamber was 2.66×10^{-7} Pa. The binding energy scale of the XPS spectrum was calibrated with the C 1s peak (neutral C-C peak at binding energy of 284.5 eV). XPS depth profile was also done to understand the diffusion and reaction during thermal annealing. The chemical states for depth profiles (etching profiles) were analyzed on the same equipment. An Ar^+ ion gun with acceleration voltage of 4 kV and filament current of 15 mA was used to etch the samples at a gas pressure of $\sim10^{-6}$ Pa. Ion bombardment was performed at an incident angle of 45^o to the surface normal.

Kratos software was used for data analyses including semi-quantitative determination of film composition and separation of several overlap peaks. The quantitative analysis for a multi element surface layer consisting of elements A, B, and C is:

$$Atomic\ \%\ of\ A = ((I_A/S_A)\ x\ 100\%)/\Sigma\ (I_i/S_i) \qquad ...(3.3)$$

(i = A, B, C)

where I_A is peak area of A, S_A is sensitivity factor of element A, I_i is peak area of all other elements, and S_i is sensitivity factor of all other elements. The value of S is based on empirical data. The software measures the intensity of a specified peak with an automatic background subtraction.

For de-convolution or peak separation purpose, especially for douplet peaks (p, d, and f), it is important to ensure that the relative intensities of the two peaks reflects the generacies of the final states (g_j = 2j + 1). Consider a sample surface containing TaN and Ta_2O_5. The XPS spectrum of Ta 4f of the sample is shown in Figure 3.4.

- the f orbital has an angular quantum number, l = 3
- hence, it has spin orbit split of j = $l \pm$ s (where s is spin number = ½) → j = 7/2 and j = 5/2
- the relative intensities of the Ta $4f_{7/2}$ and Ta $4f_{5/2}$ will be $g_{7/2}$:$g_{5/2}$ = 4:3

Additionally, the software is also able to calculate the relative amounts of TaN and Ta_2O_5 out of the total Ta 4f present based on the area under each de-convoluted curve.

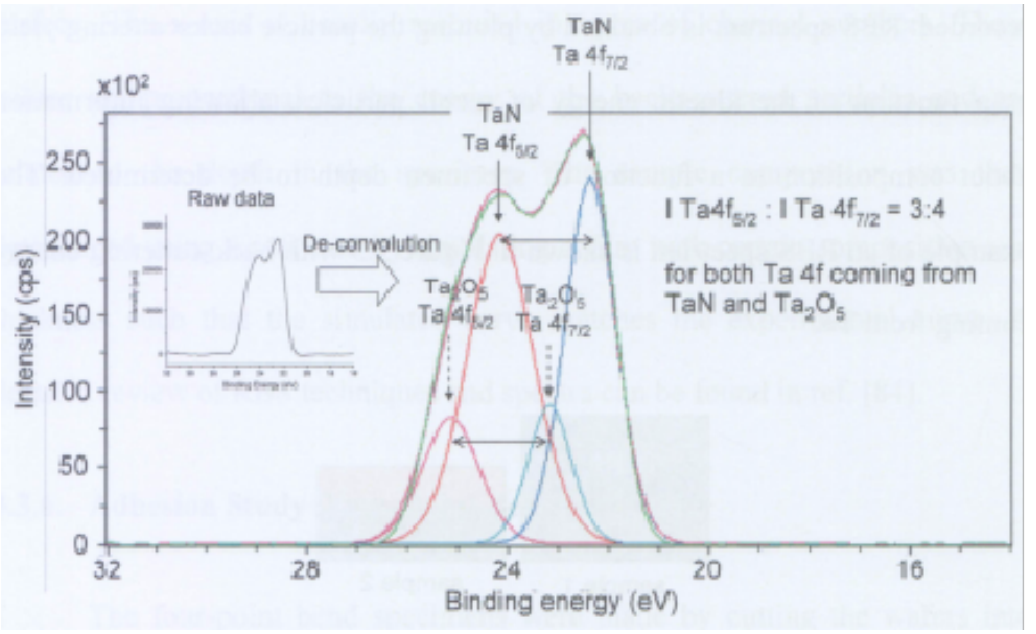

Figure 3.4 Example of XPS spectra of Ta 4f from TaN- and Ta_2O_5-containing surface, showing spin orbit splitting of $4f_{5/2}$ and $4f_{7/2}$ with relative intensity of 3:4

(2) Secondary Ion Mass Spectroscopy (SIMS)

Secondary ion mass spectrometry (SIMS) analysis was done on a time of flight (TOF) SIMS IV model by ION TOF GmbH. The Cs^+ sputter gun was used for N content monitoring during thermal annealing whereas Ar^+ sputter gun was used for non-nitrogen detection. The sputter gun was set at 1 keV and 15 nA while the analysis was done using Ga^+ gun and set at 25 keV and 1.6 to 2 pA. The sputter area is 200 x 200 μm^2, while the analysis area is 100 x 100 μm^2.

(3) Rutherford Backscattered Spectroscopy (RBS)

Rutherford backscattered spectroscopy (RBS) measurement was performed on a high voltage singletron accelerator using 2 MeV He^{++}, at 170° scattering angle, in a vacuum chamber of 5x 10^{-6} mbar. During an RBS measurement, high-energy (MeV) He^{++} ions are directed onto a sample and the energy distribution and yield of the backscattered He^{++} ions at a given angle is

recorded. RBS spectrum is obtained by plotting the particle backscattering yield as a function of the kinetic energy of recoil particles, allowing information about composition as a function of specimen depth to be determined. The example of an RBS spectrum is shown in Figure 3.5 with backscattering energy coming from Ta.

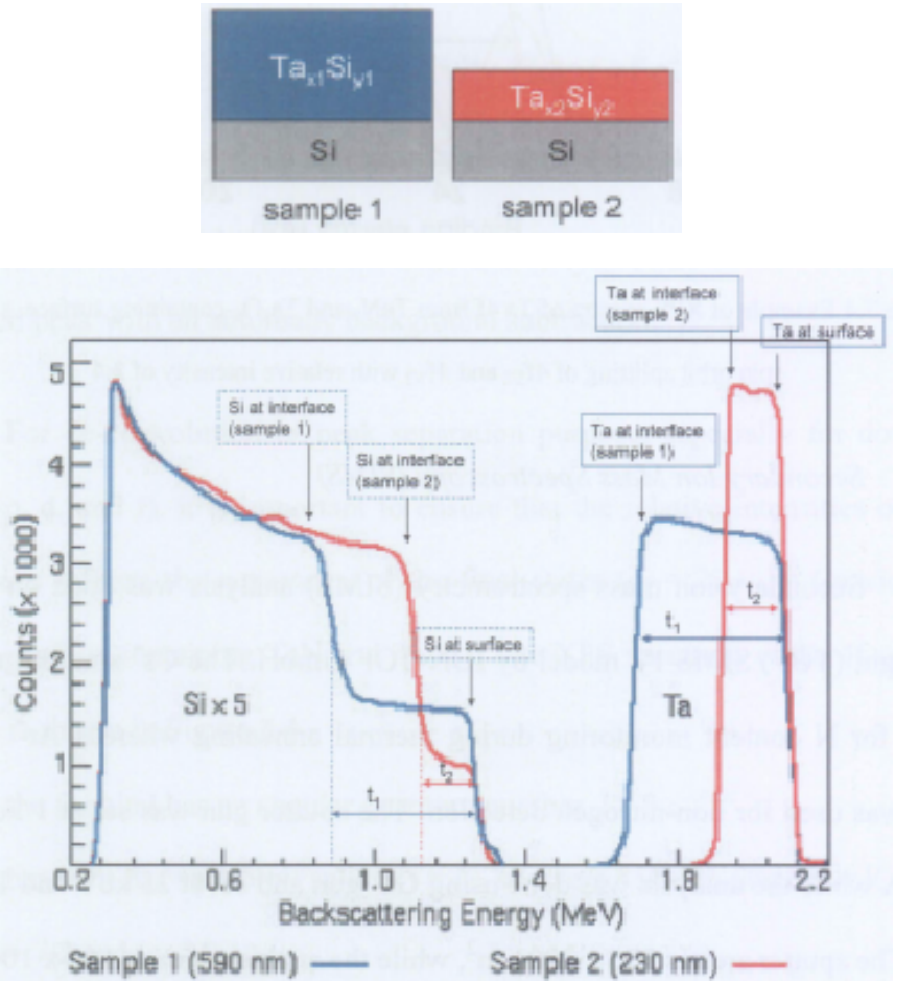

Figure 3.5 An example of RBS spectra of two different Ta_xSi_y films on Si substrate with different thicknesses [83]

For a single-element target, the backscattered particles have a continuous range of kinetic energies starting from zero, corresponding to a particle just barely able to escape from the specimen, to a characteristic maximal energy, corresponding to elastic scattering from atoms at the specimen

surface. The x-axis is usually recorded in terms of channel numbers. These values are proportional to the energy of the backscattered particles and are related to the depth in the specimen. The sample composition was then determined using a software by simulating a film with certain composition and thickness such that the simulated curve matches the experimental curve. A detailed review of RBS techniques and spectra can be found in ref. [84].

3.3.6. Adhesion Study (Four-Point Bend Test)

The four-point bend specimens were made by cutting the wafers into rectangular specimens and creating a sandwich structure by bonding two rectangular pieces using a layer of passivating polymer as shown in Figure 3.6. Note that the multilayer thin film was bonded to the back of the Si wafer so that there will only be one set of multilayer thin film at the middle of the sandwich. Great care was taken to keep the epoxy layer thin and uniform and, subsequently, a weight was applied to ensure good bonding. The samples were then cured at 100°C for 1 hour and a notch was made on one side of the Si with a precision cutter. The notch depth was 90% of the thickness of the wafer. Finally, the sample was centered between the four pins in the bend tester and loaded until it failed and the load versus crosshead displacement graphs were obtained.

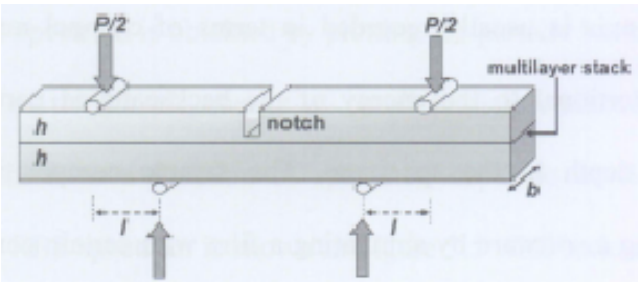

Figure 3.6 Experimental set up illustration of a simplified test structure for four-point bend test measurements

A typical load versus displacement curve obtained from four-point bend method is shown in Figure 3.7. Initially the load increases linearly as the specimen deforms elastically. At some point, the load decreases abruptly which signifies the point at which the vertical crack initiated by the notch begins to propagate through the Si. When it reaches an interface, it might be either deflected to propagate along the interface or continue through to the next material in its vertical path. The crack takes the path that requires the least energy to overcome. Thus, the crack path would be determined by the adhesion at the interface and the toughness of the material ahead. When the film adhesion is poor, the crack is likely to propagate along the interface horizontally and then the load remains relatively a constant while the displacement increases. This plateau load is used to calculate the fracture energy, G_c, of the interface by equations 3.4 and 3.5 [85]:

$$G_c = 21(1-\nu^2)M^2/4Eh^3 \qquad \ldots(3.4)$$

$$M = Pl/2b \qquad \ldots(3.5)$$

where E and ν are the elastic modulus (= 165 GPa) and Poisson's ratio (= 0.28) of Si respectively, M is the net bending moment per unit width as given by Equation 3.5, P is the load at the plateau, l , b and h are specimen dimensions shown in Figure 3.6.

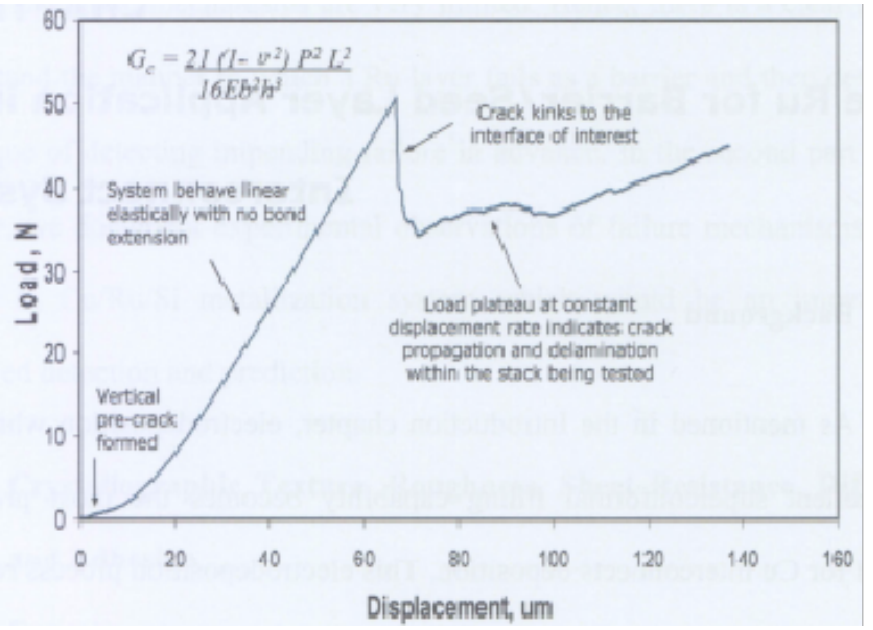

Figure 3.7 A plot of load against displacement obtained from four-point bend test [86]

CHAPTER 4

Pure Ru for Barrier/Seed Layer Application in Cu Interconnect System

4.1 Background

As mentioned in the Introduction chapter, electrodeposition which has an excellent superconformal filling capability becomes the most preferred method for Cu interconnects deposition. This electrodeposition process requires a continuous seed layer to allow void free superfilling to achieve reliable Cu metallization. Surface condition and microstructure of the seed layer will affect texture and grain size of the overlying Cu film that will eventually determine the interconnect reliability. This dependency will become more complicated due to complex grain structure and texture of Cu films in narrow trenches and vias in damascene integration [73]. A strongly textured seed layer will promote the growth of a similar texture in the electroplated film. Moreover, large Cu grains are easier to grow on a smooth seed layer. With proper seed layer, the grains of electroplated Cu films in trenches will be quite large and a near-bamboo structure, which is desirable, can be obtained [69].

First part of the results reported in this chapter relates to the effects of Ru seed cum barrier layer on Cu texture and morphology in a Cu/Ru/low-κ structure. The results are compared to a Ta layer in the structure. Sheet resistance of the film stack before and after annealing was examined. Diffusion of Cu into low-κ through Ru barrier is also discussed and adhesion of Ru to low-κ is assessed. Second part relates to barrier failure mechanism. Studies on

Ru barrier failure mechanisms are very limited. Hence, there is a clear need to understand the manner in which a Ru layer fails as a barrier and then develop a technique of detecting impending failure in advance. In the second part of this chapter, we document experimental observations of failure mechanisms of Ru barrier in Cu/Ru/Si metallization system which would be an impetus for advanced detection and prediction.

4.2 Crystallographic Texture, Roughness, Sheet Resistance, Diffusion, and Adhesion

4.2.1 Experiments

A Black Diamond™ (SiCOH-based) was chosen as the low-κ material for this investigation because it is currently the industry-standard low-κ dielectric solution for $\leq$ 90 nm Cu/low-κ interconnects with a dielectric constant, κ, of ≤ 3.0 [87]. Four sets of blanket samples of:

- x Ru/low-κ
- x Ru/10 nm Ta/low-κ
- Cu/x Ru/low-κ
- Cu/x Ru/10 nm Ta/low-κ

with Ru thickness, x, of 10, 25, and 50 nm were prepared for the study. Samples of Ta/low-κ and Cu/Ta/low-κ with 50 nm Ta were also prepared as a basis for comparison. Schematic of three layers are illustrated in Figure 4.1.

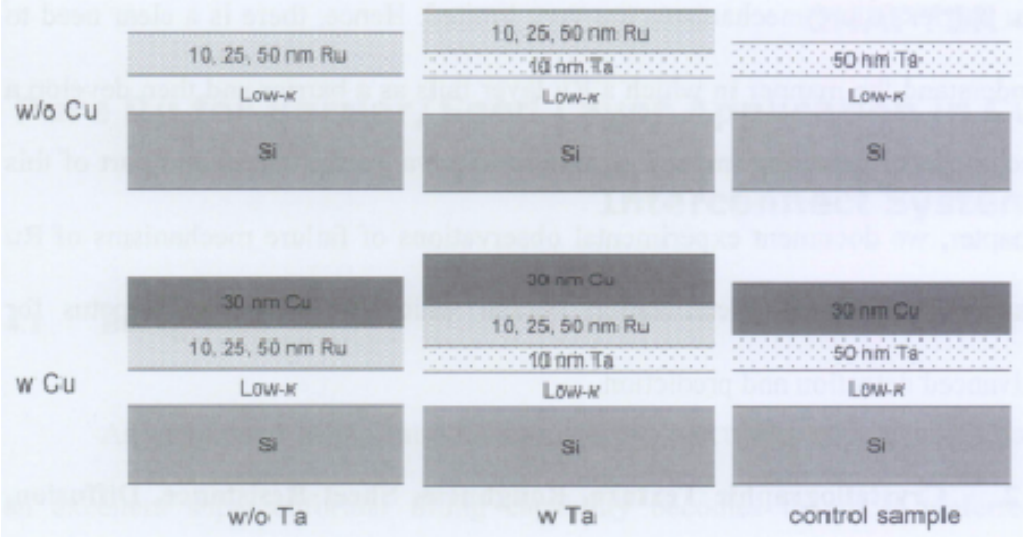

Figure 4.1 Schematic of sample stacks

Ru (99.95% pure) or Ta (99.95% pure) were sputter deposited onto a pre-cleaned low-κ covered p-type Si(100) wafer using a physical vapor deposition Endura^{TM} sputtering system, employing Ar gas, 5 mTorr pressure, 450 W power, and at room temperature. Mild solvent cleaning was performed using iso-propanol alcohol (IPA) on air-exposed Ru or Ta surfaces prior to Cu deposition. Cu (99.99% pure) was then sputter deposited onto the Ru or Ta/low-κ using a Cryo Vac sputtering machine at room temperature, 10^{-6} Torr base pressure, 20 mTorr working pressure, and 10 sccm Ar gas flow rate. For diffusion study, samples were subsequently annealed at 300°C and 500°C for 1 hour in a high vacuum ambient (10^{-5} Torr).

Thin film x-ray diffraction (XRD) was carried out using a Rigaku Dmax 2200 using 1.542 Å (Cu $K\alpha$) incident x-rays whereas surface roughness was measured using Digital Instrument Dimension 3100 atomic force microscope (AFM) in a scan area of 1 x 1 μm^2 and raster resolution of 256 lines per area. A Kratos AXIS spectrometer for x-ray photoelectron spectroscopy (XPS) with

monochromatic Al *Kα* x-ray radiation at 1486.71 eV was used to investigate Cu and Ru diffusion while high resolution transmission electron microscope (HRTEM) investigations were carried out in a JEOL 2010 TEM (200kV). The four-point bend method was employed to assess adhesion.

4.2.2 Results and Discussion

A. Relationship between Cu(111) texture and type and thickness of underlying seed layer

Figure 4.2 shows XRD spectra of as-deposited Cu on different samples. Note that only Cu(111) reflection is prominent at $2\theta = 43.29°$ (Joint Committee for Powder Diffraction Standards (JCPDS) card no. 04-0836) while other Cu peaks prominent in powder diffraction such as Cu(200) and Cu(220) are absent at their respective diffraction angles of $2\theta = 50.43°$ and $2\theta = 74.13°$. Hexagonal Ru peaks are clearly observed in the Ru-containing stacks (sample 1 to 6) at $2\theta = 38.38°$, 42.15°, 44°, and 58.32° (JCPDS card no. 06-0663). XRD spectra of the sample with Ta layer (sample 7) shows that the crystal structure of the Ta layer is β-Ta which is tetragonal, indicated by clear β-Ta peaks at $2\theta = 33.69°$, 36.28°, 37.39°, 38.2°, 39.24°, and 44.05° (JCPDS card no. 25-1280).

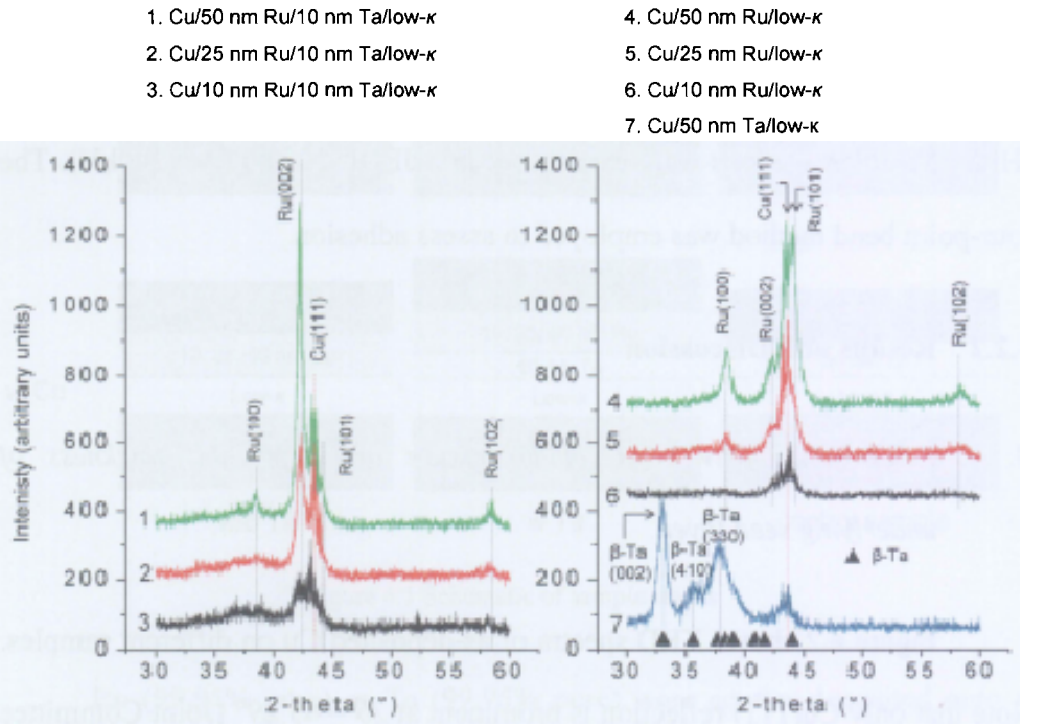

Figure 4.2 X-ray diffractograms of as-deposited Cu on different substrates

The deposited Cu films appear to have a (111) texture and this is more pronounced when Cu is deposited directly on Ru than on Ta. Note that the Cu thicknesses and XRD data collection times for all the samples are the same. Hence, changes in Cu(111) peak intensity could be mainly attributed to the change in the Cu film texture. Cu(111) peak intensity on Ru is four times higher than that on Ta with the same Ru and Ta thickness (comparing samples 4 and 7). It can be deduced from Figure 4.2 that β-Ta layer mainly has (002) orientation (sample 7) while Ru on low-κ has (101) orientation (sample 4 to 6). Insertion of Ta(002) in between Ru and low-κ (sample 1 to 3) alters the Ru preferred orientation from Ru(101) to Ru(002).

Figure 4.3 shows a change in Cu(111) peak intensity against underlying layer nominal thickness on different types of underlying materials (Ru/Ta, Ru, and Ta). It was observed that Cu(111) intensity increases as Ru thickness

increases in both Ru-containing stacks. Additionally, Cu(111) intensity is higher on Ru(002) when Ru film is thin. However, when film thickness is increased to 50 nm, Cu(111) intensity on Ru(101) is higher than on Ru (002). Texture of Cu films correlates strongly with type as well as thickness of seed layer. This is thought to be effect of crystal orientation and lattice mismatch between Cu and the seed layer [77]. Figure 4.4 shows atomic arrangement of FCC Cu, HCP Ru, and tetragonal β-Ta on the relevant planes of interest.

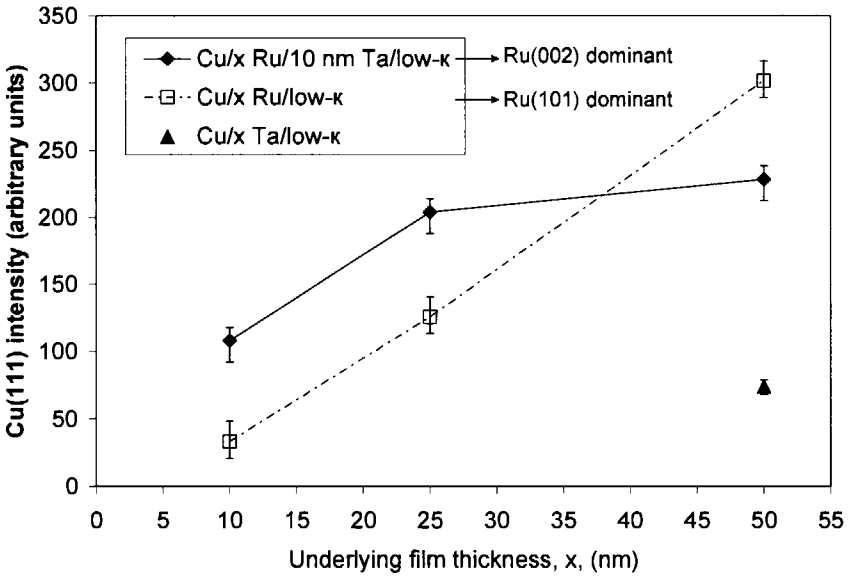

Figure 4.3 Plot of Cu(111) XRD peak intensity against underlying film (Ru or Ta) nominal thickness

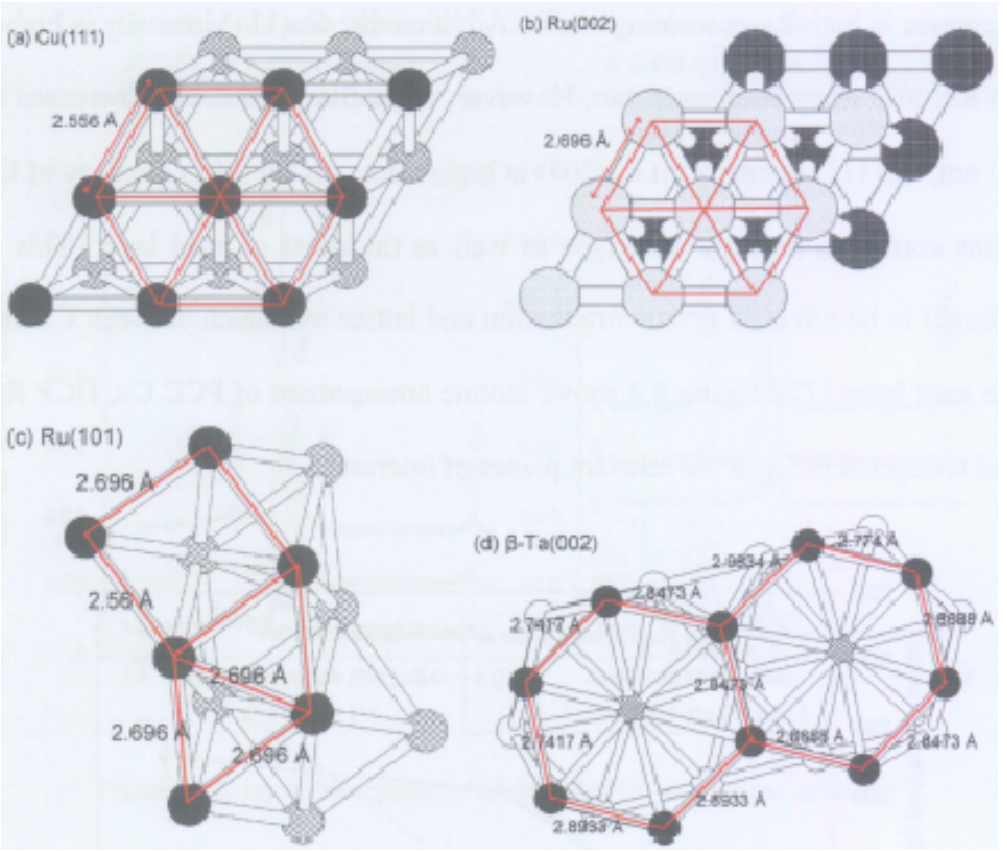

Figure 4.4 Lattice structure and atomic arrangement patterns of (a) Cu(111) (b) Ru(002) (c) Ru(101) and (d) β-Ta(002)

Note that atomic arrangement of Ru on (002) plane in Figure 4.4b has hexagonal symmetry, similar to that of Cu(111) in Figure 4.4a hence, easier seeding of Cu(111) on Ru(002) could be expected. Furthermore, knowing lattice parameter and atomic arrangement in the plane, average inter-atomic distances on the respective interface planes can be calculated. Using this value, inter-atomic distance (lattice) mismatch can be estimated. Table 4.1 shows the calculated lattice mismatch. It is observed that lattice mismatch at Cu(111) - Ta(002) interface is larger (~10%) than that at Cu(111) - Ru(101) (~4%) or Cu(111) - Ru(002) (~5%) interfaces. Consequently, seeding of a Cu(111) crystallographic texture will be easier on Ru than on Ta. Additionally lower lattice mismatch of Ru(002) - Ta(002) (~5.2%) compared to Ru(101) - Ta(002)

(~6.4%) interfaces explains the change in Ru texture from Ru(101) to Ru(002) when Ta(002) is inserted in between Ru and low-κ.

Table 4.1 Calculated lattice mismatch of Ta to Cu, Ru to Cu, and Ru to Ta on the relevant planes of interest

	Crystal Structure	Lattice constant (Å)	Average inter-atomic distance (Å)	Lattice mismatch with Cu(111)	Lattice mismatch with Ta(002)
Cu	FCC	a = b = c = 3.613 (ICSD*-53247)	Cu(111) = 2.556	0%	-
β-Ta	Tetragonal	a = b = 10.211, c = 5.3064 (ICSD-280872)	β-Ta(002) = 2.846	10.19%	0%
Ru	HCP	a = b = 2.696, c = 4.269 (ICSD-54236)	Ru(101) = 2.662	3.97%	6.46%
			Ru(002) = 2.696	5.19%	5.27%

*ICSD = Inorganic Crystal Structure Database

Lattice mismatch of Cu(111) - Ru(002) (~5%) is larger than that of Cu(111) - Ru(101) (~4%); however, Cu(111) intensity is stronger on Ru(002) than on Ru(101) when Ru thickness is less than 50 nm in our samples (see Figure 4.3). This could be due to the good match of the atomic arrangement pattern of Cu(111) and Ru(002) as both are hexagonal. For comparison, even β-Ta(002) atomic arrangement is similar to Ru(002) and Cu(111) but the lattice mismatch is large. Hence, β-Ta(002) does not promote Cu(111) growth as clear from the data in Figure 4.3. Therefore, both lattice mismatch and atomic arrangement affect the resulted Cu(111) intensity.

For FCC metals (such as Cu), the closest packed (111) plane has the lowest surface energy, so it is more stable and hence, preferred for interconnect application [88]. Furthermore crystallographic texture has an effect on electromigration (EM) performance of Cu. Ryu *et al.* [30] reported that the EM lifetime of (111) CVD Cu is four times longer than that of (200) CVD Cu.

Hence, Ru seeding appears to provide a Cu texture that is beneficial for EM resistance.

B. *Effect of Ru on Cu film surface morphology*

AFM and SEM micrographs of as-deposited Cu do not indicate any apparent difference in surface morphology among the various samples. The measured root mean square (RMS) Cu surface roughness shown in Figure 4.5 is consistent with the AFM micrographs. Surface roughness of as-deposited Cu film is almost independent on substrate type. A smooth Cu surface with RMS < 1.5 nm could be readily obtained on both Ru and Ta substrates.

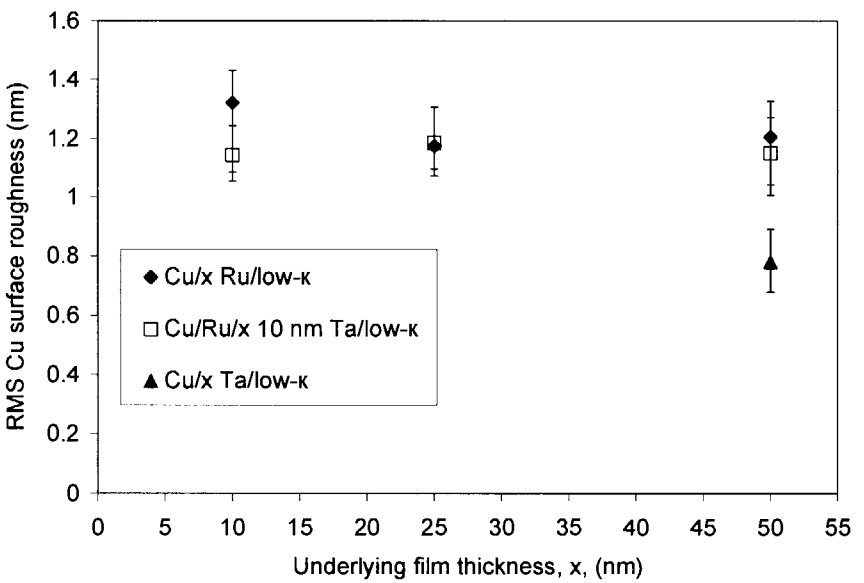

Figure 4.5 RMS roughness of as-deposited Cu on different substrates with varying thickness

C. *Diffusion of Cu into low-κ through Ru barrier*

Sample with the thinnest Ru layer (10 nm) deposited directly on low-κ dielectric, was chosen for diffusion and barrier property evaluation. The diffusion of Cu through Ru was investigated in Cu/10 nm Ru/low-κ samples

annealed at 300° and 500°C. As-deposited and vacuum annealed samples were then analyzed by XPS depth profiling and the concentrations of important elements obtained are shown in Figure 4.6. The distributions of low-κ, Ru, and Cu across the sample thickness were analyzed as a function of etching time. Atomic concentrations were calculated from peak area of each element at every depth level with consideration to their relative sensitivity factors. The depth profiling was stopped when Ru signal became undetectable. The low-κ (SiCOH-based) layer was identified by the appearance of Si, O, and C atoms.

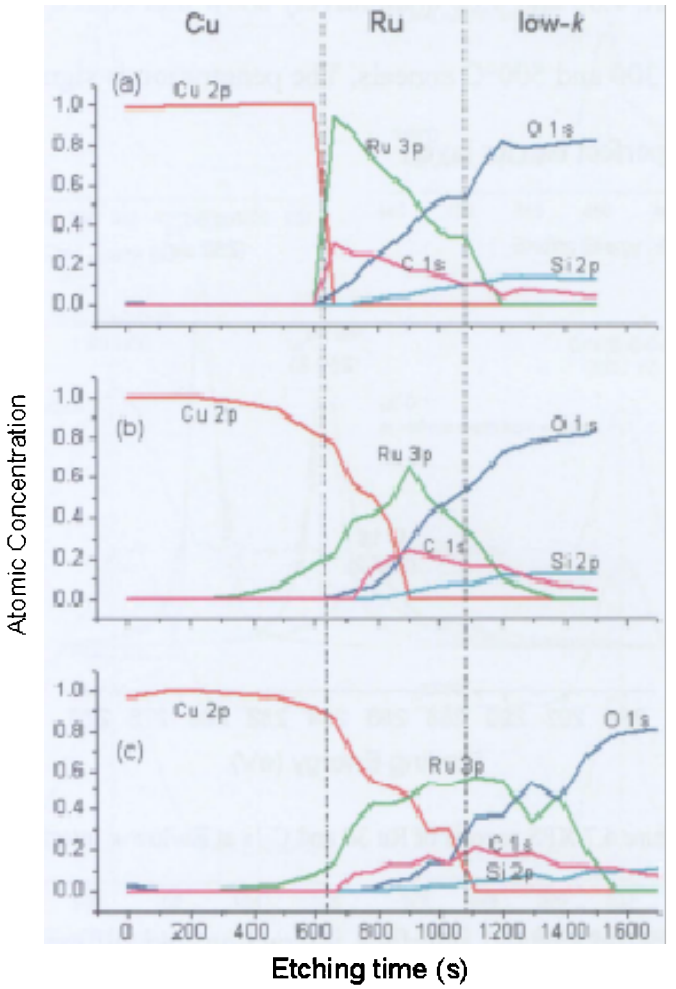

Figure 4.6 XPS depth profiling of 30 nm Cu/10 nm Ru/low-κ (a) as-deposited (b) 300°C and (c) 500°C annealed, with its estimated initial interface marked by the dotted line

In the as-deposited sample shown in Figure 4.6a, Cu/Ru interface is clearly defined but Ru/low-κ interface is not. This is because of certain difficulties in determining Ru and C atomic concentrations at interface. Binding energy of C 1s electrons is 285.2 eV [89] which overlaps with Ru $3d_{3/2}$ binding energy of 284.2 eV [89]. Hence, the C 1s peak tends to fall within envelope of Ru 3d peak as shown in Figure 4.7, causing inaccuracies. To minimize this inaccuracy, Ru 3p peak was used for atomic concentration determination and further analysis. However, Cu diffusion could be characterized despite this difficulty. Figure 4.6b and 4.6c qualitatively show that both Cu and Ru diffuse into low-κ after 300 and 500°C anneals. The penetration is significant, implying that Ru is not a perfect barrier layer.

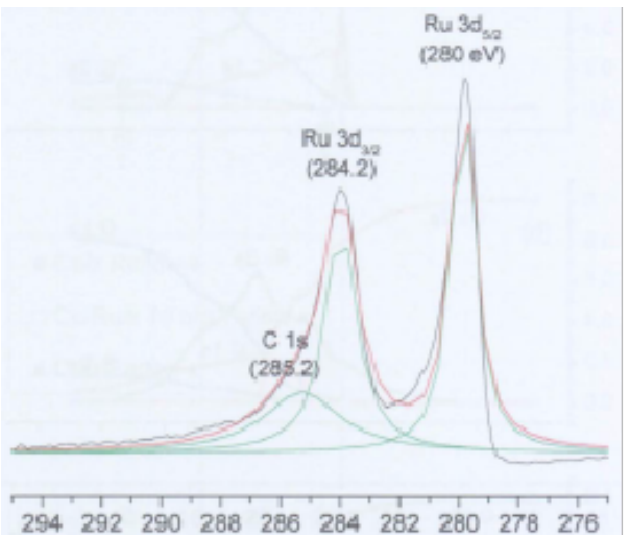

Figure 4.7 XPS spectra of Ru 3d and C 1s at Ru/low-κ interface

To further understand interface interaction and diffusion, XPS narrow scan analyses were done to identify any phase formation at interface. Figure 4.8 presents XPS narrow scan of Cu 2p (Figure 4.8a), Ru 3p (Figure 4.8b), Si 2p (Figure 4.8c), and O 1s (Figure 4.8d) peaks of as-deposited, 300°C, and 500°C

annealed 30 nm Cu/10 nm Ru/low-κ samples at specific depth level from sample surface. Any changes in binding energy upon annealing could be expected if there is any interfacial reaction between the layers.

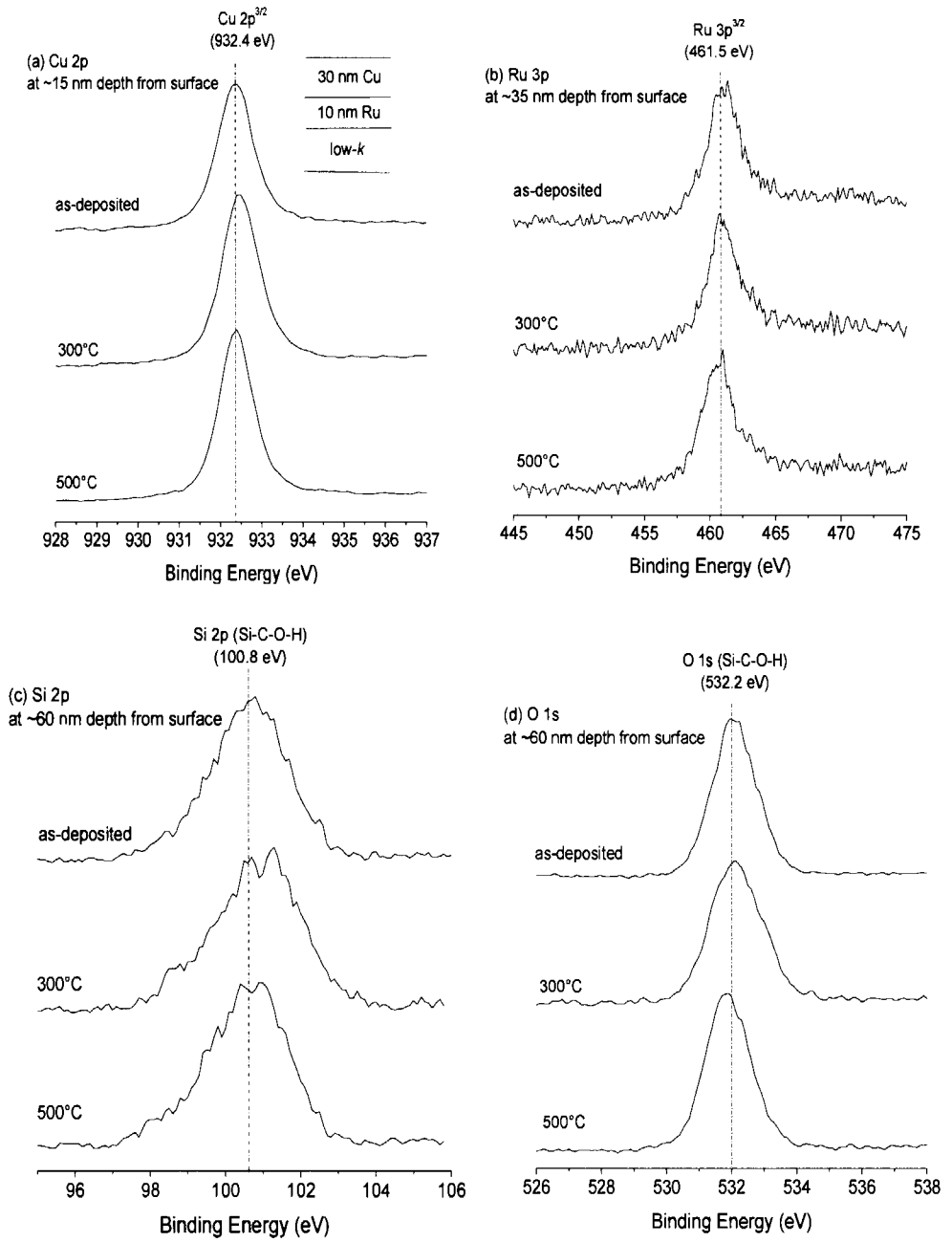

Figure 4.8 XPS narrow scans of as-deposited, 300°C, and 500°C annealed 30 nm Cu/10 nm Ru/low-κ samples (a) Cu 2p (b) Ru 3p (c) Si 2p and (d) O 1s at a specific depth from sample surface indicated

The observed electronic binding energy of each element is close to reported data in literature [89]. Cu and Ru are present in their elemental state, Cu^0 (932.4 eV) and Ru^0 (461.5 eV). In low-κ layer, Si-C (100 eV), Si-O (100.8 eV) and O-C (532.2 eV) bonds were observed. No significant shift in binding energy was observed upon annealing, indicating no interfacial phase has been formed under thermal annealing.

To further analyse any interfacial interaction and identify the phases present at interface, cross sectioned samples were prepared for TEM observation. Sectional TEM micrographs of as-deposited and 500°C annealed 30 nm Cu/10 nm Ru/low-κ are compared in Figure 4.9. It is clear that Ru layer consists of columnar crystals. Both Cu/Ru and Ru/low-κ interfaces are clearly defined in the as-deposited sample (Figure 4.9a) but evidence of diffusion (both Cu and Ru) is apparent at Ru/low-κ interface after thermal annealing (Figure 4.9b). This is clear in the magnified micrograph of the circled local area at the Ru/low-κ interface in Figure 4.9b where new nanocrystals appear to have formed within the low-κ region. These are possibly Ru and Cu that have diffused into the low-κ and have crystallized. This microscopic observation agrees with XPS results that showed definite concentration of Ru and Cu in the low-κ at the same interface (Figure 4.6c). Conclusive identification of these crystals could not be made by diffraction or EDX due to their nanosize.

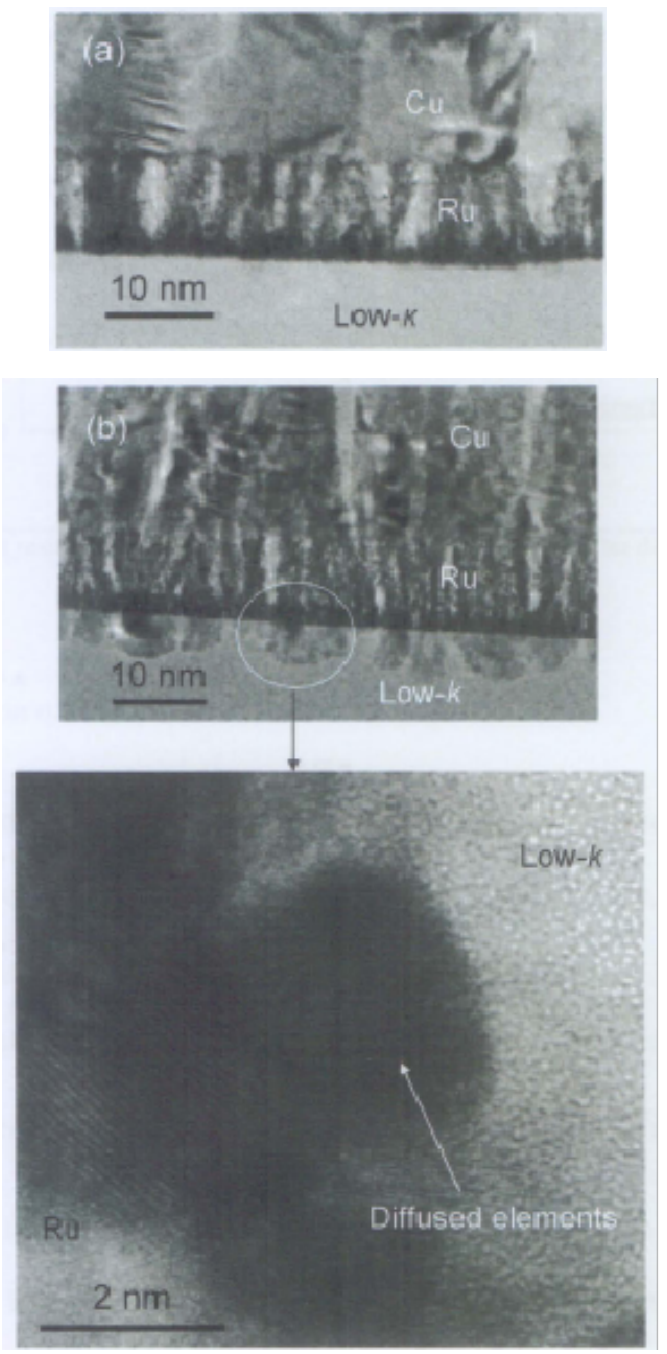

Figure 4.9 TEM micrographs of 30 nm Cu/10 nm Ru/low-κ (a) as-deposited (b) 500°C annealed

D. Sheet resistance

Figure 4.10 shows sheet resistance of as-deposited samples plotted against the underlying film (Ru or Ta) thickness. Electrical resistance in a metal thin film arises due to electron scattering by phonons, point defects, impurities,

grain boundaries, and film surfaces and interfaces [90]. It is observed that sheet resistance increases as Ru thickness decreases. This can be explained by an increase in relative contribution from interface (Cu/Ru and Ru/low-κ or Ru/Ta interfaces) scattering [91] as film thickness decreases and approaches its mean free path. Insertion of 10 nm Ta into the sample stacks decreases the sheet resistance by almost a constant value of 12.04 ± 2.701 Ω/sq since it provides additional conducting path for the electrons.

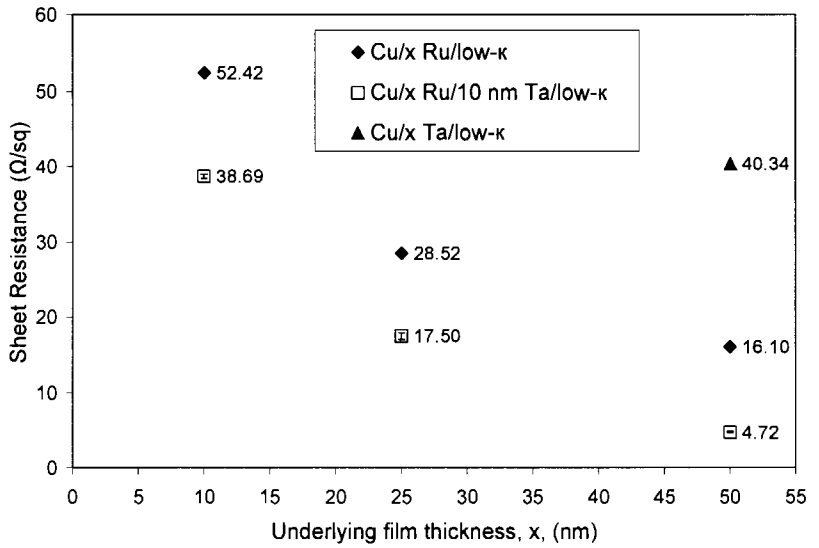

Figure 4.10 Sheet resistance of as-deposited samples plotted against the underlying film (Ru or Ta) thickness

Figure 4.11 shows sheet resistance of Cu/10 nm Ru/ low-κ sample before and after annealing. The sheet resistance was found to decrease drastically after 300°C annealing. Grain growth and defects elimination during the annealing in both Cu and Ru films may have lead to this decrease. In addition, diffusion of Ru, followed by Cu, into the low-κ may also increase the effective conducting layer thickness. Further annealing at higher temperatures does not appear to increase the sheet resistance of the sample.

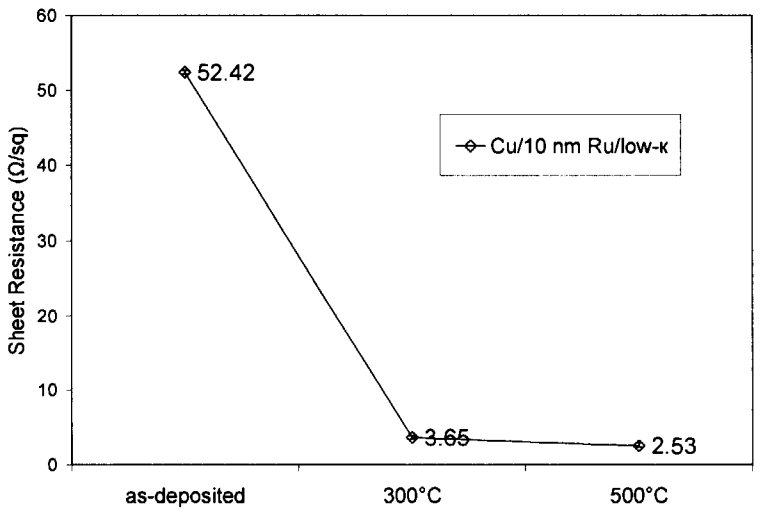

Figure 4.11 Sheet resistance of Cu/10 nm Ru/low-κ sample before and after different annealing conditions

E. Adhesion of Ru to low-κ

Adhesion study was done using a four-point bend adhesion tester on samples without Cu overlayer, namely Ru/low-κ, Ru/Ta/low-κ, and Ta/low-κ stacks since the interface of interest is Ru/low-κ and Ta/low-κ interfaces. The sample preparation and detail measurements have been described in Chapter 3, Section 3.3.6.

The critical fracture energy, G_c, for interface decohesion resulting from the four-point bend tests are plotted against different sample stacks in Figure 4.12. Comparing adhesion energy of Ru/10 nm Ta/low-κ samples for different Ru thicknesses, it is clear that adhesion energy decreases as Ru thickness increases. This observation could be attributed to changes in residual stress of the Ru layer as its thickness increases. Residual stress in the Ru layer was determined using the Williamson-Hall method [82] from the Ru film diffraction

data. The method has been described in Chapter 3, Section 3.3.4. The calculated values are plotted against the Ru thickness in Figure 4.13.

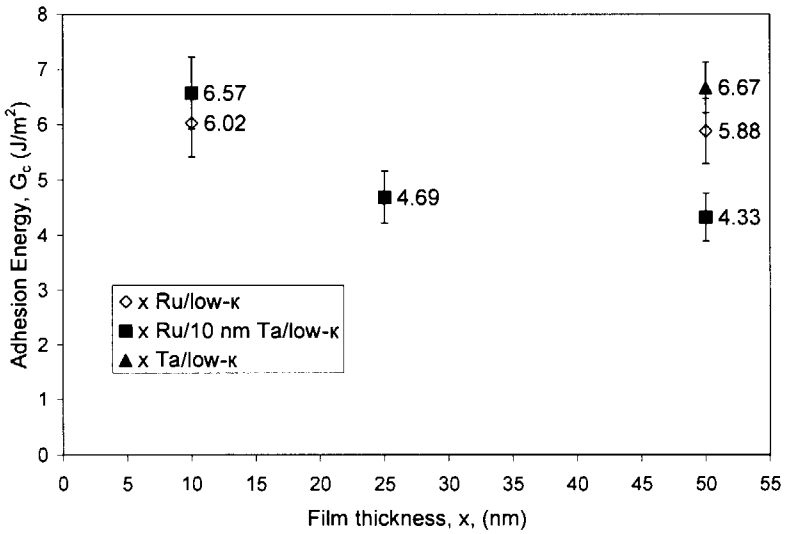

Figure 4.12 Adhesion energy, G_c, obtained from four-point bend test plotted against underlying film thickness

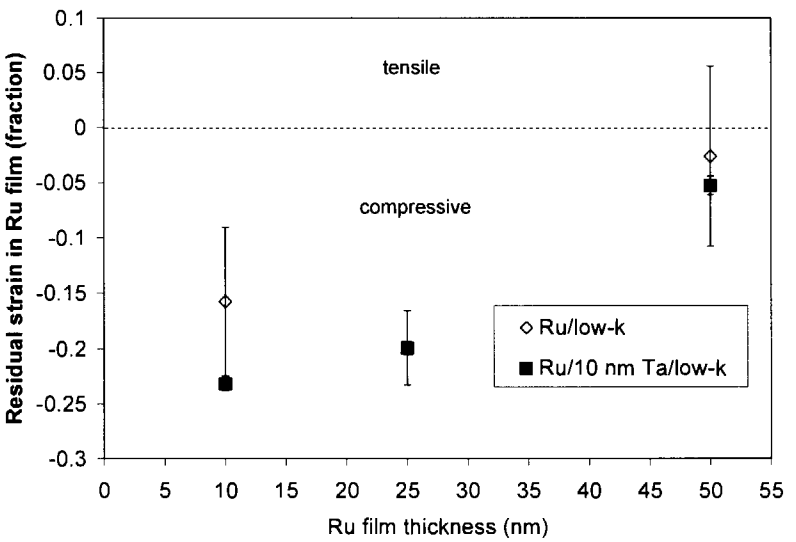

Figure 4.13 Calculated residual strain (in fraction) in Ru film plotted against Ru film thickness

These calculated results indicate that the Ru film has compressive stress initially and tends to become tensile as its thickness increases. This would lead to lower adhesion energy in the four-point bend test which is in agreement with

data reported by Litteken *et al.* [92]. Litteken *et al.* analyzed effects of an adjacent ductile layer (Cu) thickness on adhesion energy of TaN/SiO_2 interface, both experimentally and by simulation. They found that varying residual stress of the ductile film significantly affects extent of plastic energy dissipation and consequently G_c in four-point bend test. Moreover, they reported that the value of G_c increased by ~50% when Cu film residual stress was decreased from 306 to -59 MPa (from tensile to compressive strain). The data is replotted in Figure 4.14 to show the variation in adhesion energy with residual strain in Ru film. It can be seen that interface adhesion energy decreases as the film becomes less compressive as it thickens.

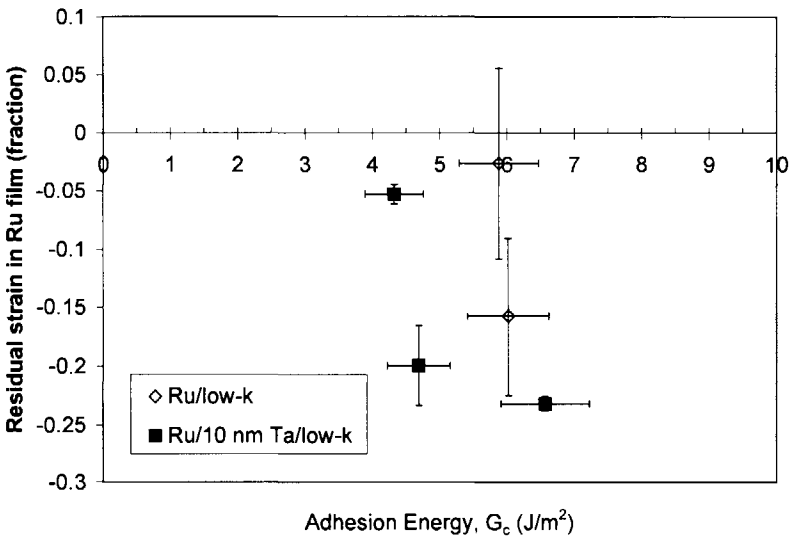

Figure 4.14 Ru film residual strain (in fraction) plotted against interface adhesion energy, G_c

XPS scans were done on both sides of delaminated surfaces after four-point bend test to establish the fracture path. The scan results are shown in Figure 4.15. Note that there are two spectrums in each graph. These correspond to the XPS scans from the top half and bottom half surfaces of the failed samples.

(a) Ru/Ta/low-κ

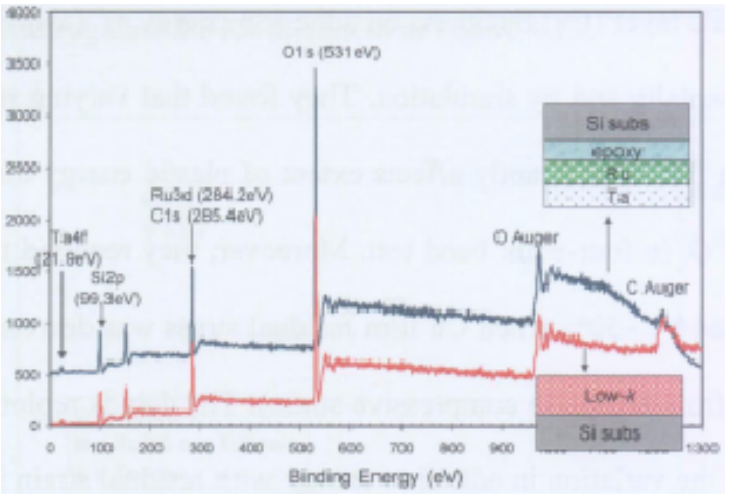

(b) Ta/low-κ

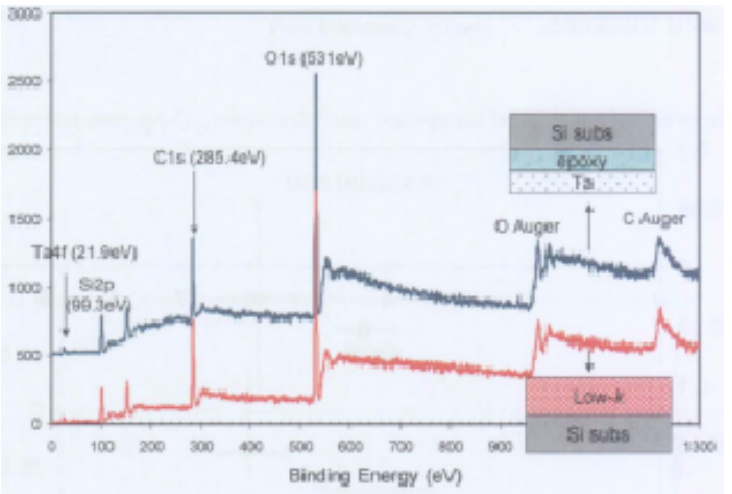

(c) Ru/low-κ

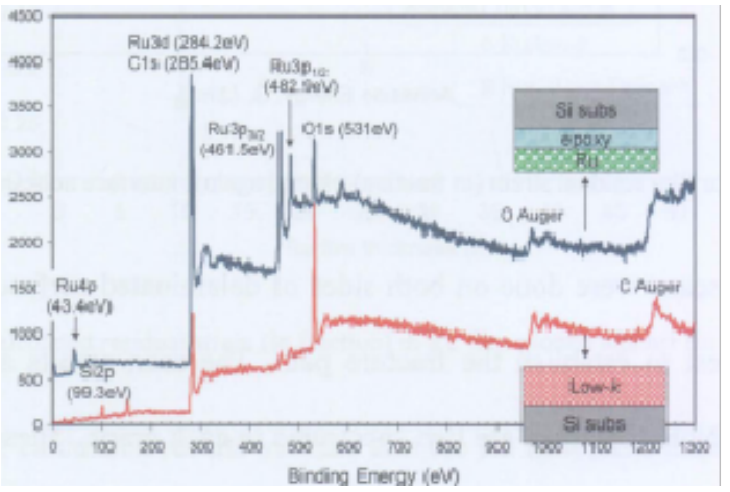

Figure 4.15 XPS scan on the surface of the top and bottom halves of the failed samples after four-point bend test (a) Ru/Ta/low-κ (b) Ta/low-κ (c) Ru/low-κ stacks

The XPS spectra of Ru/Ta/low-κ (Figure 4.15a) are identical to that of Ta/low-κ (Figure 4.15b) except for additional Ru 3d peaks at 280 eV and 284.2 eV (overlap with C 1s peak) at the top half of the failed Ru/Ta/low-κ sample. This indicates that the main path of delamination in Ru/Ta/low-κ and Ta/low-κ stacks is the Ta/low-κ interface. Since Ru/low-κ stack does not have a Ta-interface, hence it is likely to delaminate along the Ru/low-κ interface. The XPS spectra of delaminated surfaces of Ru/low-κ (Figure 4.15c) show additional Ru peaks at 43.4 eV, 461.5 eV and 482.9 eV on the top half of the samples while the bottom half is free of any Ru peaks, which confirms that the main delamination path is along Ru/low-κ interface.

Figures 4.16 and 4.17 show deconvolution of Ta 4f, Ru 3p, Si 2p, O 1s, and C 1s binding energy obtained from surfaces of failed Ru/Ta/low-κ and Ru/low-κ samples respectively. In Figure 4.16b, Ru 3p peak was negligible, confirming that Ru layer was not exposed; hence, the main delamination path in Ru/Ta/low-κ sample was along Ta/low-κ and not Ru/Ta interface. Additionally, in Figure 4.16a, Ta-C and Ta-O bonds were observed in addition to Ta-Ta bond, indicating that Ta does form good bonding with the underneath low-κ layer. In comparison, the samples without Ta layer (Figure 4.17) show that Ru exists mainly in elemental form and it has less bonding with low-κ compared to Ta, as exemplified by the weak Ru-O peak in Figure 4.17a. The bottom part of the failed samples in both cases (Ru/Ta/low-κ and Ru/low-κ) mainly showed the low-κ layer. This low-κ layer was signified by the presence of Si-O, Si-C, and Si-Si bonds shown in Figures 4.16c and 4.17b, O-C and O-Si bonds in Figures 4.16d and 4.17c, as well as C-O, C-C, and C-Si bonds in Figures 4.16e and 4.17d.

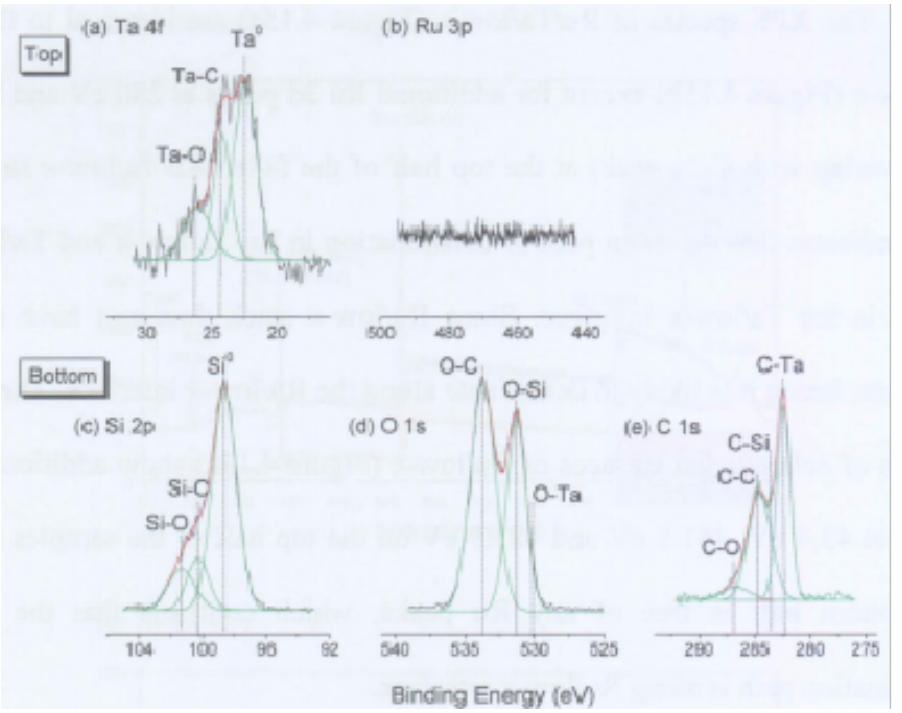

Figure 4.16 Deconvolution of (a) Ta 4f (b) Ru 3p spectra from the surface of the top half of the failed Ru/Ta/low-κ samples after four-point bend test (c) Si 2p (d) O 1s and (e) C 1s spectra from the surface of the bottom half of the failed Ru/Ta/low-κ samples after four-point bend test

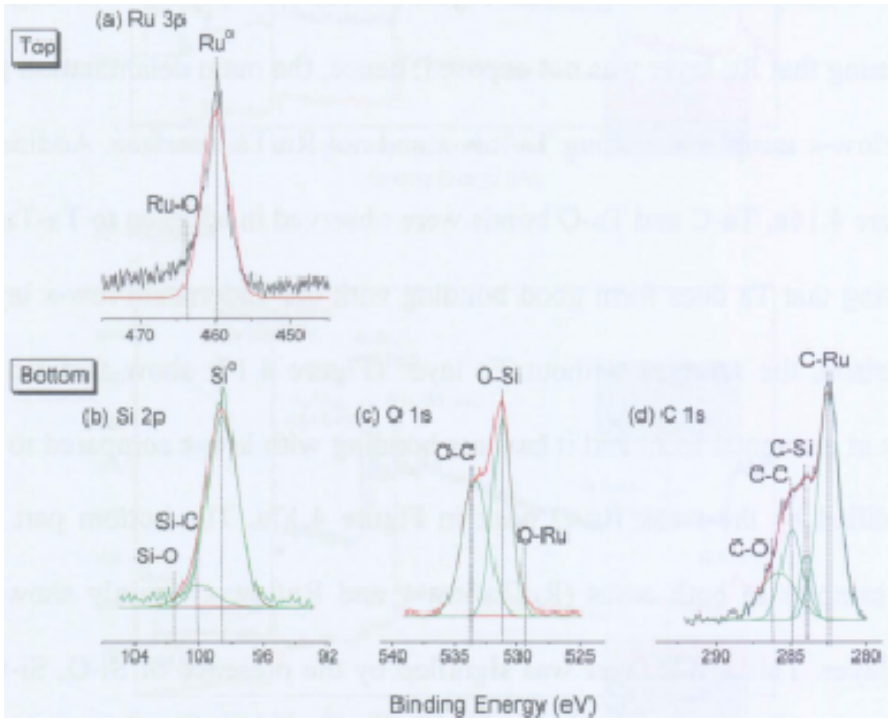

Figure 4.17 Deconvolution of (a) Ru 3p spectra from the surface of the top half of the failed Ru/low-κ samples after four-point bend test (b) Si 2p (c) O 1s and (d) C 1s spectra from the surface of the bottom half of the failed Ru/low-κ samples after four-point bend test

Adhesion energy of Ru/Ta/low-κ stack is slightly higher to that of Ru/low-κ stack for the same Ru thickness of 10 nm. Two factors could influence this observation namely, (i) nature of interface and (ii) residual stress. 10 nm Ru/low-κ sample has ~32% higher residual stress (more tensile) compared to having 10 nm Ta in between the Ru and low-κ. Furthermore higher bond energy of Ta-O (799.1 kJ/mol) [93] when compared to Ru-O (528.4 kJ/mol) [93] implies that Ru/Ta/low-κ should have an adhesion energy higher than Ru/low-κ.

4.3 Ru Barrier Failure Mechanism in Cu/Ru/Si System

Three sets of blanket samples of 50 nm Cu/x Ru/Si with Ru thickness, x, of 10, 20, and 30 nm were prepared to further understand the barrier failure mechanism. Two control samples of 20 nm Ru/Si and 50 nm Cu/Si were also prepared for comparison with the other samples. Si substrate instead of dielectric (SiO_2 or low-κ) was chosen for barrier failure analyses to provide quick and easy detection of failure. Reaction of Cu and Si to form silicide is easier to detect than diffusion of Cu in dielectric. In this study, barrier failure was assessed by the following three methods:

- monitoring the disappearance of Cu(111) XRD peaks and the appearance of Cu-silicide diffraction peaks,
- surface observation using FESEM (barrier failure was indicated by increase in surface roughness caused by silicide formation),
- monitoring the film sheet resistance using a four-point probe technique (increase in film sheet resistance due to silicide formation was used as an indication of the barrier failure).

It is significant to note that each of these methods leads to a different annealing temperature at which failure to be initiated. This is because of the different sensitivities of the method employed. Subsequently, the best method for this purpose will become apparent.

4.3.1 Cu Silicide Formation in Cu/Si

XRD spectra of as deposited and annealed Cu/Si samples are shown in Figure 4.18. Predominant Cu reflections at 2θ values of 43.29° (111) and 50.43° (200) (JCPDS card no. 04-0836) are clearly identifiable in the as-deposited sample and some of the samples annealed at low temperatures. Tetragonal Cu silicide (η′- Cu,Si), which is usually represented as Cu_3Si [94], was first detected in sample annealed at 500°C by its reflections at 2θ = 44.785° (320) and 45.473° (312) (JCPDS card no. 23-0224). Cu has a small ionic radius and relatively weak interaction with Si lattice, causing it to have high mobility in Si [94]. Additionally Cu dissolves interstitially in Si and when it reaches saturation, it could form a silicide [35].

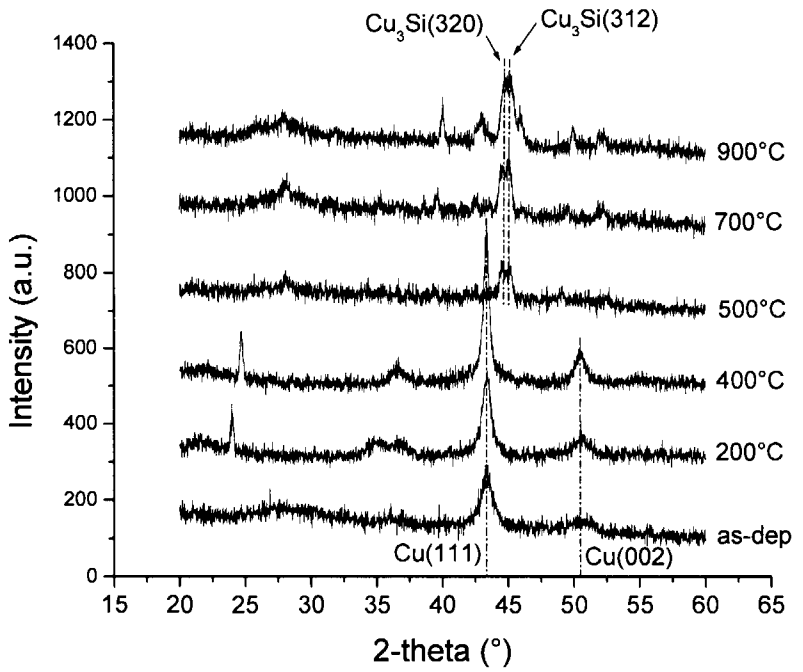

Figure 4.18 XRD spectra of 50 nm Cu/Si sample before and after different annealing conditions

The progress of the Cu/Si interface reaction is well captured in the series of FESEM micrographs of Cu surface layer shown in Figure 4.19. An initially smooth Cu surface begins to roughen as annealing temperature increases, reflecting formation of islands of Cu_3Si crystals beneath. The roughness is detectable even at temperatures as low as 300°C although XRD did not detect this phase. For temperatures lower than 300°C, the roughening was not evident. With increasing temperature, Cu_3Si crystals grow and get exposed to the surface at 900°C. Shape of the Cu_3Si crystals in Figure 4.19 is irregular, contradicting a report by Suh *et al.* [95] who observed pyramid-like Cu_3Si crystals in their Cu/(100)Si system when the Cu overlayer was etched off.

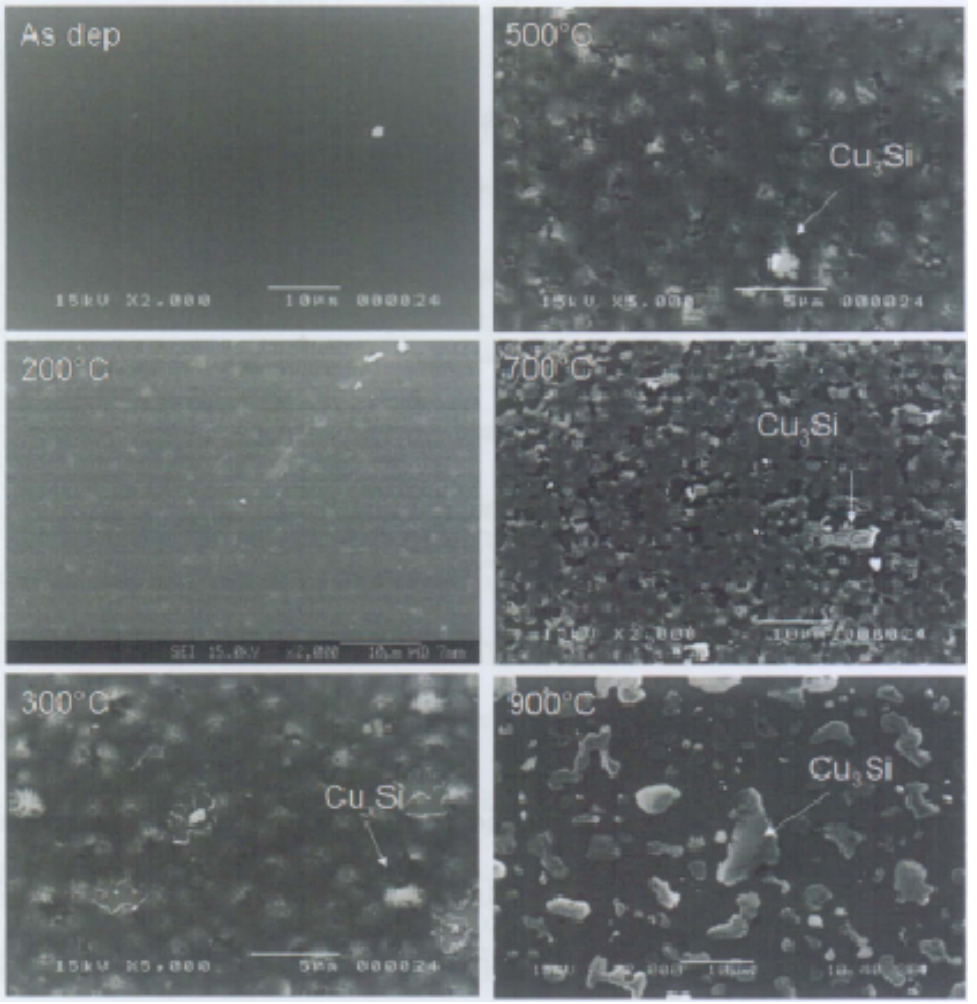

Figure 4.19 FESEM micrograph of 50 nm Cu/Si surface before and after annealing at the temperatures indicated

Furthermore, an abrupt, ten fold increase occurred in sheet resistance of Cu/Si sample at about 200°C, as shown in Figure 4.20, followed by persistently high sheet resistance at higher annealing temperatures. This increase in sheet resistance could be attributed to rapid Cu dissolution in Si, leading to Cu-silicide formation. At 200°C, neither XRD nor FESEM indicated any significant evidence for interface interactions in the sample yet its sheet resistance measurement shows that permanent damage has been done to the Cu metallization. Whilst this is expected in absence of any diffusion barrier layer, the high sensitivity of sheet resistance measurement in comparison with XRD

and FESEM techniques is worth noting. However, note that sheet resistance is not affected any further by subsequent formation and growth of silicides. Thus, sheet resistance measurement may be useful to pinpoint initiation of barrier failure but may not be effective to study the subsequent interface interactions. Cabral *et al.* [96] also has reported that sheet resistance measurement could be effective in rapid determination of Cu diffusion barrier failure.

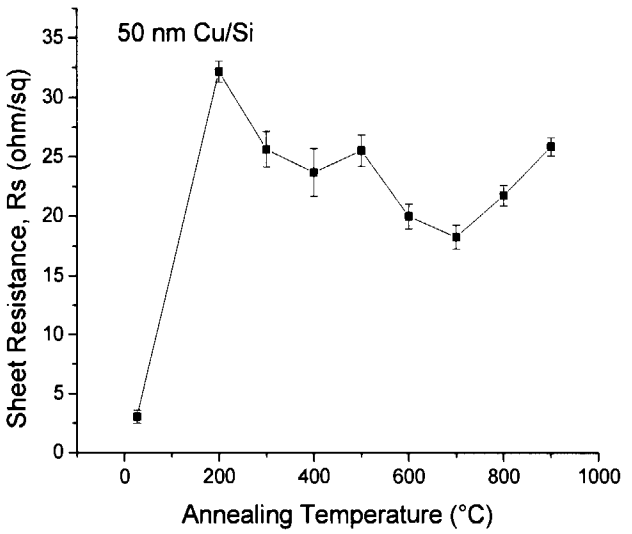

Figure 4.20 Average sheet resistance of 50 nm Cu/Si sample after different annealing conditions

4.3.2 Ru Silicide Formation in Ru/Si

To understand how Ru interacts with Si, Ru/Si bilayer was investigated. XRD spectra obtained on Ru/Si samples annealed at different temperatures are shown in Figure 4.21. Major peaks of hexagonal Ru are evident at 2θ = 42.15° (002) and 44.00° (101) (JCPDS card no. 06-0663). Orthorhombic Ru_2Si_3 is detectable for samples annealed at 700°C and higher, while Ru peaks disappear from the diffractograms. Many reflections of Ru_2Si_3 at 2θ = 25.59° (102), 32.36° (200), 41.71° (222), 46.42° (240) and 46.77° (124) (JCPDS card no.32-0978) prove its presence conclusively.

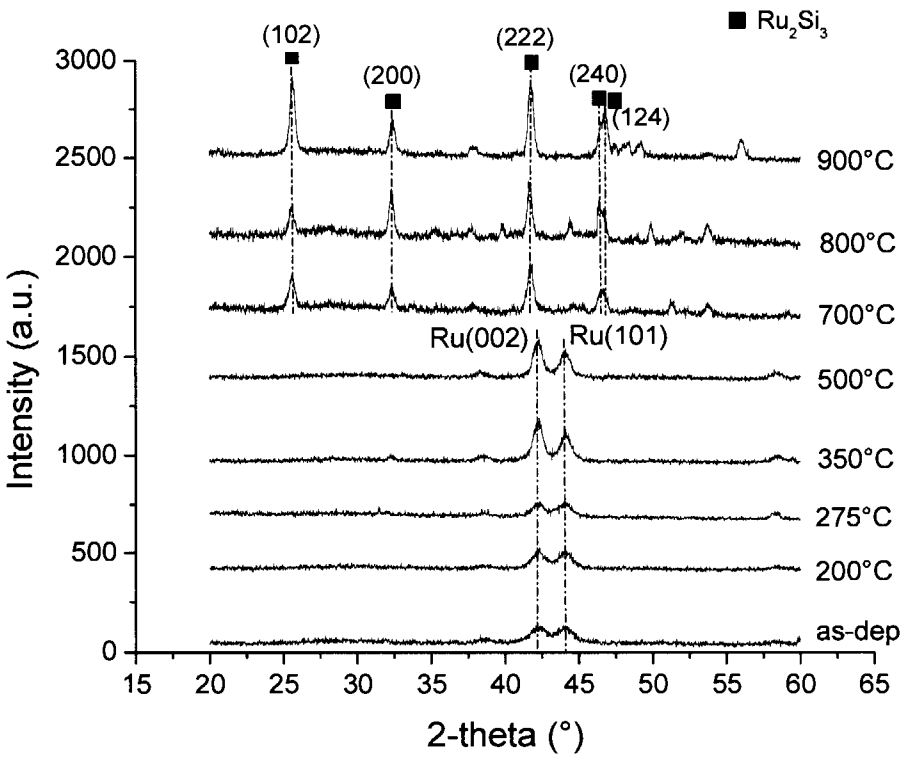

Figure 4.21 XRD spectra of 20 nm Ru/Si sample before and after different annealing conditions

FESEM examination of Ru surface did not show any significant changes to film roughness, as in Cu/Si, when annealed even at 700°C although XRD demonstrates presence of Ru_2Si_3. This could be due to different morphologies of Ru_2Si_3 and Cu_3Si. The Cu_3Si phase appears to form as isolated crystals at the interface which leads to film surface roughness. In contrast, Ru_2Si_3 may be more evenly distributed over the interface in the form of very small crystallites with a consequence of reduced surface roughness.

Sheet resistance measurements in Figure 4.22 did not show any dramatic changes, as for Cu/Si, but an increase after 700°C was noticeable. This is commensurate with the detection of Ru_2Si_3 by XRD. Thus, Ru_2Si_3 formation requires a higher temperature than Cu_3Si which is a positive result for the use of Ru as a barrier for Cu. It must also be noted that any interdiffusion between Ru

and Si does not seem to affect the resistivity of the Ru layer, in contrast to Cu/Si diffusion couple.

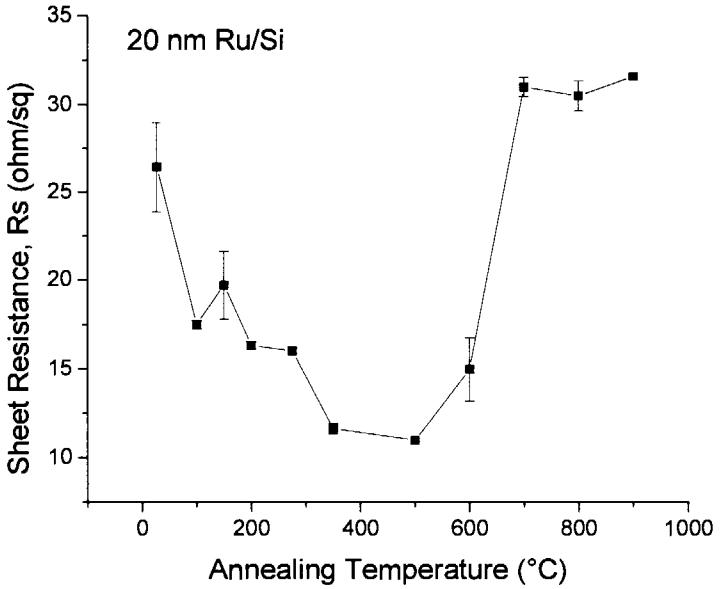

Figure 4.22 Average sheet resistance of 20 nm Ru/Si sample after different annealing conditions

Si was reported to be the dominant diffusion species in interaction between Si substrate and Ru film [97]. To verify this, concentration of Ru and Si were determined by SIMS depth profiling. Figure 4.23 shows concentration profiles of Si and Ru in Ru/Si samples after different annealing conditions. Si concentration in Ru increases with increase of annealing temperature while that of Ru in Si is relatively unchanged up to 700°C. By examining the recorded intensity of Si in Ru (counts/s) in the SIMS profile, it is observed that the amount of Si in Ru film increased by ~5 times after 200°C of annealing (Figure 4.23b) and further increased by ~20 times after 500°C of annealing (Figure 4.23d) in comparison to the as-deposited one. Therefore, diffusion of Si into Ru dominates over the reverse diffusion of Ru into Si. This is unlike the case of Cu/Si system, where Cu diffuses into Si substrate [37].

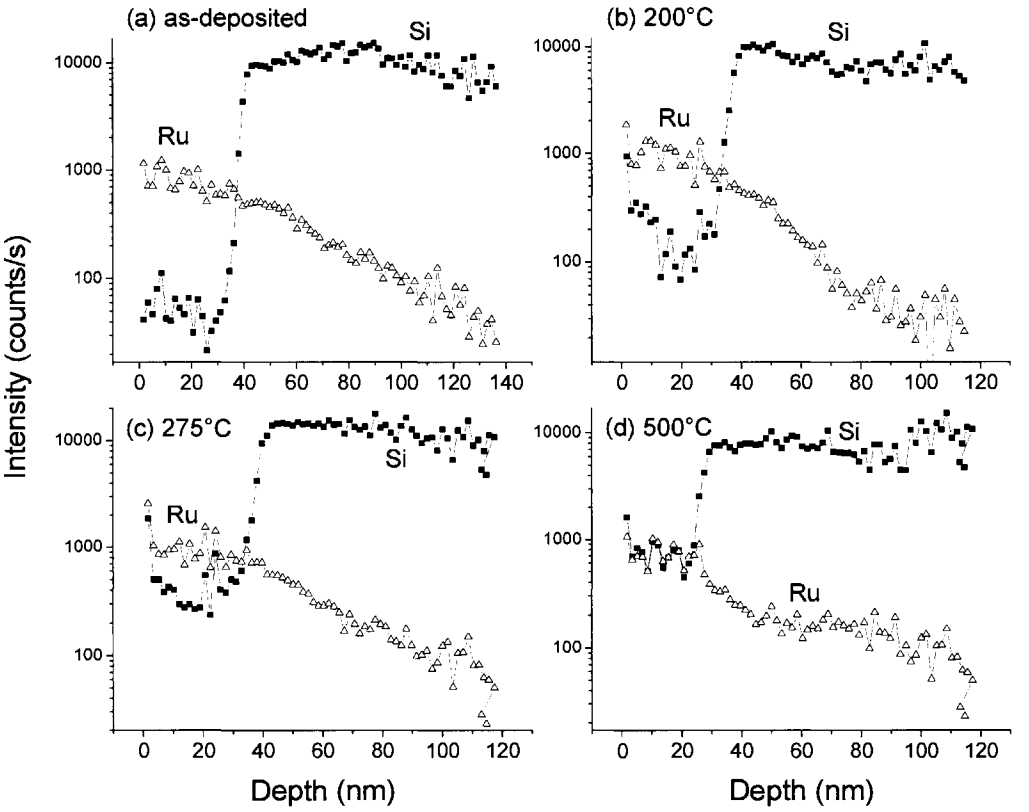

Figure 4.23 SIMS depth profile of 20 nm Ru/Si sample (a) as-deposited and after (b) 200°C (c) 275°C and (d) 500°C of annealing (obtained using Cs^+ gun)

4.3.3 Ru Barrier Breakdown in Cu/Ru/Si

The ability for Ru to be an effective barrier requires the investigation of Cu/Ru/Si trilayer samples. The behavior of these samples on annealing was not equivalent to the combined effect of the individual bilayers of Ru/Si and Cu/Si as will be discussed below.

It was clear from XRD spectra that both Cu- and Ru-silicides form in Cu/Ru/Si samples. An example is shown in Figure 4.24 for Cu/10 nm Ru/Si. Cu and Ru peaks are clearly observable in the as-deposited sample. These peaks become stronger with annealing, signifying grain growth of Cu and Ru. Complete consumption of Ru to form its silicide (Ru_2Si_3) is manifested at

700°C, followed by appearance of Cu_3Si at 800°C. Note that even Cu peaks are not detectable at 700°C, implying that all Cu has diffused into the layers beneath. In the other samples with different Ru thickness, the respective silicides were detected at the same temperatures, implying that the key parameter is temperature rather than Ru layer thickness. The barrier failure, as indicated by the sequence of phases formed, is primarily determined by Ru silicide formation. Once this phase forms, subsequent Cu diffusion into the substrate is rapid destroying the metallization.

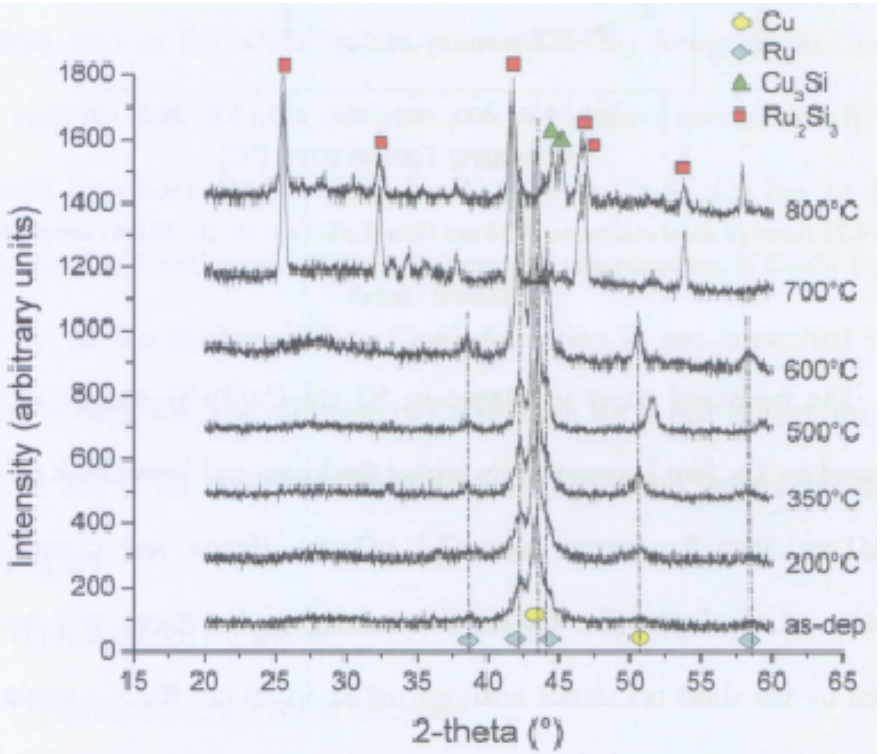

Figure 4.24 XRD spectra of 50 nm Cu/10 nm Ru/Si sample before and after different annealing conditions

The XRD observations are supported by sheet resistance measurement shown in Figure 4.25 where an increase in sheet resistance is noted at 600°C and higher. If we adopt this as the temperature for initiation of barrier breakdown, then Cu/Ru/Si breakdown initiation occurs at a temperature in

between that of Cu/Si (200°C) and Ru/Si (700°C) systems. It is lower than that for Ru/Si system and could be attributed to Cu/Ru intermixing.

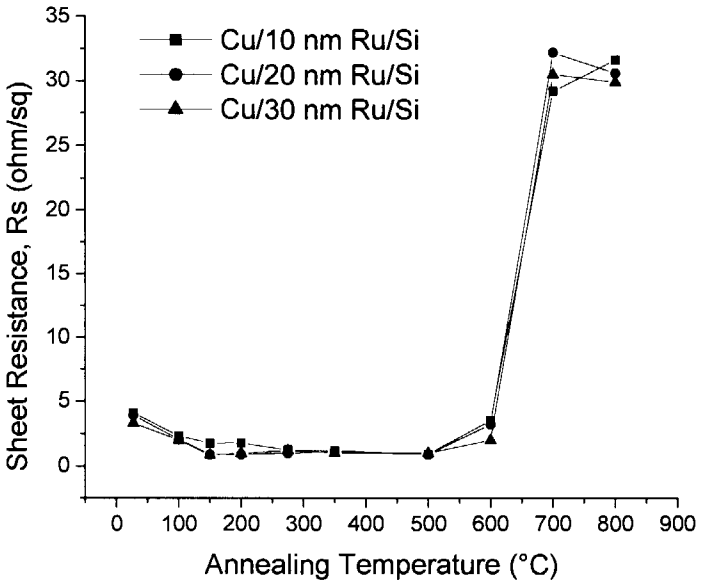

Figure 4.25 Average sheet resistance of 50 nm Cu/x Ru/Si (x = 10, 20, 30 nm) sample after the different anneals

The measured sheet resistance in 50 nm Cu/Ru/Si sample should be dominated by Cu film because of its higher thickness and lower bulk resistivity (1.7 μΩ.cm) than Ru barrier layer (7.1 μΩ.cm). Hence, any change in the resistivity of Cu layer (i.e. Cu/Ru intermixing at interface) will be easily detected by the sheet resistance analyzer unlike in 20 nm Ru/Si sample where the Ru layer is very thin and has a relatively higher inherent resistivity than Cu.

It must be noted that barrier failure detectable by sheet resistivity appears to be independent of the Ru barrier thickness (Figure 4.25). To predict the effect of Ru thickness, a Cu diffusion distance in Ru layer could be determined by knowing the diffusivity of Cu in Ru layer. Diffusion distance could be calculated using Equations 4.1 and 4.2:

$$d = 2\sqrt{(Dt)} \qquad ...(4.1)$$

$$D = D_0 \exp(-Q/kT) \qquad ...(4.2)$$

where d is diffusion distance, D is diffusion coefficient, Q is activation energy, R is gas constant (8.31 J/mol.K) and T is temperature in Kelvin. However, the thermodynamic data for Cu diffusion in Ru is not available in the literature.

Diffusion depends on temperature, time, and distance. A possible reason for the independence of Cu_3Si formation temperature on Ru thickness in Cu/Ru/Si sample is that the diffusion of Cu through Ru is probably not the rate controlling step in the whole failure process. Ru_2Si_3 formation in Cu/Ru/Si system need not depend on Ru thickness as Ru is in direct contact with Si (there is a Ru/Si interface). On the other hand, to form Cu_3Si, Cu has to diffuse through Ru. The kinetics will depend on time and temperature. If Cu_3Si forms at 800°C for all Ru thickness, then Cu_3Si formation is not controlled by Cu diffusion through Ru. The diffusion of Cu through Ru is fast enough for Cu_3Si to form at 800°C for all Ru thickness up to 30 nm. Other factors that may be controlling are:

(1) reaction of Cu and Si

(2) diffusion across Ru/Si interface

In (1), the reaction $3Cu + Si \rightarrow Cu_3Si$ may control, but our Cu/Si samples (Section 4.3.1) show reaction at temperatures as low as 300°C. Hence, this factor is not controlling. In (2), there might already be some Ru_2Si_3 at the interface. Diffusion of Cu through Ru_2Si_3 may be limiting. Since the thickness of Ru_2Si_3 is likely to be the same (independent of Ru thickness), diffusion of Cu through this silicide is independent on Ru thickness. At 800°C, Cu diffusion

through the silicide layer is adequate to form Cu_3Si. Note that Ru/Si study (Section 4.3.2) shows that Ru_2Si_3 is almost a continuous layer at the interface. Hence, diffusion of Cu through Ru_2Si_3 is likely the rate controlling step, thus it is independent of Ru thickness.

Another possible reason for this might be due to the annealing duration used in this study. Annealing for 1 hour may be long enough for the Cu diffusion at 700°C to reach the interface and react with Si to form Cu_3Si. Hence, thickness effect could not be detected. A shorter annealing duration may be necessary to detect the thickness effect on the barrier performance.

The surface morphology changes observed by FESEM are depicted in Figure 4.26. A triangular-prismatic shaped, new phase (approximately 5 μm in size) became clearly visible after 700°C anneal. At 800°C this phase ripened to larger sizes but seem to retain the triangular-prismatic shape. EDX analysis was done to confirm the phase composition of the triangular-prismatic particles. However, it is challenging to get a reliable quantitative analysis using EDX as electrons would penetrate deeper into the Si substrate. Hence, signals from layer beneath the particles would also be detected. Qualitatively, it was observed that the particles contain much higher Ru concentration compared to other areas. Hence, the particles are probably the Ru_2Si_3 phase detected by XRD. The Cu_3Si phase could not be identified by FESEM/EDX as the Cu EDX signal is widespread on the sample surface.

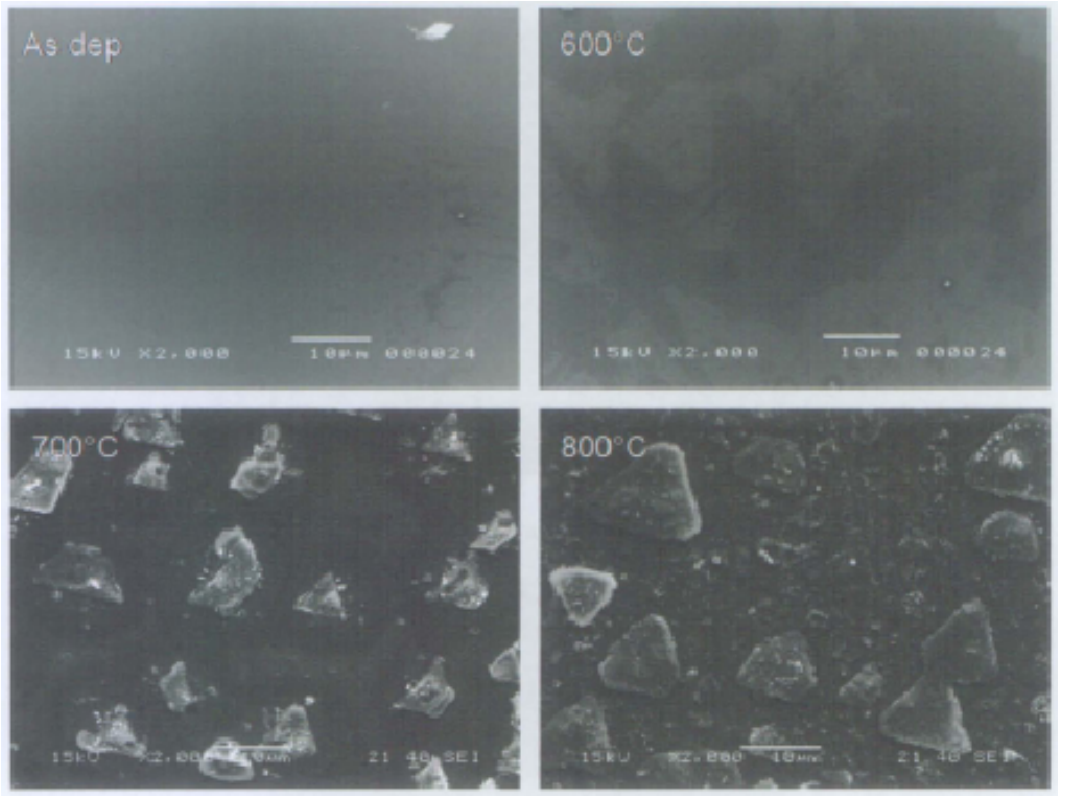

Figure 4.26 FESEM micrograph of Cu/20 nm Ru/Si surface before and after annealing at the temperatures indicated

To further understand the mechanisms involved and confirm the phases, cross-sectional TEM investigations were done on one sample (Cu/20 nm Ru/Si), as-deposited and annealed at 600, 700 and 800°C. Cross-sectioned TEM micrograph in Figure 4.27 shows that Ru layer deposited on Si is polycrystalline with columnar grains. An amorphous, native SiO_2 layer of thickness of about 2 nm is clear in the micrograph.

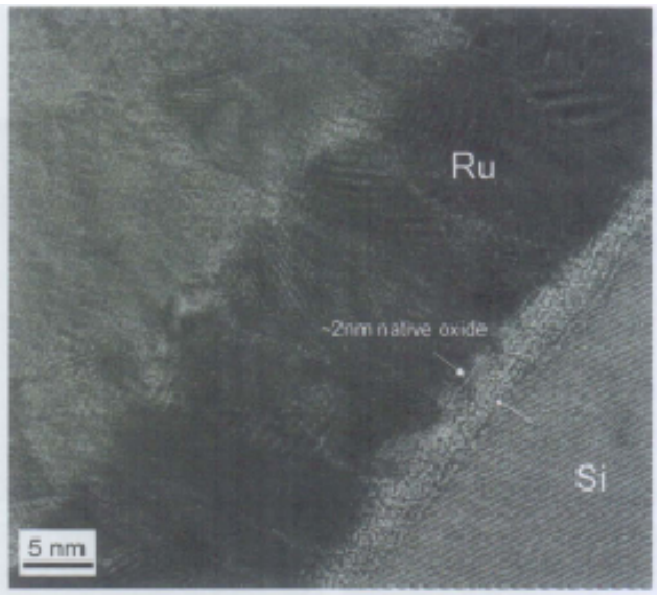

Figure 4.27 HRTEM micrographs showing columnar microstructure of ~20 nm as-deposited Ru on Si substrate

The TEM micrographs obtained on annealed samples are shown in Figure 4.28. Annealing at 600°C retains well defined Cu/Ru and Ru/native-oxide/Si interfaces (Figure 4.28a). Columnar polycrystalline nature of Ru barrier is also clearly seen in this micrograph. However, it must be noted that a slight increase in sheet resistance was measured at 600°C although no microstructure evidence for it is visible. After 700°C annealing, neither the Cu layer and nor the Cu/Ru interface was clear (Figure 4.28b). Cu diffusion appears to have begun in earnest. The layer next to the substrate must consist of Ru_2Si_3, as demonstrated by XRD. The Ru_2Si_3 layer thickness in Figure 4.28b is not uniform, but the film is almost continuous. If one examines the Ru/Si interface closely, small crystals (arrowed) can be seen to grow into the substrate from the oxide layer (inset in Figure 4.28b). This could be an early formation of Cu_3Si phase but may be too small to give XRD reflections. This further supports the notion that Cu diffusion begins before 700°C and is enhanced when Ru_2Si_3 forms. Cu_3Si phase ripens at 800°C as shown in Figure 4.28c, indicating that the

reaction continues to advance and the phase continues to grow into the Si substrate.

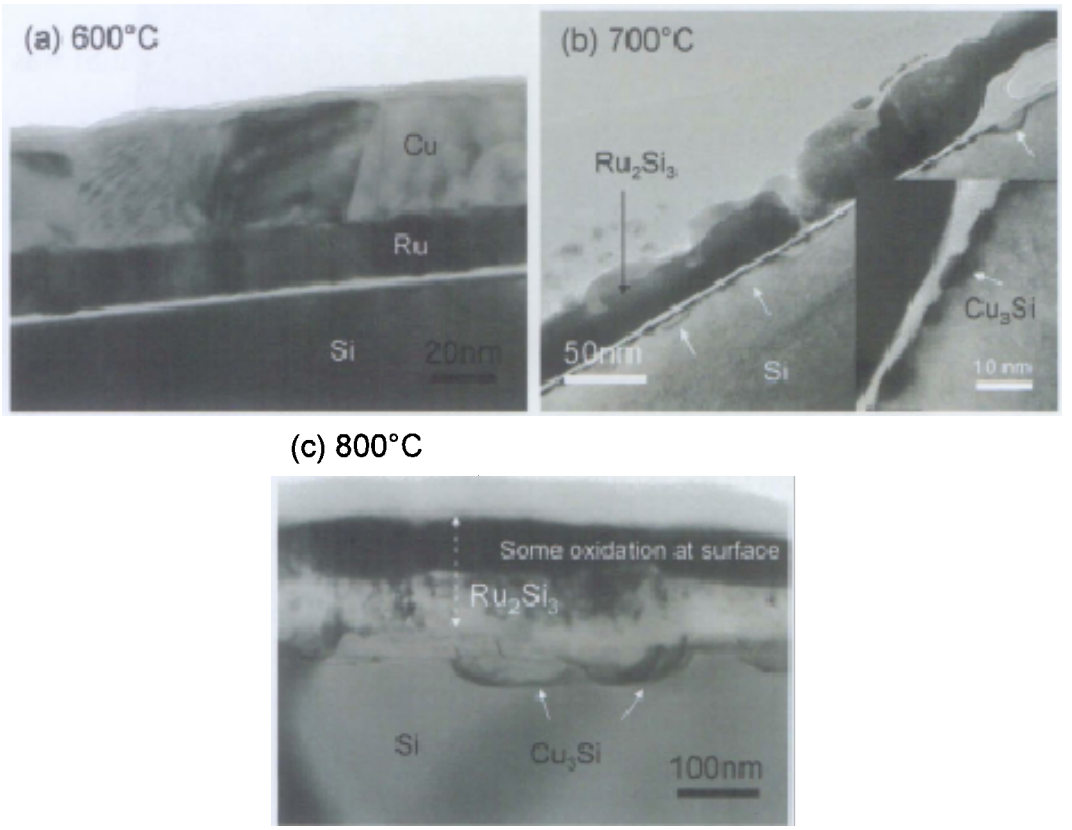

Figure 4.28 TEM bright field micrographs of Cu/20 nm Ru/Si samples annealed at (a) 600°C (b) 700°C and (c) 800°C

TEM investigation appears to signify that the directions of growth for Ru_2Si_3 and Cu_3Si are different. Ru_2Si_3 grows into the Ru layer while Cu_3Si grows into the Si. The latter growth direction is in contrast to Cu_3Si growth in Cu/Si sample where the silicides grew towards the surface. These observations imply that Ru_3Si_2 growth is sustained by diffusion of Si into Ru while that of Cu_3Si is caused by the diffusion of Cu into Si. Cu diffusant has to cross the Ru layer and the Ru_2Si_3 layer to become deeply embedded into the Si. The effect on the sheet resistivity of Cu/Ru/Si is delayed to higher temperatures compared to that in Cu/Si which is a positive result for the performance of Ru as a diffusion

barrier. There are clear indications that Ru_2Si_3 is probably providing the barrier property rather than Ru itself. Although Ru_2Si_3 is detected by XRD at 700°C, in both Ru/Si and Cu/Ru/Si samples, it was probably forming at temperatures lower than 700°C in order to delay the Cu_3Si formation. Note that Cu_3Si was detected when annealed at temperatures as low as 300°C in Cu/Si. Hence, Ru_2Si_3 is a necessary interface reaction layer for effective barrier properties of Ru in Cu/Ru/Si stacks.

EELS elemental mapping and line scan (Figure 4.29) were done to identify phases present in the sample after 800°C. Figure 4.29a shows the bright field TEM image where elemental maps of Ru, Cu, and Si (Figure 4.29b-d) were obtained. Figure 4.29e shows scanning TEM image on the same sample where the line scan was obtained. Both elemental map (Figure 4.29b, c, d) and line scan (Figure 4.29f) results show that Ru-silicide was forming on sample surface and Cu-silicide in the substrate. It was confirmed that Ru-silicide grows into the Ru layer from the Ru/Si interface (Figure 4.29b) whereas Cu-silicide formed at the Ru/Si interface and appears to grow into the Si substrate (Figure 4.29c). This could be due to the diffusing species which contribute to the silicide formation being different for each silicide. Si is the diffusant for Ru_2Si_3 formation while Cu diffusion is the main reason for Cu_3Si formation.

(a) Bright field TEM image (b) Ru EELS

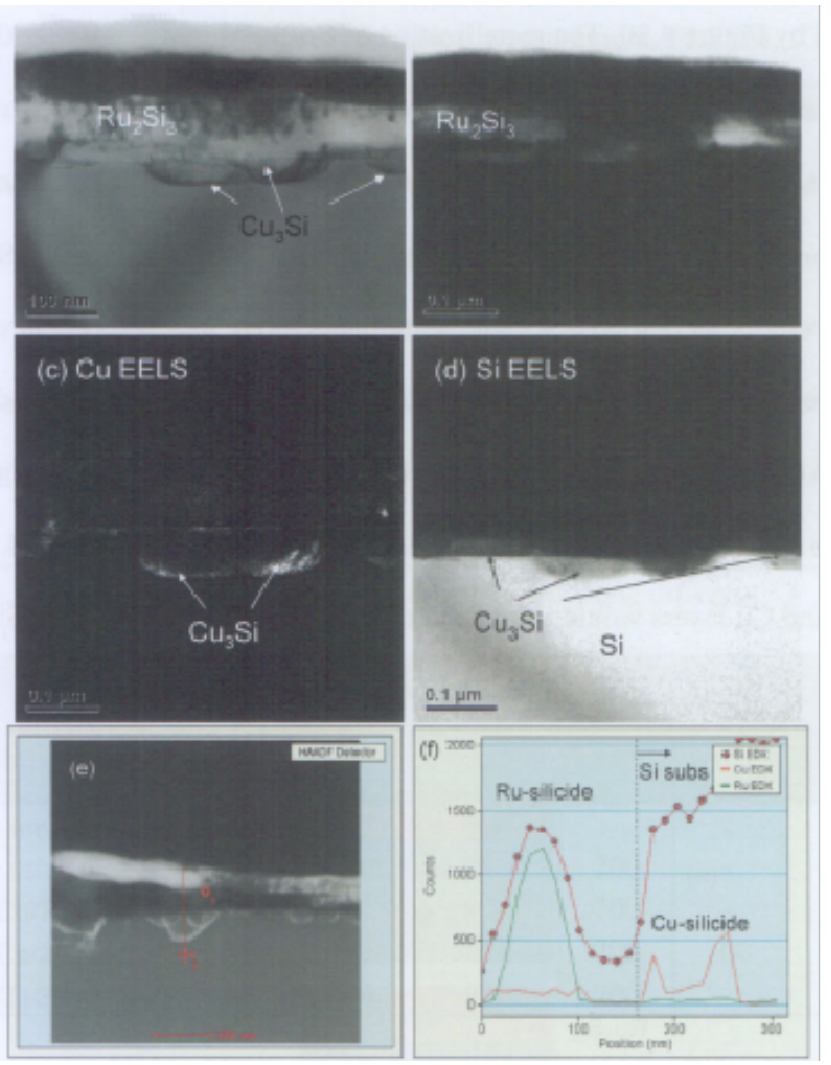

Figure 4.29 (a) Bright field TEM micrograph of 800°C annealed Cu/20 nm Ru/Si sample, EELS elemental map of (b) Ru (c) Cu (d) Si (the dashed white line represents the estimated film/substrate interface) (e) scanning TEM micrograph showing a line scan along the sample thickness (f) Ru, Cu, and Si EDX profiles along the line marked in figure (e)

Therefore, it is clear that good barrier properties could be derived from a continuous Ru layer for up to ~700°C and thereafter, breakdown becomes imminent when Ru is transformed to Ru_2Si_3. At this point Cu diffusion accelerates and Cu_3Si is nucleated in the substrate from the native oxide layer and grows inwards. This is the reason for not detecting Cu_3Si phase on the

surface by FESEM. This mechanism of barrier failure may be schematically depicted by Figure 4.30. The metallization of Cu/Ru/Si is still intact without any interfacial reaction at 600°C as indicated by clear distinction of Cu, Ru, and Si layers as shown in Figure 4.30a. Annealing at 600°C - 700°C causes initial formation of Ru_2Si_3 phase at Ru/Si interface (Figure 4.30b). This Ru_2Si_3 phase grows towards the Ru layer as annealing temperature increases (Figure 4.30c). Concurrently Cu diffusion also continues to occur across the Ru and Ru_2Si_3 layers. At 700°C Cu_3Si phase forms at Ru_2Si_3/Si interface and grows into the Si substrate as the annealing temperature increases. At 800°C (Figure 4.30d) all the Ru and Cu layers would have been converted into Ru_2Si_3 and Cu_3Si phases, indicating complete failure of the barrier.

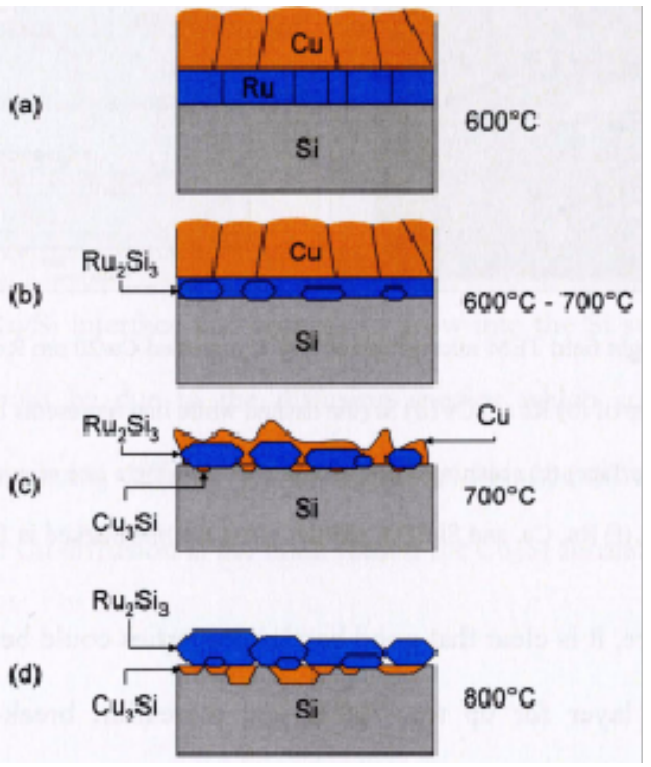

Figure 4.30 Schematic depiction of the barrier failure mechanism in Cu/Ru/Si (a) before barrier breakdown (b) initiation of barrier breakdown with the nucleation of Ru_2Si_3 (c) complete consumption Ru to form Ru_2Si_3 and early formation of Cu_3Si (d) complete barrier failure where Ru_2Si_3 + Cu_3Si are formed

Table 4.2 compares failure temperatures obtained by different characterization techniques (sheet resistance measurement, FESEM, XRD, and TEM). It is clear that resistivity measurement always indicates a lower failure temperature when compared to other microstructural methods. Additionally Ru_2Si_3 forms at 700°C with and without the presence of a Cu overlayer. However, Cu_3Si forms at 500°C when there is no Ru, and forms at 800°C when Ru barrier is present. The apparent breakdown of the barrier properties of Ru is independent on Ru thickness.

Table 4.2 Summary of failure temperature obtained using different techniques

Sample	Failure Temperature (°C)					
	R_s	FESEM	XRD		TEM	
			Cu_3Si	Ru_2Si_3	Cu_3Si	Ru_2Si_3
50 nm Cu/Si	200	300	500	-	-	-
20 nm Ru/Si	700	>700	-	700	-	700
50 nm Cu/10 nm Ru/Si	600	700	800	700	-	-
50 nm Cu/20 nm Ru/Si	600	700	800	700	700	700
50 nm Cu/30 nm Ru/Si	600	700	800	700	-	-

4.4 Summary of Results

In the initial part of this chapter, the effect of Ru underlayer on the texture and surface roughness of Cu films, the diffusion barrier properties of Ru, and its adhesion to low-κ were investigated using sample stacks of Cu/Ru/low-κ, Cu/Ru/Ta/low-κ and the control sample of Cu/Ta/low-κ. Conclusions that could be drawn from this part of the work are:

- Ru promotes a more pronounced Cu(111) texture than Ta when their thicknesses are similar. This could be attributed to the lower lattice

mismatch (~4 - 5%) between the Cu(111) plane and Ru(101) or Ru(002) planes compared to that of Ta(002) (~10%). Further, the degree of texture appears to increase with increase of the Ru layer thickness.

- Physical vapor deposited Cu films on both Ru and Ru/Ta layers are adequately smooth with RMS roughness of ~0.8 - 1.4 nm. This is independent on Ru thickness as well as those of layers underneath.
- Significant penetration of Cu and Ru into low-κ occurs at temperature as low as 300°C, indicating that Ru is not an effective diffusion barrier layer. Additionally, XPS study shows no interfacial reaction in Cu/Ru/low-κ sample upon annealing as indicated by negligible shifts in the binding energies of the elements.
- The adhesion strength of Ru/low-κ interface is approximately 6 J/m^2 which is similar to that of Ta/low-κ interface (~6.5 J/m^2). The slight difference in the adhesion strength is attributed to the better bonding between the Ta film and the low-κ substrate, as indicated by formation of Ta-O and Ta-C bonds at Ta/low-κ interface. To the contrary, less Ru-O and Ru-C bonds were detected at Ru/low-κ interface.
- The low-κ interface i.e. Ru/low-κ and Ta/low-κ, appears to be the weakest interface in the stacks which led to delamination in four-point bend tests.

Subsequently, breakdown of the pure Ru diffusion barrier was investigated experimentally in detail using Cu/Si, Ru/Si, and Cu/Ru/Si stacks as they are exposed to high temperatures, for Ru thicknesses of 10 - 30 nm. This part of the work leads to the following conclusions:

- Without the presence of Ru barrier layer, the Cu/Si sample fails at temperature as low as 200°C as signified by ~16 times increase in sheet resistance although FESEM and XRD studies indicate Cu_3Si formation only after annealing at 300°C and 500°C respectively.
- Without the presence of Cu overlayer, Ru_2Si_3 formation in the Ru/Si sample was observed to occur after 700°C of annealing as examined by both sheet resistance and XRD methods.
- In the Cu/Ru/Si sample, microstructural evidence for barrier failure, in the form of triangular-prismatic Ru_2Si_3 phase, becomes detectable in FESEM and XRD when annealed at 700°C. Thereafter, Cu diffusion accelerates through Ru and Ru_2Si_3 layers leading to rapid deterioration in the conductivity of the metallization. Eventually, Cu_3Si phase was observed to form at 800°C.
- Sheet resistance measurements in Cu/Ru/Si sample shows a slight increase in sheet resistance after 600°C of annealing which is attributed to the Cu and Ru diffusion, followed by a sharp increase after 700°C which is attributed to the silicide formation.
- The early sign of barrier failure detected by sheet resistivity measurements at 600°C is worth noting. Thus, sheet resistivity measurement could be a very useful tool to determine the health of the barrier layer.
- TEM study in Cu/Ru/Si sample shows that the Cu_3Si phase nucleates on the native oxide film on Ru/Si interface and grows into the substrate. To the contrary, Ru_2Si_3 grows into the Ru layer. The difference in the silicide growth direction is attributed to the different diffusing species

i.e. Cu is the diffusing species in Cu_3Si formation whereas Si is the diffusing species in the Ru_2Si_3 formation.

- This interface reaction sequence is independent of the Ru layer thickness for the thickness range investigated (10 - 30 nm), indicating that the diffusion of Cu through Ru_2Si_3 is the likely rate controlling step, not diffusion through the Ru itself.

CHAPTER 5

Analysis of Ru-N Barrier in Cu Interconnect System

5.1 Background

As pointed out in Literature Review in Chapter 2, Ru was investigated as a barrier material for Cu metallization because:

- It has an ability to facilitate direct deposition without a seed layer [22].
- It has low solubility in Cu [23] which is beneficial since its impurity doping effect on Cu resistivity will be minimal.
- Ru is compatible with the established CVD and ALD technologies unlike Ta [12].
- It has a good adhesion to Cu, even in an absence of a seed layer [24, 29]. Our previous results on pure Ru (in Chapter 4) has also demonstrated good adhesion of 10 nm Ru to low-κ dielectric (adhesion energy, G_c, of 6.02 ± 10% J/m^2), comparable to that of Ta to low-κ (G_c = 6.57 ± 10% J/m^2).

Despite these merits, Chan *et al.* [29] claimed that Ru is inadequate as diffusion barrier layer because a ~15 nm Ru barrier layer failed after annealing at 450°C for 10 minutes in a Cu/Ru/Si system. Based on our study on pure Ru reported in Chapter 4, Cu/Ru/Si system with ~20 nm Ru does not fail until 700°C anneal for 1 hour, identified by almost ten times increase in sheet resistance due to silicide formation. On the other hand, Cu/Ru/low-κ system failed after annealing at temperature as low as 300°C due to fast diffusion of Cu

and Ru into the dielectric. Therefore, to exploit the benefits of Ru in Cu metallization, its barrier performance must be enhanced. Chapter 4 shows that pure Ru is not an adequate barrier but is a good seed layer. Hence, we proceeded to improve its diffusion barrier properties. The failure temperature being independent of Ru thickness is an important indication that it is not a conventional diffusion barrier where diffusion of Cu through Ru is minimized. Chapter 4 shows that the diffusion barrier effect is caused by possibly the Ru-silicide at the Ru/Si interface. Now we attempt to improve the inherent diffusion barrier properties of Ru by dissolving nitrogen. Introduction of an element with small atomic size (such as B, N or C) into a film was reported to improve the film barrier properties by amorphization [98] and/or grain boundary stuffing [99]. N was chosen for this study since its incorporation into the film by sputtering is relatively easy, simply by introducing N_2 gas into the deposition chamber.

First part of this chapter reports effect of N incorporation into Ru layer on films microstructure, sheet resistance, silicide formation temperature, as well as Cu and Ru diffusion during thermal annealing. A modification noted in film microstructure due to high level of dissolved N in Ru film is discussed. Subsequent work in analytical electron microscopy has given clear evidence for N dissolution in Ru when sputtered in N_2 atmosphere. Later part of this chapter reports these findings, as well as study on Ru-N thermal stability including evidence for cavity/void formation at Cu/Ru interface during N out-diffusion from Ru films upon annealing.

5.2 Experiments

Two types of substrates were chosen for the study, namely p-Si(111) wafer and p-Si(111) with SiO_2 cover. A 10 nm thick Ru layer (99.95% purity) was sputter deposited onto pre-cleaned wafers in a Cryo Vac magnetron sputtering machine at room temperature, 10^{-6} Torr base pressure, and 5 mTorr working pressure. Deposition was done in two gas atmospheres; (i) Ar at a flow rate of 10 sccm for Ru film, (ii) N_2 at a flow rate of 10 sccm for Ru-N film. After that, Cu (99.99% pure) was sputter deposited onto the Ru or Ru-N layer in the same machine under the same sputtering condition, using only Ar as the sputtering gas. Samples with the following layer stacks were produced:

- Ru/Si
- Ru-N/Si
- Cu/Ru/Si
- Cu/Ru-N/Si
- Cu/Ru/SiO_2
- Cu/Ru-N/SiO_2

The first four sets of samples were prepared to study the effect of N on Ru barrier properties, particularly on the barrier failure by reaction of Cu and Si. The latter two sets of samples on SiO_2 substrate were prepared to study the diffusion of Cu into SiO_2 through Ru-N layer in comparison to that through pure Ru film. Samples were then annealed for 1 hour at progressively increasing temperatures up to 900°C in a high-vacuum ambient of 10^{-5} Torr.

Samples were analyzed in a Rigaku Dmax 2200 x-ray diffractometer (XRD) using 1.542 Å (Cu K_α) incident x-ray and in a Kratos AXIS

spectrometer for x-ray photoelectron Spectroscopy (XPS) with monochromatic Al K_α X-Ray radiation at 1486.71 eV. Cross-sectioned samples were examined in a FEI Tecnai F30 (300 kV) transmission electron microscope (TEM) equipped with electron energy loss spectroscopy (EELS) and energy dispersed x-ray spectroscopy (EDX) detectors for elemental analysis. The TEM samples were prepared conventionally using mechanical grinder and polisher, dimpling, and ion milling. A secondary ion mass spectroscopy (SIMS) with a Cs^+ sputtering gun was employed to monitor N content within the Ru layer when annealed.

5.3 Results and Discussion

5.3.1. Effect of Dissolved Nitrogen on Structural Properties, Silicide Formation, Sheet Resistance, and Diffusion

A. Structural properties of pure Ru and Ru-N films

Figure 5.1 shows XRD spectra of as-deposited Ru and Ru-N films on Si. Ru/Si sample in Figure 5.1a consistently exhibits prominent Ru hexagonal peaks at 2θ = 38.38° (100), 42.15° (002), 44.00° (101), 58.32° (102), 69.40° (110), and 78.38° (103) (JCPDS card no. 06-0663), whereas Ru-N/Si sample in Figure 5.1b gives a single broad peak at 2θ = 33.58°. The difference in the XRD data could be attributed to the difference in microstructure as well as crystal structure of Ru-N in contrast to that of Ru. The amorphous nature of Ru-N film deposited under N_2 gas was confirmed using TEM which will be discussed at the later part of this chapter.

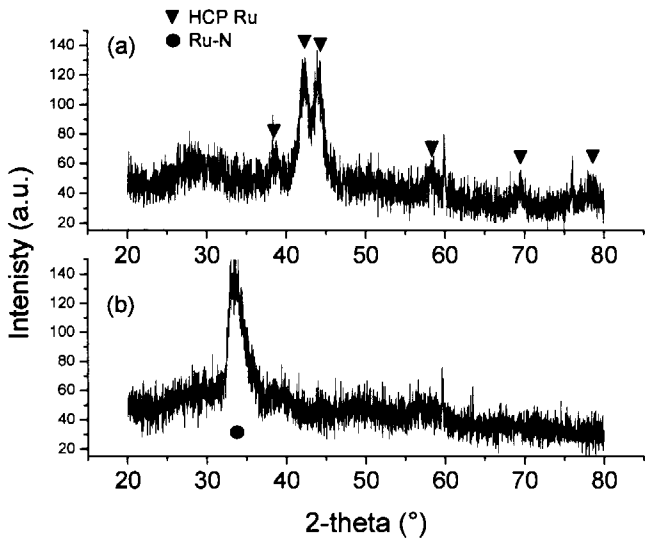

Figure 5.1 XRD spectra of as-deposited (a) Ru/Si and (b) Ru-N/Si

B. Silicide formation under thermal annealing

Silicide formation is often used as a quick indication of barrier failure. XRD spectra obtained from Ru/Si and Ru-N/Si as well as Cu/Ru/Si and Cu/Ru-N/Si after aging at various temperatures are shown in Figure 5.2a – 5.2d in an order of increasing thermal stress. Ru/Si samples (Figure 5.2a) consistently exhibit prominent Ru hexagonal peaks from as-deposited condition up to 500°C. These peaks are initially broad but become progressively sharper and higher in intensity as the annealing temperature is increased. This signifies gradual grain growth of an initially nanocrystalline Ru with increasing annealing temperature. For annealing at 700°C and higher, orthorhombic Ru_2Si_3 is detected with peaks at 2θ = 25.59° (102), 32.36° (200), 41.71° (222), 46.42° (240), 46.77° (124), and 53.83° (205) (JCPDS card no. 32-0978) while Ru peaks disappear. It is known that Si is a dominant diffusion species in the chemical interaction between Si wafer and Ru film [97]. Thus, Ru would have converted to the silicide at the higher temperatures.

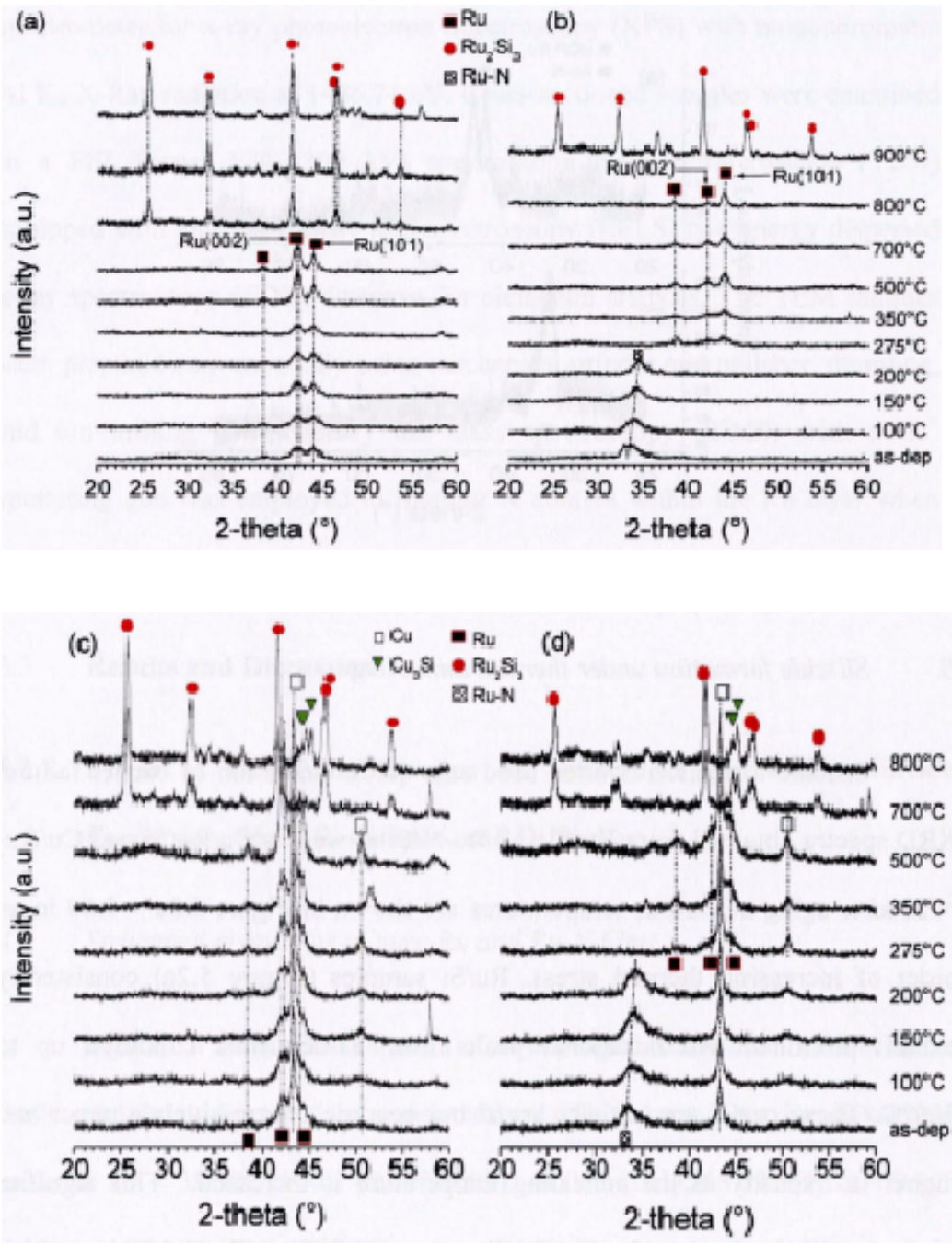

Figure 5.2 XRD spectra of (a) Ru/Si (b) Ru-N/Si (c) Cu/Ru/Si (d) Cu/Ru-N/Si with increasing of annealing temperature

The spectra obtained in Ru-N/Si (Figure 5.2b) show some important differences compared to Ru/Si (Figure 5.2a). In as-deposited state up to 200°C, Ru peaks are not detectable but a single broad and weak peak appears at 2θ = ~33.5° (Figure 5.2b). It may indicate the presence of some ultrafine,

nanocrystals in an amorphous matrix. We attribute the amorphization to the presence of dissolved N in the Ru layer, causing expansion of the Ru lattice. It should be noted that Ru is not known to form a stable nitride and hence, the N is forced to dissolve in the Ru crystal. The lattice distortion caused by dissolution of excessive N destroys the crystal structure making it amorphous. Annealing at temperatures up to 200°C does not cause any significant change in the XRD spectra except for a noticeable shift of the only peak to higher 2θ values. This indicates some lattice relaxation during the annealing process. For samples, when annealed at temperatures higher than 275°C, this peak is absent but Ru hexagonal peaks evident in Ru/Si samples begin to appear. Extinction of this unknown peak and appearance of Ru peaks could be attributed to out-diffusion of N atoms and crystallization in Ru layer that will be discussed at a later part of this chapter.

Ru grains grow and at high temperatures Ru_2Si_3 begins to form. From the XRD results, it is clear that Ru silicide is not detected until 900°C in Ru-N/Si (Figure 5.2b), but in Ru/Si, the silicide is formed at 700°C (Figure 5.2a). However, with the presence of Cu layer on top of the Ru (in Cu/Ru/Si and Cu/Ru-N/Si), Cu silicide was observed to accompany Ru silicide formation after 700°C (Figure 5.2c and 5.2d). A similar phenomenon was reported previously for Re on Si with and without a Cu overlayer [100]. Temperature of $ReSi_2$ formation, which is normally over 900°C, is lowered to only 550°C with the presence of Cu. Lin *et al.* [52] also reported the lowering of $TaSi_2$ formation temperature by 200°C with the presence of Cu overlayer on TaB_x/Si structure. They attributed the lowering of silicide formation temperature to the presence of diffused Cu which is instrumental in breaking Si–Si bonds as it moves. When

Cu diffuses through the barrier film and reaches the barrier/Si interface, it results in formation of either Si self-interstitials or vacancies in the Si lattice. Concentration of these point defects is greatly enhanced during thermal annealing, and promotes reaction of Si with barrier and Cu.

Lavoie *et al.* [101] reported the effect of an additional element on silicide formation and silicide phase transition temperature in the case of Co silicide. They reported that depending on miscibility of the elements in the respective silicide phases, the silicide formation temperature may be increased or decreased. A change in miscibility will lead to changes in entropy of mixing that directly affect phase nucleation. This implies that if the silicide phase and the additional elements are miscible, the silicide formation temperature will be lowered [101].

In our study, a decrease in N content in Ru film during thermal annealing was observed. The loss of N is possibly because of N out diffusion to surface/atmosphere and/or N segregation to Ru/native-SiO_2 interface (detail discussion will be presented in subsequent sections). N has good miscibility in SiO_2 and Si, and is likely to form Si-oxynitride phase at interface (Gibbs free energy of formation, ΔG_f^0, of Si-nitride = -326.10 ± 125.52 kJ, ΔG_f^0 of Si-oxide = -824.93 ± 12.55 kJ at room temperature [102]). Such an oxynitride phase is favored over the Ru_2Si_3 phase, resulting in higher Ru_2Si_3 formation temperature. However, with the presence of Cu overlayer, Cu diffusion towards Si substrate will occur, accompanying N interfacial segregation. Cu has a high tendency to form Cu-silicide to lower the total energy. In addition, Cu is immiscible with N hence, once the Cu interacts with Si at the interface, Cu-silicide will be formed

at 700°C. When the non-continuous Cu-silicide is formed at 700°C, Si-oxynitride will be destroyed, exposing Ru directly to the Si substrate. At 700°C, Ru and Si have just enough driving force to form Ru-silicide. Therefore, both, Cu- and Ru-silicides are formed simultaneously at 700°C in Cu/Ru-N/Si system.

Note that Ru grains which crystallized accompanying N out diffusion have mainly (101) orientation (<101> direction normal to the plane of the film) as shown in Figure 5.2b whereas Ru grains in pure Ru/Si sample have predominantly (002) orientation (Figure 5.2a). Figure 5.3 shows the relative intensity of Ru(001)/Ru(002) after different annealing conditions in Ru/Si and Ru-N/Si films. Note that Ru-N/Si samples annealed at temperature < 275°C and Ru/Si samples annealed at temperature ≥ 700°C do not have hexagonal Ru peaks. In as-deposited and 100°C annealed Ru/Si sample, the Ru film seems to have a random texture since the ratio of Ru(101)/Ru (002) is close to a value of 1. Upon annealing at higher temperature, Ru(002) becomes more dominant in Ru/Si film, indicated by a decrease in $I_{Ru(101)}/I_{Ru(002)}$. In contrast, the crystallized Ru film from amorphous Ru-N exhibits Ru(101) as the predominant peak. Furthermore, the Ru(101) intensity increases with increase in temperature. The value of $I_{Ru(101)}/I_{Ru(002)}$ ratio of Ru-N/Si film at 800°C is ~2.63, close to that of pure Ru from powder diffraction data (JCPDF file no. 06-0663) of 2.857. Hence, pure Ru deposited using Ar on Si substrate has (002) texture whereas that from crystallized Ru-N will have (101) texture, similar to Ru powder diffraction.

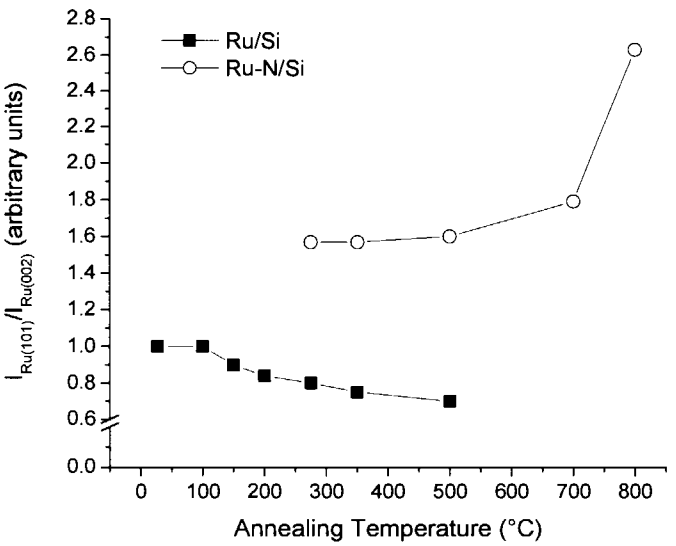

Figure 5.3 Ratio of peak intensities in XRD spectra of 500°C annealed (a) Ru/Si and (b) Ru-N/Si

C. Sheet Resistance

Effect of thermal annealing in film sheet resistance is shown in Figure 5.4. The sheet resistance of Ru/Si remains relatively unchanged at low temperatures (Figure 5.4a). At 700°C and higher, a slight increase is observed which could be due to Ru_2Si_3 formation. Sheet resistance of the as-deposited Ru-N/Si is about ten times higher than that of as-deposited Ru/Si. A gradual decrease is shown up to 200°C, followed by a sharp decrease at 275°C to almost the same sheet resistance value as for Ru/Si. Further increase in annealing temperature for Ru-N/Si results in only minimal change as for Ru/Si. And after 900°C, its sheet resistance increases due to silicide formation which agrees with the XRD data.

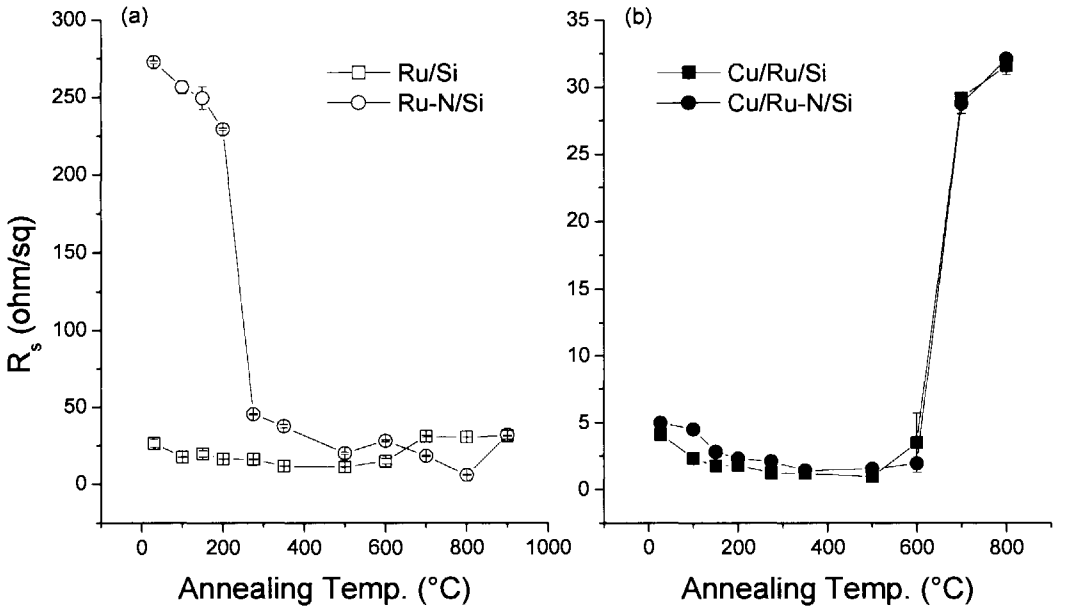

Figure 5.4 Plots of average sheet resistance of Ru/Si, Ru-N/Si, Cu/Ru/Si, and Cu/Ru-N/Si structures against annealing temperature

Note a sharp drop in sheet resistance of Ru-N film after 275°C of annealing. This drop is accompanied by Ru crystallization and agrees well with the XRD data in Figure 5.2b and 5.2d. The concurrence of Ru crystallization and a sharp drop in sheet resistance signifies that they both are triggered by the same event, namely the out-diffusion of dissolved N from the Ru-N/Si samples.

Both samples with Cu overlayer (Figure 5.4b) show lower total sheet resistance compared to those without Cu due to much lower resistivity of Cu which becomes the main current conducting path. Hence, the sharp decrease in sheet resistance due to N out diffusion, which was clear in previous samples, was not detectable in these samples. In contrast, a sharp increase was observed after 700°C due to Ru- and Cu-silicide formation which agrees with the XRD results in Figures 5.2c and 5.2d.

D. Cu and Ru diffusion

To study Cu and Ru diffusion in the dielectric, samples on SiO_2 substrate were prepared. In order for Cu or Ru to react with Si in SiO_2, Si-O bonds must be broken. SiO_2 is a very stable compound (ΔG_f^0 = -824.93 kJ ± 12.55 kJ [102]) and hence, Cu and Ru will preferably diffuse into dielectric without reacting at the interface. The elemental distribution within the films was investigated using XPS. The results of XPS depth profiling of Cu/Ru/SiO_2 and Cu/Ru-N/SiO_2 film stacks are shown in Figure 5.5. Lateral distribution of Cu and Ru were analyzed as a function of etching time. Figure 5.5a shows distribution of Cu (left figure) and Ru (right figure) across the Ru/Si sample thickness after various annealing conditions. The same elements are shown in Figure 5.5b for Ru-N/Si sample. The initial interface of Cu/Ru is drawn at the etching time where Cu concentration is half of its maximum concentration, whereas the Ru/SiO_2 interaface is determined at the etching time where Ru concentration is half of its maximum concentration. The initial interfaces are marked by the dotted line in Figures 5.5a and 5.5b.

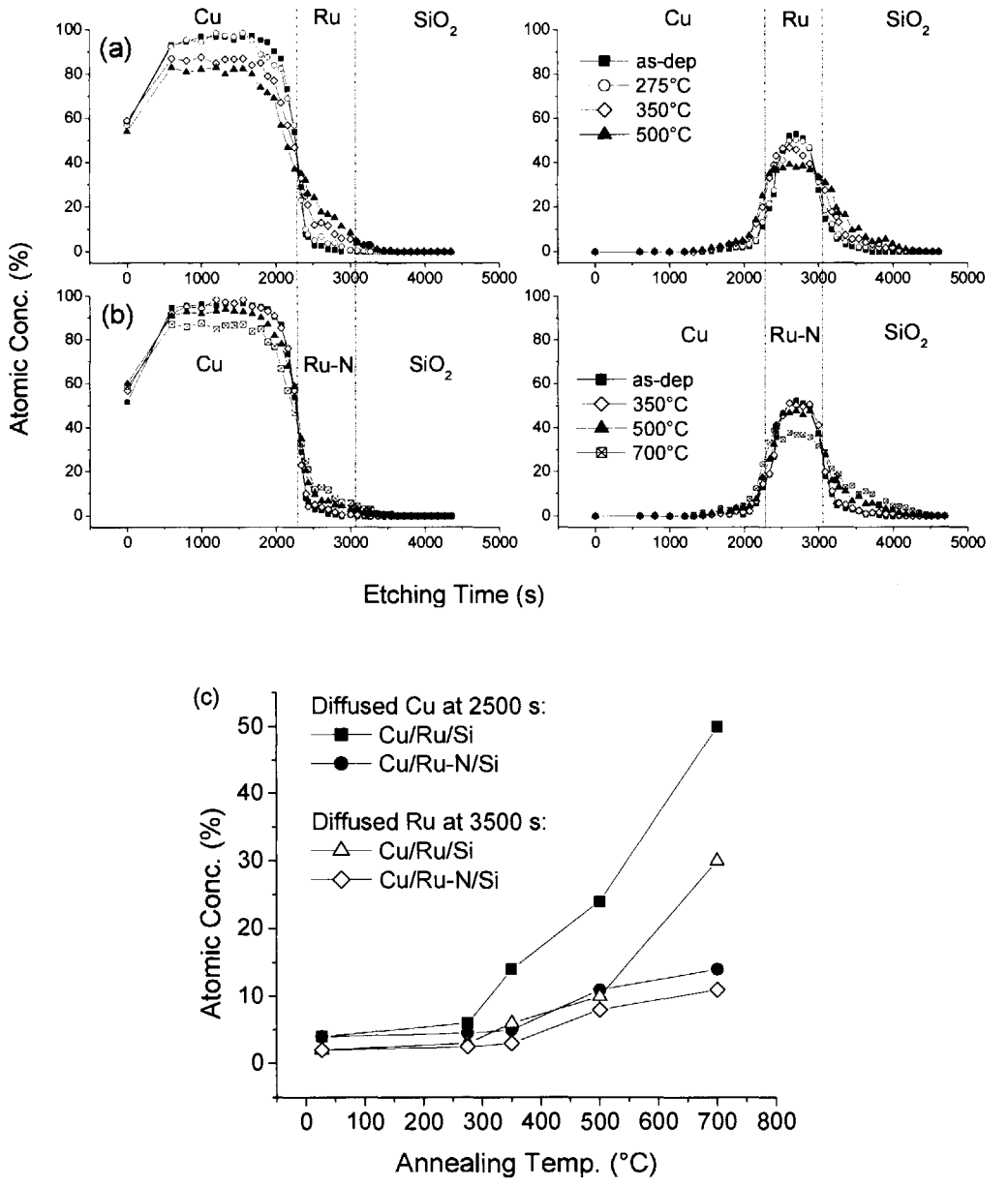

Figure 5.5 XPS depth profiling of Cu and Ru in (a) Cu/Ru/SiO_2 (b) Cu/Ru-N/SiO_2 stacks after the different anneals (c) Plots of atomic concentration of diffused Cu and Ru (at 2500 and 3500 seconds of etching time respectively) against annealing temperature

Comparing the figures, it appears that 350°C annealing for 60 minutes hardly causes any detectable diffusion of Cu and Ru in Cu/Ru-N/SiO_2 stack (Figure 5.5b), while the Cu/Ru/SiO_2 stack (Figure 5.5a) shows definite signs of diffusion near the interfaces. However, after 500°C and 700°C anneals, diffusion of Cu and Ru into the oxide is detectable in Cu/Ru-N/SiO_2 also.

To demonstrate the difference in the diffusion depths of Cu and Ru in the two samples, their respective concentrations at two specific depths are compared. The concentrations of Cu at 2500 seconds is determined from Figures 5.5a and 5.5b and is replotted in Figure 5.5c against the annealing temperature. This depth is well inside the Ru layer and hence, is a comparison of Cu concentration at identical depth in the Ru films. Similarly, Ru concentration at 3500 seconds of etching time is plotted in Figure 5.5c which is a comparison of Ru concentration in SiO_2. It is clearly shown that Cu and Ru diffusion is slower in Cu/Ru-N/SiO_2 stack compared to that in Cu/Ru/SiO_2.

5.3.2 Nanocrystallization or Amorphization of Ru Films by Incorporation of High N Content

XRD investigation (Section 5.3.1) showed that films deposited under N are amorphous. This was confirmed with cross sectional TEM investigations. Figure 5.6 shows a series of micrographs of the different samples investigated. Ru sputtered in Ar (Figure 5.6a and 5.6b) shows polycrystalline and columnar microstructure. Grain boundaries within the columnar microstructure could be energetically favorable paths for Cu diffusion. In comparison, Ru sputtered in N is predominantly amorphous with some isolated nanocrystals of the order of 3 nm (Figure 5.6c – 5.6f). Note that ~3 - 4 nm native SiO_2 is always present at film/Si substrate interface. Figure 5.6d shows an amorphous region of Ru-N film whereas Figure 5.5e shows a nanocrystalline region in the Ru-N film with a nanocrystal arrowed. Figure 5.5f shows Ru-N film deposited on SiO_2, demonstrating the same mixture of nanocrystalline and amorphous structures.

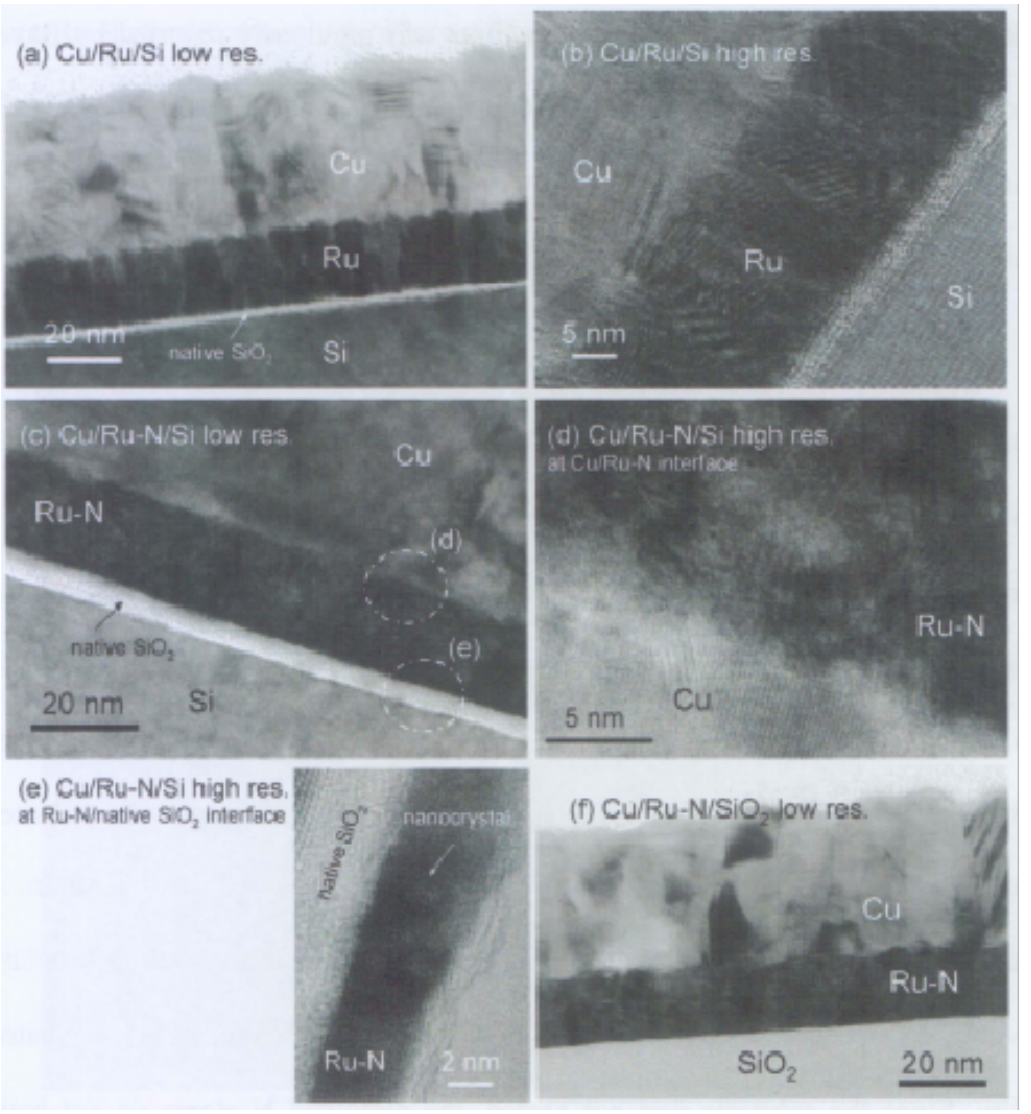

Figure 5.6 Cross sectional TEM micrographs of as-deposited Cu/Ru/Si (a) low res. (b) high res. (showing columnar structure of Ru), as-deposited Cu/Ru-N/Si (c) low res. (d) high res. at Cu/Ru-N interface (showing amorphous region) (e) high res. at Ru-N/native SiO_2 interface (showing nanocrystalline region) and (f) Cu/Ru-N/SiO_2 (low res.)

This non-columnar microstructure in Ru-N does not provide any easy diffusion path for Cu, and hence, the film could be a more effective diffusion barrier than the columnar Ru. When Ru is sputtered in N atmosphere, N will be forced to dissolve at interstitial sites disrupting the Ru crystallization. Dissolution of high level of N probably causes the Ru film to be more amorphous rather than polycrystalline. The use of nitrogen reactive sputtering to

achieve nanocrystalline or amorphous films was previously reported by Baker in WN_x [103], Tsukimoto in TaN [104], Liu Y. in TaWN [53], and Gupta in Fe and permalloy ($Ni_{80}Fe_{20}$) [98]. However, to the best of our knowledge, amorphization of a Ru thin film by N incorporation was not reported before.

An amorphous or a fine-grain structure can be obtained in the sputtering process during condensation of adatoms onto the substrate. If low atomic number reactive gas ions, such as nitrogen, are in the vicinity of adatoms, they may get entrapped and dissolved at interstitial sites of the solid. The stable crystal structure of Ru at room temperature is hexagonal close packed. The ratio of atomic radii of N and Ru is r_N/r_{Ru} = 0.65/1.339 = 0.485. This ratio is larger than the ratio of 0.414 that could be accommodated in the larger octahedral sites of the close packed structures of Ru. This leads to substantial internal strain. A high level of such interstitials could therefore promote nanocrystalline structure with shorter range ordering, or even an amorphous structure, in the deposited film. Since the substrate was not heated, the dissolved N atoms do not have adequate mobility to diffuse out, react or rearrange to form another phase. Such process may occur on heating with consequential changes in the Ru film. This will be discussed in Section 5.3.3.

5.3.3 Thermal Stability of Ru-N Barrier (Microstructural Evolution, N Out Diffusion, Voids Formation)

A. Microstructural evolution of annealed Ru-N films

Figure 5.7 shows a series of high resolution TEM micrographs of Ru and Ru-N layers on Si. Figures 5.7a, b, and c show microstructural changes of

pure Ru film with annealing, whereas Figures 5.7d, e, and f show that of Ru-N film. A ~2 nm native oxide layer is visible in all samples at Ru/Si interface.

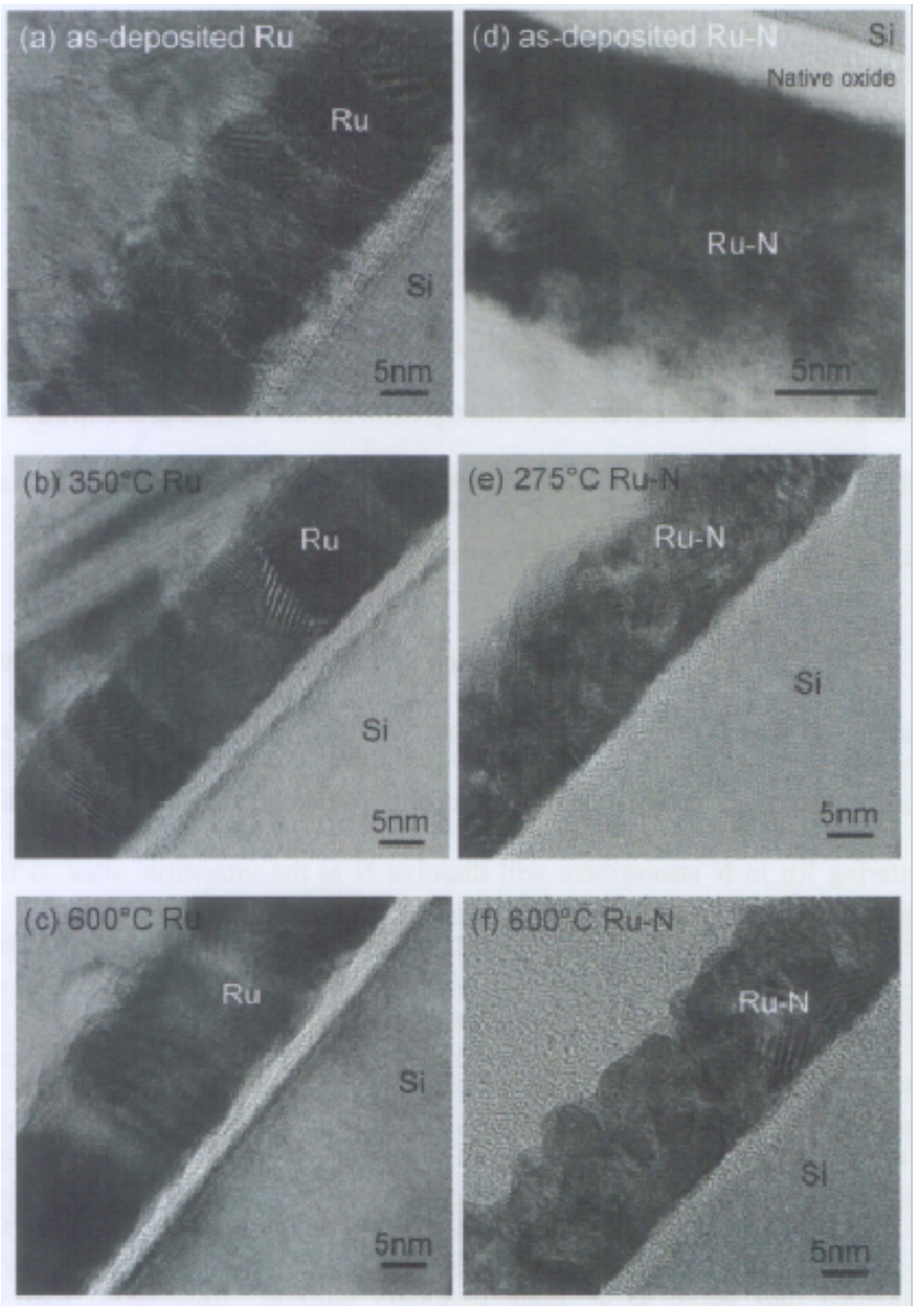

Figure 5.7 High resolution TEM micrographs of Ru/Si samples (a) as-deposited and after (b) 350°C (c) 600°C of annealing and Ru-N/Si samples (d) as-deposited and after (e) 275°C (f) 600°C of annealing

Ru deposited under Ar has columnar grains with ~5 - 7 nm crystallite width as shown in Figure 5.7a. A small, but gradual grain growth is evident as the annealing temperature increases (Figure 5.7b and 5.7c). In contrast, Ru-N film is predominantly amorphous with some isolated nanocrystals of the order of ~2 - 3 nm in the as-deposited state as shown in Figure 5.7d. Annealing causes crystallization and the layer becomes completely nanocrystalline at 275°C (Figure 5.7e). This observation is in agreement with XRD results presented at Figure 5.2 earlier. Annealing at even higher temperatures causes grain growth to ~4 - 5 nm at 350°C, and eventually to ~6 - 7 nm at 600°C. The grain structure in Ru-N is equiaxed, unlike the columnar structure in pure Ru, and remains equiaxed up to 600°C as shown in Figure 5.7f.

Unlike the columnar structure in Figure 5.7a, the equiaxed microstructure does not provide a continuous grain boundary for easy diffusion path and therefore is likely to be more effective in preventing Cu diffusion. Sputtering Ru in N atmosphere will dissolve N at the interstitial sites. A high level of such interstitial N will disrupt Ru crystallization causing the film to become amorphous. Annealing releases the dissolved N, decomposes the unstable Ru-N crystallites, and provides the necessary activation energy to the Ru atoms to form stable Ru hexagonal crystals. Ru crystal growth will reject any residual N to grain boundaries. A high concentration of N at Ru grain boundaries may serve as a "grain boundary stuffing" mechanism that will impede the Cu diffusion through Ru grain boundaries since Cu also does not form a stable nitride. As a result, diffusion of Cu through Ru layer is slowed down even if the Ru is crystallized into equiaxed polycrystalline film by annealing the Ru-N layer. The XPS depth profiling investigations (Section

5.3.1) support this argument as it proves that Cu diffusion through Ru-N films is slower than through Ru at all annealing temperatures, even if the Ru-N film is crystallized.

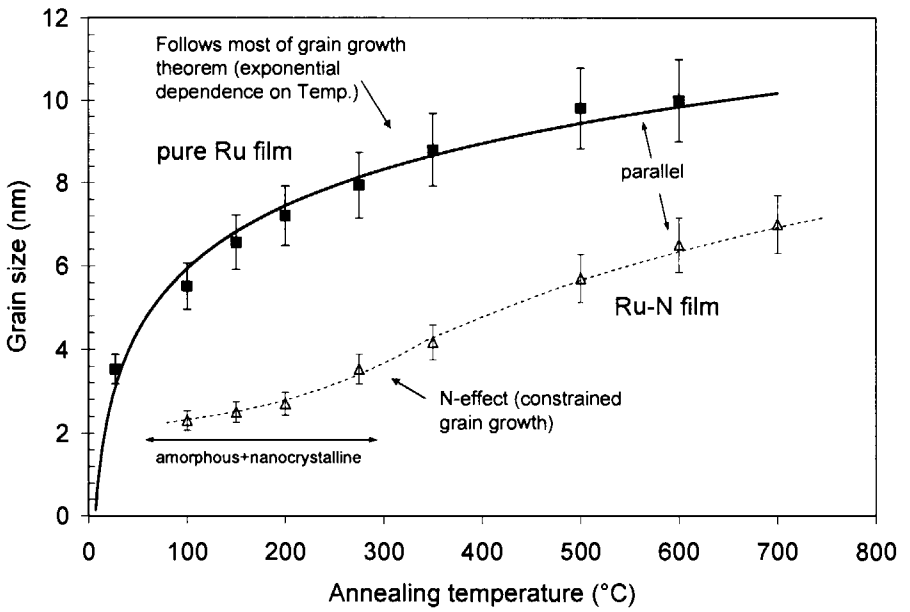

Figure 5.8 Plot of average grain size of Ru in Ru/Si and Ru-N/Si samples against different annealing conditions

Grain size of Ru was determined from the TEM micrographs. The grain size of the pure Ru was taken as average diameter of Ru columnar grain whereas that of Ru-N film is the average size of the nanocrystal grains. The grain size of Ru in Ru/Si and Ru-N/Si samples are plotted against annealing temperatures in Figure 5.8. The grain growth of Ru in pure Ru thin film seems to follow the normal grain growth model with exponential dependence of grain size on temperature as can be approximated by Equations 5.1 and 5.2:

$$d^n - d_o^n = k.t \qquad \ldots(5.1)$$

$$k = k_0 \exp(-Q/RT) \qquad \ldots(5.2)$$

where d is final grain size, d_0 is initial grain size, t is time required to reach a given grain size, k is a temperature dependent constant, k_0 is a constant, T is the absolute temperature and Q is the activation energy for boundary mobility. It is clearly observed that growth of Ru grains is constrained up to ~275°C when N is incorporated into the film. Only after annealing at temperature higher that 300°C, when most of the N has diffused out, Ru grains begin to grow in a similar manner to that of pure Ru as demonstrated by the slope of the curves. Note that slope of the grain size vs. annealing temperature graph in Ru-N/Si is parallel to that of Ru/Si sample at $T \geq 275$°C indicating the similar grain growth behavior.

B. N out diffusion during thermal annealing

The mechanism proposed in Section 5.3.2 where N is presumed to dissolve in Ru, making the Ru-N film become amorphous, which subsequently crystallizes on annealing releasing the N is a hypothesis based on circumstantial evidence. To establish its truth, N content measurements are required. This was done by auger electron spectroscopy (AES) and TEM-EELS techniques. Figure 5.9 shows AES scan on as-deposited Ru-N film on Si. From AES data, N content in the as-deposited Ru-N was estimated to be ~8 - 10 at%.

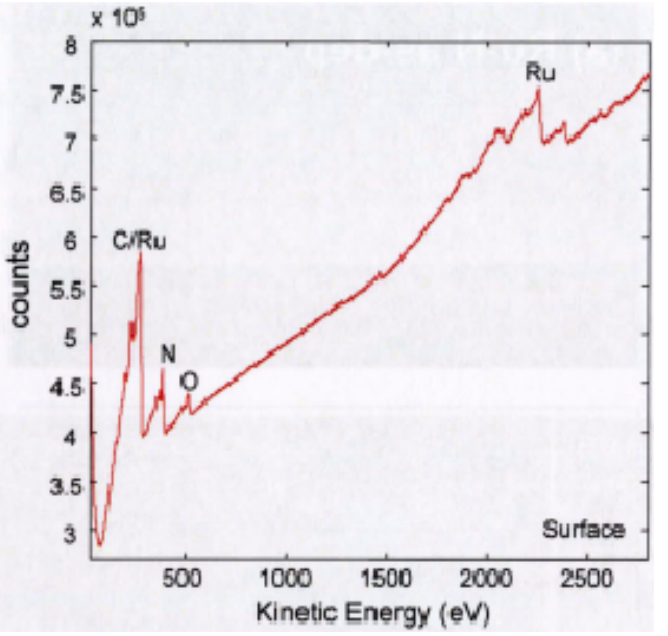

Figure 5.9 AES surface scan on Ru-N/Si sample

EELS line scans were done in a TEM to assess N distribution in as-deposited Ru-N sample. Figure 5.10a shows scanning TEM images of as-deposited Cu/Ru-N/SiO_2 sample, showing a line scan across its thickness. The resulting elemental line profiles are shown in Figure 5.10b for Cu and Ru, as well as in Figure 5.10c for N and O. Note that the Ru and Cu profiles were obtained using EDX whereas that of N and O were obtained using EELS to optimize the detection counts.

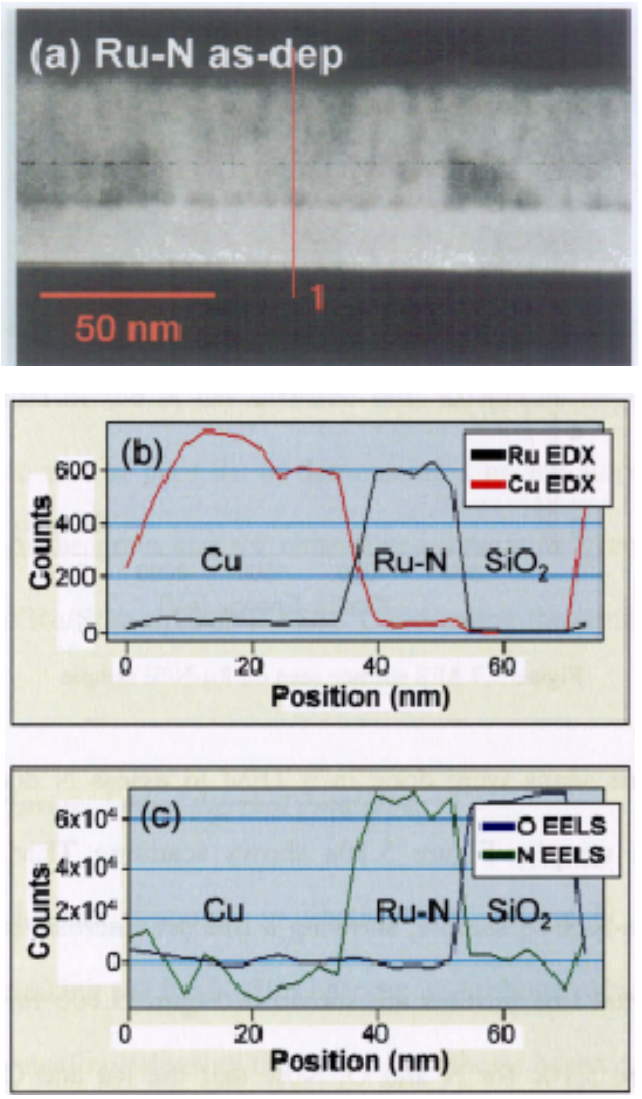

Figure 5.10 (a) High angle annular dark field (HAADF) scanning TEM images (b) Ru and Cu EDX profiles, and (c) N and O EELS profiles of as-deposited Cu/Ru-N/SiO_2 sample

It is clear from N EELS profile in Figure 5.10c that N appears to be uniformly distributed in the Ru layer. For a more precise evaluation, N and Ru elemental maps were acquired on Ru-N samples annealed at 200, 250, and 275°C. These maps are shown in Figure 5.11 together with their bright field TEM image counterparts. The scanned area of analysis is 15 nm x 15 nm as shown in the high resolution micrographs in Figure 5.11 (far left). N mappings of Ru-N films annealed at different temperatures are shown in Figure 5.11 (middle). Ru mappings of the same samples are shown in Figure 5.11 (far right).

Note that the magnifications of the maps are much higher than the micrographs resulting in pixel resolution. It is observed that the N signal remains high and uniform in Ru-N layer up to 200°C, and thereafter, it decreases. A slight non-uniformity in N distribution is apparent at 250°C. However, at 275°C and higher temperatures, N is not measurable or below the EELS detection limit.

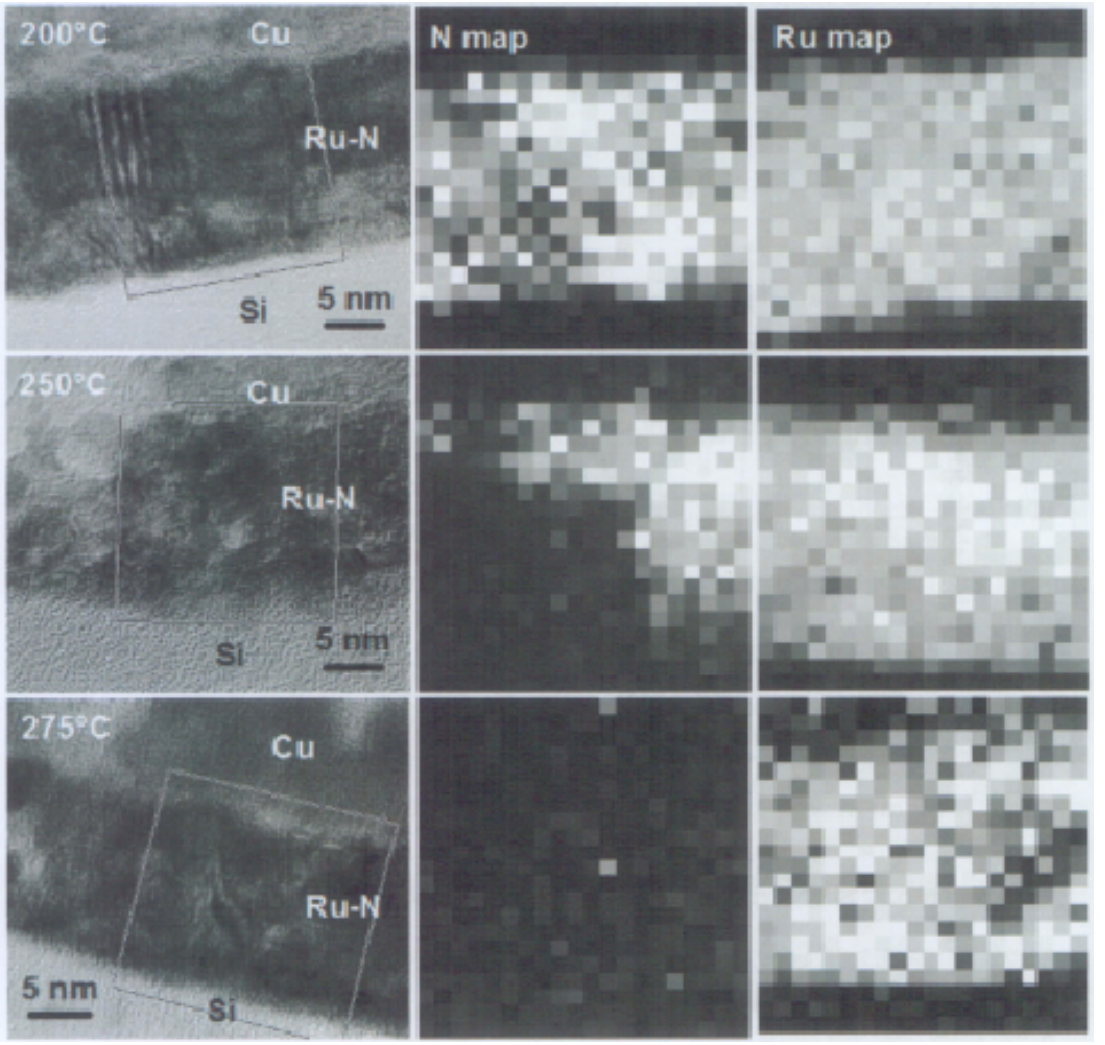

Figure 5.11 High resolution TEM micrographs showing scanned area, N and Ru elemental mappings of Ru-N samples annealed at different conditions obtained using EELS

SIMS depth profiling analyses were done on Ru-N films after various annealing conditions to confirm the N out-diffusion. N content was recorded and plotted against the etching time as shown in Figure 5.12 with the

approximated film/substrate interface marked by the dotted line. Note the presence of a hump near Ru-N/Si interface. This hump is caused by the sudden change in the etching rate when it comes to the interface. Hence, this hump should not be regarded as the real N profile. A reduction in N content with increase in annealing temperature is clearly observed. Note that the average N content remains high up to 200°C and sharply diminishes for anneals at 275°C and higher.

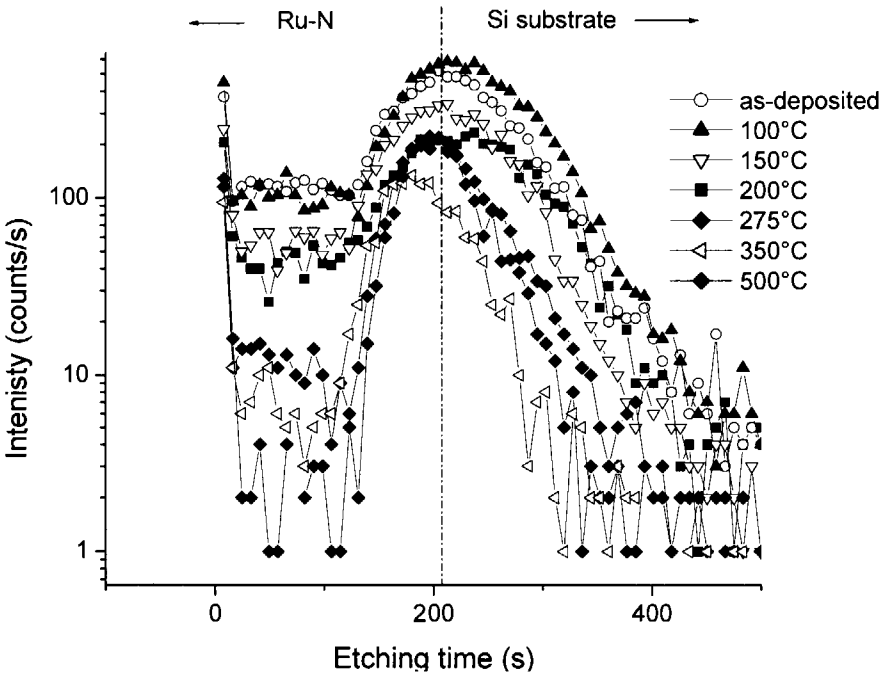

Figure 5.12 SIMS depth profile of N content in Ru-N film after the different anneals

The N out diffusion in Ru-N films during annealing was hypothesized in earlier part of this chapter from indirect resistivity measurements. Improvement in barrier property observed for Ru-N compared to Ru was also previously attributed to the "stuffing" effect arising from N segregation to grain boundaries. However, the elemental maps obtained in this work (Figure 5.11) do not appear to show any clear evidence for grain boundary segregation of N. This could be due to the small size (< 5 nm) of the Ru nanocrystals, resulting in

signals from many crystals overlapping in one location of the map (the foil thickness is ~20 - 30 nm, significantly larger than the grain size). Thus, collecting unadulterated signals from a grain boundary is difficult in this sample. Furthermore, at low anneal temperatures; a substantial part of the film could be amorphous. These amorphous components probably have actually a uniform N content, without any segregation. This also adulterates the EELS signal at each point of the samples.

C. Voids formation

In addition to decrease in N content on annealing at higher temperatures, void formation was observed at the Cu/Ru interface in Ru-N samples annealed at T ≥ 275°C independent of the type of substrate i.e. both oxidized and unoxidized wafers showed void formation. Such voiding was absent in all Ru films deposited in Ar gas. TEM bright field micrographs of pure Ru films after different annealing conditions are shown in Figure 5.13 (left) whereas that of Ru-N films are shown in Figure 5.13 (right) with the voids arrowed. Pure Ru films deposited on Si or SiO_2 do not show any voids even up to 700°C. However, voids are clearly observed at Cu/Ru-N interface in Cu/Ru-N/Si and Cu/Ru-N/SiO_2 samples annealed at temperature ≥ 275°C. Their size range is ~20 - 30 nm and did not change significantly with increase of annealing temperature. It must be noted that such voids were not seen in the Ru-N samples annealed at low temperatures, where EELS showed a high N content. Therefore, we attribute voiding to nucleation and growth of N_2 gas bubbles by coalescence of N atoms diffusing out of the Ru film. Note that the nitrides of Ru and Cu are unstable at these temperatures. Interfaces being good nucleating sites made

them the preferred locations for voids formation. It must be noted that no voiding was observed at the Ru/SiO_2 interface. This can be explained by the fact that N can conveniently dissolve into SiO_2 to form Si-oxynitrides.

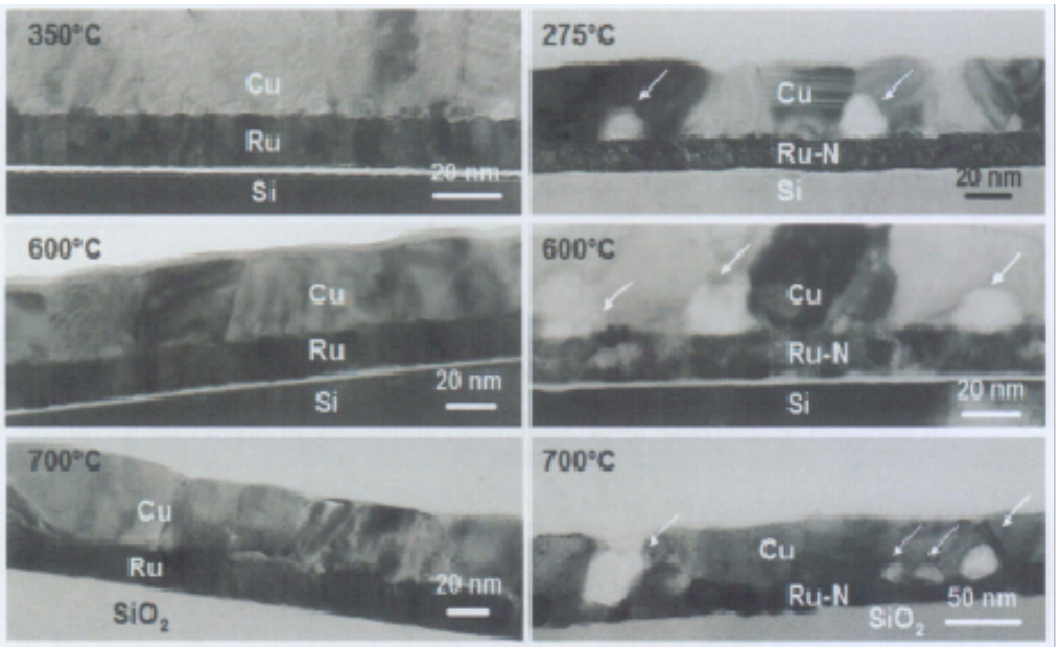

Figure 5.13 TEM micrographs of Ru (left) and Ru-N (right) samples annealed at different conditions showing void formation at the Cu/Ru interface in Ru-N samples with the voids arrowed

A simple semi-empirical model for N release available in literature assumes a homogeneous film from which interstitial N migrates to the surface [105]. For diffusion controlled processes, a characteristic time, τ, for the N release is given by the Equations 5.3 and 5.4:

$$\tau = (2d)^2/(\pi^2 D) \qquad \ldots(5.3)$$

$$D = D_0 \exp(-Q/RT) \qquad \ldots(5.4)$$

where d is the film thickness, D is diffusion coefficient, Q is activation energy, R is gas constant (8.31 J/mol.K), and T is temperature in Kelvin. However, diffusion data of N in Ru is not available to calculate the characteristic time. Besides, the process of N out diffusion in our situation is more complicated

because the films consist of a mixture of nanocrystals and amorphous phase. The enhanced role of grain boundary diffusion in nanocrystals and the simultaneous transformation from amorphous to crystalline states are complicating factors.

Therefore, it is clear that incorporating N into the Ru film helps to improve the microstructure. However, the early N out diffusion is detrimental to the overall film properties. A mechanism of barrier failure may be schematically depicted as in Figure 5.14. Ru-N film is amorphous in the as-deposited state with the N uniformly distributed in the Ru layer (Figure 5.14a). Since Ru does not form any stable nitrides, annealing causes N out diffusion with concomitant Ru crystallization. The N rejected from the lattice out diffuses from the Ru layer and could possibly get accumulated at Ru grain boundaries as well as Cu/Ru and Ru/native SiO_2 interfaces (Figure 5.14b). N at Ru/native SiO_2 interface would possibly dissolve into the SiO_2, forming Si-oxynitride while the N at Cu/Ru interface would possibly reach saturation and begin to nucleate N_2 bubles at about 275°C (Figure 5.14c). Ru crystallization progresses with higher temperature. At 600°C the Ru layer becomes fully nanocrystalline (Figure 5.14d). The void size remains unchanged even when the annealing temperature is raised since most of the N has out diffused at 275°C. Complete barrier failure occurs at 700°C where Ru_2Si_3 and Cu_3Si are formed (Figure 5.14e). Note that the formation of Ru_2Si_3 and Cu_3Si occurs simultaneously at 700°C in Cu/Ru-N/Si sample, unlike in the case of Cu/Ru/Si sample where Ru_2Si_3 is formed first at 700°C followed by Cu_3Si at 800°C as observed by XRD (Section 5.3.1). This difference could be attributed to the different microstructures.

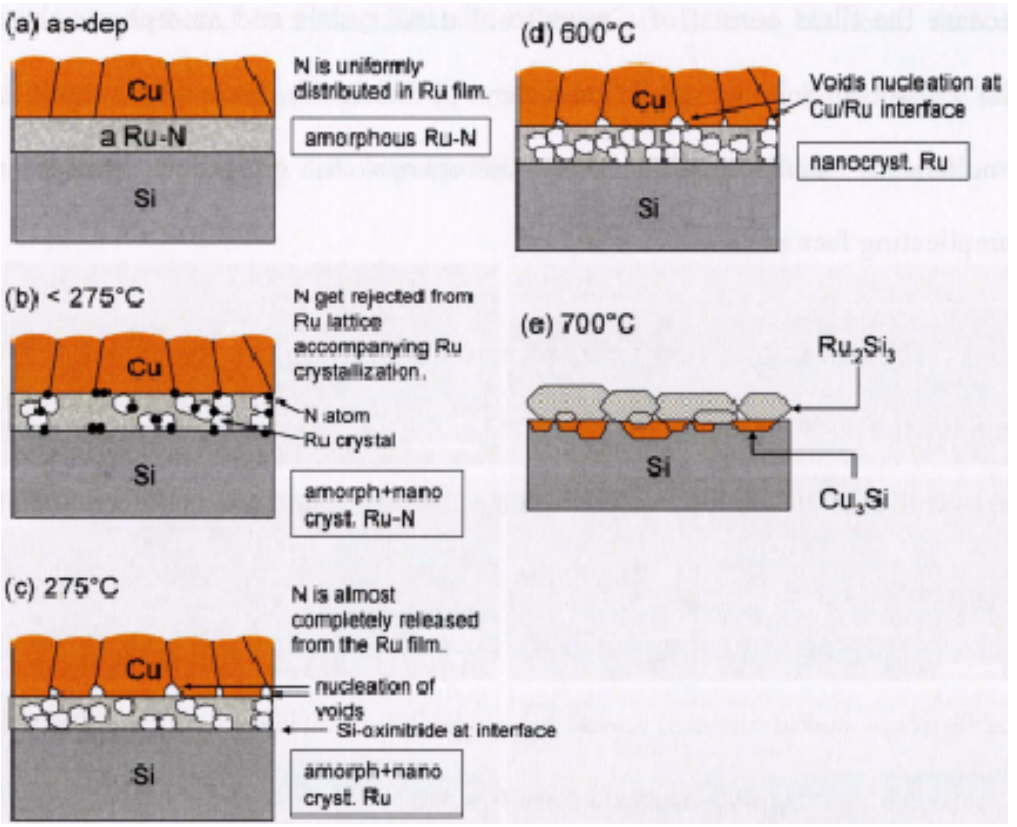

Figure 5.14 Schematic depiction of the barrier failure mechanism in Cu/Ru-N/Si (a) as-deposited films (b) crystallization of Ru, N is being rejected out of Ru crystals (c) initiation of barrier breakdown by nucleation of voids due to N saturation at interface (d) N is completely released from the film, Ru film become nanocrystalline with equiaxed grains (e) complete barrier breakdown, formation of Ru_2Si_3 and Cu_3Si

The information regarding silicide formation discussed in Section 5.3.1 could be used to construct a schematic equilibrium diagram for the Ru(N)-Cu-Si ternary system at 700°C section at which most information is obtained. This is shown in Figure 5.15. We do not have adequate information at other temperatures to complete this diagram. This diagram demarcates the solubility limits for Cu and Ru(N) in Si.

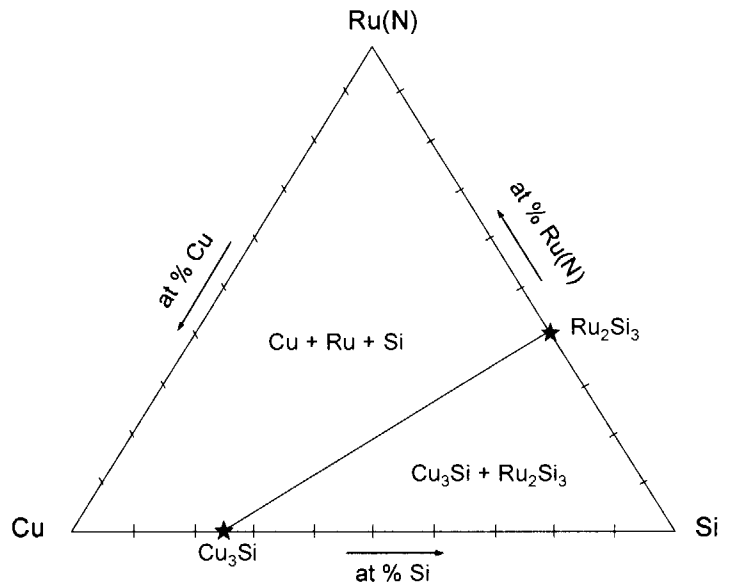

Figure 5.15 Isothermal section of Ru(N)-Cu-Si ternary phase diagram at 700°C

5.4 Summary of Results

N dissolution in Ru was experimented to improve the barrier properties of pure Ru in this part of the project. Barrier performace of stacks of Ru-N/Si and Cu/Ru-N/Si were assessed by exposing to high temperatures and compared to that of pure Ru stacks. The conclusions that could be drawn from this part of the work are:

- Ru sputter deposited in N_2 gas (Ru-N) results in a layer whose microstructure consists of a mixture of amorphous and nanocrystalline phases with ~8 - 10 at% N uniformly distributed in the film, whereas Ru sputter deposited in Ar gas (pure Ru) exhibits a columnar grained microstructure, in the as-deposited state.
- Sheet resistance of Ru-N film is about ten times higher than that of Ru but on annealing at 275°C, it reduces sharply to that of pure Ru, indicating a loss of N from the layer.

- XPS study shows that diffusion of Cu through Ru-N film is slower than in pure Ru at all temperatures.
- XRD study shows that formation of Ru_2Si_3 occurs at 900°C in Ru-N film which is 200°C higher than in pure Ru.
- Annealing at temperatures ≥ 275°C causes N out-diffusion concomitant with crystallization of Ru. The rejected N atoms nucleate N_2 gas bubbles at the Cu/Ru interface. It grows to a size range of ~20 - 30 nm and is easily observable as voids in the TEM. These will adversely affect the Cu/Ru interface adhesion.
- Grain growth in Ru-N is constrained up to 275°C. Annealing at higher temperatures, when N has been removed from solution, the grain growth behaviour returns to that of pure Ru.
- The improved barrier performance of Ru-N is possibly caused by its amorphous structure. Heating to temperatures above 275°C causes crystallization of Ru leading to deterioration of the barrier property to the levels of pure Ru.

CHAPTER 6

Analysis of Ru-W-N and Ru-Ta-N Barriers in Cu Interconnect System

6.1 Background

Our previous studies on Ru-N discussed in Chapter 5 show that high dissolution of N in Ru film helps to produce a favorable film microstructure and slow down the Cu diffusion through the Ru film. However, due to high thermal instability of Ru-nitride, N out diffusion was observed to occur at a relatively low temperature of ~275°C and lead to formation of voids at Cu/Ru interface. This was found to be the mechanism that leads to failure of the barrier. To improve the thermal stability of the Ru-N, elements which are good nitride formers were added into Ru film to prevent N precipitation and suppress the void formation.

Figure 6.1 shows calculated enthalpies of metal nitride formation, ΔH_f^0, at 0 K for 5d transition metals reported by Haglund *et al.* [106]. This is used as a basis for material selection in this study.

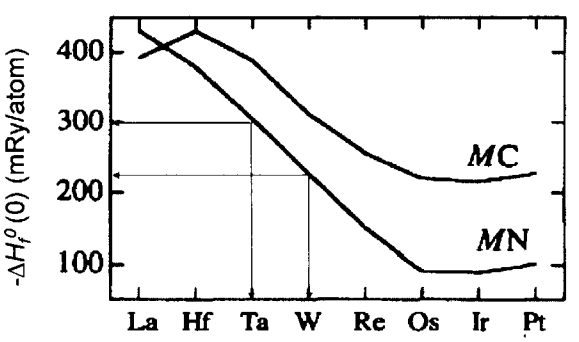

Figure 6.1 Reported data on enthalpies of formation of 5d transition metal nitrides (MN) and carbides (MC) at 0 K [106] (1 Ry (Rydberg) = 2.17987 x 10^{-18} Joule)

Experimental information on bonding energies of solid compound is generally expressed as enthalpies of formation, ΔH_f^0. This quantity represents the energy gained in forming a compound (e.g. metal nitride) from the constituent elements (metal and nitrogen) in their stable state at some reference temperature. A large negative ΔH_f^0 indicates that the compound will have lower energy. Hence, it is more stable when it is formed. Among the good nitride forming elements shown in Figure 6.1, W and Ta were chosen since they are more common materials used in IC metallization. Additionally, W- and Ta-based materials have been widely studied as barrier materials in Cu interconnect.

6.2 Experiments

Ru (99.95% purity) and W (99.95% purity) or Ta (99.95% purity) were co-sputtered onto a pre-cleaned Si substrate in a Cryo Vac sputtering machine at room temperature, 10^{-5} Torr base pressure, and 30 mTorr working pressure. Deposition was done in Ar gas at a constant flow rate of 20 sccm, mixed with N_2 gas at a varying flow rate of 0, 5, and 10 sccm for 180 seconds. Target current was maintained at -0.8 A for all metal targets. Cu (99.99% pure) was then sputter deposited onto selected Ru-W-N or Ru-Ta-N samples using the same machine under the same sputtering condition. Cu target current was -0.8 A and Ar flow rate was 20 sccm. Samples were then annealed for 1 hour at progressively increasing temperatures up to 800°C in a high vacuum ambient of 10^{-5} Torr.

Kratos AXIS Ultra x-ray photoelectron spectroscopy (XPS) with a monochromatized Al *Kα* x-ray source (1486.71 eV) was used to assess N

content in the film as well as to understand W and N or Ta and N chemical bonding configurations before and after annealing. Transmission electron microscopy (TEM) investigations were carried out in a JEOL 2100 equipped with an energy dispersive x-ray (EDX) detector, operated at 200 kV to examine film thickness variation with different N_2 flow rate and microstructure changes during thermal annealing. Rutherford backscattered spectroscopy (RBS) measurement was performed on a high voltage singletron accelerator using 2 MeV He^{++}, at 170° scattering angle, in a vacuum chamber of 5 x 10^{-6} mbar. Samples were also analyzed using Rigaku Dmax 2200 x-ray diffractometer (XRD) (Cu $K\alpha$ = 1.542 Å) to understand phase transformations and silicide formations under thermal annealing. A field emission scanning electron microscope (JEOL JSM 6340F) operated at 15 kV was used for surface analysis of the samples. Resmap four-point probe sheet resistance analyzer was employed to monitor the sheet resistance change of the film with thermal annealing.

In this chapter, discussion on Ru-W-N and Ru-Ta-N are presented concurrently to have a clearer comparison. First, effect of N_2 flow rate on thickness, resistivity and microstructure of as-deposited Ru-W-N and Ru-Ta-N will be discussed. Subsequently, this chapter reports thermal stability of the barriers. Effects of annealing temperature on film properties, including nitrogen release will then be examined. Barrier failure mechanism is finally proposed.

6.3 Results and Discussion

6.3.1 Effect of N_2 Flow Rate on As-deposited Film Properties

A. Film Thickness and Resistivity

Discussion on film thickness is presented here for Ru-W-N and Ru-Ta-N films since the film thickness was found to vary with N_2 flow rate unlike in the case of pure Ru and Ru-N films where only one deposition condition was used. Since the film thickness of samples deposited with different conditions is not constant, sheet resistance measurement could not be used as a direct comparison between the different films. To account for the film thickness, film resistivity (= sheet resistance x film thickness) is used in the analyses instead of film sheet resistance.

Table 6.1 presents film thicknesses, deposition rate, film sheet resistance, and resistivity values.

Table 6.1 List of film thickness, deposition rate, sheet resistance, and resistivity of co-sputtered Ru-based barrier

	Ru-W-N				Ru-Ta-N		
N_2 flow rate (sccm)	0	5	10	15	0	5	10
Film thickness (nm)	109.24	126.56	133.80	138.09	154.70	125.20	115.30
Deposition rate (nm/s)	0.61	0.70	0.74	0.77	0.86	0.70	0.64
Rs (Ω/□)	64.2	123.58	214.63	372.02	85.54	212.93	499.77
ρ (μΩcm)	701.32	1564.03	2871.75	5137.22	1323.36	2665.86	5762.37

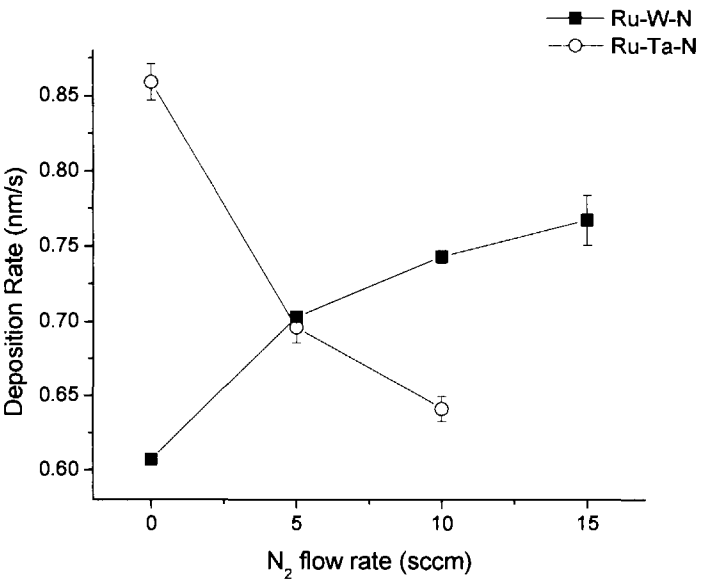

Figure 6.2 Deposition rates of Ru-W-N and Ru-Ta-N films as a function of N_2 flow rates

The film thicknesses were measured accurately using bright field TEM imaging. Film deposition rate was calculated based on film thickness divided by deposition time of 180 seconds (e.g. deposition rate of Ru-W-N film with 0 sccm N_2 = 109.24 nm/180 s = 0.61 nm/s). It is observed that the deposition rate varies with N_2 flow rate as shown in Figure 6.2. Interestingly, opposite trends are exhibited for Ru-W-N and Ru-Ta-N films. In Ru-Ta-N, film growth rate decreases whereas in Ru-W-N, the deposition rate increases with increase of N_2 flow rate. The deposition rate could either increase or decrease depending on the rates of chemical reaction and sputtering. Reaction between W and N or Ta and N during Ru-W or Ru-Ta co-sputtering in Ar + N_2 gas mixture could be expected. Ru was not expected to form stable nitride during deposition since Ru does not form strong bond with N. Chemical reaction between W and N or Ta and N might take place on the target surface and/or on the substrate. If the chemical reaction is on the target surface and occurs faster than the sputtering rate, then nitride phase would be formed on W or Ta target surface. Nitride phase has higher resistivity and lower sputter yield than pure metal. To verify

whether nitride was formed on target surface, target voltage was recorded. If the higher resistance nitride phase was formed, the target voltage should increase when N_2 gas is introduced. Figure 6.3 shows the recorded target voltage when the N_2 flow rate was varied while maintaining the target current at 0.8 A.

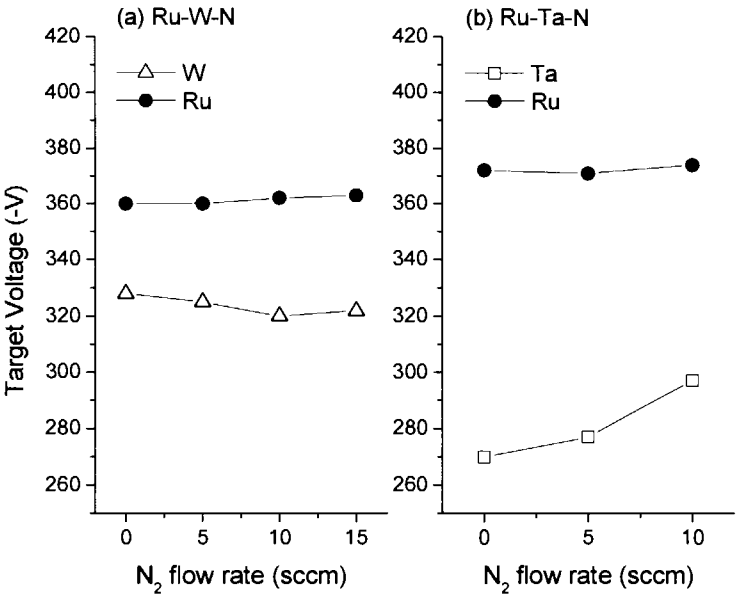

Figure 6.3 Target voltages as a function of N_2 flow rates in (a) Ru-W and (b) Ru-Ta co-sputtering processes

In Ru-W-N film deposition, it is observed that both W and Ru target voltages are relatively independent of N_2 flow rate as shown in Figure 6.3a, indicating that no higher resistivity nitrides were formed on target surfaces during deposition. Formation of WN_x on W target has been reported for W-N reactive sputtering process when N_2 partial pressure is higher than 17% in 10 mTorr working pressure [103]. In this study, 30 mTorr working pressure was used. Due to equipment limitation, this value could not be lowered any further as the plasma would not be generated for lower pressures. This higher working pressure could increase gas collisions in the chamber and hence, hinder the formation of WN_x on W target surface, causing the reaction to be slower than

the sputtering rate. Thus in Ru-W-N deposition, both Ru and W targets in this study were likely to be sputtered in "metallic mode", and W-nitride formation was likely to occur on the substrate. Compared to N_2, Ar has relatively a better mass matched with W. Hence, Ar would be responsible for the sputtering whereas N would be responsible for reaction with W on the substrate. More WN_x would be formed on substrate when more N is present in the chamber leading to increase on the overall film thickness.

In Ru-Ta-N deposition, it is observed that negative Ta target voltage increases with N_2 flow rate as shown in Figure 6.3b, indicating that higher resistivity TaN_x might be forming on Ta target surface during deposition. Hence, Ta and N reaction could be faster than the sputtering rate, unlike in the case of W and N discussed earlier. This is possibly due to ease of TaN_x formation (ΔG_f^0 (300 K) = -435.74 ± 29.29 kJ) compared to that of WN_x (ΔG_f^0 (300 K) = -290.49 ± 18.85 kJ) [102]. With increase of N_2 flow rate, more TaN_x will be formed on the Ta target, resulting in further lowering of deposition rate. Formation of Ta-nitride on Ta target surface during Ta-N reactive sputtering process was also reported by several groups in the literature [107-109].

Film resistivity was calculated from sheet resistance data multiplied by the film thickness. Resistivity of the as-deposited Ru-W-N and Ru-Ta-N films is dependent on the composition and crystal structure of the films. Variation of film resistivity with N_2 flow rate is shown in Figure 6.4. Resistivity of Ru-W-N and Ru-Ta-N films increases with N_2 flow rate. This could be due to the influence of the nitride phases formed in the deposited films which have inherently higher resistivity values than the metals. It may also be because of

more interstitial N incorporated in the deposited film when N_2 flow rate is increased. Sputter-deposited Ru-Ta-based films show higher resistivity (almost twice) compared to Ru-W-based films. This could be due to intrinsically higher resitivity of Ta (13 μΩ.cm) than W (5 μΩ.cm).

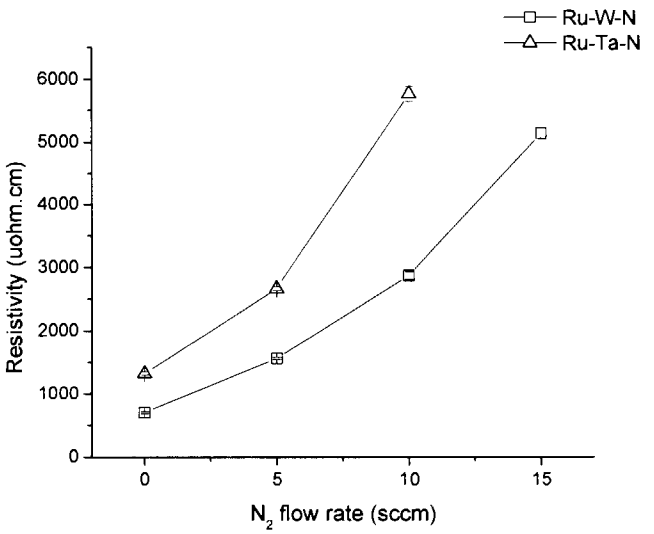

Figure 6.4 Ru-W-N and Ru-Ta-N films resistivity as a function of N_2 flow rates

The Ru-W film shows a resistivity of ~701 μΩ.cm. As soon as N was incorporated, the film resistivity increased to ~1564 μΩ.cm. When N_2 flow rate was increased further to 10 and 15 sccm, film resistivity increased significantly to ~2871 and ~5177 μΩ.cm respectively. Similarly for Ru-Ta-N film, resistivity of the film without N was ~1323 μΩ.cm. When N_2 was introduced, the film resistivity increased to ~2665 and ~5762 μΩ.cm for N_2 flow rates of 5 and 10 sccm respectively.

Depending on the N concentration in the film, the reported resistivity of reactively sputtered W-nitride ranges from 200 to 600 μΩ.cm [95] whereas that of reactively sputtered Ta-nitride ranges from 300 to 1800 μΩ.cm [34]. Ru-W-N and Ru-Ta-N films sputtered in this study seem to have an even higher

resistivity compared to that of pure W-nitride or Ta-nitride films. The presence of Ru (ρ = 7.1 $\mu\Omega$.cm) in the film may alter the nitride stoichiometry and thereby increase the total resistivity. The amorphous nature of the film and high oxygen content could also be reasons for the high film resistivity. Electrical resistivity of the film could be lowered by optimizing further the chamber base pressure as well as N_2 partial pressure to get a correct film stoichiometry.

B. W-nitride and Ta-nitride formation during film deposition

The Ru-W-N and Ru-Ta-N films were analyzed by XPS to determine the chemical bonding configurations and chemical composition.

(i) Ru-W-N

- *Chemical states of the elements*

Electronics binding energy of W 4f, N 1s, Ru 3d, and O 1s of as-deposited Ru-W-N films for the different N_2 flow rates are presented in Figure 6.5. As-deposited surface of Ru-W film (N_2 = 0 sccm) in Figure 6.5a exhibits four W 4f characteristic peaks at 31.6, 33.6, 35.5, and 37.5 eV. The first two peaks represent respectively W $4f_{7/2}$ and W $4f_{5/2}$ electrons of elemental tungsten (zero oxidation state), W^0, [89] and the later two peaks at higher binding energies correspond to those of tungsten oxide, WO_3 [103]. Although the samples were conventionally cleaned before XPS analysis, a brief exposure to air prior to measurement may have caused some surface oxidation. The oxides may also have come from residual oxygen in the deposition chamber and the vacuum furnace.

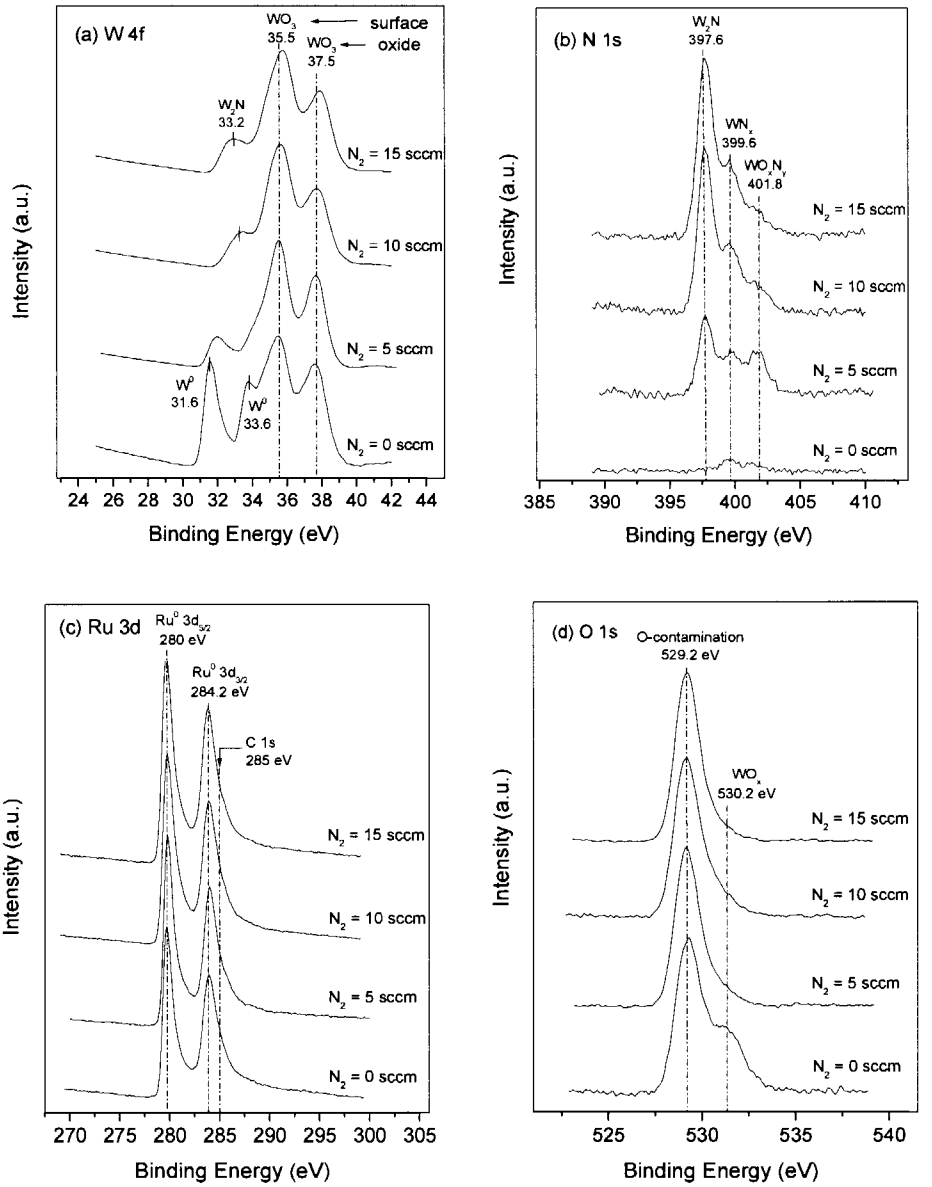

Figure 6.5 Electronic binding energy of (a) W 4f (b) N 1s (c) Ru 3d (d) O 1s of as-deposited Ru-W-N surface with different N_2 flow rates

Shifts in W 4f peaks due to formation of metastable WN were reported to be ~2 eV [89]. Whereas reported values for W 4f peak shifts due to the formation of W_2N vary from as high as 1.7 eV [110] to as low as 0.25 eV [111]. On the contrary, some papers, reported nearly no peak shift due to formation of W_2N [112]. A shift of 1.6 eV was however measured in our samples deposited with Ar + N_2 (33.2 eV) compared to that deposited in pure Ar (31.6 eV) as can

be clearly seen in Figure 6.5a for sample with N_2 flow rate of 10 and 15 sccm. This 1.6 eV shift could be attributed to the presence of W_2N phase. Baker *et al.* [103] reported that in reactive sputtering of W and N, steady-state compositions of W-nitride film is ~33 at% N and ~66 at% W, which correspond to the equilibrium compound W_2N. Any additional incorporation of N in W will form metastable WN or other higher WN_x phases and would require more energetic processes such as ion-assisted deposition or bias sputtering which may result in non-equilibrium growth of films.

For Ru-W-N surface (N_2 = 5 sccm) in Figure 6.5a, it should be noted that peaks at 33.6 eV (W^0) and 35.5 eV (WO_3) overlap with peaks of W_2N at 33.2 and 35.2 eV respectively. Evidence for the presence of W_2N is available in the binding energy of N 1s peak (at 397.6 eV) as shown in Figure 6.5b. This value is close to previously reported values for N 1s in W_2N at 397.0 eV [110] and 397.3 eV [113]. In addition to the appearance of N 1s at 397.6 eV, peaks at 399.6 and 401.8 eV are also observed. The binding energy of 399.6 eV corresponds to the reported binding energy of N 1s in a non-equilibrium W-nitride, WN_x, resulted from N implantation into W surface of 400.0 eV [114]. The binding energy of 401.8 eV could be attributed to W-oxynitride, WO_xN_y, because it agrees well with data reported by Kim *et al.* [115]. The presence of WN_x and WO_xN_y should also appear in W 4f binding energy; however, their electronic binding energies may be close to that of W_2N causing them to be un-resolvable.

Samples deposited using higher N_2 flow rate at 10 and 15 sccm in Figure 6.5a do not show any presence of W^0 spectra, indicating that most of the W has

reacted with N to form W-nitride and/or W-oxynitride during film deposition. The chemical state of Ru 3d shown in Figure 6.5c does not indicate any significant changes when N_2 flow rate is varied signifying that Ru does not form any strong bonds with N. O 1s binding energy in Figure 6.5d shows two prominent peaks at 529.2 and 530.2 eV. O 1s peak at lower binding energy is likely coming from air contamination and this is common for any XPS measurements, whereas O 1s peak at the higher binding energy is likely to be from surface WO_3. Qualitatively it is observed that the amount of WO_3 is higher in sample without N.

- *Chemical composition*

Determination of the precise atomic concentrations from this XPS data was difficult due to overlapping of C 1s (285 eV) and Ru $3d_{3/2}$ (284.2 eV) peaks as shown in Figure 6.5c. Despite this, quantitative analysis could still be made if we have a reliable reference sample. Sample with the highest N_2 flow rate was taken to be the reference sample to get a good reading on N content. Its composition was determined accurately using RBS which can result in a better accuracy in determining film composition compared to XPS. The compositions of the other samples were calculated by careful XPS curve fitting and normalization to the RBS data of the reference sample. Compositions calculated in this manner are listed in Table 6.2 and the data is plotted in Figure 6.6.

Table 6.2 Ru-W-N film composition with different N_2 flow rate (at%)

N_2 flow rate (sccm)	O 1s	N 1s	Ru	W 4f
0	31.14	0	40.78	28.09
5	30.49	10.75	35.38	23.40
10	28.45	15.23	35.40	20.91
15	27.78	20.64	33.10	18.48

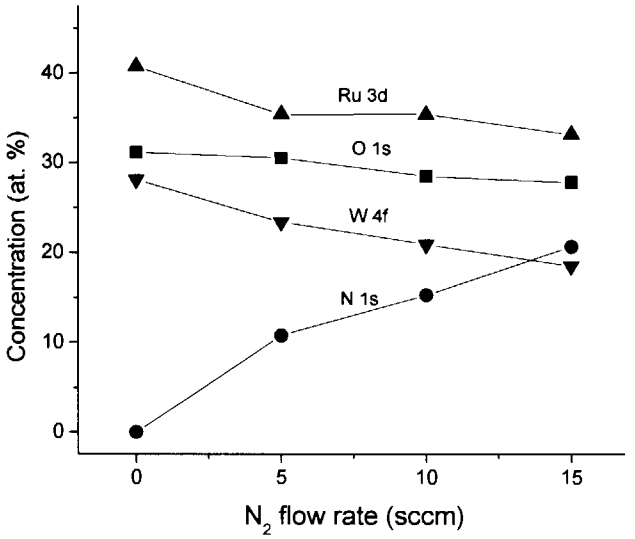

Figure 6.6 Plot of Ru 3d, O 1s, W 4f, and N 1s atomic concentration against N_2 flow rates of as-deposited Ru-W-N samples

Note that the O concentration obtained is relatively high because of the presence of surface oxide. The N content in Ru-W-N film increases as the N_2 flow rate increases while the total amount of W decreases as can be seen in Figure 6.6. In the sample without nitrogen (0 sccm), the concentration of Ru is about ~40 at%. But when the N is introduced, the Ru concentration decreases to about ~35 at% and thereafter remains relatively constant with varying N_2 flow rate. Hence, changing the N_2 flow rate mainly affects the W and N concentrations. Reaction between W and N was expected to occur during the deposition to form the W_2N. In addition, excess or un-reacted N might be present in the interstitial sites when the films get saturated with N.

De-convolution of W 4f binding energy curves was done to determine relative amounts of different W-state (W^0, W_2N, and WO_3) out of the total W present in each film surface and the results are shown in Figure 6.7. Note that the binding energy of W4f is a duplet hence, each phase has two peaks corresponding to $W4f_{7/2}$ and $W4f_{5/2}$. In sample with N_2 = 0 sccm shown in Figure 6.7a, W exists in two phases, W^0 and WO_3. W_2N phase with binding energies of 33.2 eV and 35.2 eV appear in film with N_2 = 5 sccm (Figure 6.7b), in addition to W^0 and WO_3 phases. Whereas sample with 10 sccm N_2 (Figure 6.7c) consists of W_2N and WO_3 phases, and has no W^0. Relative amounts of W in the different W-states were calculated from the area under each de-convoluted peak and the data is presented in Table 6.3 and also plotted in Figure 6.8.

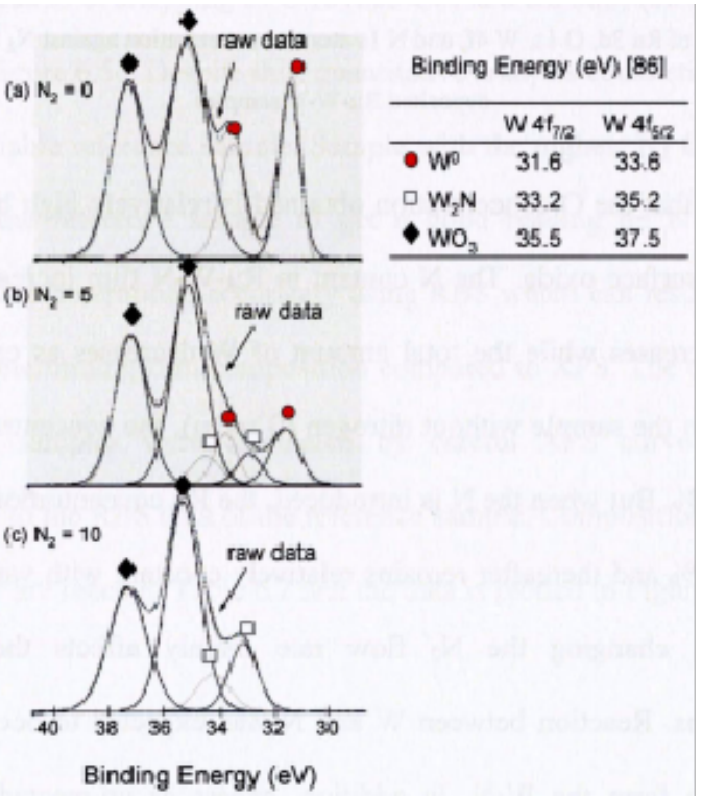

Figure 6.7 W 4f curve de-convolution for as-deposited Ru-W-N samples with N_2 flow rate of (a) 0 sccm (b) 5 sccm and (c) 10 sccm with binding energy data listed in the table

Table 6.3 Calculated relative amounts of W in different chemical states in Ru-W-N samples surface deposited under different N_2 flow rates

N_2 flow rate (sccm)	Relative amount (fraction)		
	W^0	W_2N	WO_3
0	0.18	0	0.82
5	0.16	0.12	0.72
10	0	0.23	0.77
15	0	0.28	0.72

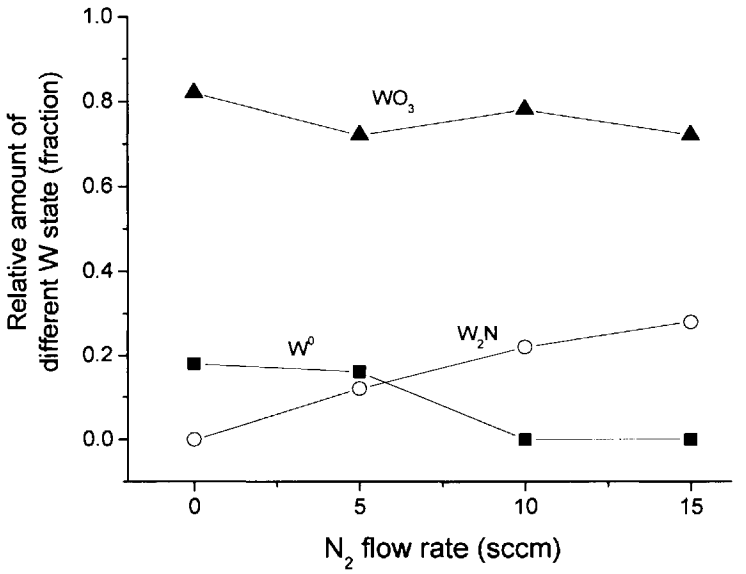

Figure 6.8 Plot of relative amount of different W states in Ru-W-N films with different N_2 flow rates

Table 6.3 and Figure 6.8 show that the amount of W_2N increases with increase in N_2 flow rate whereas that of W^0 decreases, keeping the WO_3 content relatively constant. Additionally the amount of WO_3 in sample without N is relatively higher compared to that in samples with N, showing an agreement with the O 1s binding energy data presented earlier in Figure 6.5d. Note that due to high concentration of surface oxide, the absolute value of the phases given above may not be accurate. However, the relative amount and the corresponding trend of W and W_2N content with variation of N_2 flow rates should be reliable. Hence, depending on the N_2 flow rate, the final film might have excess/un-

reacted W (for example sample with N_2 flow rate = 5 sccm) or excess interstitial N (N_2 flow rate $\geq$ 10 sccm). However, when the amount of W and N matched, they would react to form W_2N. This deduction is justified by the detail scan of W 4f binding energy (Figures 6.5 and 6.7) where:

- W^0 + WO_3 were observed in sample with N_2 flow rate = 0 sccm
- W^0 + W_2N + WO_3 were observed in sample with N_2 flow rate = 5 sccm
- W_2N + WO_3 were observed in sample with N_2 flow rate = 10 and 15 sccm

Curve de-convolutions were also done on N 1s binding energy since apparently it consists of three overlaped peaks (raw data in Figure 6.5b). Figure 6.9 shows relative amount of N in its different state for samples with different N_2 flow rate. N 1s binding energy data show that W-nitride can exist in different phases (W_2N, WN_x, and WO_xN_y). However, the amount of W_2N is more dominant compared to the other phases as shown in Figure 6.9. It is observed that as N_2 flow rate increases, the amount of W_2N and WN_x increases whereas that of WO_xN_y decreases, indicating higher tendency of W to react with N instead of O when more N is present.

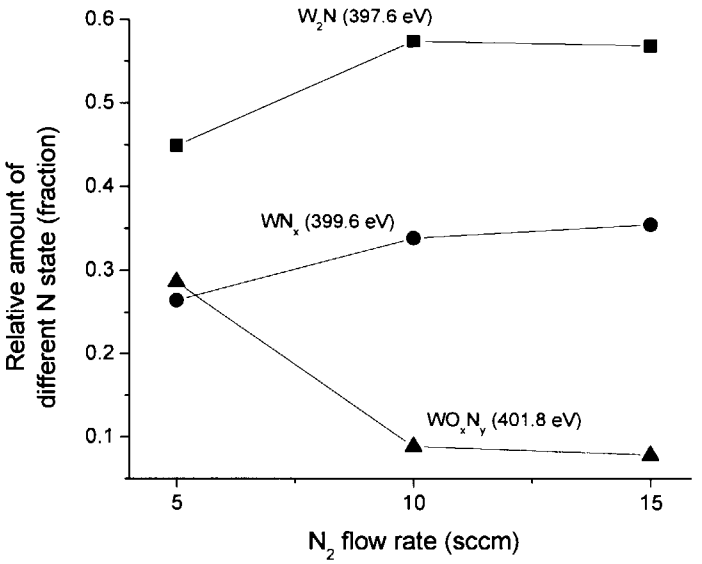

Figure 6.9 Plot of relative amount of different N states in Ru-W-N films with different N_2 flow rates

(ii) Ru-Ta-N

- *Chemical states of the elements*

The chemical states of the different elements in Ru-Ta-N films and their concentrations were also determined using XPS. Figure 6.10 shows the characteristic peaks of Ta 4f, N 1s, Ru 3p and O 1s for as-deposited Ru-Ta-N films obtained with different N_2 flow rates. In all samples, peaks corresponding to Ta-surface oxide (Ta_2O_5) were detected at binding energies of 26.6 eV (Ta $4f_{7/2}$) and 28.6 eV (Ta $4f_{5/2}$) as shown in Figure 6.10a. This Ta $4f_{7/2}$ binding energy value is close to the reported data for Ta $4f_{7/2}$ from Ta_2O_5 of 25.69 eV [116] and 26.1 eV [117]. In sample without N (0 sccm), besides Ta_2O_5 peaks, additional two peaks at binding energis of 22.6 eV (Ta $4f_{7/2}$) and 24.6 eV (Ta $4f_{5/2}$) are clearly observed which is attributed to the presence of metallic Ta (Ta^0). Zhang *et al.* [116] reported similar values for metallic Ta of 21.8 eV (Ta

$4f_{7/2}$) and 23.8 eV (Ta $4f_{5/2}$). Hence, in sample without N_2, the Ta exists as Ta^0 and Ta_2O_5.

When N_2 was introduced into the film, binding energy of Ta $4f_{7/2}$ and Ta $4f_{5/2}$ shifted to a higher value by ~2.4 eV (from 22.6 and 24.6 eV) to 25.0 and 27.0 eV respectively. These values agree well with a reported data by Wang *et al.* [118] on TaN film sputtered with N_2 partial pressure of 0.5 mTorr on SiO_2/Si substrate. They reported Ta $4f_{7/2}$ and Ta $4f_{5/2}$ binding energies associated with TaN film of 24.9 eV and 26.9 eV respectively. These confirm the formation of TaN in our deposited film since the values are also close to other reported data on TaN [116, 119].

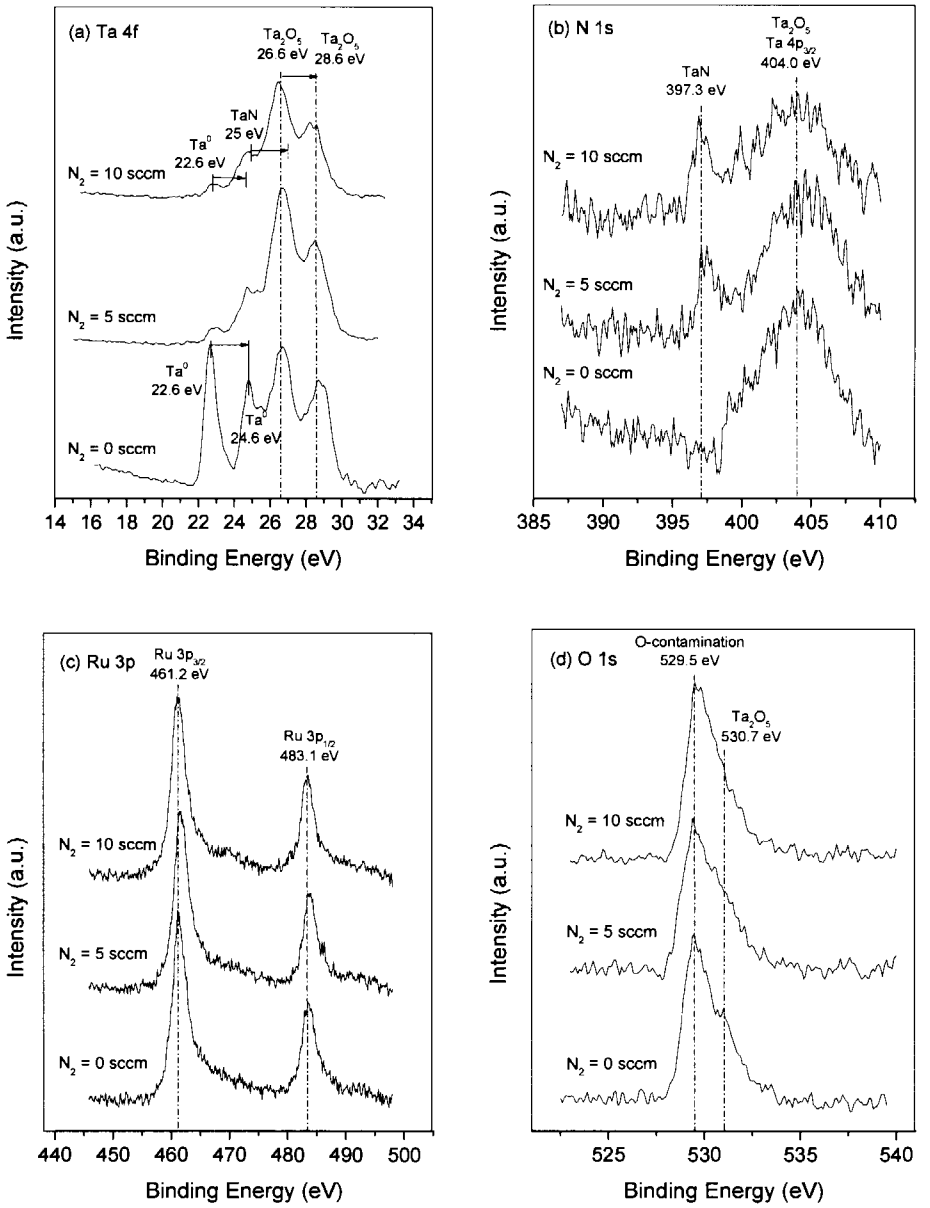

Figure 6.10 Electronic binding energy of (a) Ta 4f (b) N 1s (c) Ru 3p (d) O 1s of as-deposited Ru-Ta-N sub-surface (~20 nm under the surface to avoid high content of surface Ta-oxide) with different N_2 flow rates

The binding energy of N 1s (Figure 6.10b) was observed at ~397.3 eV, confirming the presence of TaN. Additionally, it can be observed that the N 1s core level at ~397.3 eV which is associated with TaN overlaps with the Ta 4p core level at ~404.0 eV which is associated with Ta_2O_5 [119]. Unlike in the case of Ru-W-N, Ru-Ta-N films deposited in Ar + N_2 show only one clear N 1s

binding energy. Other N 1s peaks which might arise from other Ta-nitrides with different stoichiometry or Ta-oxynitride at higher binding energies might overlap with Ta $4p_{3/2}$ peak from Ta_2O_5, hence are difficult to be identified.

As observed with Ru-W-N, introduction of N_2 during co-deposition of Ru-Ta does not change Ru binding energy, signifying that Ru does not form strong bond with N as shown in Figure 6.10c. O 1s binding energy in Figure 6.10d shows two peaks at 529.5 eV, coming from air contamination and at 530.7 eV, arising from surface Ta_2O_5. Qualitatively it is also observed that the relative amount of Ta_2O_5 is higher in sample with less N.

- *Chemical composition*

Compositions of Ru-Ta-N films were determined in a similar way to that of Ru-W-N films. As in the case of Ru-W-N, it is observed in that the concentrations of O and Ru do not change much with N_2 flow rate. This indicates that variation in N_2 flow rate during film deposition would only affect the Ta and N concentration. Figure 6.11 clearly demonstrates that the Ta concentration decreases as the N_2 flow rate increases while the N concentration increases from 19.15 at% (at N_2 = 5 sccm) to 30.5 at% (at N_2 = 10 sccm). Thus, the trends observed in Ru-Ta-N and Ru-W-N with regard to the dependence of chemical composition on the N_2 flow rate are similar.

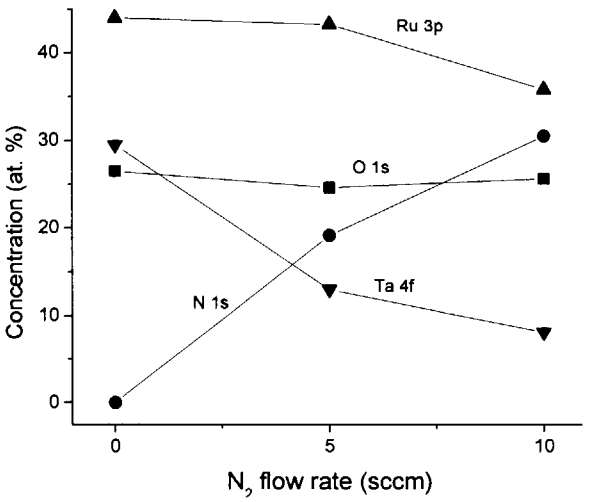

Figure 6.11 Plot of Ru 3p, O 1s, N 1s, and Ta 4f atomic concentration against N_2 flow rates of as-deposited Ru-Ta-N samples

To further understand the TaN formation during Ru-Ta co-sputtering in Ar + N_2 gas, Ta 4f binding energy curves were de-convoluted as shown in Figure 6.12. Similar with binding energy of W 4f, Ta 4f is also a duplet and hence, each phase has two peaks corresponding to Ta $4f_{7/2}$ and Ta $4f_{5/2}$.

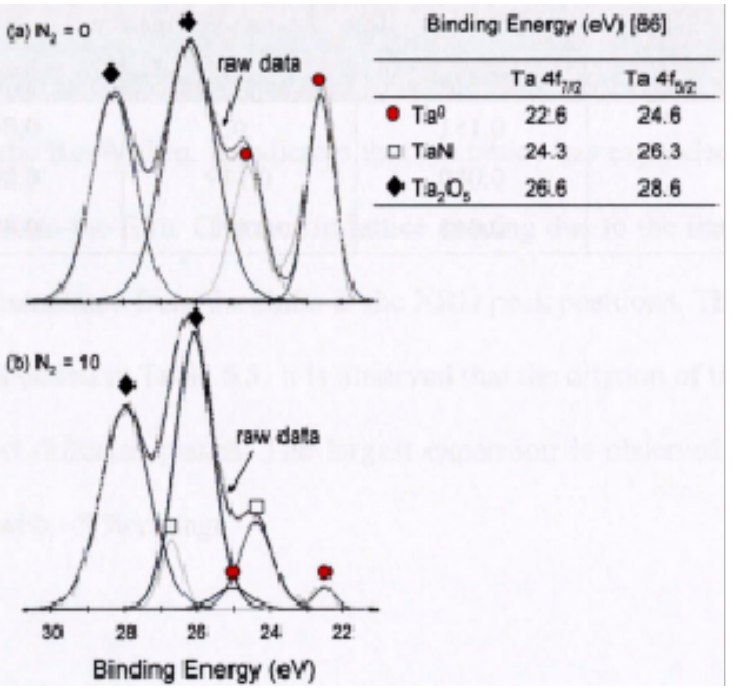

Figure 6.12 Ta 4f curve de-convolution for as-deposited Ru-Ta-N samples with N_2 flow rate of (a) 0 sccm (b) 10 sccm with binding energy data listed in the table

In the sample with N_2 = 0 sccm (Figure 6.12a), Ta exists in two phases, Ta^0 and Ta_2O_5. TaN at binding energies of 24.3 and 36.3 eV appear in films with nitrogen (Figure 6.12b), in addition to Ta^0 and Ta_2O_5 phases. The relative amounts of different Ta-states in different samples with different N_2 flow rates were determined from the area under each de-convoluted peak of each Ta-state. The results are presented in Table 6.4 and Figure 6.13. Similar to Ru-W-N films, the amount of TaN in Ru-Ta-N film increases whereas that of elemental Ta decreases as N_2 flow rate increases (Figure 6.13). The amount of Ta_2O_5 remains unchanged when N_2 flow rate is 5 sccm but shows a decrease when N_2 flow rate is 10 sccm as shown in Figure 6.13. Note that the amount of metallic Ta is almost negligible when the film has N, confirming the ease of TaN formation during film deposition.

Table 6.4 Calculated relative amounts of Ta with different chemical states in Ru-Ta-N samples surface deposited under different N_2 flow rates

N_2 flow rate (sccm)	Relative amount (fraction)		
	Ta_metallic	Ta_nitride	Ta_oxide
0	0.151	0	0.849
5	0.080	0.119	0.801
10	0.045	0.471	0.484

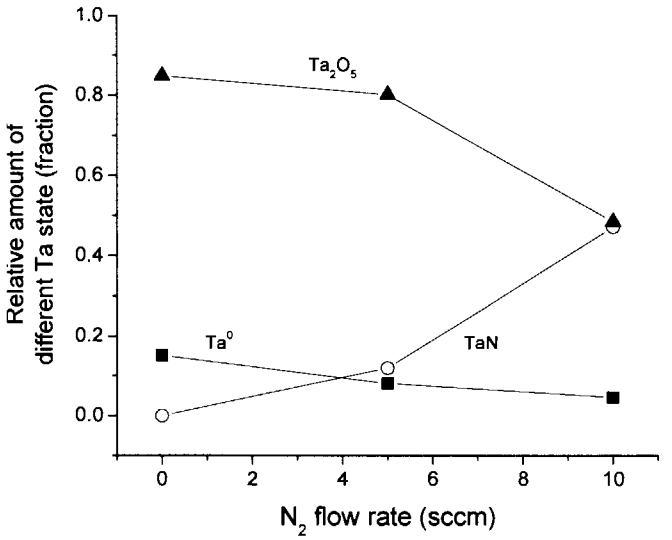

Figure 6.13 Plot of relative amount of different Ta states in Ru-Ta-N films with different N_2 flow rates

C. *Microstructure*

The films were analysed using XRD to understand the effect of N_2 flow rate on film microstructure. Figure 6.14 shows XRD data of pure Ru (reference sample) and a Ru-W film with N_2 flow rate of 0 sccm. It is clear that the hexagonal Ru peaks are shifted to lower 2θ angles from the standard peak positions in the Ru-W film. It indicates that Ru lattice has expanded when W is incorporated into the film. Changes in lattice spacing due to the introduction of W could be calculated from the shifts in the XRD peak positions. The calculated results are tabulated in Table 6.5. It is observed that the dilation of the Ru lattice is unequal on different planes. The largest expansion is observed to occur at (002) plane with ~3 % change.

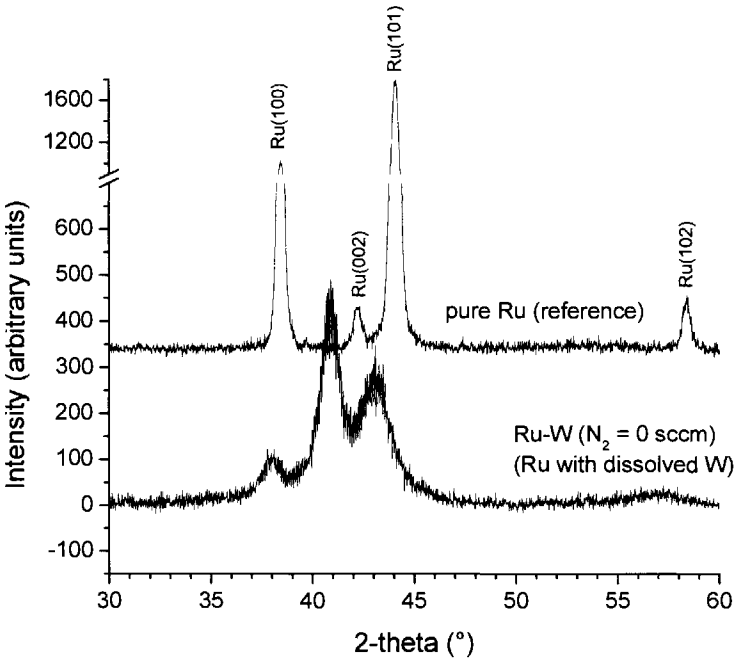

Figure 6.14 XRD spectra of pure Ru (reference sample) and as-deposited Ru-W (N_2 = 0 sccm)

Table 6.5 Calculated lattices spacing of pure Ru and Ru-W films based on XRD data

(hkl)	Ru		Ru-W		Δd/d (%)
	2θ (°)	d_0 (Å)	2θ (°)	d (Å)	
(100)	38.467	2.3383	38.02	2.364758	1.119
(200)	42.267	2.13645	40.85	2.207226	3.207
(101)	44.056	2.05375	43.11	2.096604	2.044

Films deposited under a gas mixture of Ar and N_2 does not show clear distinctive peaks as shown in Figure 6.15; instead they give a single broad reflection with relatively weak intensity at 2θ from 35° to 45°. This suggests that the film is composed of nanosized grains. The hump is broader with higher N_2 flow rate, indicating that the film becomes more amorphous with increase of N content. It should be noted that the highest intensity is located at 2θ = ~40.5°, which is very close to cubic α-W (2θ = 40.262° (110)) (JCPDS card no. 04-0806). However, there are several other peaks which may overlap in the broad

hump as listed in Table 6.6. Thus, it is suggested that mixture of Ru, W, W_2N and WN could be formed. However, XPS study presented earlier (Section 6.3.1B) did not show W 4f binding energy of WN for all the samples under study. It could be because of its minimum amount which maybe lower than the XPS detection limit. Hence, from the XRD data, with comparison to the XPS results, it can be deduced that Ru-W film deposited using N_2 = 0 sccm has Ru crystals with expanded lattice due to W incorporation. Ru-W-N film deposited using N_2 = 5 sccm is mainly composed of Ru + W + W_2N phases whereas that deposited using N_2 = 10 and 15 sccm primarily consists of Ru + W_2N phases.

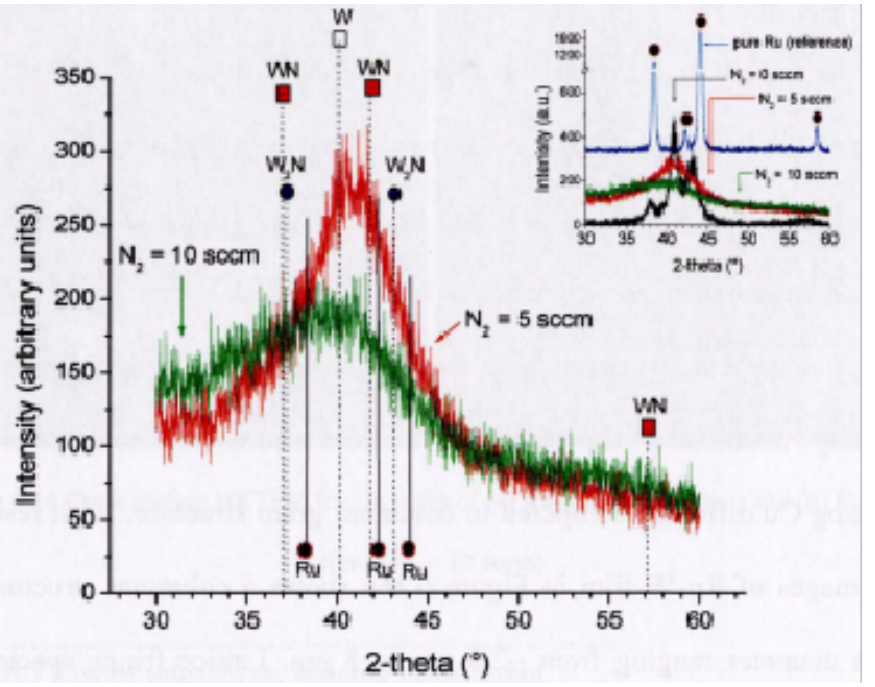

Figure 6.15 XRD spectra of as-deposited Ru-W-N (N_2 = 5 and 10 sccm) [Inset: XRD spectra of pure Ru and as-deposited Ru-W-N (N_2 = 0, 5, and 10 sccm) for clear comparison]

Table 6.6 List of possible peaks which overlap in the broad XRD hump of as-deposited Ru-W-N

	(hkl)	2θ (°)	JCPDF card no.
cubic α-W	(111)	40.262	04-0806
fcc β-W_2N	(111)	37.73	25-1257
	(200)	44.113	
hexagonal δ-WN	(001)	36.931	25-1256
	(100)	41.872	
hexagonal Ru	(100)	38.385	06-0663
	(002)	42.151	
	(101)	44.00	

As the phases could not be confidently determined with XRD and XPS, TEM was resorted to further confirm the phases and also film microstructure. TEM micrographs and their selected area electron diffraction (SAD) patterns of Ru-W and Ru-W-N (N_2 = 10 sccm) films are shown in Figure 6.16. It is clearly observed that Ru-W deposited under pure Ar gas is crystalline and has a columnar microstructure whereas Ru-W-N deposited under Ar + N_2 shows nanocrystalline microstructure and hence, has a diffused SAD pattern. As previously mentioned, this kind of microstructure is more effective in preventing Cu diffusion compared to columnar grain structure. High resolution TEM images of Ru-W film in Figure 6.16a shows a columnar structure with column diameter ranging from ~2.5 nm to 5 nm. Lattice fringe spacing was measured and the value varies from 2.083 to 2.292 Å. These values are close to calculated data presented earlier in Table 6.5 on interplanar spacing of Ru in Ru-W film based on diffraction peaks shift ($d_{(100)}$ = 2.365, $d_{(200)}$ = 2.207, $d_{(101)}$ = 2.0967 Å). Bulk of Ru-W-N film shows nanocrystals with size of few nm (≤ 3 nm) as shown in Figure 6.16b. The lattice fringe spacing in the HRTEM images is identified to be in a range of 1.875 to 2.375 Å. However, we are unable to

identify the phases in Ru-W-N films in order to determine their orientation. A comparison of the possible phases is given in Table 6.7 by their d-spacings.

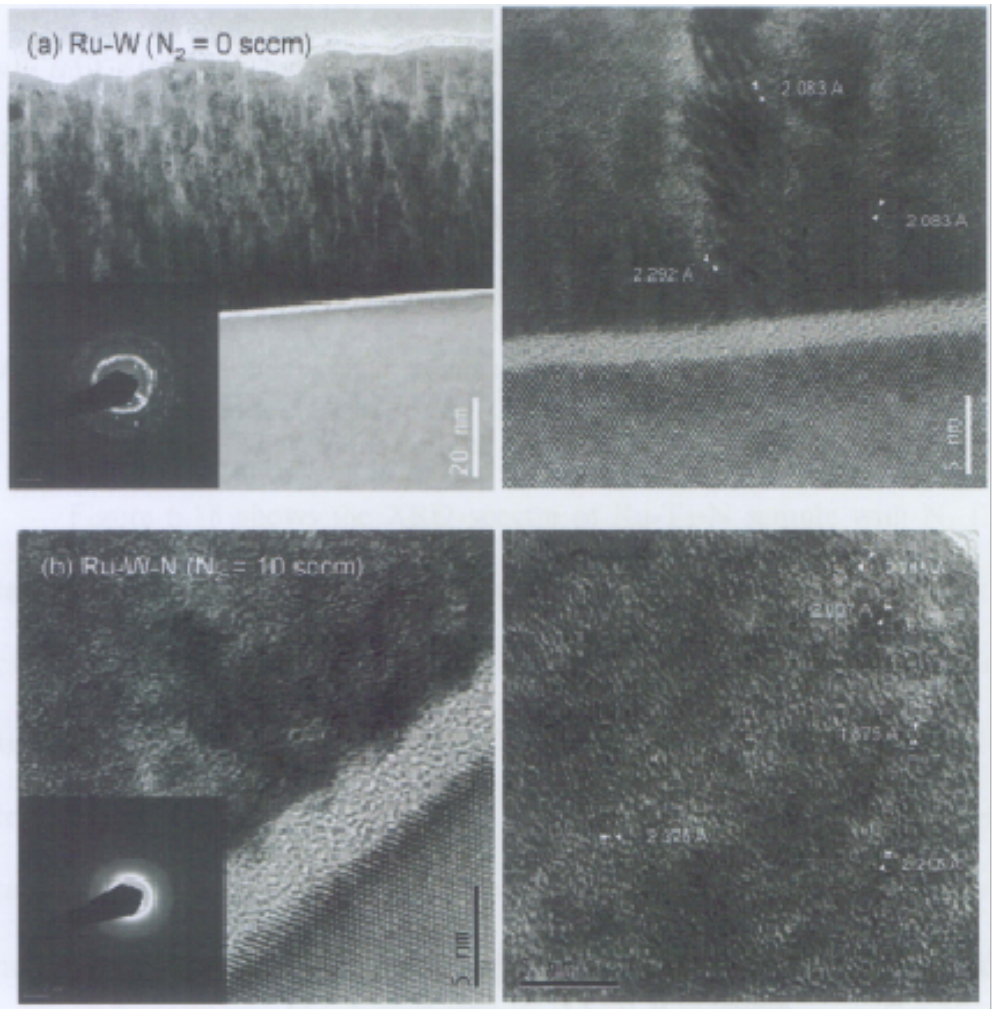

Figure 6.16 Cross section HRTEM micrographs of (a) Ru-W (N_2 = 0 sccm) and (b) Ru-W-N films (N_2 = 10 sccm)

Table 6.7 List of interplanar spacing of different possible elements and compounds in Ru-W-N film

	(hkl)	d (Å)
hexagonal Ru	(100)	2.343
	(002)	2.141
	(101)	2.056
cubic W	(110)	2.238
fcc β-W_2N	(111)	2.382
	(200)	2.063
hexagonal δ-WN	(100)	2.505
	(101)	1.875

Figure 6.17 shows XRD spectra of as-deposited pure Ru (reference sample) and Ru-Ta film. Note that incorporation of Ta into Ru film does not give hexagonal Ru peaks unlike in the case of Ru-W where the hexagonal Ru peaks were still clearly observed at lower 2θ positions. The Ru-Ta film gives two broad peaks approximately at 2θ = 40° and 45°. It could be an indication that the film consists of nanocrystals. The smaller hump at 45° is likely coming from crystalline Ta_2O_5 surface oxide. Whereas the hump at 37° to 45° could be an overlap of different possible peaks, such as hexagonal, Ru, cubic α-Ta, and tetragonal β-Ta. Their 2θ peak positions are listed in Table 6.8.

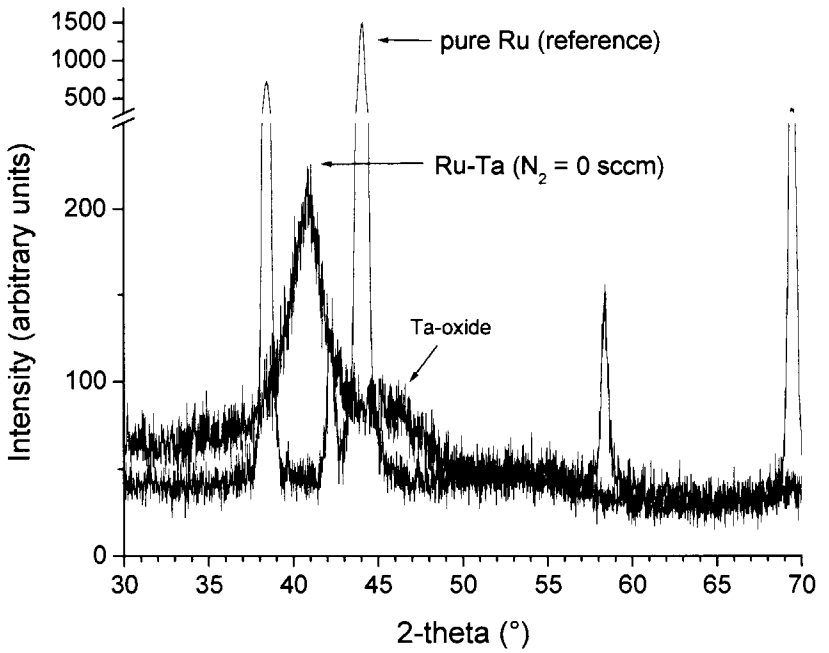

Figure 6.17 XRD spectra of pure Ru (reference sample) and as-deposited Ru-Ta (N_2 = 0 sccm)

Table 6.8 List of possible peaks which overlap in a XRD peak of as-deposited Ru-Ta

	(hkl)	2θ (°)	JCPDF card no.
cubic α-Ta	(110)	38.472	04-0788
tetragonal β-Ta	(002)	33.692	25-1280
	(410)	36.281	
	(330)	37.392	
	(202)	38.200	
	(212)	39.240	
	(411)	40.208	
	(331)	41.186	
	(312)	44.050	

Figure 6.18 shows the XRD spectra of Ru-Ta-N sample with N_2 flow rate of 5 and 10 sccm. The film becomes more amorphous as N concentration increases. The presence of different Ta-nitrides ($TaN_{0.1}$, Ta_4N, Ta_2N, TaN, Ta_3N_5, $TaN_{0.8}$) are possible in Ru-Ta-N film since diffraction peaks of those nitrides are very close to each other with 2θ position of the highest peak intensity ranges from 35.3° for $TaN_{0.8}$ to 38.7° for Ta_2N. Hence, the film may be amorphous with nanocrystals of Ru, Ta, as well as different Ta-nitrides. However, the XPS results in Section 6.3.1B showed only TaN phase in Ru-Ta-N (N_2 = 5 and 10 sccm) films. The presence of the different Ta-nitrides was difficult to confirm with XPS since they might have similar Ta 4f binding energies.

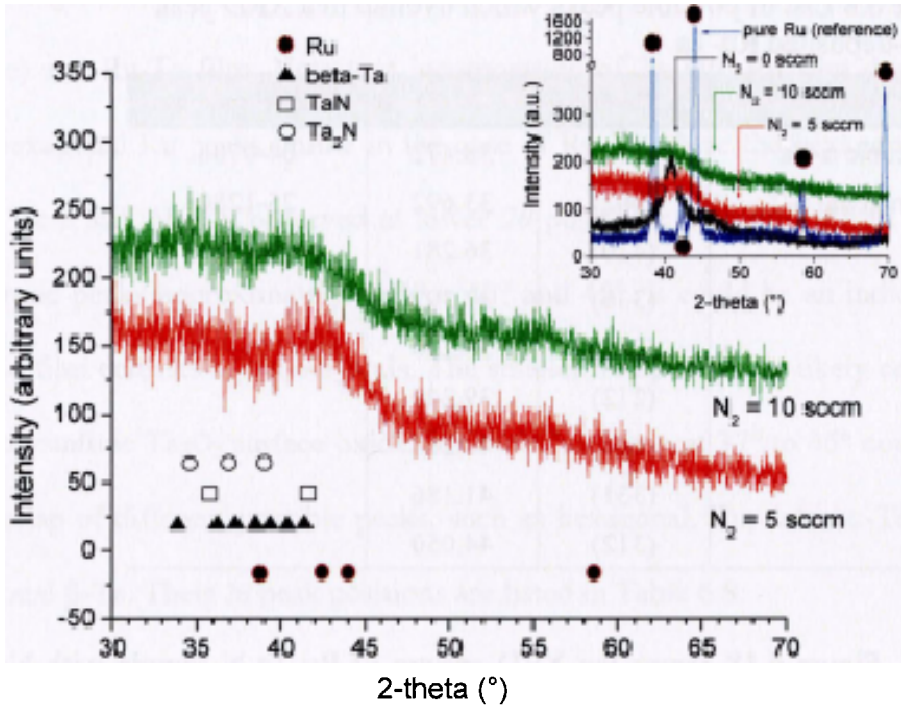

Figure 6.18 XRD spectra of as-deposited Ru-Ta-N (N_2 = 5 and 10 sccm) [Inset: XRD spectra of pure Ru and as-deposited Ru-Ta-N (N_2 = 0, 5, and 10 sccm) for clear comparison]

TEM cross section investigations were also done on Ru-Ta-N films and the micrographs obtained are presented in Figure 6.19. Ru-Ta film without N (as shown in Figure 6.19a) consists of many nanocrystals with some amorphous region. This is confirmed by its SAD pattern in Figure 6.19b. Table 6.9 lists interplanar spacing data of different possible elements in Ru-Ta film. Ru-Ta-N film deposited using 5 sccm N_2 in Figure 6.19c has completely amorphous microstructure and hence, shows diffused SAD pattern as shown in Figure 6.19d.

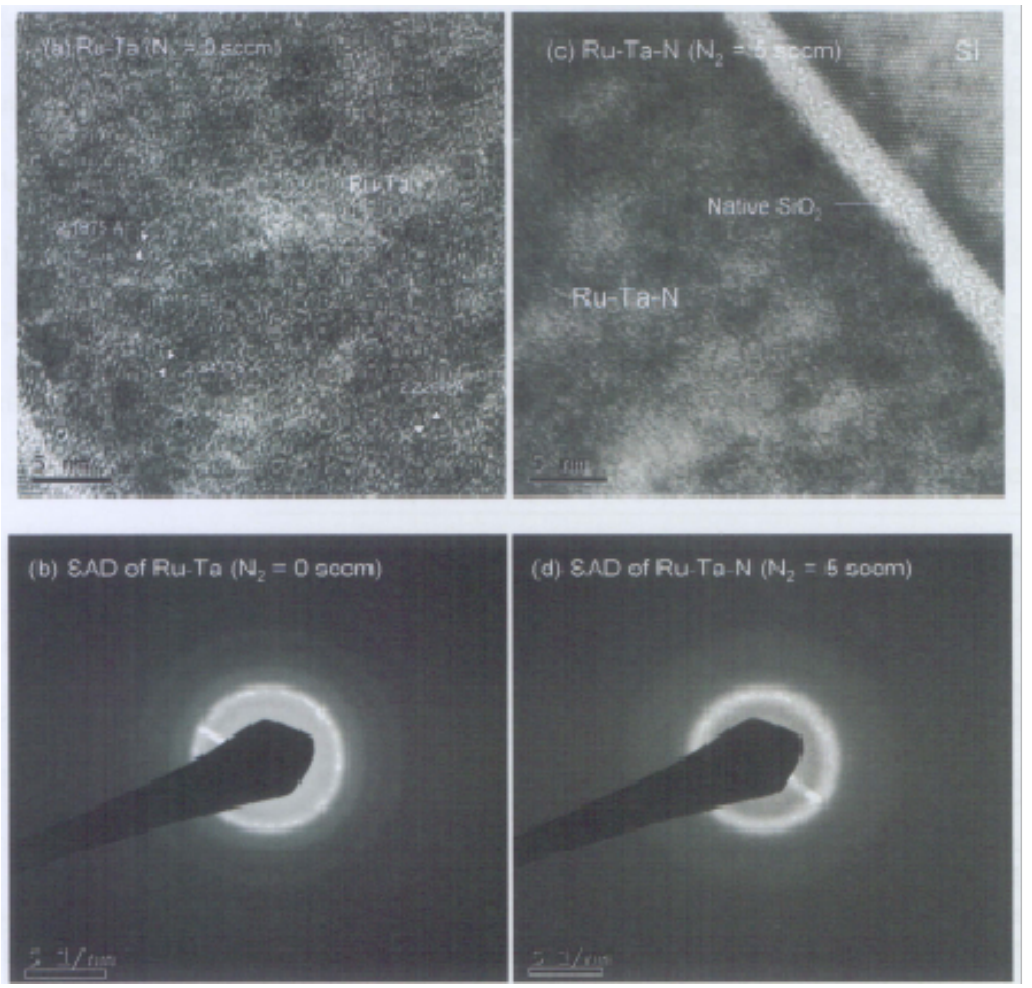

Figure 6.19 (a) HRTEM micrographs and (b) SAD pattern of Ru-Ta (N_2 = 0 sccm) film (c) HRTEM micrographs and (d) SAD pattern of Ru-Ta-N (N_2 = 5 sccm) film

Table 6.9 List of interplanar spacing of different possible elements in Ru-Ta (N_2 = 0 sccm) film

	(hkl)	d (Å)
hexagonal Ru	(100)	2.343
	(002)	2.141
	(101)	2.056
α-Ta	(110)	2.338
β-Ta	(202)	2.356
	(212)	2.295
	(411)	2.241
	(331)	2.189

Table 6.10 summarizes the film microstructure and phases present in the as-deposited Ru-W-N and Ru-Ta-N for different N content based on the XPS, XRD, and TEM investigations attempted so far.

Table 6.10 Microstructure of and phases present in as-deposited Ru-W-N and Ru-Ta-N films

	N_2 flow rate (sccm)	microstructure	phase present
Ru-W-N	0	polycrystalline (columnar)	Ru + W
	5	nanocrystalline	Ru + W + W_2N
	10	nanocrystalline + amorphous	Ru + W_2N
	15	amorphous	Ru + W_2N
Ru-Ta-N	0	nanocrystalline + amorphous	Ru + Ta
	5	amorphous	Ru + TaN
	10	amorphous	Ru + TaN

*note that surface oxide (WO_3 or Ta_2O_5) is always present in the films.

Note that in samples without N (0 sccm), Ru-W has polycrystalline microstructure whereas Ru-Ta has a mixture of nanocrystalline and amorphous microstructure. This could be explained due to larger difference in Ta and Ru atomic radii compared to that of W and Ru (atomic radius of Ru = 0.13 nm, Ta = 0.145 nm, W = 0.137 nm [33]). Since the atomic radii of Ru and W are

similar, W can substitutionally sit in Ru atom position without disrupting the Ru lattice. On the other hand, Ta is much bigger than Ru. Incorporation of Ta during Ru deposition will interrupt the growth of Ru lattice and therefore results in nanocrytalline microstructure. Additionally, with the same N_2 flow rate, N incorporation into Ru-Ta-N film is much higher (~double) than that in Ru-W-N film (e.g. for sample with N_2 = 10 sccm, N content in Ru-Ta-N is ~30 at%, in Ru-W-N is ~15 at% (refer to Figure 6.6 and 6.11). This explains the difference in stoichiometry of W_2N and TaN. When reacting with N and forming nitride, Ta was found to have higher oxidation state (Ta^{3+}) than W ($W^{1.5+}$), indicating its higher tendency to form nitride compared to W. Incorporation of higher N amount also results in more amorphous microstructure. This elucidates why Ru-Ta-N film is more amorphous compared to Ru-W-N film when deposited with the same N_2 flow rate.

6.3.2 Thermal Stability of Ru-W-N and Ru-Ta-N Barriers

A. Changes in films resistivity with temperature

As in Chapter 4 and 5 for pure Ru and Ru-N films, the resistivity changes in Ru-W-N and Ru-Ta-N films were also investigated as a function of annealing temperature and N_2 flow rate. Figure 6.20 shows the manner in which film resistivity decreases on increase in thermal annealing temperature. The film resistivity decreases after annealing at every temperature but a sharp drop is evident between 300°C and 400°C for both Ru-W-N and Ru-Ta-N samples. This could be attributed to several processes that maybe occurring in this temperature regime, namely:

(i) grain growth

(ii) lattice defects (stacking faults, etc.) annihilation

(iii) Ru crystallization and

(iv) impurity (N) segregation or out diffusion.

The relative contribution of each of these processes to the total decrease in resistivity is not clearly quantifiable, but the important effects of the processes could be described qualitatively. Grain growth and reduction in intergranular voids contribute to the resistivity decrease due to decreased defect and grain boundary population which are electron scattering features. Note that the decrease in resistivity is larger for films with higher N content, indicating a higher thermodynamic driving force for expelling the excess N. This indicates that N-out diffusion may have a more dominant effect in causing reduction in film resistivity. The effect of Ru crystallization and impurity segregation would be further discussed in Section 6.3.2C and 6.3.2D. With increasing annealing temperature, the resisitivity of all films decrease further and converge to the measured resistivity value of Ru-W or Ru-Ta (N_2 = 0 sccm) film, confirming that N effect is the most significant process. Contrary to the behaviour of Ru and Ru-N films reported in Chapter 4 and 5, there is no significant increase in film resistivity up to 800°C resulting from silicide formation. This is an indication of the higher thermal stability of the Ru-W-N and Ru-Ta-N films when compared to the films without the W or Ta.

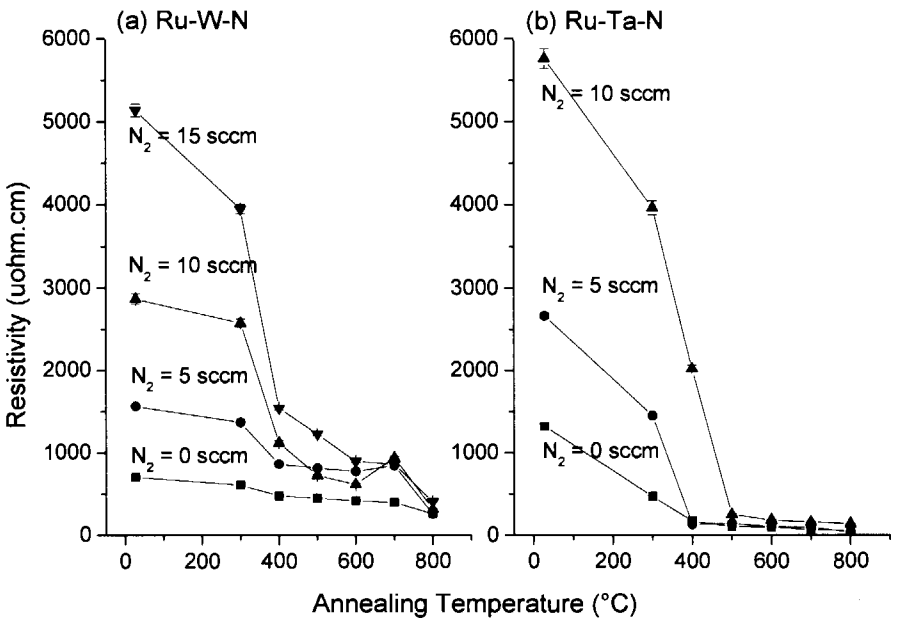

Figure 6.20 Plot of Film resistivity of Ru-W-N and Ru-Ta-N films with different N_2 flow rates under different annealing conditions

B. Nitrogen release from Ru-W-N and Ru-Ta-N under thermal annealing

(i) Ru-W-N

It is well known that nitrogen is released during annealing in W-based nitrides [51, 95, 120-122]. Lin *et al.* [120] reported that when a sputter-deposited WN_x film was annealed at high temperatures (> 800°C) all film was converted to pure W irrespective of nitrogen content. Other literatures also reported that nitrogen was released from a plasma-enhanced CVD WN_x film when annealed at ~800°C, and the amount of released N was dependent on the initial N content of the film [121], and on the annealing conditions [122]. In our study also, N release from Ru-W-N films was observed on annealing, as indicated by the sharp decrease in film resistivity upon annealing at 400°C in Figure 6.20.

To verify the N release with annealing, XPS scans were done on the annealed Ru-W-N samples. Figure 6.21 presents the chemical states of W 4f (Figure 6.21a) and N 1s (Figure 6.21b) for Ru-W-N (N_2 = 10 sccm) after different annealing treatments. The samples with other N_2 flow rates exhibit similar behaviors. Surface WO_3 is always present on as-deposited as well as annealed samples. W_2N at binding energy of 33.2 eV is clearly observed in the as-deposited sample. W 4f binding energy had minimum change when the films were annealed at temperature < 500°C. It implies that the chemical bonding of W and N did not undergo much change up to that temperature. However, a shift in the binding energy of W 4f is observed towards a lower value for annealed samples. When temperature was increased to > 500°C, nitride peaks gradually disappear and metallic W peaks appeared at the binding energy of 31.6 eV. It signified conversion of W-nitride into metallic W due to N-release. Escaping of N atoms during annealing was further confirmed by a decrease in N 1s peak intensity after annealing. Note that N 1s peak almost disappeared after annealing at 600°C although the presence of little amount of W-nitride was still observed based on W 4f binding energy. This could be due to the lower relative sensitivity value of N 1s (0.25) compared to that of W 4f (1.4375) [123]. Position of N 1s binding energy (at 397.7 eV) was relatively constant after annealing, indicating that the bonding of N with W in Ru-W-N does not change significantly.

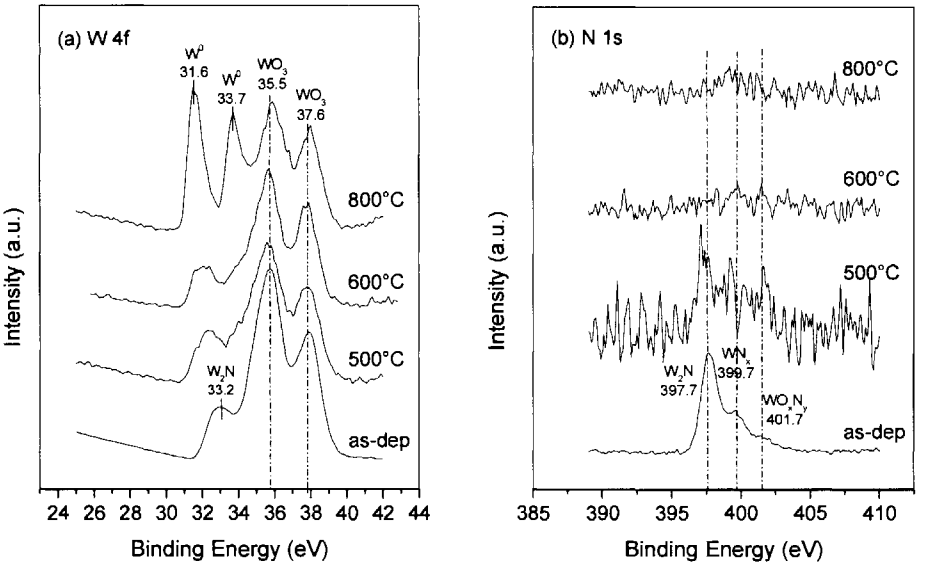

Figure 6.21 Electronic binding energy of (a) W 4f (b) N 1s of as-deposited and 500, 600, and 800°C annealed Ru-W-N surface (N_2 = 10 sccm)

To further analyse the N release, relative amounts of W in its different states were determined by XPS curve fitting and calculated from the area under each de-convoluted peak. Figure 6.22 shows relative amount of W in its different state as a function of annealing temperature. It is clear that the amount of W-nitride decreases and that of W-metallic increases with annealing.

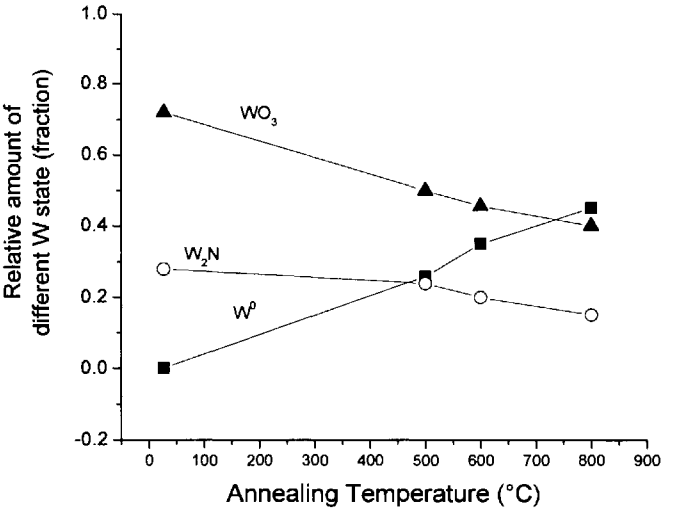

Figure 6.22 Plot of relative amount of different W states in Ru-W-N (N_2 = 10 sccm) films under different annealing conditions

(ii) Ru-Ta-N

Similarly for Ru-Ta-N, XPS scans were done on these films to verify the N out diffusion. Figure 6.23 shows chemical state of Ta 4f and N 1s for Ru-Ta-N (N_2 = 10 sccm) after different annealing conditions. Samples with other N_2 flow rate indicate similar trend. Ta_2O_5 (binding energy of 26.6 eV) is always present in as-deposited and annealed samples. In as-deposited state, TaN at 24.3 eV and a little amount of Ta^0 at 22.6 eV are clearly observed. Upon annealing, the Ta^0 peak at binding energy of 22.6 eV appears to become stronger. Additionally Ta_2N at binding energy of 23.1 eV starts to appear after annealing, indicating conversion of some of the TaN into elemental Ta and Ta_2N due to N out diffusion. A decrease in N 1s peak intensity is also clearly observed after annealing. N 1s peak was negligible after 500°C of annealing, however, some Ta-nitrides were still observed from Ta 4f binding energy. This could be due to the lower relative sensitivity value of N (0.25) compared to that of Ta (1.25) [123].

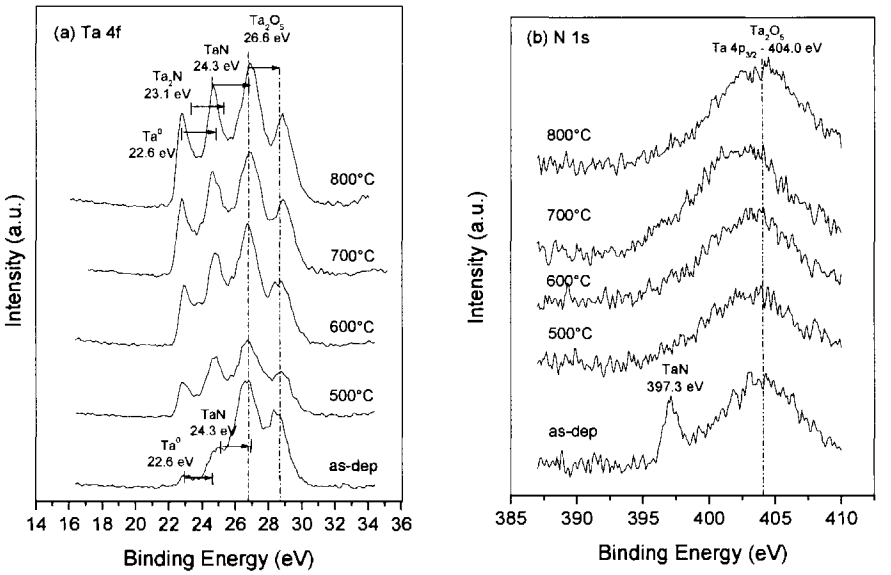

Figure 6.23 Electronic binding energy of (a) Ta 4f (b) N 1s of as-deposited and 500, 600, 700, and 800°C annealed Ru-Ta-N surface (N_2 = 10 sccm)

Curve de-convolutions are needed to separate all the overlapping peaks in the Ta 4f binding energy to further understand the TaN evolution with thermal annealing. Figure 6.24 shows the Ta 4f binding energy of as-deposited and 500°C annealed Ru-Ta-N films after de-convolution. Ta exists in three different states in the as-deposited film, namely: Ta^0, TaN, and Ta_2O_5 as shown in Figure 6.24a. It was observed that after 500°C, additional state of Ta-nitride appeared at lower binding energy (Figure 6.24b). This is attributed to formation of another Ta-nitride with lower oxidation state, Ta_2N, with Ta $4f_{7/2}$ and Ta $4f_{5/2}$ binding energies of 23.2 and 25.2 eV respectively. The relative amounts of Ta in its different states were calculated from the area under each de-convoluted peak and the results are presented in Figure 6.25.

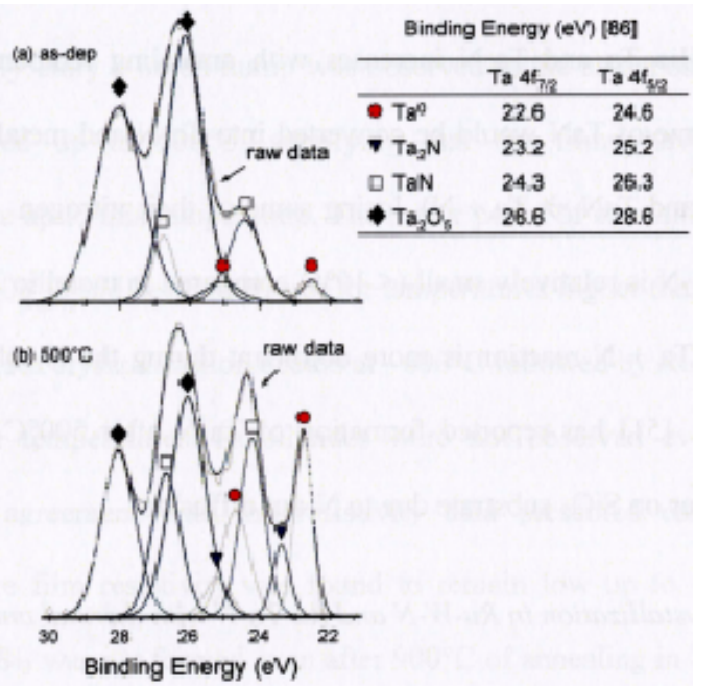

Figure 6.24 Ta 4f curve de-convolution of as-deposited and 500°C annealed Ru-Ta-N (N_2 = 10 sccm) with binding energy data listed in the table

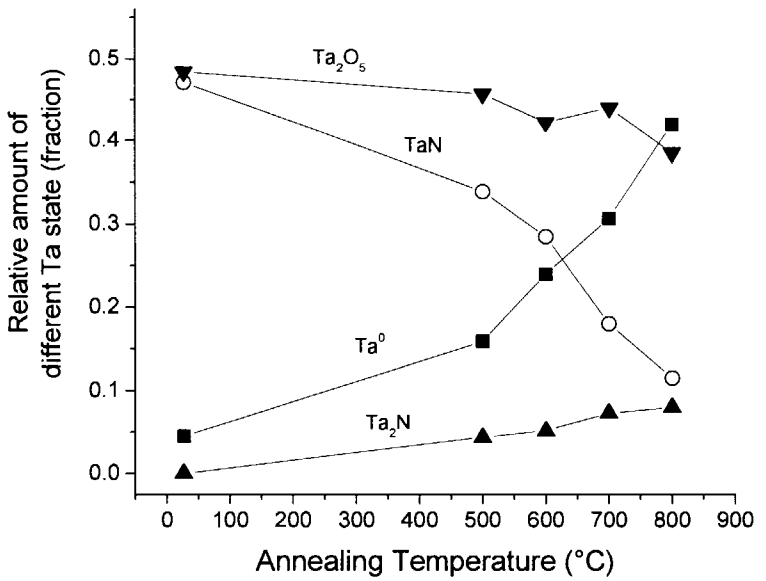

Figure 6.25 Plot of relative amount of different Ta states in Ru-Ta-N (N_2 = 10 sccm) films under different annealing conditions

It can be seen in Figure 6.25 that the amount of TaN decreases whereas that of metallic Ta and Ta_2N increases with annealing temperature. During annealing, some of TaN would be converted into Ta_2N and metallic Ta (2TaN → Ta_2N +N and TaN → Ta + N), losing some of their nitrogen. However, the amount of Ta_2N is relatively small (< 10%) compared to metallic Ta, indicating that TaN → Ta + N reaction is more dominant during the N release process. Hubner *et al.* [51] has reported formation of Ta_2N after 500°C annealing of TaN/Ta bilayer on SiO_2 substrate due to N-out diffusion.

C. Ru crystallization in Ru-W-N and Ru-Ta-N with thermal annealing

Ru crystallization was thought to be one of the reasons for the sharp decrease in film resistivity from 300°C to 400°C of annealing. XRD analyses were done on annealed samples to verify the Ru crystallization. Figure 6.26 shows XRD spectra of Ru-W-N/Si sample (N_2 = 10 sccm) after various annealing conditions.

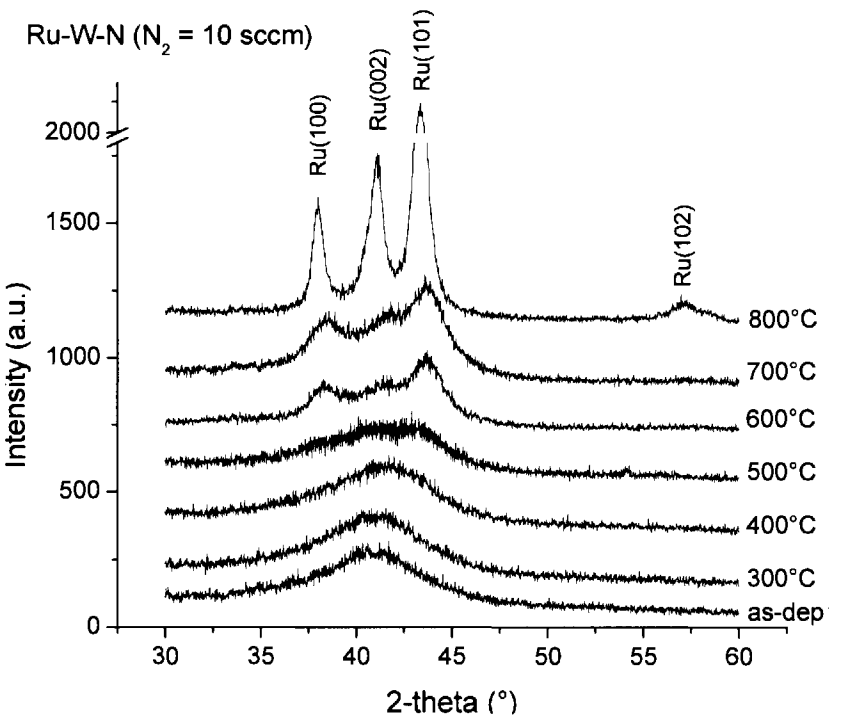

Figure 6.26 XRD spectra of Ru-W-N film (N_2 = 10 sccm) after different annealing conditions

Initially, only a broad hump was observed in the as-deposited state and when annealed up to 500°C, signifying that the films have amorphous microstructure up to this temperature. The major peaks of crystalline Ru started to appear at 600°C and became clearer for temperatures higher than 600°C. This indicates that Ru crystzallization occurs at ~600°C followed by Ru grain growth at the higher temperatures. Ru-silicides were not observed even at 800°C, showing an agreement with the resistivity data presented earlier (Section 6.3.2A) where film resistivity was found to remain low up to 800°C for all samples. Ru_2Si_3 was not formed even after 900°C of annealing in both Ru-W/Si and Ru-W-N/Si systems. Note that in the case of pure Ru/Si and Ru-N/Si systems, Ru_2Si_3 formation occurs after 700°C and 900°C of annealing respectively (Section 5.3.1). Delay in Ru-silicide formation in Ru-W-N/Si system to a temperature higher than 900°C could be attributed to the presence of N, W, or W-nitride in the film.

Figure 6.27 shows XRD spectra of Ru-Ta-N sample (N_2 = 10 sccm) after various annealing conditions. A very broad hump appears in as-deposited film which implies an amorphous structure for the film. This hump becomes sharper and higher in intensity with annealing up to 400°C, indicating that the films become less amorphous upon annealing, possibly due to release of some interstitial N. The peaks corresponding to hexagonal Ru start to appear at ~600°C and become clearer after annealing at 700°C and higher. These peaks become sharper and stronger with increase of temperature which could be due to Ru grain growth. When compared with XRD data for Ru-W-N, it is observed that crystallization in both films, Ru-W-N and Ru-Ta-N, occur at almost the same temperature, which is ~600°C.

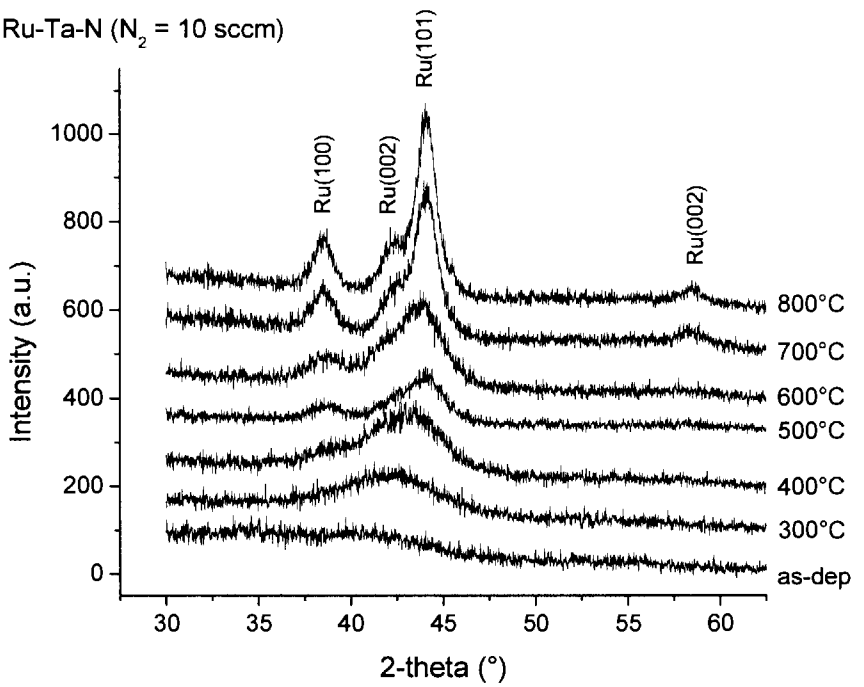

Figure 6.27 XRD spectra of Ru-Ta-N film (N_2 = 10 sccm) after different annealing conditions

To give a clearer comparison among the different Ru-based film properties, the critical temperatures for pure Ru, Ru-N, Ru-W-N, and Ru-Ta-N

films including the onset of Ru crystallization and Ru_2Si_3 formation temperatures (observed by XRD and resistivity changes) are listed in Table 6.11.

Table 6.11 Comparison of all critical temperatures for pure Ru, Ru-N, Ru-W-N, and Ru-Ta-N films on Si substrate (w/o Cu overlayer), in °C

	pure Ru	Ru-N	Ru-W-N (N_2 = 10 sccm)	Ru-Ta-N (N_2 = 10 sccm)
Onset of Ru crystallization (XRD)*	-	275	600	600
Ru_2Si_3 formation (XRD)	700	900	> 900	> 900
Resistivity change				
a sharp drop in resistivity	-	275	400	400
a large increase in resistivity	700	900	> 900	> 900

* Ru crystallization temperature is the temperature where hexagonal Ru peaks appear clearly in the XRD

With the presence of a nitride forming element (W or Ta), the onset of Ru crystallization occurs at a much higher temperature (600°C) compared to that in Ru-N film (275°C), indicating a higher thermal stability of the Ru-W-N and Ru-Ta-N films. Additionally, silicide formation occurs at higher temperature with the presence of additional element (Ru-N at 900°C, Ru-W-N and Ru-Ta-N at >900°C) compared to that in pure Ru (700°C).

D. Elements segregation in Ru-W-N during thermal treatment

To understand the elements or phases distribution in the film, TEM analyses were done on as-deposited and annealed Ru-W-N films. Samples with medium N_2 flow rate of 10 sccm were chosen for this study since these films have high enough W-nitride content without being highly saturated with excess N, unlike in the case of film with low (5 sccm) or high (15 sccm) N_2 flow rate.

Figure 6.28 shows cross-sectioned TEM micrographs of Ru-W-N (N_2 = 10 sccm)/Si samples, as-deposited and after different annealing conditions (400°C to 800°C). A native SiO_2 is always present at Ru-W-N/Si interface. The as-deposited Ru-W-N film has predominantly amorphous microstructure with few nanocrystals as shown in Figure 6.28a. Additionally, the as-deposited film appears to be homogeneous across the film thickness. However, upon annealing at 400°C, a thin (~1.8 nm) dark continuous layer was observed at film/native-SiO_2 interface as shown in Figure 6.28b, with the dark layer marked by a dotted white line. The darker contrast in the TEM micrographs could be due to more scattering or absorption of the electrons caused by more interaction of electrons with atoms in that region. Such contrast was not observed at Cu/Ru interface. The average thickness of the dark layer increases from ~1.8 nm at 400°C (Figure 6.28b) to ~2.2 nm at 500°C (Figure 6.28c), ~3.5 nm at 600°C (Figure 6.28d) and ~4.7 nm at 700°C (Figure 6.28e). Hence, this layer appears to increase in thickness with increase in annealing temperature. However, it eventually disappeared after 800°C as shown in Figure 6.28f, possibly due to N release from the W-nitride. In these series of micrographs, Ru crystallization is also clearly observed upon annealing.

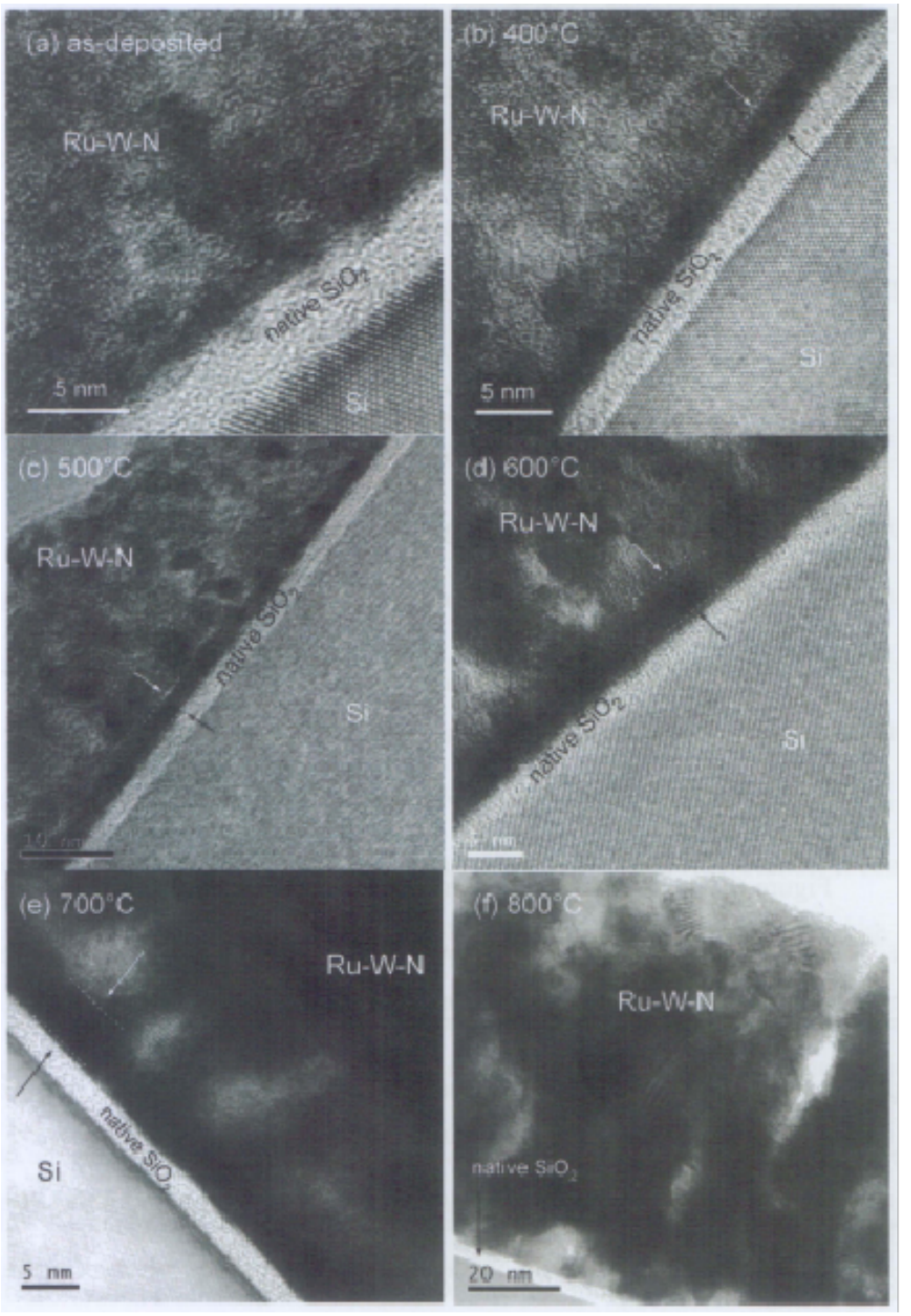

Figure 6.28 TEM bright field micrographs of (a) as-deposited (b) 400°C (c) 500°C (d) 600°C (d) 700°C and (d) 800°C annealed Ru-W-N films (N_2 = 10 sccm)

EDX analyses were done at Ru-W-N/Si film interface and the bulk film to identify the dark layer at interface.

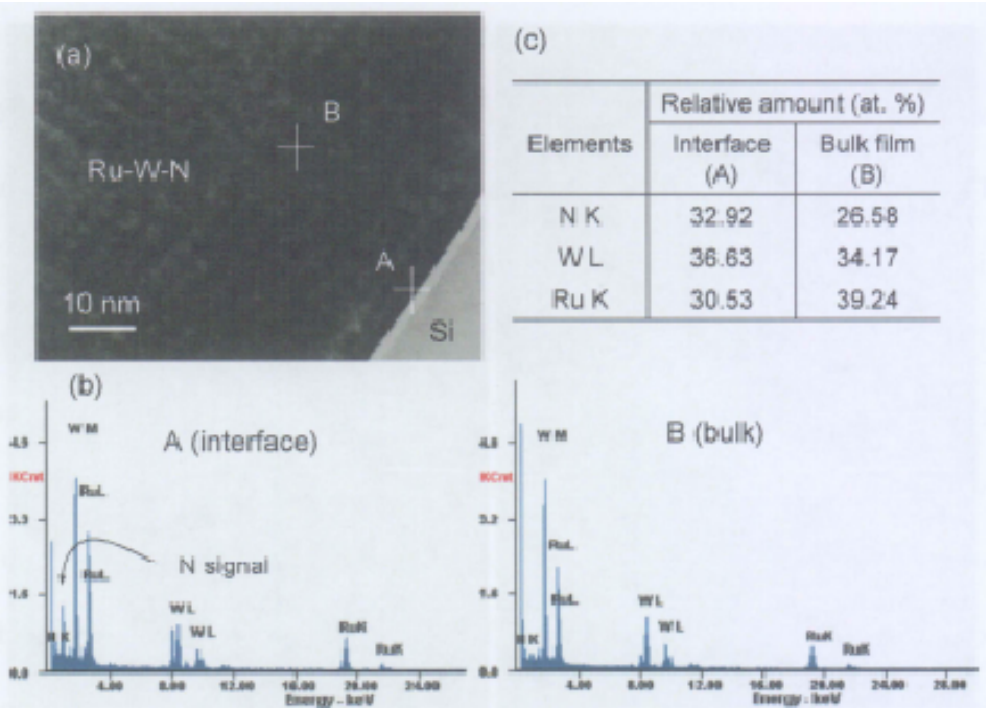

Elements	Relative amount (at. %)	
	Interface (A)	Bulk film (B)
N K	32.92	26.58
W L	36.63	34.17
Ru K	30.53	39.24

Figure 6.29 (a) TEM micrograph of 500°C annealed Ru-W-N (N_2 = 10 sccm) film on Si, showing region A and B where the EDX measurements were performed (b) EDX spectra obtained from location A and B (c) relative amount of elements at location A and B

Figure 6.29a presents the TEM micrograph of 500°C annealed Ru-W-N (N_2 = 10 sccm) film, showing region A and B where the EDX analyses were performed. The EDX spectra are shown in Figure 6.29b. It is clear that the N signal is much stronger at film interface (A) compared to that in the bulk (B). Semi-quantitative analysis was done on the EDX spectrum acquired at the two spots (A and B) by calculating the relative concentration of Ru, W, and N only, without taking into account Si and O signal which also appeared in the spectrum. The results of this are presented in Figure 6.29c. It was found that the relative amounts of N at interface (32.92 at%) is higher than that in the bulk film (26.58 at%). Additionally, the relative amount of W at interface (36.63 at%) was also found to be slightly higher than that at bulk film (34.17 at%). Consequently the relative amount of Ru is higher in the bulk film (39.24 at%)

than that in the interface (30.53 at%). Hence, there appears to be a tendency for N and W to segregate to the Ru-Si interface during annealing. However, it is not clear that the segregation of N is by N interstitial diffusion or diffusion of W-nitride. The later case is less probable as the activation energy for diffusion of W or WN_x is expected to be relatively high (however, diffusion data of W in Ru is not available). Note that the W enrichment at interface (by ~2.5 at%) is much lesser than that of N (by ~6 at%).

A possible reason for this segregation could be the low solubility of the segregated elements in the host material Ru. Or in other words, the segregated element is immiscible with the host material. The element which is being expelled from the host lattice during thermal annealing may segregate towards defect sites such as (i) grain boundary (ii) free surface or (iii) interface. N is immiscible in Ru since Ru is not known to form a stable nitride. Hence, it could be expected that the N atoms in the Ru-W-N film could attempt to bond with W to form W-nitride. Upon annealing, N and/or W-nitride are being expelled from the Ru lattice as the consequence of Ru crystallization. Hence, the concentration of N and/or W-nitride at Ru grain boundary could become higher than that in the Ru grain. Additionally, it must be noted that the segregation is towards the film/substrate interface and not towards Ru surface. This can be explained in terms of the higher affinity of N to Si than Ru or W (ΔH_f^0 (W_2N) = -17 kcal/mole, ΔH_f^0 (Si_3N_4) = -178 kcal/mole [124], ΔG_f^0 (W-N) = -290.49 ± 18.85 kJ, ΔG_f^0 (Si-N) = -326.10 ± 125.52 kJ [102]). Although a stable native SiO_2 is present at interface, possibly there are some Si dangling bonds which may provide a driving force for the N segregation towards the interface. Since N also has certain affinity to W, it is likely that the segregation of N towards interface

also lead to some W diffusion towards the same interface in an attempt to be attached to N because of its higher affinity to N than Ru. This might lead to actual nitride formation, at least, as atomic clusters if not as a separate, distinct phase. Hence, W-N bonds must first be dissociated in order for the N to react with Si at the interface. Conversion of W-nitride into pure W in Ru-W-N film was observed to occur at temperature of ~500°C – 600°C as discussed previously in Section 6.4.2. Hence, with higher anneling temperature, more free N will be available at the interface to react with Si. This explains the growth of the dark layer at interface with annealing.

In order to further confirm the enrichment of N or WN_x at the film/substrate interface, chemical analyses with depth profiling were done using techniques such as XPS, SIMS, and RBS. However, XPS and SIMS data could not give clear evidence of any enrichment of N or W at film interface. This maybe because the layer of interest is too thin (< 5 nm) as can bee seen from the TEM micrographs in Figure 6.28, hence could be easily etched away during the depth profiling process although a slow etching rate was employed. Ion etching might also cause some changes in matrix composition [125]. This might lead to insensitivity of XPS and SIMS techniques especially when the segregation is not very strong. RBS technique appears to give a better sensitivity and resolution for low enrichment. No film etching is necessary for RBS analysis hence, the film composition is expected to be un-changed during the analysis. Since the layer of interest is very thin (< 5 nm) and the total layer thickness is relatively thick (~120 nm), the detector was positioned at 65° from normal direction (instead of using the normal procedure to position the detector at 10° from the normal direction) during RBS detection so that He^+ ions would travel

longer inside the film of interest. Figure 6.30 shows the RBS data obtained on as-deposited and annealed Ru-W-N/Si samples.

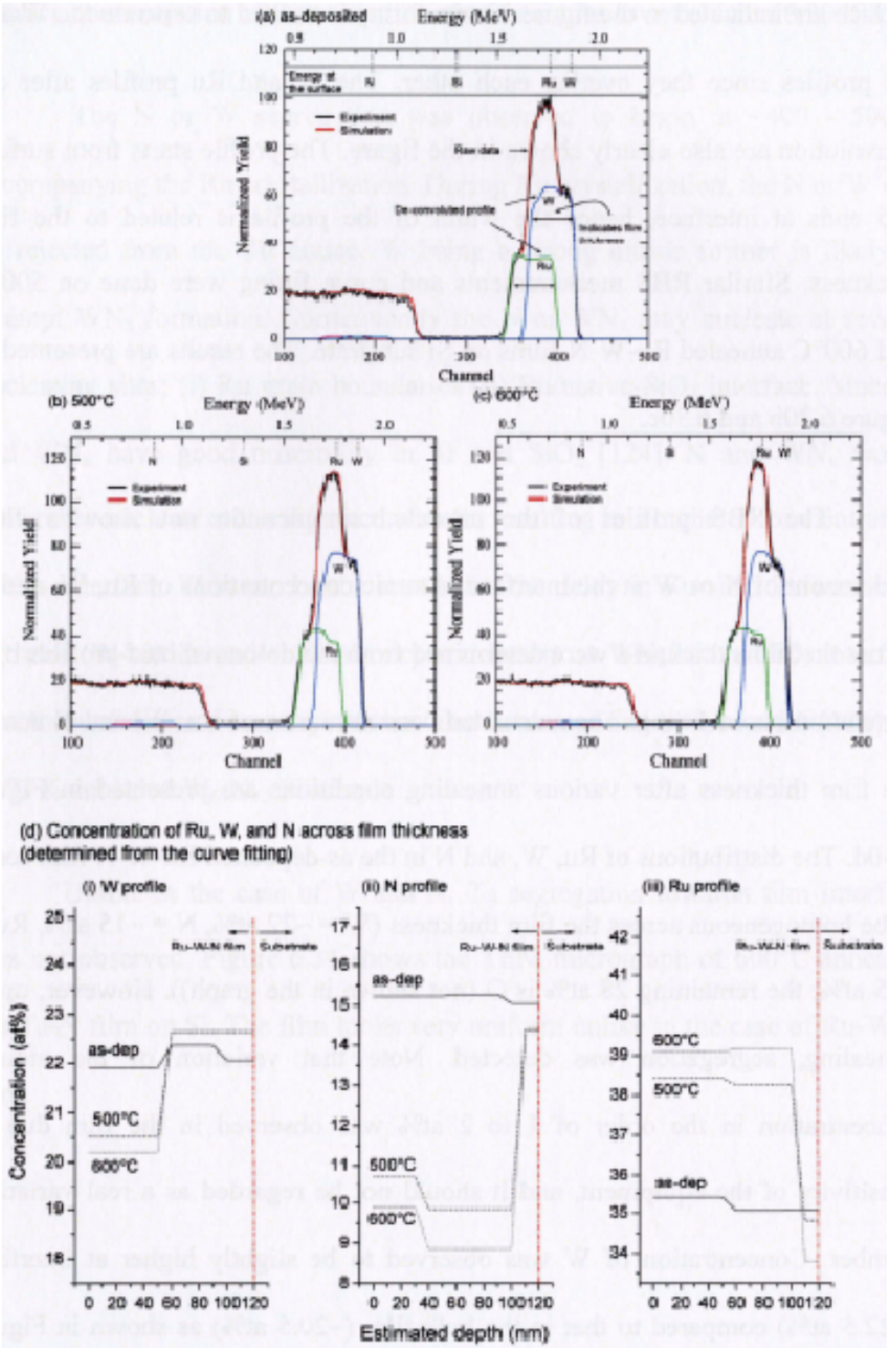

Figure 6.30 RBS spectra of Ru-W-N (N_2 = 10 sccm)/Si film (a) as-deposited (b) after 500°C (c) 600°C annealing (d) concentration profile of Ru, W, and N across the film thickness at various annealing conditions (obtained from the curve fitting of RBS profiles in (a)-(c))

Figure 6.30a shows the RBS profile of as-deposited Ru-W-N film on Si. The backscattered ion energies coming from Ru, W, Si, and N present in sample surface are indicated in the figure. Curve fitting is needed to separate the W and Ru profiles since they overlap each other. The W and Ru profiles after de-convolution are also clearly shown in the figure. The profile starts from surface and ends at interface, hence the width of the profile is related to the film thickness. Similar RBS measurements and curve fitting were done on 500°C and 600°C annealed Ru-W-N films on Si substrate. The results are presented in Figure 6.30b and 6.30c.

The RBS profiles of the annealed samples do not show a clear enrichment of N or W at the interface. Atomic concentrations of Ru, W, and N across the films thickness were determined from the de-convoluted profiles by a simulation-based fitting. The calculated concentrations of Ru, W, and N across the film thickness after various annealing conditions are presented in Figure 6.30d. The distributions of Ru, W, and N in the as-deposited Ru-W-N film seem to be homogeneous across the film thickness (W = ~22 at%, N = ~15 at%, Ru = ~35 at%, the remaining 28 at% is O (not shown in the graph)). However, upon annealing, segregation was detected. Note that variation of the atomic concentration in the order of 1 to 2 at% was observed in the film due to sensitivity of the equipment, and it should not be regarded as a real variation number. Concentration of W was observed to be slightly higher at interface (~22.5 at%) compared to that in the bulk film (~20.5 at%) as shown in Figure 6.30d(i). The total amount of N was found to decreases after anneling as shown in Figure 6.30d(ii), in agreement with previous XPS study showing N out diffusion. Additionally, it was observed that the concentrations of N at film

interface (14 at%) are higher than that inside the bulk film (~10 - 11 at%). As the consequence of W and N enrichment at interface upon annealing, the relative concentration of Ru at that interface becomes lower (Figure 6.30d(iii)).

The N or W segregation was observed to begin at ~400 - 500°C accompanying the Ru crystallization. During Ru crystallization, the N or W will be rejected from the Ru lattice. W being a strong nitride former is likely to attempt WN_x formation. Consequently the N or WN_x may nucleate at several nucleating sites; (i) Ru grain boundaries (ii) Ru/native-SiO_2 interface. Since N and WN_x have good miscibility in Si and SiO_2 [124], N and WN_x would preferably nucleate at the interface with Si, resulting in a higher N concentration at this interface. This can be the reason for the delay in Ru-silicide formation. Nitrides (W-nitride and/or Si-nitride) enrichment at WN_x/native-SiO_2 interface in a form of discrete nanocrystals has also been reported by Lee *et al.* [126] for 1273 K annealed $W_{67}N_{33}$/Si sample.

Unlike in the case of W and N, Ta segregation towards film interface was not observed. Figure 6.31 shows the TEM micrograph of 600°C annealed Ru-Ta-N film on Si. The film looks very uniform unlike in the case of Ru-W-N film.

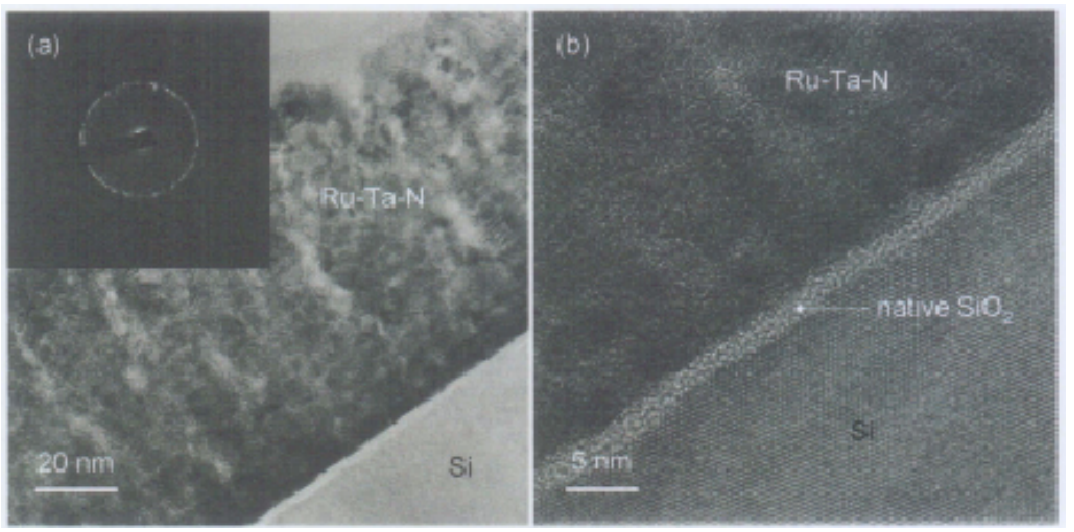

Figure 6.31 TEM micrographs of Ru-Ta-N/Si after 600°C annealing (a) low resolution micrograph with its SAD pattern, showing polycrystalline film (b) higher resolution micrograph, showing uniform interface

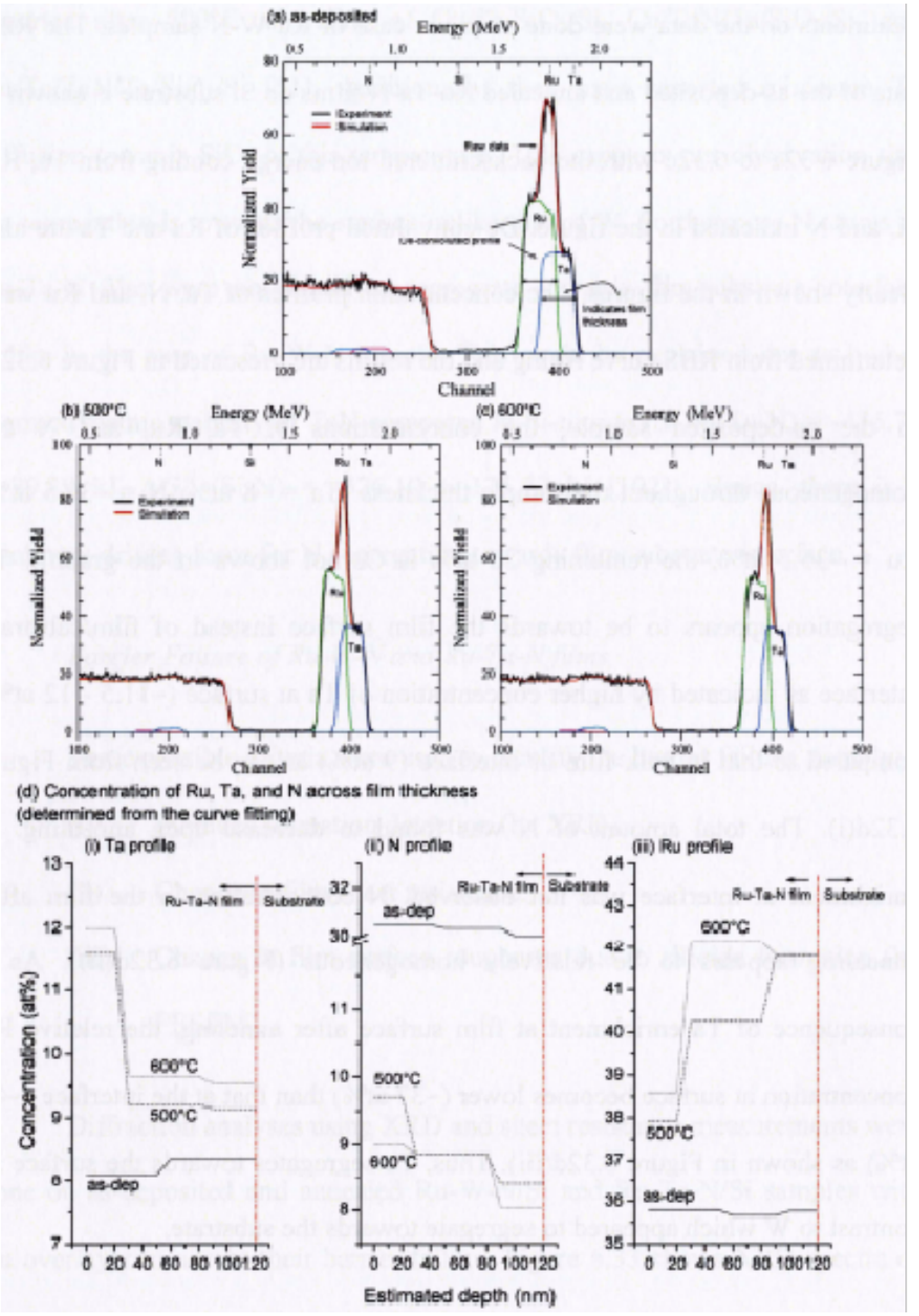

Figure 6.32 RBS spectra of Ru-Ta-N (N_2 = 10 sccm)/Si film (a) as-deposited (b) after 500°C (c) 600°C annealing (d) concentration profile of Ru, Ta, and N across the film thickness at various annealing conditions (obtained from the curve fitting of RBS profiles in (a)-(c))

To verify the elements distribution, RBS measurements and analyses were also done on these set of films before and after annealing. Similar

treatments on the data were done as in the case of Ru-W-N samples. The RBS data of the as-deposited and annealed Ru-Ta-N films on Si substrate is shown in Figure 6.32a to 6.32c with the backscrattered ion energy coming from Ta, Ru, Si, and N indicated in the figure. De-convoluted profiles of Ru and Ta are also clearly shown in the figures. The concentration profiles of Ta, N, and Ru were determined from RBS curve fitting and the results are presented in Figure 6.32d. In the as-deposited sample, the concentrations of Ta, Ru, and N are homogeneous throughout the sample thickness (Ta = ~8 at%, N = ~30.5 at%, Ru = ~35.5 at%, the remaining 26 at% is O (not shown in the graph)). Ta segregation appears to be towards the film surface instead of film/substrate interface as indicated by higher concentration of Ta at surface (~11.5 - 12 at%) compared to that in bulk film or interface (9 at%) as can be seen from Figure 6.32d(i). The total amount of N was found to decrease upon annealing. N enrichment at interface was not observed. N concentration in the film after annealing appears to be relatively homogeneous (Figure 6.32d(ii)). As a consequence of Ta enrichment at film surface after anneling, the relative Ru concentration at surface becomes lower (~37 at%) than that at the interface (~40 at%) as shown in Figure 6.32d(iii). Thus, Ta segregates towards the surface in contrast to W which appeared to segregate towards the substrate.

Oxygen on the outer surface could provide a driving force for diffusion of Ta which depends primarily on its affinity for oxygen. The Gibb's free energy of formation, ΔG_f^0, of Ta_2O_5 is -763.77 ± 20.92 kJ, being much more negative than that of WO_3 = -504.67 ± 20.92 kJ [102]. Hence, compared to W, Ta has a higher tendency to react with oxygen from ambient to form Ta_2O_5. Diffusion of Ta towards Cu surface followed by formation of Ta_2O_5 has been

reported after 500°C annealing of Cu/Ta/SiO_2/Si, Cu/TaN/Ta/SiO_2/Si, and Cu/Ta/TaN/Ta/SiO_2/Si [51]. Additionally, they have reported minimum Ta diffusion towards SiO_2 at this temperature. This supports our observation that Ta segregation is towards the surface unlike that of W. Furthermore N atoms in Ru-Ta-N film were not found to segregrate towards film/substrate interface unlike in the case of Ru-W-N sample. This could be explained due to higher thermodynamic stability of TaN compared to Si-nitride (ΔG_f^0 (Ta-N) = -435.74 ± 29.29 kJ, ΔG_f^0 (Si-N) = -326.10 ± 125.52 kJ [102]). Hence, there is a minimum driving force for N segregation towards film/substrate interface.

E. Barrier Failure of Ru-W-N and Ru-Ta-N films

Three possible criteria were used to identify the barrier failure, namely:

(i) Silicides formation detection (by XRD).

(ii) Change in film sheet resistance.

(iii) Change in film surface roughness due to silicide formation (by FESEM).

Diffraction analyses using XRD and sheet resistance measurements were done on as-deposited and annealed Ru-W-N/Si and Ru-Ta-N/Si samples with Cu overlayer to access their barrier failure. Figure 6.33 shows XRD spectra of Cu/Ru-W-N/Si (N_2 = 10 sccm) samples under different annealing conditions. As-deposited sample and those annealed up to 600°C (Figure 6.33) only show Cu peaks at 2θ = 43.3° and 50.4°. However, after 700°C of annealing, hexagonal Ru peaks start to appear in addition to reduction of the Cu peak intensity at 43.3°. The Ru peaks could possibly be present in 600°C annealed sample, since Ru crystallization begins at ~600°C as discussed in Section 6.4.3.

Hence, 700°C could be an onset temperature for barrier failure, initiated by Cu diffusion through a crystallized Ru-W-N barrier. Once Cu reached Si, it would be converted into Cu-silicide. Complete barrier breakdown was observed at 800°C when Ru_2Si_3 + Cu_3Si + WSi_2 were formed.

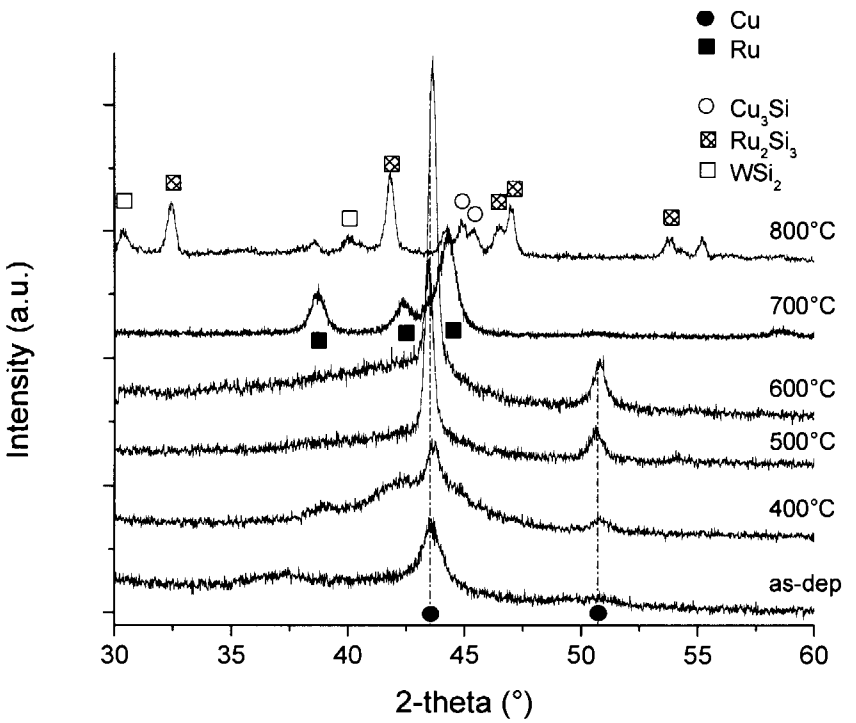

Figure 6.33 XRD spectra of Cu/Ru-W-N/Si (10 sccm N_2) sample after varying annealing conditions

Figure 6.34 shows XRD spectra of Cu/Ru-Ta-N/Si (N_2 = 10 sccm) samples under different annealing conditions. As deposited samples up to 600°C mainly show Cu peaks. Ru peaks start to appear after 600°C without a decrease in Cu peaks intensity. Note that the Ru peaks are relatively weak, indicating that the film might still be amorphous or nanocrystalline. Cu peaks continue to increase in intensity up to 600°C, signifying Cu grain growth. Cu diffusion into Ru-Ta-N barrier up to this temperature is probably minimal.

Barrier failure was initiated by formation of Ru_2Si_3 and Cu_3Si at 700°C, followed by $TaSi_2$ at 800°C.

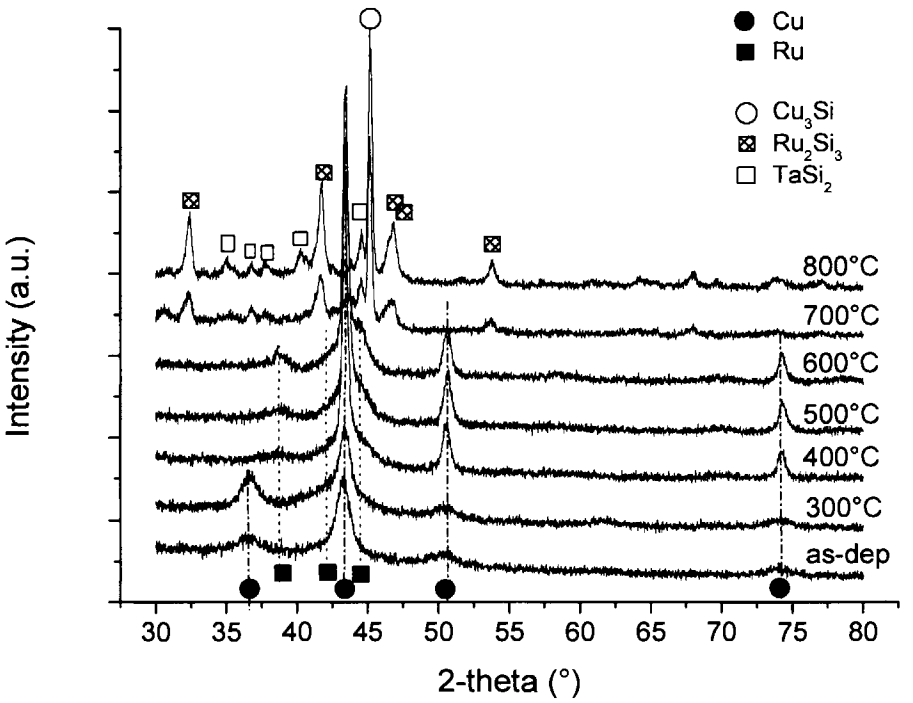

Figure 6.34 XRD spectra of Cu/Ru-Ta-N/Si (10 sccm N_2) sample after varying annealing conditions

To give a clearer comparison of barrier failure of Ru-W-N and Ru-Ta-N films with that of pure Ru and Ru-N films, Table 6.12 lists the silicides detection temperature by XRD for those barrier films. Ru_2Si_3 formation temperature is ~700°C for pure Ru, Ru-N, and Ru-Ta-N films. Although Ru_2Si_3 is only detected after 800°C in Ru-W-N sample, Cu diffusion as indicated by a decrease in Cu(111) peak intensity is clearly observable after 700°C of annealing. Cu_3Si formation can occur simultaneously with Ru_2Si_3 (in Ru-N and Ru-W-N samples) or at a higher temperature (in pure Ru and Ru-Ta-N samples).

Table 6.12 Silicide detection temperatures for pure Ru, Ru-N, Ru-W-N, and Ru-Ta-N (w Cu overlayer) in °C

	pure Ru	Ru-N	Ru-W-N	Ru-Ta-N
Ru_2Si_3	700	700	800	700
Cu_3Si	800	700	800	700
WSi_2	-	-	800	-
Ta_2Si	-	-	-	800

Figure 6.35 shows changes in sheet resistance of Cu/Ru-W-N/Si and Cu/Ru-Ta-N/Si (N_2 = 10 sccm) as a function of annealing temperature together with that of Cu/Ru/Si and Cu/Ru-N/Si for comparison. The sheet resistance of the Cu/Ru-W-N/Si sample starts to increase slightly after annealing at 700°C due to diffusion of Cu into the crystallized Ru-W-N film, decreasing the total conductive layer thickness. The sheet resistance of Cu/Ru-W-N/Si increases significantly after annealing at 800°C whereas that of Cu/Ru-Ta-N/Si samples at 700°C. Cu/Ru/Si and Cu/Ru-N/Si samples show increase in sheet resistance after 700°C. It is to be noted that the temperatures where the sheet resistance increases significantly are the same as the temperatures where silicide formation is first observed by XRD. This indicates that the increase in sheet resistance is caused by the loss of Cu due to copper silicide formation. From the sheet resistance measurement, it is shown that Ru-W-N film has a better stability compared to the others. This could be due to the presence of segregated N and/or WN_x at interface which delay the silicides formation.

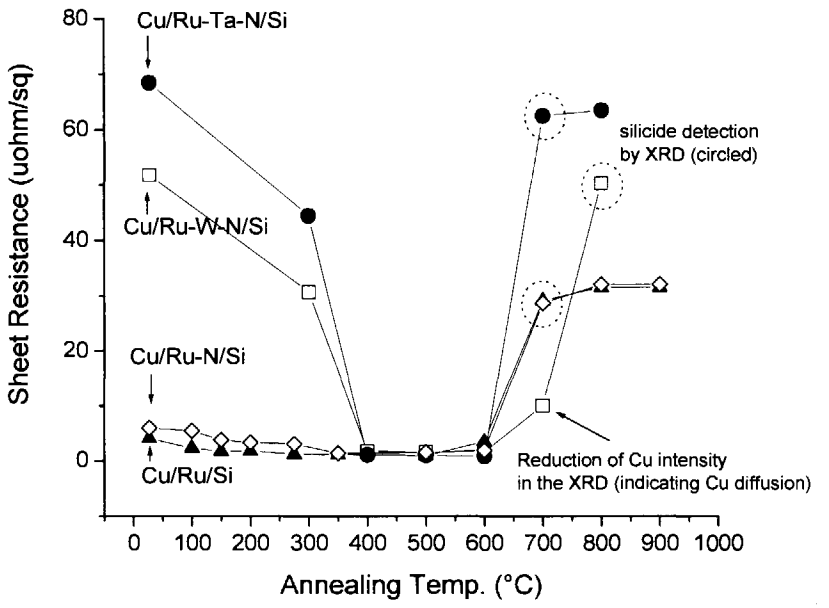

Figure 6.35 Sheet resistance of Cu/Ru/Si, Cu/Ru-N/Si, Cu/Ru-W-N/Si (N_2 = 10 sccm) and Cu/Ru-Ta-N/Si (N_2 = 10 sccm) samples after varying annealing conditions

Figure 6.36 shows FESEM micrographs of Cu/Ru-W-N/Si surface after different annealing conditions. The sample surface is smooth up to 600°C. After 700°C of annealing, bright round particles with a size ranges from 0.8 to 1.3 μm were observed uniformly on the sample surface. These particles are likely the initiation of Cu-silicide formation. Cracks are observed on film surface when large Cu_3Si particles form destroying the Ru-W-N film. The cracks seem to grow to become holes/voids as the Cu-silicide continues to enlarge with higher annealing temperature. After 800°C, several particles with different contrast appear on the whole sample surface giving a rough texture to the surface. These particles are possibly the different silicides (Ru-, W-, and Cu-silicides). FESEM observations agree well with XRD data showing that some Cu diffusion, indicated by reduction in Cu diffraction intensity, occured at 700°C, followed by Ru_2Si_3 + Cu_3Si + WSi_2 formation at 800°C.

Figure 6.37 shows the FESEM of Cu/Ru-Ta-N/Si sample surfaces after different annealing conditions. The changes in the surface morphology caused by the formation of silicides are quite similar compared to Cu/Ru-W-N/Si samples. The sample surface is still intact up to 600°C. After 700°C annealing, holes/voids were observed on the film surface with bright particles inside. The particles become bigger at higher temperature. However, the film on top of the particles looks more uniform compared to the Ru-W-N surface at the same temperature of 800°C. The voids observed in 800°C annealed Ru-W-N and Ru-Ta-N films shown in Figure 6.36d and 6.37d could be deformation of the film surface caused by subsurface growth of silicide particles. When the silicide particles grow and become large, cracking could occur to relieve the film stress. Sharp cracks are unstable and hence, could get rounded into voids at higher temperature ("defect related void formation"). Further increase in temperature would accelerate the growth of the voids to reduce surface/interface energy.

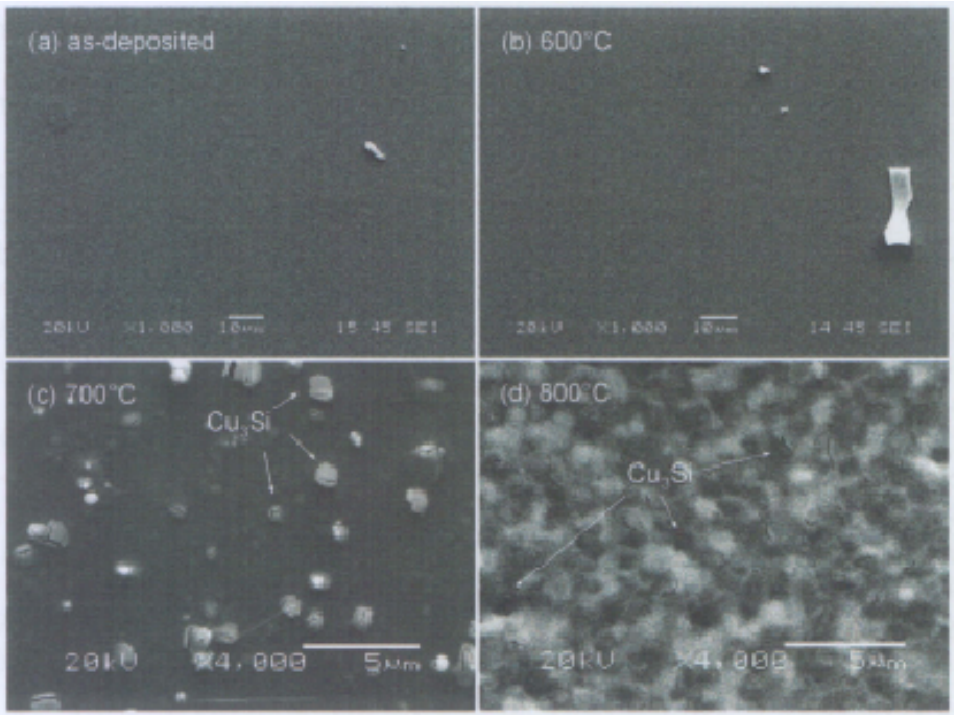

Figure 6.36 FESEM micrographs of Cu/Ru-W-N/Si (N_2 = 10 sccm) under different annealing conditions

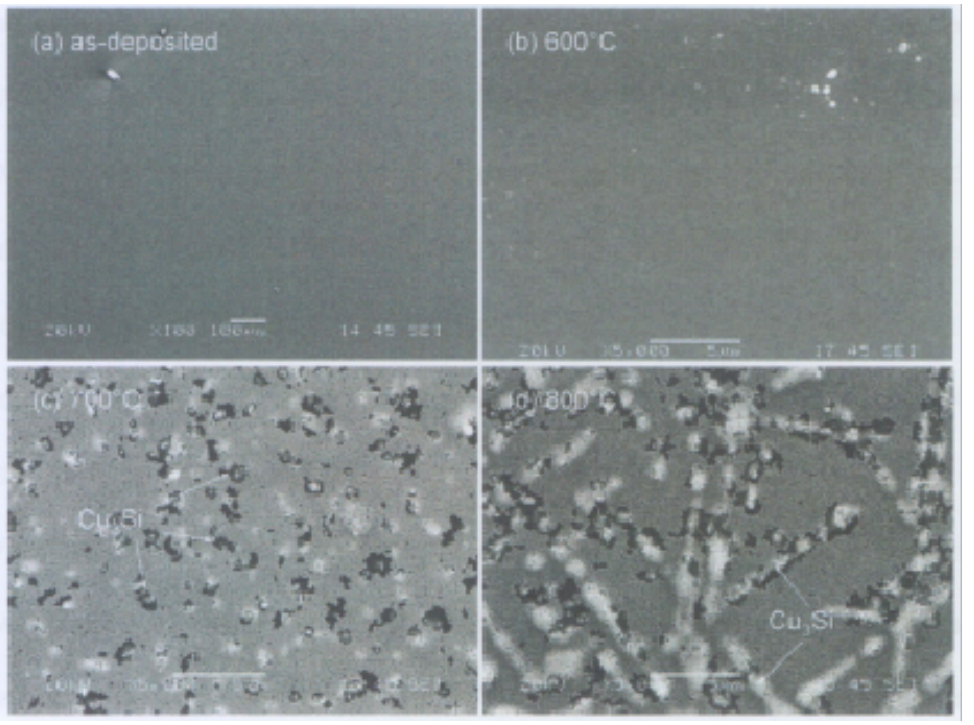

Figure 6.37 FESEM micrographs of Cu/Ru-Ta-N/Si (N_2 = 10 sccm) under different annealing conditions

From XRD, sheet resistance, and FESEM analyses, different barrier failure mechanisms could be deduced for Ru-W-N and Ru-Ta-N films. Barrier failure of Ru-W-N film was initiated by crystallization of Ru as a consequence of N-release at ~500°C - 600°C. Cu diffusion through crystallized Ru-W-N film was observed to begin at 700°C as observed from the XRD data. Cu diffusion was then followed by formation of Cu-silicide together with Ru- and W-silicides at 800°C, destroying the barrier layer. However, in the case of Ru-Ta-N, most of N was released at slightly higher temperature of ~600°C. This is possibly due to higher stability of Ta-N bond (ΔG_f^0 (300 K) = -435.74 ± 29.29 kJ) compared to W-N bond (ΔG_f^0 (300 K) = -290.49 ± 18.85 kJ) [102]. Ru crystallization in Ru-Ta-N film occurs accompanying the N release. The barrier failure of Ru-Ta-N film was initiated by formation of Ru_2Si_3 + Cu_3Si at 700°C followed by formation of Ta_2Si at 800°C. If we consider a maximum working temperature of a barrier as 50°C lower than the silcide formation temperature, it can be concluded that the maximum working temperature of Ru-W-N is ~750°C and that of Ru-Ta-N is ~650°C. This maximum working temperature is similar as in the case of pure Ru (650°C); however, Cu diffusion is expected to be slower in Ru-W-N and Ru-Ta-N films due to their amorphous microstucture. The amorphous Ru-W-N and Ru-Ta-N films are also thermally more stable compared to that of Ru-N film where N-out diffusion and void nucleation was observed to occur at very low temperature of 275°C, although the silicides were formed only after 700°C. Hence, Ru-W-N and Ru-Ta-N are effective diffusion barriers against Cu and can be considered viable candidates for a future Cu diffusion barrier.

6.4 Summary of Results

The aim of this part of the work is to retain the N dissolved in Ru to temperatures higher than 275°C by alloying with element of high N affinity. Film stacks containing Cu/Ru-W-N/Si and Cu/Ru-Ta-N/Si made by co-sputtering technique were examined. Depending on the N_2 flow rate during deposition (0 - 15 sccm), the resulted film composition of Ru-W-N is 33 - 41 at% of Ru, 18.5 - 28 at% of W, 0 - 20.6 at% of N, and 28 - 31 at% of O whereas that of Ru-Ta-N is 36 - 44 at% of Ru, 9 - 30 at% of Ta, 0 - 30 at% of N, and 25 - 26 at% of O. Effect of N_2 flow rate on film deposition rate, resistivity and microstructure were assessed initially. An extensive study of the chemical nature of N in these films and its distribution were done as this was imperative to explain the results. The conclusions that could be drawn are:

- Film deposition rate was dependent on nitride formation on the W or Ta targets during deposition. When co-sputtered with W target to produce Ru-W films, the deposition rate increased as N_2 flow rate is increased. Whereas for Ru-Ta co-sputtering with Ta target, deposition rate decreased as N_2 flow rate increased. This is due to the formation of TaN_x on the Ta target surface.
- The resistivity of the films increased as N_2 flow rate during sputtering increased. This is due to nitride formation with W/Ta or N dissolution in the alloy. The resistivity of the Ru-W-based films was in the range of 700 - 5100 μΩ.cm while that of Ru-Ta-based films was in the range of 1300 - 5700 μΩ.cm.
- The Ru-W-N and Ru-Ta-N films were amorphous as the Ru-N film.

- The resistivity of the films decreased with increase of annealing temperature and a large decrease was observed at about 400°C. Note a similar decrease was obtained for Ru-N film in Chapter 5 at 275°C. This sharp decrease is attributed to N release and the accompanied Ru crystallization, as for Ru-N films. This phenomenon occurs at a higher temperature in these alloyed films when compared with unalloyed Ru-N, indicating a higher thermal stability of the amorphous structure of these films.
- Nitrogen atoms in these alloyed films are bound to W/Ta and exist in the form of nitrides. In Ru-W-N, W_2N was the dominant nitride state of the N while in Ru-Ta-N, TaN was the main nitride state. However, no nitride phases were identifiable in XRD spectra or in TEM investigations.
- Enrichment of N and W at the film/substrate interface was observed in annealed Ru-W-N by TEM/EDX and further confirmed by RBS depth profiling. Hence, a bilayer structure of a Ru-rich layer on top and a N- or WN_x-rich layer adjacent to the substrate were self-formed during thermal annealing. The N- or WN_x-rich layer has a darker contrast in the TEM micrographs and its thickness appears to increase with increase of annealing temperature.
- Annealed Ru-Ta-N films do not show any N or Ta enriched self-formed layers as in the case of Ru-W-N films. Evidence was noted for Ta segregation towards the film surface instead of the film/substrate interface. This is attributed to the high tendency of Ta to form Ta_2O_5 surface oxide. Additionally, the higher affinity of N to Ta than to Si

prevents the N segregation towards the film/substrate interface, unlike in the case of Ru-W-N.

- Disintegration of W_2N phase into W^0 + N occurs upon annealing in the range 500 - 600°C whereas the disintegration of TaN phase into Ta^0 + Ta_2N was observed to occur at the slightly higher temperature of 600°C. This temperature signifies the N release from the nitride phases which will adversely affect the barrier performance.
- Ru crystallization in Ru-W-N and Ru-Ta-N films occurs at a temperature range similar to that of N release from the nitride phases.
- Silicide formation is concurrent with rapid Cu diffusion. In the Ru-W-based film, Cu diffusion was observed upon annealing at 700°C followed by Ru_2Si_3 + Cu_3Si + WSi_2 formation at 800°C; on the other hand, in Ru-Ta-based film, both Cu_3Si and Ru_2Si_3 formed simultaneously at 700°C followed by $TaSi_2$ at 800°C, as observed by XRD.
- Sheet resistance measurement and FESEM study show similar barrier failure temperatures of 700°C for both Ru-W-N and Ru-Ta-N films.
- Therefore, Ru-W-N and Ru-Ta-N films are stable up to about 650°C and thus are potential candidates for Cu barrier application.

Table 6.13 summarizes the films properties in as-deposited state and after thermal annealing.

Table 6.13 Summary of as-deposited and annealed Ru-W- and Ru-Ta-based films properties

				Ru-W-N				Ru-Ta-N		
				N = 0	N = 5	N = 10	N = 15	N = 0	N = 5	N = 10
as-deposited	Film composition			Ru W	Ru W W_2N	Ru W_2N	Ru W_2N excess N	Ru Ta	Ru TaN	Ru TaN
	Resistivity (μΩ.cm)			~700	~1500	~2800	~5100	~1300	~2600	~5700
	Microstructure			polycryst (columnar)	nanocryst.	nanocryst + amorphous	amorphous	nanocrys.	nanocryst + amorphous	amorphous
Under thermal annealing	Onset of Ru crystallization (°C)			-	-	500 - 600	600	-	-	600
	N release temp. (°C)			-	-	W_2N → W 500 - 600	-	-	-	TaN → Ta_2N + Ta 600
	Silicide formation temperature (°C)	w/o Cu	Ru_2Si_3	-	-	> 900	-	-	-	> 900
		w/Cu	Ru_2Si_3	-	-	800	-	-	-	700
			Cu_3Si	-	-	800	-	-	-	700
			WSi_2	-	-	800	-	-	-	-
			$TaSi_2$	-	-	-	-	-	-	800

CHAPTER 7

CONCLUSIONS AND RECOMMENDATIONS

7.1 Summary of Results

Different Ru-based barrier materials namely pure Ru, Ru-N, Ru-W-N and Ru-Ta-N were studied for barrier application in Cu interconnects. The summaries drawn from the previous chapters are recapitulated in this chapter.

In the initial part of this work, the effects of Ru underlayer on the texture and surface roughness of Cu films, the diffusion barrier properties of Ru, and its adhesion to low-κ were investigated using sample stacks of Cu/Ru/low-κ, Cu/Ru/Ta/low-κ and the control sample of Cu/Ta/low-κ. Conclusions that could be drawn from this part of the work are:

- Ru promotes a more pronounced Cu(111) texture than Ta when their thicknesses are similar. This could be attributed to the lower lattice mismatch (~4 - 5%) between the Cu(111) plane and Ru(101) or Ru(002) planes compared to that of Ta(002) (~10%). Further, the degree of texture appears to increase with increase of the Ru layer thickness.
- Physical vapor deposited Cu films on both Ru and Ru/Ta layers are adequately smooth with RMS roughness of ~0.8 - 1.4 nm. This is independent on Ru thickness as well as those of layers underneath.
- Significant penetration of Cu and Ru into low-κ occurs at temperature as low as 300°C, indicating that Ru is not an effective diffusion barrier layer. Additionally, XPS study shows no interfacial reaction in

Cu/Ru/low-κ sample upon annealing as indicated by negligible shifts in the binding energies of the elements.

- The adhesion strength of Ru/low-κ interface is approximately 6 J/m^2 which is similar to that of Ta/low-κ interface (~6.5 J/m^2). The slight difference in the adhesion strength is attributed to the better bonding between the Ta film and the low-κ substrate, as indicated by formation of Ta-O and Ta-C bonds at Ta/low-κ interface. To the contrary, less Ru-O and Ru-C bonds were detected at Ru/low-κ interface.
- The low-κ interface i.e. Ru/low-κ and Ta/low-κ, appears to be the weakest interface in the stacks which led to delamination in four-point bend tests.

Subsequently, breakdown of the pure Ru diffusion barrier was investigated experimentally in detail using Cu/Si, Ru/Si, and Cu/Ru/Si stacks as they are exposed to high temperatures, for Ru thicknesses of 10 - 30 nm. This part of the work leads to the following conclusions:

- Without the presence of Ru barrier layer, the Cu/Si sample fails at temperature as low as 200°C as signified by ~16 times increase in sheet resistance although FESEM and XRD studies indicate Cu_3Si formation only after annealing at 300°C and 500°C respectively.
- Without the presence of Cu overlayer, Ru_2Si_3 formation in the Ru/Si sample was observed to occur after 700°C of annealing as examined by both sheet resistance and XRD methods.
- In the Cu/Ru/Si sample, microstructural evidence for barrier failure, in the form of triangular-prismatic Ru_2Si_3 phase, becomes detectable in

FESEM and XRD when annealed at 700°C. Thereafter, Cu diffusion accelerates through Ru and Ru_2Si_3 layers leading to rapid deterioration in the conductivity of the metallization. Eventually, Cu_3Si phase was observed to form at 800°C.

- Sheet resistance measurements in Cu/Ru/Si sample shows a slight increase in sheet resistance after 600°C of annealing which is attributed to the Cu and Ru diffusion, followed by a sharp increase after 700°C which is attributed to the silicide formation.
- The early sign of barrier failure detected by sheet resistivity measurements at 600°C is worth noting. Thus, sheet resistivity measurement could be a very useful tool to determine the health of the barrier layer.
- TEM study in Cu/Ru/Si sample shows that the Cu_3Si phase nucleates on the native oxide film on Ru/Si interface and grows into the substrate. To the contrary, Ru_2Si_3 grows into the Ru layer. The difference in the silicide growth direction is attributed to the different diffusing species i.e. Cu is the diffusing species in Cu_3Si formation whereas Si is the diffusing species in the Ru_2Si_3 formation.
- This interface reaction sequence is independent of the Ru layer thickness for the thickness range investigated (10 - 30 nm), indicating that the diffusion of Cu through Ru_2Si_3 is the likely rate controlling step, not diffusion through the Ru itself.

N dissolution in Ru was experimented to improve the barrier properties of pure Ru in the second phase of the project. Barrier performance of stacks of Ru-N/Si and Cu/Ru-N/Si were assessed by exposing to high temperatures and

were compared to that of pure Ru stacks. The conclusions that could be drawn from this part of the work are:

- Ru sputter deposited in N_2 gas (Ru-N) results in a layer whose microstructure consists of a mixture of amorphous and nanocrystalline phases with ~8 - 10 at% N uniformly distributed in the film, whereas Ru sputter deposited in Ar gas (pure Ru) exhibits a columnar grained microstructure, in the as-deposited state.
- Sheet resistance of Ru-N film is about ten times higher than that of Ru but on annealing at 275°C, it reduces sharply to that of pure Ru, indicating a loss of N from the layer.
- XPS study shows that diffusion of Cu through Ru-N film is slower than in pure Ru at all temperatures.
- XRD study shows that formation of Ru_2Si_3 occurs at 900°C in Ru-N film which is 200°C higher than in pure Ru.
- Annealing at temperatures $\geq$ 275°C causes N out-diffusion concomitant with crystallization of Ru. The rejected N atoms nucleate N_2 gas bubbles at the Cu/Ru interface. It grows to a size range of ~20 - 30 nm and is easily observable as voids in the TEM. These will adversely affect the Cu/Ru interface adhesion.
- Grain growth in Ru-N is constrained up to 275°C. Annealing at higher temperatures, when N has been removed from solution, the grain growth behaviour returns to that of pure Ru.
- The improved barrier performance of Ru-N is possibly caused by its amorphous structure. Heating to temperatures above 275°C causes

crystallization of Ru leading to deterioration of the barrier property to the levels of pure Ru.

In the third phase of the work, alloying Ru-N film with an element of high N affinity was experimented to retain the N in solution to temperatures higher than 275°C. Film stacks containing Cu/Ru-W-N/Si and Cu/Ru-Ta-N/Si made by co-sputtering technique were examined. Depending on the N_2 flow rate during deposition (0 - 15 sccm), the chemical composition of the resulting film varied. The chemical composition of the Ru-W-N films were in the range: 33 - 41 at% of Ru, 18.5 - 28 at% of W, 0 - 20.6 at% of N, and 28 - 31 at% of O whereas those of Ru-Ta-N were 36 - 44 at% of Ru, 9 - 30 at% of Ta, 0 - 30 at% of N, and 25 - 26 at% of O. Effects of N_2 flow rate on film deposition rate, resistivity and microstructure were assessed initially. An extensive study of the chemical nature of N in these films, and its distribution, were done as this was imperative to explain the results. The conclusions that could be drawn are:

- Film deposition rate was dependent on nitride formation on the W or Ta targets during deposition. When co-sputtered with W target to produce Ru-W films, the deposition rate increased as N_2 flow rate is increased. Whereas for Ru-Ta co-sputtering with Ta target, deposition rate decreased as N_2 flow rate increased. This is due to the formation of TaN_x on the Ta target surface.
- The resistivity of the films increased as N_2 flow rate during sputtering increased. This is due to nitride formation with W/Ta or N dissolution in the alloy. The resistivity of the Ru-W-based films was in the range of

700 - 5100 μΩ.cm while that of Ru-Ta-based films was in the range of 1300 - 5700 μΩ.cm.

- The Ru-W-N and Ru-Ta-N films were amorphous as the Ru-N film.
- The resistivity of the films decreased with increase of annealing temperature and a large decrease was observed at about 400°C. Note a similar decrease was obtained for Ru-N film in Chapter 5 at 275°C. This sharp decrease is attributed to N release and the accompanied Ru crystallization, as for Ru-N films. This phenomenon occurs at a higher temperature in these alloyed films when compared with unalloyed Ru-N, indicating a higher thermal stability of the amorphous structure of these films.
- Nitrogen atoms in these alloyed films are bound to W/Ta and exist in the form of nitrides. In Ru-W-N, W_2N was the dominant nitride state of the N while in Ru-Ta-N, TaN was the main nitride state. However, no nitride phases were identifiable in XRD spectra or in TEM investigations.
- Enrichment of N and W at the film/substrate interface was observed in annealed Ru-W-N by TEM/EDX and further confirmed by RBS depth profiling. Hence, a bilayer structure of a Ru-rich layer on top and a N- or WN_x-rich layer adjacent to the substrate were self-formed during thermal annealing. The N- or WN_x-rich layer has a darker contrast in the TEM micrographs and its thickness appears to increase with increase of annealing temperature.
- Annealed Ru-Ta-N films do not show any N or Ta enriched self-formed layers as in the case of Ru-W-N films. Evidence was noted for Ta

segregation towards the film surface instead of the film/substrate interface. This is attributed to the high tendency of Ta to form Ta_2O_5 surface oxide. Additionally, the higher affinity of N to Ta than to Si prevents the N segregation towards the film/substrate interface, unlike in the case of Ru-W-N.

- Disintegration of W_2N phase into W^0 + N occurs upon annealing in the range 500 - 600°C whereas the disintegration of TaN phase into Ta^0 + Ta_2N was observed to occur at the slightly higher temperature of 600°C. This temperature signifies the N release from the nitride phases which will adversely affect the barrier performance.
- Ru crystallization in Ru-W-N and Ru-Ta-N films occurs at a temperature range similar to that of N release from the nitride phases.
- Silicide formation is concurrent with rapid Cu diffusion. In the Ru-W-based film, Cu diffusion was observed upon annealing at 700°C followed by Ru_2Si_3 + Cu_3Si + WSi_2 formation at 800°C; on the other hand, in Ru-Ta-based film, both Cu_3Si and Ru_2Si_3 formed simultaneously at 700°C followed by $TaSi_2$ at 800°C, as observed by XRD.
- Sheet resistance measurement and FESEM study show similar barrier failure temperatures of 700°C for both Ru-W-N and Ru-Ta-N films.
- Therefore, Ru-W-N and Ru-Ta-N films are stable up to about 650°C and thus are potential candidates for Cu barrier application.

7.2 Discussion of Key Results

7.2.1 Suitability of Ru and Its Alloy for Barrier/Seed Layer

Different Ru-based barrier materials have been studied for barrier/seed application in Cu interconnects. Their suitability for Cu seed application was assessed mainly based on their ability to promote smooth Cu surface, Cu(111) texture, and strong adhesion with dielectric layer which are listed in Table 7.1 in comparison with the currently used barrier material, Ta.

Table 7.1 Crystallographic texture, its effect on Cu texture and roughness, and adhesion energy of Ta and Ru-based films

Film	Substrate	Film texture		Effect on Cu overlayer		Adhesion energy to dielectric (J/m^2)
		as-dep	annealed	Cu(111) texture	smooth Cu surface	
Ta	Dielectric	Ta(002)	Ta(002)	x	√	~ 6.67
Pure Ru	Dielectric	Ru(101)	Ru(101)	√	√	~ 6 - 5.8
	Ta/dielectric	Ru(002)	Ru(002)	√	√	~ 6.5 - 4.3
	Si	Ru(002)	Ru(002)	√	√	-
Ru-N	Si	amorphous	Ru(101)	√	√	-
Ru-W	Si	Ru(002)	Ru(002)	√	√	-
Ru-W-N	Si	amorphous	Ru(101)	√	√	-
Ru-Ta	Si	amorphous	Ru(101)	√	√	-
Ru-Ta-N	Si	amorphous	Ru(101)	√	√	-

Generally Ru-based films are able to promote strong Cu(111) texture both in Ru(002) and Ru(101) texture due to low lattice mismatch with Cu compared to that of Ta. Additionally strong Cu(111) texture could be resulted in both crystalline and amorphous Ru. Crystallization of Ru from an initially amorphous state produces Ru with stronger Ru(101) texture instead of Ru(002). However both Ru(002) and Ru(101) has low lattice mismatch with Cu(111)

hence good adhesion with Cu. Furthermore deposition of Cu on different Ru-based films also result in smooth surface with RMS value < 2 nm. Ru adhesion to low-κ is reasonably high, comparable to that of Ta to low-κ.

Suitability of Ru-based material for Cu barrier application was assessed essentially based on their microstructure and thermal stability. Table 7.2 lists the microstructure of different Ru-based films (as-deposited).

Table 7.2 Microstructure of different Ru-based barrier film (as-deposited)

Film	**Gas flow rate (sccm)**	**Microstructure**
Pure Ru	Ar = 10	Columnar polycrystalline
Ru-N	N_2 = 10	Nanocryst + amorphous
Ru-W	Ar = 20	Columnar polycrystalline
Ru-W-N	Ar = 20, N_2 = 5	Nanocryst + amorphous
Ru-W-N	Ar = 20, $N_2 \geq 10$	Amorphous
Ru-Ta	Ar = 20	Nanocryst + amorphous
Ru-Ta-N	Ar = 20, $N_2 \geq 5$	Amorphous

Different microstructure could be resulted by having different deposition condition. Generally adding Nitrogen into the sputtering gas would promote development of more irregular/amorphous microstructure. This type of microstructure is preferred for diffusion barrier application due to the presence of minimum diffusion path (grain boundary). However amorphous film is metastable, it would eventually crystallize at higher temperature hence it is important to understand the crystallization temperature which in-turn was found to be related to the nitrogen release temperature from the film.

Table 7.3 list the N-release and crystallization temperature from an initially amorphous Ru-based films detected by several means.

Table 7.3 Ru crystallization & N-out diffusion temperature of different Ru-based films

	↓ Rs	XRD	SIMS	EELS	XPS	Remarks
Ru-N	275	275	275	275	-	Interstitial N diffuses out from Ru lattice
Ru-W-N (N_2 = 10 sccm)	400	500	500	-	700	W_2N converted into W
Ru-Ta-N (N_2 = 10 sccm)	400	500	500	-	>700	TaN converted into Ta_2N and Ta

It was observed that significant drop in sheet resistance could be used as the most sensitive yet easiest way to indicate film crystallization and N-release. Ru doped with N experienced N out diffusion at relatively low temperature (< 300°C) since Ru does not form strong bond with N. However by having nitride forming element incorporated into the films such as W and Ta, N-release temperature could be improved. When the Ru-X-N film was highly saturated with N, the excess interstitial N would get released initially during annealing at temperature of ~400°C. However the N which was bonded to W or Ta would only get released at relatively high enough temperature related to the bond dissociation energy of the W-N and Ta-N bonds.

Additionally it was observed that N release could result in voids formation. During annealing the N was expected to get released from the bulk film and went towards the film surface as well as to the interface. However voids were observed only at the Ru film surface or Cu/Ru film interface (if the film has Cu overlayer) and no voids were observed at Ru/substrate interface because the N might just bond with the native SiO_2 to form Si-oxynitride. Furthermore voids were formed at much higher temperature in Ru-X-N film compared to Ru-N film due to the strong nitride bonding as shown in Table 7.4.

Table 7.4 Void formation temperature of different Ru-based films

	Temp. (°C)	Detection method
Ru-N in Cu/Ru-N/Si stack	275	Cu/Ru interface - TEM
Ru-W-N (N_2 = 10 sccm) No Cu overlayer	600	Surface - FESEM
Ru-Ta-N (N_2 = 10 sccm) No Cu overlayer	800	Surface - FESEM

7.2.2 Reaction and Phase Formation Mechanism

Upon annealing at high temperature, Cu and Ru diffuse into the Si substrate and eventually silicides would be formed. Silicides formation could be detected by several means such as increase in sheet resitance, XRD and FESEM. Table 7.5 lists the silicide formation temperatures of various sample stacks.

Table 7.5 Silicide formation temperature of Ru-based barrier films

		w/o Cu overlayer				with Cu overlayer			
		Ru/Si	Ru-N/Si	Ru-W-N/Si	Ru-Ta-N/Si	Ru/Si	Ru-N/Si	Ru-W-N/Si	Ru-Ta-N/Si
↑ Rsh		700	900	>900	>900	700	700	600	700
XRD	Ru_2Si_3	700	900	>900	>900	700	700	800	700
	Cu_3Si	-	-	-	-	800	700	800	800
	WSi_2	-	-	>900	-	-	-	800	-
	$TaSi_2$	-	-	-	>900	-	-	-	800
FESEM	silicides	-	-	-	-	700	700	600	700

Silicide formation temperature is higher in Ru-N and Ru-X-N compared to pure Ru for film without Cu overlayer. This is attributed to the presence of N at Ru/substrate interface which might have better miscibility in SiO_2 native

oxide than in the silicide hence led to changes in the entropy of mixing that eventually increased the silicide formation temperature.

For films with Cu overlayer, the effect of N in delaying the Ru_2Si_3 formation temperature was nullified by the presence of diffused Cu. Depending on the film composition especially at the interface where the silicides were formed, silicide formation temperature might be higher or lower however it was observed that the silicides formation temperature is above 600°C in Cu/Ru-based/Si system. Hence Ru-X-N films are generally sufficient diffusion barrier films up to 600°C.

7.2.3 Barrier Failure Mechanism

Table 7.6 summarizes the different barrier failure mechanism of different Ru based barrier layer.

Table 7.6 Barrier failure mechanism of different Ru based barrier layer

Pure Ru	Ru-N	Ru-W-N	Ru-Ta-N
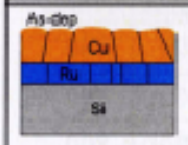	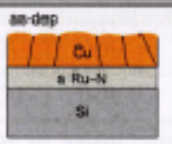	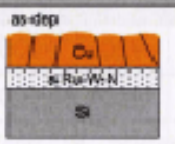	
	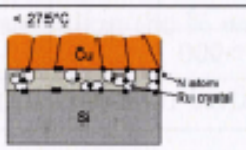		
	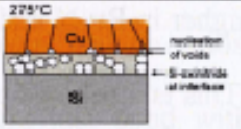	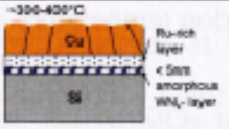	

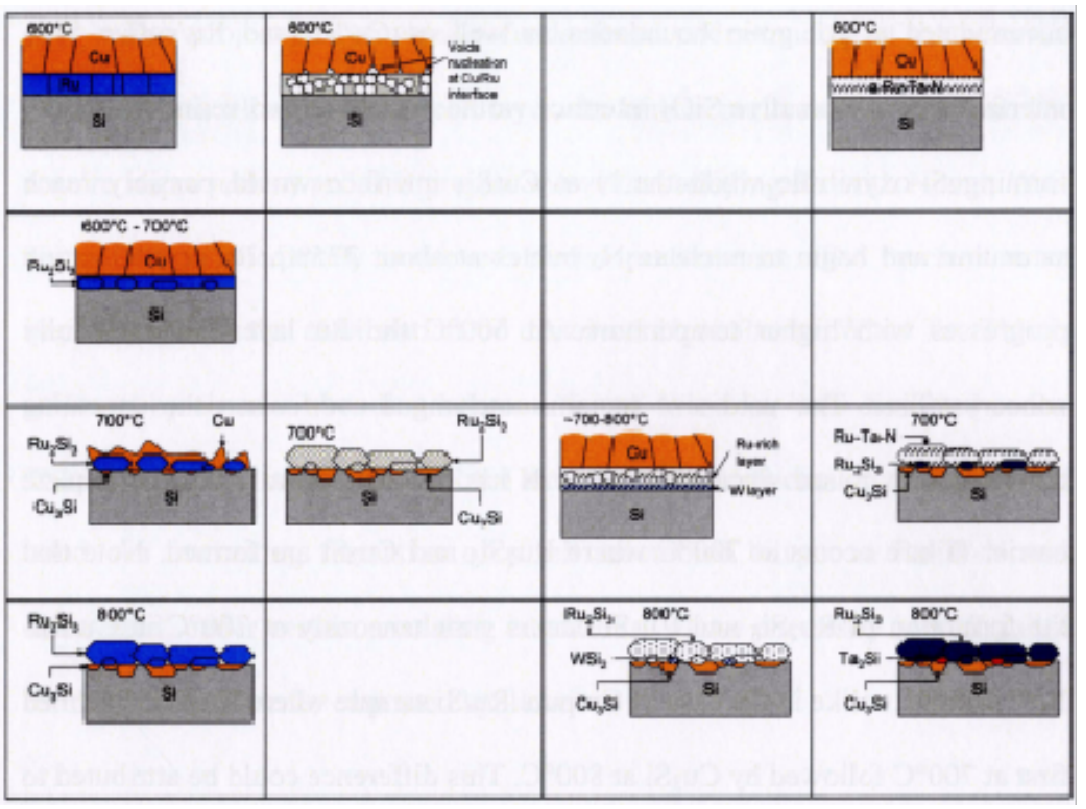

The metallization of Cu/pure Ru/Si is still intact without any interfacial reaction at 600°C as indicated by clear distinction of Cu, Ru, and Si layers. Annealing at 600°C - 700°C causes initial formation of Ru_2Si_3 phase at Ru/Si interface. This Ru_2Si_3 phase grows towards the Ru layer as annealing temperature increases. Concurrently Cu diffusion also continues to occur across the Ru and Ru_2Si_3 layers. At 700°C Cu_3Si phase forms at Ru_2Si_3/Si interface and grows into the Si substrate as the annealing temperature increases. At 800°C all the Ru and Cu layers would have been converted into Ru_2Si_3 and Cu_3Si phases, indicating complete failure of the barrier.

Ru-N film is amorphous in the as-deposited state with the N uniformly distributed in the Ru layer. Since Ru does not form any stable nitrides, annealing causes N out diffusion with concomitant Ru crystallization. The N rejected from the lattice out diffuses from the Ru layer and could possibly get

accumulated at Ru grain boundaries as well as Cu/Ru and Ru/native SiO_2 interfaces. N at Ru/native SiO_2 interface would possibly dissolve into the SiO_2, forming Si-oxynitride while the N at Cu/Ru interface would possibly reach saturation and begin to nucleate N_2 bubles at about 275°C. Ru crystallization progresses with higher temperature. At 600°C the Ru layer becomes fully nanocrystalline. The void size remains unchanged even when the annealing temperature is raised since most of the N has out diffused at 275°C. Complete barrier failure occurs at 700°C where Ru_2Si_3 and Cu_3Si are formed. Note that the formation of Ru_2Si_3 and Cu_3Si occurs simultaneously at 700°C in Cu/Ru-N/Si sample, unlike in the case of Cu/pure Ru/Si sample where Ru_2Si_3 is formed first at 700°C followed by Cu_3Si at 800°C. This difference could be attributed to the different microstructures.

As-deposited Ru-W-N and Ru-Ta-N samples have amorphous microstructure. Nitrogen atoms in these alloyed films are bound to W or Ta and exist in the form of nitrides. Enrichment of N and W at the film/substrate interface was observed upon annealing at temperature of ~300-400°C. Hence, a bilayer structure of a Ru-rich layer on top and a N- or WN_x-rich layer adjacent to the substrate were self-formed during thermal annealing. Silicide formation is concurrent with rapid Cu diffusion. Annealed Ru-Ta-N films do not show any N or Ta enriched self-formed layers as in the case of Ru-W-N films. In the Ru-W-based film, Cu diffusion was observed upon annealing at 700°C followed by Ru_2Si_3 + Cu_3Si + WSi_2 formation at 800°C; on the other hand, in Ru-Ta-based film, both Cu_3Si and Ru_2Si_3 formed simultaneously at 700°C followed by $TaSi_2$ at 800°C.

This project has provided a fundamental understanding of the behavior of pure Ru as a barrier cum seed layer. Its barrier performance was found to require improvement and this project shows that alloying Ru with N and, W or Ta, results in adequately improved barrier performance. The mechanism of improvement is the stabilization of dissolved N in Ru by W or Ta. This is achieved by chemical bonding between N and, W or Ta, both dissolved in Ru. The stabilization is effective until the temperature is high enough to destroy this bond. An interesting formation of a self assembled bilayer in Ru-W-N was discovered, under certain annealing conditions, whose chemistry is well suited for the intended barrier cum seed application.

7.3 Recommendations for Future Works

Further studies on Ru-based barrier material are required and the following directions are proposed:

1. To obtain the diffusivity and the activation energy of Cu diffusion in pure Ru layer. Diffusion couples of Cu/Ru could be created and annealed at different temperatures and, possibly, even for different times, and the resulting Cu concentration profiles in the Ru film should be determined by depth profiling using XPS. The experimental concentration profiles must be mathematically fitted to the solution to the diffusion equation and the operating diffusivity for each case must be determined. One may use the solution for non-steady state, semi-infinite plate given below as a first approximation, to determine the D value for each time and temperature case.

$$\frac{C_x - C_o}{C_s - C_o} = 1 - erf\left(\frac{x}{2\sqrt{Dt}}\right)$$

In this equation, C_x is the Cu concentration at a distance x from the interface, C_o is the initial concentration (= 0) and C_s is the concentration of Cu at the interface with Ru (= 1), D is the diffusivity of Cu in Ru at the annealing temperature T and t is the annealing time. For more accurate determination a solution to the exact diffusion couple must be determined. Thereafter, the Arrhenius equation

$$D = D_0 \exp(-Q/kT)$$

may be used to determine the activation energy Q, where R is gas constant and T is temperature in Kelvin.

2. To assess the platability of Ru-based barriers, especially when N and nitride forming elements are added together to the film. Making amorphous and thermally stable barrier film by incorporating N and nitride forming elements would increase film resistivity significantly which may degrade its Cu plateability. Hence it is important to optimize the N and nitride content in the barrier such that it has sufficient barrier property with good seeding ability.

3. To understand the performance of the barriers under electrical stress (e.g. Bias Temperature Stress, Capacitance-Voltage, leakage current measurements, etc). This is to study the barrier reliability. In this regard, metal-oxide-semiconductor (MOS) sandwich sample containing the Ru-based barrier material or dual damascene structure could be prepared.

4. To study the feasibility of using ALD technique to deposit Ru-based barriers (Ru-W-N or Ru-Ta-N). However this would depend on the availability of the precursors.

LIST OF PUBLICATIONS

Journal Papers

1. M. Damayanti, T. Sritharan, S. G. Mhaisalkar, and Z. H. Gan, "Effects of Dissolved Nitrogen in Improving Barrier Properties of Ruthenium", *Applied Physics Letters*, **88**, 044101 (2006).
2. M. Damayanti, T. Sritharan, Z. H. Gan, S. G. Mhaisalkar, N. Jiang, and L. Chan, "Ruthenium Barrier/Seed Layer for Cu/low-κ Metallization: Crystallographic Texture, Roughness, Diffusion and Adhesion", *Journal of The Electrochemical Society*, **153** (6), J41 (2006).
3. M. Damayanti, T. Srithatan, S. G. Mhaisalkar, H. J. Engelmann, E. Zschech, A. V. Vairagar, and L. Chan, "Microstructural evolution of annealed ruthenium-nitrogen films", *Electrochemical Solid-state Letters*, **10**, 15 (2007).
4. M. Damayanti, T. Sritharan, S. G. Mhaisalkar, E. Phoon, and L. Chan, "Mechanism of failure of Ru barrier in Cu/Ru/Si System", *Journal of Materials Research*, **22**, 9 (2007).
5. M. Damayanti, T. Sritharan, Y. Li, S. G. Mhaisalkar, "XPS Study of N-release from Ru-W-N and Ru-Ta-N Barriers in Cu Interconnects", in preparation.
6. M. Damayanti, T. Sritharan, S. G. Mhaisalkar, "Effect of Nitrogen Flow Rate on Thickness, Resistivity and Microstructure of as-deposited Ru-W-N Barrier Layer", in preparation.
7. M. Damayanti, T. Sritharan, Y. Li, S. G. Mhaisalkar, "Thermal Stability of Ru-W-N Barrier in Cu Interconnects", in preparation.

REFERENCES

1. Yue, J.T., *Reliability*, in *ULSI Technology*, C.Y. Chang and S.M. Sze, Editors. 1996, McGraw-Hill: USA. p. 656.
2. Torres, T., *Advanced Copper Interconnections for Silicon CMOS Technologies.* Appl. Surf. Sci., 1995. **91**: p. 112.
3. Chang, C.A., *Formation of Copper Silicides from Cu(100)/Si(100) and Cu(111)/Si(111) Structures.* J. Appl. Phys., 1990. **67**: p. 566.
4. Broniatowski, A., *Multicarrier Trapping by Copper Microprecipitates in Silicon.* Phys. Rev. Lett., 1989. **62**: p. 3074.
5. Lakshminarayanan, S., et al., *Contact and Via Structures with Copper Interconnects Fabricated Using Dual Damascene Technology.* IEEE Electr. Dev. Lett., 1994. **15**: p. 307.
6. Kim, J.J., et al., *Investigation of Various Copper Seed Layers for Copper Electrodeposition Applicable to Ultralarge-scale Integration Interconnection.* J. Vac. Sci. Technol. B, 2003. **21**: p. 1.
7. Peters, L., *Making a Better Copper Barrier*, in *Semicond. Int.* 2003. p. 26.
8. Furuya, A., et al. *Pore-sealing by etch-byproduct followed by ALD-Ta adhesion layer for Cu/porous low-k interconnects.* in *Interconnect Technology Conference*. 2004: IEEE.
9. Liu, J., et al. *In Situ XPS Study of ALD Ta(N) Barrier Formation on Organosilicate Dielectric Surface.* in *MRS Spring Meeting*. 2004: Materials Research Society.
10. Peng, C.H., et al. *A 90 nm Generation Copper Dual Damascene Technology with ALD TaN Barrier.* in *Electron Devices Meeting*. 2002: IEEE.
11. Singer, P., *Copper Challanges for the 45 nm Node*, in *Semicond. Int.* 2004.
12. Rossnagel, S., *The Latest in Ru-Cu Interconnect Technology*, in *Solid State Technology*. 2005, Solid State Technology.
13. Reid, J. and S. Mayer. in *Advanced Metallization Conference*. 2000. Warrendale PA.
14. Hara, T. and S. Sakata, *Stress in Copper Seed Layer Employing in the Copper Interconnection.* Electrochem. Solid-State Lett., 2001. **4**: p. G77.
15. Cooney, E.C., et al., *Effects of Collimator Aspect Ratio and Deposition Temperature on Copper Sputtered Seedlayers.* J. Vac. Sci. Technol. A, 1999. **17**: p. 1898.
16. Lee, W.H., et al., *Chemical vapor deposition of an electroplating Cu seed layer using hexafluoroacetylacetonate Cu (1,5-dimethylcyclooctadiene).* J. Vac. Sci. Technol. A, 2001. **19**: p. 2974.
17. Hwang, E.S. and J. Lee, *Surfactant-Assisted Metallorganic CVD of (111)-Oriented Copper Films with Excellent Surface Smoothness.* Electrochem. Solid-State Lett., 2000. **3**: p. 138.
18. Weiss, K., et al., *Development of different copper seed layers with respect to the copper electroplating process.* Microelectron. Eng., 2000. **50**: p. 433.
19. ITRS (2004) *International Technology Roadmap for Semiconductor (2004 Update).* **Volume**, 74

20. Radisic, A., et al., *Direct Copper Electrodeposition on TaN Barrier Layers.* J. Electrochem. Soc., 2003. **150**: p. C362.
21. Radisic, A., et al., *Nucleation and Growth of Copper on TiN from Pyrophosphate Solution.* J. Electrochem. Soc., 2001. **148**: p. C41.
22. Lane, M.W., et al., *Liner Materials for Direct Electrodeposition of Cu.* Appl. Phys. Lett., 2003. **83**: p. 12.
23. Massalki, T.B., *Binary Phase Alloy Diagrams*, ed. H. Okamoto. 1990: ASM International.
24. Chyan, O., T.N. Arunagiri, and T. Ponnuswamy, *Electrodeposition of Copper Thin Film on Ruthenium: A Potential Diffusion Barrier for Cu Interconnects.* J. Electrochem. Soc., 2003. **150**(5): p. C347.
25. Zavadil, K.R., D. Ingersoll, and R. J. W., Jr, *Electrochemical and Surface Spectroscopic Investigation of Copper(111) Films on Ruthenium(0001).* J. Electroanal. Chem. Interfacial Chem., 1991. **318**: p. 223.
26. Stuve, E.M., et al., *Ultrahigh Vacuum and Electrochemical Co-characterization Studies of Cu on Ru(0001).* Chem. Phys. Lett, 1988. **149**: p. 557.
27. Huong, C.N.V. and M.J.G. Tejera, *Underpotential Deposition of Copper and Silver on Polycrystalline Ruthenium Electrodes.* J. Electroanal. Chem. Interfacial Chem., 1988. **244**: p. 249.
28. Quiroz, M.A. and Y. Meas, *Characterization of a Ruthenium Electrode by Underpotential Deposition of Copper.* J. Electroanal. Chem. Interfacial Chem., 1983. **157**: p. 165.
29. Chan, R., et al., *Diffusion Studies of Copper on Ruthenium Thin Film.* Electrochem. Solid-State Lett., 2004. **7**(8): p. G154.
30. Ryu, C., et al. *Effect of Texture on The Electromigration of CVD Copper.* in *35th International Reliability Physics Symposium.* 1997. New York.
31. Zhang, Y., et al., *Underpotential Deposition of Copper on Electrochemically Prepared Conductive Ruthenium Oxide Surface.* Electrochem. Solid-State Lett., 2004. **7**(9): p. C107.
32. Josell, D., et al., *Seedless Superfill: Copper Electrodeposition in Trenches with Ruthenium barriers.* Electrochem. Solid-State Lett., 2003. **6**(10): p. C143.
33. Winter, M., *WebElements*. 1993.
34. Chunmei, W., *Electrical and Mechanical Properties of Ta-N-Cu Nanocomposite Thin Films*, in *Mechanical and Aerospance Engineering*. 2007, Nanyang Technological University: Singapore.
35. Istratova, A.A. and E.R. Weber, *Physics of Copper in Silicon.* J. Electrochem. Soc., 2002. **149**: p. G21.
36. Liu, C.S. and L.J. Chen, *Interfacial reactions of ultrahigh-vacuum-deposited Cu thin films on atomically cleaned (111)Si. I. Phase formation and interface structure.* J. Appl. Phys., 1993. **74**: p. 5501.
37. Hull, R., ed. *Properties of Crystalline Silicon.* 1999, INSPEC: London.
38. Gronover, C.R.M., *Microelectronics Material.* 1989.
39. Nicolet, M.A., *Diffusion Barriers in Thin Films.* Thin Solid Films, 1978. **52**: p. 415.
40. Katelus, H.P. and M.A. Nicolet, *Diffusion Barriers in Semiconductor Contact Metallization*, in *Diffusion Phenomena in Thin Films and*

Microelectronic Materials, D. Gupta and P.S. Ho, Editors. 1988, Noyes Publication: Park Ridge, New Jersey.

41. Baluffi, R. and J.M. Blakely, *Special Aspects of Diffusion in Thin Films.* Thin Solid Films, 1975. **25**: p. 363.
42. Kaloyeros, A.E. and E. Eisenbraun, *Ultrathin Diffusion Barriers/liners for Gigascale Copper Metallization.* Annu. Rev. Mater. Sci., 2000. **30**: p. 363.
43. Pokela, P., *Amorphous Diffusion Barriers for Electronic Device Applications*. 1991, Helsinki University of Technology: Helsinki.
44. Nicolet, M.A., ed. *Diffusion in Amorphous Materials*. 1994, TMS: Warrendale.
45. Wang, S.Q. in *ULSI-IX Conference*. 1994: Mater. Res. Soc. .
46. Chang, C. and C. Hu, *Reaction between Cu and TiSi2 across different barrier layers.* Appl. Phys. Lett., 1990. **57**: p. 617.
47. Arunagiri, T.N., et al., *5 nm ruthenium thin film as a directly plateable copper diffusion barrier.* Appl. Phys. Lett., 2005. **86**: p. 083104.
48. Kwon, O.K., et al., *Plasma-Enhanced Atomic Layer Deposition of Ruthenium Thin Films.* Electrochem. Solid-State Lett., 2004. **7**(4): p. C46.
49. Qu, X.P., et al., *Improved barrier properties of ultrathin Ru film with TaN interlayer for copper metallization.* Appl. Phys. Lett., 2006. **88**: p. 151912.
50. Wu, W.F., et al., *Effects of Nitrogen Plasma Treatment on Tantalum Diffusion Barriers in Copper Metallization.* J. Electrochem. Soc., 2003. **150**(2): p. G83.
51. Hubner, R., et al., *Structure and thermal stability of graded Ta-TaN diffusion barriers between Cu and SiO2.* Thin Solid Films, 2003. **437**: p. 248.
52. Lin, S.T., Y.L. Kuo, and C. Lee, *Characteristics of sputtered TaBx thin films as diffusion barriers between copper and silicon.* Appl. Surf. Sci., 2003. **220**: p. 349.
53. Liu, Y., et al., *Diffusion barrier performance of reactively sputtered Ta–W–N between Cu and Si.* Microe. Eng., 2004. **75**: p. 309.
54. Laurila, T., et al., *Amorphous layer formation at the TaC/Cu interface in the Si/TaC/Cu metallization system.* Appl. Phys. Lett., 2002. **80**: p. 6.
55. Kim, H.C. and T.L. Alford, *Investigation on diffusion barrier properties of reactive sputter deposited TiAl N O thin films for Cu metallization.* Thin Solid Films, 2004. **449**: p. 6.
56. Ee, Y.C., et al., *Barrier property of TiSiN films formed by low frequency, high density inductively coupled plasma process.* Surf. Coat. Technol., 2005. **193**: p. 291.
57. Lee, W.H., et al., *Effect of density on the diffusion barrier property of TiNx films between Cu and Si.* Matl. Chem. Phys., 2004. **85**: p. 444.
58. Nam, K.T., et al., *Improved diffusion barrier by stuffing the grain boundaries of TiN with a thin Al interlayer for Cu metallization.* Appl. Phys. Lett. **75**: p. 16.
59. Wu, W.F., et al., *PECVD-Ti/TiNx Barrier with Multilayered Amorphous Structure and High Thermal Stability for Copper Metallization.* Electrochem. Solid-State Lett., 2003. **6**(2): p. G27.

60. Kim, S.H., et al., *Atomic-layer-deposited WNxCy thin films as diffusion barrier for copper metallization.* Appl. Phys. Lett., 2003. **82**: p. 25.
61. Becker, J.S. and R.G. Gordon, *Diffusion barrier properties of tungsten nitride films grown by atomic layer deposition from bis(tert-butylimido) bis(dimethylamido) tungsten and ammonia.* Appl. Phys. Lett., 2003. **82**: p. 14.
62. Tsai, M.H., J.W. Yeh, and J.Y. Gan, *Diffusion barrier properties of AlMoNbSiTaTiVZr high-entropy alloy layer between copper and silicon.* Thin Solid Films, 2007. **Article in press**.
63. Song, Z.X., K.W. Xu, and H. Chen, *The characterization of Zr–Si–N diffusion barrier films with different sputtering bias voltage.* Thin Solid Films, 2004. **468**: p. 203.
64. Ou, K.L., et al., *Interfacial reactions and electrical properties of hafnium-based thin films in Cu/barrier/n+–p junction diodes.* Microe. Eng., 2005. **77**: p. 184.
65. Song, S., et al., *Diffusion barrier performances of thin Mo, Mo-N and Mo/Mo-N films between Cu and Si.* Thin Solid Films, 2005. **476**: p. 142.
66. Singh, S.K., et al., *Hot-wire chemical-vapor-deposited nanometer range a-SiC:H diffusion barrier films for ultralarge-scale-integrated application.* J. Vac. Sci. Technol. B, 2006. **24**: p. 2.
67. Murarka, S.P., *Metallization: Theory and practice for VLSI and ULSI.* 1993, Butterworth, Heinemann.
68. Diamand, Y.S., *Barrier Layers for Cu ULSI Metallization.* Journal of Electronic Materials, 2001. **30**(4): p. 336.
69. Wong, S.S., et al. *Effects of Barrier/Seed Layer on Copper Microstructure*. in *Advanced Metallization Conference*. 1998. Tokyo, Japan.
70. K. Jow, G.B.A., M. Sanganeria, G. Harm, H. Fu, X. Tang, G. Kooi, GW. Ray, M. Danek. *TDDB and voltage-ramp reliability of SiC-base dielectric diffusion barriers in Cu/ low-k interconnects*. in *41st Annual IEEE International Reliability Physics Symposium (IRPS)*. 2003.
71. ET. Ogawa, J.K., G. Haase, CH. Mogul, JW. McPherson. *Leakage breakdown and TDDB characteristics of porous low-k silica-based interconnect dielectrics*. in *IEEE International Reliability Physics Symposium (IRPS)* 2003.
72. West, A.C., S. Mayer, and J. Reid, *A Superfilling Model that Predicts Bump Formation.* Electrochem. Solid-State Lett., 2001. **4**(7): p. C50.
73. Ryu, C., et al. *Electromigration of Submicron Damascene Copper Interconnects*. in *Symposium on VLSI Technology Tech. Digest*. 1998.
74. Murarka, S.P., et al., *Advanced Multilayer Metallization Schemes with Copper as Interconnection Metal.* Thin Solid Films, 1994. **236**: p. 257.
75. Nandan, R., et al. in *Materials Research and Society Symposium*. 1992.
76. Ding, P.J., et al., *Thermal Annealing of Buried Al Barrier Layers to Passivate the Surface of Copper Films.* Appl. Phys. Lett., 1994. **65**: p. 14.
77. Chin, Y.L., B.S. Chiou, and W.F. Wu, *Effect of Aluminum Seed Layer on the Crystallographic Texture and Electromigration Resistance of Physical Vapor Deposited Copper Interconnect.* Jpn. J. Appl. Phys., 2000. **39**: p. 6708.

78. Sasaki, K., et al., *Realization of Cu(111) Single-Oriented State on SiO2 by Annealing Cu-Zr Film and the Thermal Stability of Cu-Zr/ZrN/Zr/Si Contact System.* Jpn. J. Appl. Phys., 2001. **40**: p. 4661.
79. Lee, W.H., et al., *Diffusion Barrier and Electrical Characteristics of A Self-aligned MgO layer obtained from a Cu(Mg) alloy film.* Appl. Phys. Lett., 2000. **77**: p. 14.
80. Josell, D., et al., *Iridium Barriers for Direct Copper Electrodeposition in Damascene Processing.* Electrochem. Solid-State Lett., 2006. **9**(2): p. C48.
81. Josell, D., C. Witt, and T.P. Moffat, *Osmium Barriers for Direct Copper Electrodeposition in Damascene Processing.* Electrochem. Solid-State Lett., 2006. **9**(2): p. C41.
82. Gayle, F.W. and F.S. Biancaniello, *Stacking faults and crystallite size in mechanically alloyed Cu-Co.* Nanostruct. Mater., 1995. **6**: p. 429.
83. *Rutherford Backscattering Spectroscopy (RBS).* [cited; Available from: **http://www.eaglabs.com/techniques/analytical_techniques/rbs.php**.
84. W. K. Chu, J.W. Mayer, and M.A. Nicolet, *Backscattering Spectrometry.* 1978, New York: Academic Press.
85. Charalambides, P.G., et al., *Development of a test method for Measuring the Mixed Mode Fracture Resistance of Bimaterial Interfaces.* Mechanics of Materials, 1990. **8**: p. 269.
86. Dauskardt, R.H., et al., *Adhesion and Debonding of Multi Layer Thin Film Structures.* Eng. Fract. Mech., 1998. **61**: p. 141.
87. AMAT (2008) *Applied Producer Black Diamond PECVD.* **Volume**,
88. Zhang, J.M., F. Ma, and K.W. Xu, *Calculation of the Surface Energy of FCC Metals with Modified Embedded-Atom Method.* Appl. Surf. Sci., 2004. **229**: p. 34.
89. Wagner, C.D., et al., *Handbook of X-ray Photoelectron Spectroscopy*, ed. G.E. Muilenberg. 1979, Eden Prairie, MN: Perkin-Elmer.
90. Liu, H.D., et al., *Thickness dependent electrical resistivity of ultrathin (< 40 nm) Cu films.* Thin Solid Films, 2001. **384**: p. 151.
91. Tellier, C.R. and A.J. Tosser, *Size Effect in Thin-Films.* 1982, Amsterdam: Elsevier.
92. Litteken, C.S., S. Strohband, and R.H. Dauskardt, *Residual stress effects on plastic deformation and interfacial fracture in thin-film structures.* Acta Materialia, 2005. **53**: p. 1955.
93. Kerr, J.A., *CRC Handbook of Chemistry and Physics, A Ready Reference Book of Chemical and Physical Data.* 81 ed, ed. D.R. Lide. 2000, USA: CRC Press.
94. Chromik, R.R., W.K. Neils, and E.J. Cotts, *Thermodynamic and Kinetic Study of Solid State Reactions in the Cu-Si System.* J. Appl. Phys., 1999. **86**: p. 4273.
95. Suh, B.S., et al., *Properties of Reactively Sputtered WNx as Cu Diffusion Barrier.* Thin Solid Films, 1999. **348**: p. 299.
96. Cabral, C., et al., *The use of in situ X-ray diffraction, optical scattering and resistance analysis techniques for evaluation of copper diffusion barriers in blanket films and damascene structures.* Thin Solid Films, 2001. **397**: p. 194.

97. Peterson, C.S., et al., *Silicides of Ruthenium and Osmium: Thin Film Reactions, Diffusion, Nucleation, and Stability.* J. Appl. Phys., 1982. **53**: p. 4866.
98. Gupta, R. and M. Gupta, *Nanocrystallization and amorphization induced by reactive nitrogen sputtering in iron and permalloy.* Phys. Rev. B, 2005. **72**: p. 024202.
99. Rha, S.K., et al., *Improved TiN film as a diffusion barrier between copper and silicon.* Thin Solid Films, 1998. **320**: p. 134.
100. Ronay, M. and R.G. Schad, *New insight into silicide formation: The creation of silicon self-interstitials.* Phys. Rev. Lett., 1990. **64**: p. 2042.
101. Lavoie, C., et al., *Effects of Alloying Elements on Cobalt Silicide Formation.* 2001, NSLS Activity Report. p. 16.
102. Selvaduray, G., *Ellingham Diagram.* 2008.
103. Baker, C.C. and A.I. Shah, *Reactive sputter deposition of tungsten nitride thin films.* J. Vac. Sci. Technol. A, 2002. **20**(5): p. 1699.
104. S. Tsukimoto, M.M., M. Murakami, *Microstructure of amorphous tantalum nitride thin films.* Thin Solid Films, 2004. **460**: p. 222.
105. Chechenin, N.G., et al., *Thermal stability of ultrasoft Fe–Zr–N films.* J. Phys. Condens. Matter., 2003. **15**: p. 7663.
106. Haglund, J., et al., *Theory of bonding in transition-metal carbides and nitrides.* Phys. Rev. B, 1993. **48**: p. 16.
107. Lin, J.C., G. Chen, and C. Lee, *Grain Boundary Diffusion of Copper in Tantalum Nitride Thin Film.* J. Electrochem. Soc., 1999. **146**: p. 1835.
108. Shinoki, F. and A. Itoh, *Mechanism of RF Reactive Sputtering.* J. Appl. Phys., 1975. **46**: p. 3381.
109. Kuo, Y.L., J.J. Huang, and S.T. Lin, *Diffusion Barrier Properties of Sputtered TaNx between Cu and Si using TaN as the Target.* Matl. Chem. And Phys., 2003. **80**: p. 690.
110. Shen, Y.G., et al., *Composition, residual stress, and structural properties of thin tungsten nitride films deposited by reactive magnetron sputtering.* J. Appl. Phys., 2000. **88**: p. 1380.
111. Lee, C.W., Y.T. Kim, and S.K. Min, *Characteristics of plasma enhanced chemical vapor deposited tungsten nitride thin films.* Appl. Phys. Lett., 1993. **62**: p. 3312.
112. Georgieva, A.K., et al., *Interface chemistry of WN/4H–SiC structures.* Appl. Surf. Sci., 1999. **151**: p. 225.
113. Chiu, H.T. and S.H. Chuang, *Tungsten nitride thin films prepared by MOCVD.* J. Mater. Res., 1993. **8**(1353).
114. Zhang, H.L., D.Z. Wang, and N.K. Huang, *The effect of nitrogen ion implantation on tungsten surfaces.* Appl. Sur. Sci., 1999. **150**: p. 34.
115. Kim, S.H., et al., *Atomic Layer Deposition of Low-Resistivity and High-Density Tungsten Nitride Thin Films Using B2H6, WF6, and NH3.* Electrochemical and Solid State Letters, 2006. **9**(3): p. C54.
116. Zhang, J.Y. and I.W. Boyd, *Thin Tantalum and Tantalum Oxide Films Grown by Pulsed Laser Deposition.* Appl. Surf. Sci., 2000. **168**: p. 234.
117. Zier, M., et al., *XPS and ARXPS Investigations of Ultra Thin TaN Films Deposited on SiO2 and Si.* Appl. Surf. Sci., 2005. **252**: p. 234.
118. Wang, Z., et al., *Influence of Surface Oxide of Sputtered TaN on Displacement Plating of Cu.* Jpn. J. Appl. Phys., 2003. **42**: p. 1843.

119. Niu, E., et al., *Synthesis and characterization of tantalum nitride films prepared by cathodic vacuum arc technique.* Appl. Surf. Sci., 2007. **253**: p. 5223.
120. Lin, J., et al., *Conversion of tungsten nitride to pure tungsten.* J. Vac. Sci. Technol. A, 1998. **16**: p. 611.
121. Lin, J., et al., *Different effect of annealing temperature on resistivity for stoichiometric, W rich, and N rich tungsten nitride films.* J. Vac. Sci. Technol. A, 1999. **17**: p. 936.
122. Ecke, R., et al., *Development of PECVD WNx ultrathin film as barrier layer for copper metallization.* Microelectron. Eng., 2002. **64**: p. 261.
123. Fairley, N., *The Casa cookbook: X-ray photoelectron spectroscopy-Data processing.* 2005: Acolyte Science.
124. Vomiero, A., et al., *Structural properties of reactively sputtered W–Si–N thin films.* J. Appl. Phys., 2007. **102**: p. 033505.
125. Willey, K.F., H.F. Arlinghaus, and T.J. Whitaker, *Routine analysis at sub-micron resolution through the use of sputtered initiated resonance ionization spectroscopy.* Appl. Sur. Sci., 1999. **144**: p. 36.
126. Lee, K.S., *Crystallization of Reactively Sputtered Amorphous Tungsten Nitride Film.* Jpn. J. Appl. Phys., 2003. **42**: p. 3368.